Exploration of how light interacts with arrays of plasmonic, metallic nanoparticles

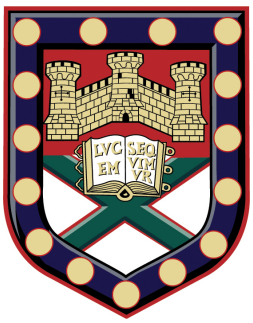

Alastair Dalziell Humphrey

School of Physics

University of Exeter

A thesis submitted for the degree of

Doctor of Philosophy in Physics

September 2015

Exploration of how light interacts with arrays of plasmonic, metallic nanoparticles

Submitted by Alastair Dalziell Humphrey to the University of Exeter as a thesis for the degree of Doctor of Philosophy in Physics
September 2015

I certify that all material in this thesis which is not my own work has been identified and that no material has previously been submitted and approved for the award of a degree by this or any other University.

Alastair Dalziell Humphrey
September 2015

I'd like to dedicate this thesis to the memory of my friend Michael Adlem (1982–2002).

Acknowledgements

This thesis represents four years of my work, but without the constant support from others in some shape or form along the way, I honestly don't think I would have ever got to this point. I must now take the time to thank those people that have helped me along the way.

Firstly, I would like to extend my utmost gratitude to my supervisor Prof. Bill Barnes for his enthusiasm, persistence and knowledge. Bill was my supervisor for my MPHYS project, and I have him to thank for instigating my keen interest in the field of plasmonics - thank you for the countless supervisor meetings over coffee, and for the opportunity to go to conferences and present my work.

I am indebted to Dr. Nina Meinzer for acting as an unofficial supervisor and for being on hand to help, especially with sample fabrication.

In the second year of my Ph.D, I was lucky enough to become an honouree member of the basementeers (Dr. Tim Starkey, Dr. Matt Nixon, Dr. Alfie Lethbridge and Luke McDonald) - YEAH! Without these guys I definitely wouldn't have made the journey! A special mention must be given to Prof. Pete Vukusic for allowing me to tag onto the natural photonics group's currys, and for making me feel like one of the group.

I owe much thanks to Nick Cole in the workshop for his time and effort fabricating components for my optical setup, as well as Chris Forrest for getting my Mac back up and running after several power cuts.

I must also thank past and present members of the EM Group that have been around in the background during my PhD: Dr. Joe Dockrey (Panda), Dr. Laura Parke (Barbie), Gareth Ward, Ben Tremain, Dr. Caroline Pouya, Dr. Rhi Mitchell-Thomas, Dr. Tom Constant, Dr. Ian Hooper (Hoops), Dr. Dimi Polyushkin, Dr. Sara Núñez-Sánchez, Dr. Helen Rance, Dr. Matt Lockyear and Daniel Hewson, sorry for others that I have forgotten.

Lastly, I must extend my thanks to my Mum, Dad and Marion for their constant encouragement and support throughout my Ph.D.

Abstract

The content of this thesis is based upon the interaction of light with metallic nanoparticles arranged in different array geometries. An incident electric field (light) can force the conduction electrons of a metallic nanoparticle to oscillate. At particular frequencies, in the optical regime for gold and silver particles, absorption and scattering of the light by the particle is enhanced, corresponding to the particle plasmon resonance. The spectral position and width of the particle plasmon resonance of an isolated single particle may be tuned by adjusting its size and shape, thus changing the surface charge distribution.

Periodic arrays of particles offer additional control over the frequency and width of the resonance attributed to the re-radiating (scattering) property of plasmonic particles. By fabricating arrays with a pitch comparable to the wavelength of an isolated single particle plasmon resonance, a coherent interaction between particles may be produced, known as surface lattice resonances (SLRs).

The electromagnetic coupling between in-plane particle plasmon modes for different particle array geometries is explored through experiment and theory. Firstly, SLRs in square, hexagonal and honeycomb arrays are investigated by normal-incidence extinction measurements and compared to a simple-coupled dipole model. Secondly, to verify the nature of the coupling between the scattered electric field associated with particle resonances, the incident electric field polarization-dependence of the extinction of rectangular arrays and chains is studied. Thirdly, the optical response of square arrays with a symmetric two-particle basis is investigated, particularly the retardation of the scattered electric field between particles in a pair. Fourthly, square arrays with an asymmetric two-particle basis are fabricated to explore the symmetric (dipole moments of both particles are parallel) and anti-symmetric (dipole moment of both particles anti-parallel) SLRs, excited by normal-incidence light.

Contents

Contents i

List of Figures v

List of Tables xv

Nomenclature xv

1 Introduction 1

1.1 Introduction . . . 1

1.2 Introduction to particle plasmons . . . 2

1.2.1 Quasi-static approximation: spherical particles . . . 3

1.3 Lorentz model . . . 4

1.4 Drude model . . . 8

1.5 Single particle response . . . 10

1.5.1 Optical cross-sections . . . 17

1.6 Two particles . . . 20

1.7 Array of particles . . . 26

1.8 Conclusion . . . 31

1.9 Thesis overview 33

2 Single particle response **37**

2.1 Introduction 37

2.2 Modelling techniques 38

2.2.1 Quasi-static approximation: non-spherical particles 38

2.2.2 Modified long-wavelength approximation 42

2.2.3 Kuwata: empirical polarizability 42

2.2.4 Mie: exact solution for spherical particles 43

2.3 Electron-beam lithography 47

2.4 Dark-field scattering measurements 50

2.5 Conclusion 56

3 Response of regular arrays of plasmonic nanoparticles **59**

3.1 Introduction 59

3.2 Modelling of array response 60

3.2.1 Coupled-dipole approximation 60

3.2.2 *S*-factor: a semi-analytical coupled-dipole model 63

3.2.3 Finite-element modelling 68

3.2.4 Comparison of methods used to model the optical response of arrays 70

3.3 Array fabrication 73

3.4 Optical charaterization techniques 75

3.5 Extinction measurements of square, hexagonal and honeycomb arrays . 79

3.6 Conclusion 90

4 Optical response of rectangular arrays **91**

4.1 Introduction 91

4.2 Polarization dependence of rectangular arrays 91

4.3 Coupling in regular arrays of plasmonic particles 97

4.4 Conclusion 105

5 Symmetric two-particle basis square arrays **107**

5.1 Introduction 107

5.2 One-particle basis square arrays 109

5.3 Two-particle basis square arrays 115

5.3.1 Retardation between particle pairs 123

5.3.1.1 Modelling approaches of particle pair 123

5.3.1.2 Extinction measurements on arrays with different particle pair centre-to-centre separations 128

5.4 Conclusion 133

6 Asymmetric two-particle basis square arrays **135**

6.1 Introduction 135

6.2 Modifications to analytical coupled-dipole model 136

6.3 Extinction measurements on arrays with an asymmetric basis 138

6.4 Conclusion 155

7 Conclusions and future work **157**

7.1 Conclusions 157

7.2 Future work 162

7.2.1 Direct extensions 162

7.2.2 Graphene-like plasmonic lattices 163

7.2.3 Surface lattice resonance mediated lasing 163

7.3 Publications and presentations 163

7.3.1 Refereed papers 163

7.3.2 Oral presentations 164

7.3.3 Poster presentations 164

References **165**

List of Figures

1.1 Scanning-electron micrographs and dark-field images of several isolated silver nanoparticles made by electron-beam lithography. 2

1.2 Amplitude and phase of the electron oscillation displacement with respect to the incident electric field calculated using the Lorentz model with various different damping parameters. 7

1.3 Comparison of the Lorentz and Drude model for the permittivity of a material. 9

1.4 Plot of the skin depth vs. wavelength for bulk silver and gold. 10

1.5 Plot of the real part of the relative permittivity vs. wavelength for silver and gold. 11

1.6 Resonant light scattering of light by a silver nanowire with the incident electric field parallel or perpendicular to the long-axis of the nanowire. . 12

1.7 Experimental nanorod data: (a) absorption spectrum illustrating the two resonances (transverse and longitudinal) and (b) the long-axis plasmon mode wavelength as a function of aspect ratio. 13

1.8 Transmission electron microscope (TEM) lateral size vs. the spectral peak wavelength for a diverse collection of individual silver nanoparticles. 14

1.9 Measured transmission spectra of 240 nm pitch square arrays of gold discs with a diameter of 130 nm with various heights. 15

1.10 Diagram to indicate the resonant energy E_{res} and line-width Γ of the plasmon resonance. 16

List of Figures

1.11 Quality factor of single nanorods and nanospheres vs. resonance energy E_{res}. 17

1.12 Dark-field spectra and scanning-electron micrographs from isolated particles (diameter $D = 95$ nm, height $h = 25$ nm) and particle pairs for varying separations. 21

1.13 Diagram indicating two possible combinations of near-field coupling for a plasmonic particle pair. 22

1.14 Spectral position of the extinction maximum vs. inter-particle distance for seven different particle-pair separations of gold discs with a diameter of 150 nm and height 17 nm. 23

1.15 Calculated plasmon line-widths (FWHM) and plasmon energies of a pair of 80 nm diameter gold nanospheres as functions of the centre-to-centre inter-particle distance D. 25

1.16 (a) scanning-electron micrograph of cylindrical particles in a hexagonal arrangement, (b) measured extinction spectra of the same arrangement but with a variety of array pitches and (c) dependence of the particle plasmon peak wavelength as a function of pitch d for the arrays in (b). . 27

1.17 Plasmon decay time and particle plasmon resonance wavelength vs. pitch (350–850 nm) of different square arrays. 28

1.18 Transmittance spectra for gold nanorod arrays in homogeneous index environment and asymmetric refractive index configuration for five array pitches. 29

1.19 (a) scanning-electron micrograph of gold disc array. (b) intensity distribution on the surface of single gold disc and on the surface of gold disc in an array. (c) near-field intensity enhancement spectra for a single isolated gold disc and for gold discs in 2D arrays of different grating pitches. 30

1.20 Schematic illustrating the two different polarizations of the incident electric field: (a) TM and (b) TE-polarized light. 31

1.21 Measured transmittance spectra of 400 nm pitch square arrays of gold nanoparticles with heights of $h = 65$ nm, 100 nm, 120 nm and 170 nm under (a) TM- and (b) TE-polarized light. 32

2.1 3:1 aspect ratio prolate and oblate spheroids. 39

2.2 Geometrical factors L_a, L_b and L_c of prolate and oblate spheroids plotted against aspect ratio R. 40

2.3 Variation of dipole particle plasmon wavelength with geometrical factor L with three different surrounding media of different refractive index. . 41

2.4 Mie calculated absorption, scattering and extinction cross-sections of four different radii silver spheres embedded in a refractive index of $n = 1.5$. 44

2.5 Comparison of extinction cross-sections calculated by quasi-static, modified long-wavelength approximation, Kuwata and Mie for three different radii of silver spheres. 46

2.6 Schematic of electron-beam lithography process outlining the key steps involved. 48

2.7 Schematic of experimental dark-field setup. 51

2.8 Colour image taken using a CCD coupled to an optical microscope illustrating the resonantly scattered light from silver nanoparticles. 52

2.9 CCD images of the dispersion of the (a) lamp, (b) dark and (c) signal spectra. 53

2.10 Dark-field scattering spectra of silver discs ($d = 110$ nm, $h = 30$ nm) arranged in a 2 μm pitch square array. 54

2.11 (a) measured and (b) Modified long-wavelength approximation calculated scattering spectra of single silver discs with various diameters ($d = 70$ nm, $d = 85$ nm, $d = 95$ nm, $d = 110$ nm and $d = 125$ nm). . . . 55

3.1 The total electric field on the central particle in the array is the sum of the incident electric field plus the scattered field from the other particles. 65

3.2 Comparison of (a) un-smoothed and (b) smoothed S-factor of a 480 nm pitch square array. 66

3.3 Calculated (a) real and (b) imaginary parts of $1/\alpha$ and $\varepsilon_0 S$ and (c) calculated extinction cross-section per particle for an oblate spheroid ($d = 120$ nm, $h = 30$ nm) in a square array with a pitch of 480 nm. . . . 67

3.4 Comparison of the three different methods used in this thesis to calculated the optical response (extinction cross-section per particle) of a square array (480 nm pitch) of silver discs ($d = 120$ nm, $h = 30$ nm). . . 71

3.5 Scanning-electron micrographs of examples of arrays made by nanosphere lithography. 73

3.6 Scanning-electron micrographs of different regions of one 50 μm × 50 μm write-field illustrating particle variation attributed to distortion of the electron-beam at the extremities. 74

3.7 Schematic of setup to measure the transmission of arrays of particles. . 76

3.8 CCD image of the dispersion of the transmission from two square arrays with different pitches: (a) 480 nm and (b) 350 nm. 78

3.9 Measured extinction spectrum of a 480 nm pitch square array of silver discs ($d = 120$ nm, $h = 30$ nm) with the incident electric field parallel to the y-axis of the array. 79

3.10 (a) schematic example of a square array and (b) dispersion diagram of the square array. 80

3.11 Scanning-electron micrographs of different array geometries (square, hexagonal and honeycomb) of silver discs ($d = 120$ nm, $h = 30$ nm). 81

3.12 (a) measured extinction cross-section per particle; (b) calculated extinction cross-section per particle and; (c) S-factor for a square array (480 nm pitch) of silver discs ($d = 120$ nm, $h = 30$ nm). 84

3.13 (a) measured extinction cross-section per particle; (b) calculated extinction cross-section per particle and; (c) S-factor for a hexagonal array (555 nm nearest neighbour separation) of silver discs ($d = 120$ nm, $h = 30$ nm). 85

3.14 (a) measured extinction cross-section per particle; (b) calculated extinction cross-section per particle and; (c) S-factor for a honeycomb array (320 nm nearest neighbour separation) of silver discs ($d = 120$ nm, $h = 30$ nm). 86

3.15 (a) measured extinction cross-section per particle of square, hexagonal and honeycomb arrays with corresponding real parts of $1/\alpha$ and $\varepsilon_0 S$ shown in (b). 88

3.16 Measured extinction vs. wavelength of the three different array geometries: (a) square, (b) hexagonal and (c) honeycomb. In each case, the incident electric field polarization is swept in 15° increments from 0° (parallel to the x-axis of the arrays) to 90° (parallel to the y-axis). . . . 89

4.1 Scanning-electron micrograph of a rectangular array with $g_x = 370$ nm and $g_y = 480$ nm, where g_x and g_y are the pitches in the x- and y-directions respectively. The particles are silver discs with $d = 120$ nm and $h = 30$ nm. 92

4.2 (a) measured extinction cross-section per particle and (b) calculated extinction cross-section per particle for a rectangular array with $g_x = 370$ nm and $g_y = 480$ nm, where g_x and g_y are the pitches in the x- and y-directions respectively. The particles are silver discs ($d = 120$ nm, $h = 30$ nm) and were illuminated with linearly-polarized light at normal incidence. 94

4.3 (a) extinction cross-section per particle and (b) S-factor for a rectangular array of silver discs ($d = 120$ nm, $h = 30$ nm), together with the calculated inverse polarizability of an isolated particle. $g_x = 370$ nm and $g_y = 480$ nm for the rectangular array, were g_x and g_y are the pitches in the x- and y-directions respectively. 95

4.4 (a) S-factor, (b) CDA and (c) FEM calculated extinction cross-section per particle of silver discs ($d = 120$ nm, $h = 30$ nm) in a $g_x = 370$ nm and $g_y = 480$ nm rectangular array, where g_x and g_y are the pitches in the x- and y-directions respectively. The electric field was either parallel to the x- or y-axis of the array. 96

4.5 Scanning-electron micrographs of silver particle arrays with different x-pitches, g_x, and same y-pitches, g_y. For all arrays $g_y = 480$ nm. (a) $g_x = 370$ nm, (b) $g_x = 480$ nm (square array), (c) $g_x = 520$ nm and (d) $g_x = 560$ nm. All the arrays consist of silver discs with a diameter of 120 nm and height of 30 nm. 98

4.6 Measured extinction cross-section per particle as a function of wavelength of arrays with different x-pitches, g_x, and same y-pitches, g_y. $g_y = 480$ nm for all of the arrays. Arrays have $g_x = 370$ nm, $g_x = 480$ nm (square array), $g_x = 520$ nm and $g_x = 560$ nm. All the arrays consist of silver discs with a diameter of 120 nm and height of 30 nm. 99

4.7 S-factor calculated extinction cross-section per particle as a function of wavelength of arrays with different x-pitches, g_x, and same y-pitches, g_y. For all of the arrays $g_y = 480$ nm. Arrays have $g_x = 370$ nm, $g_x = 480$ nm (square array), $g_x = 520$ nm and $g_x = 560$ nm. All the arrays consist of silver discs with a diameter of 120 nm and height of 30 nm. 100

4.8 S-factor calculated extinction cross-section per particle as a function of wavelength of four different pitches, g, of silver particle chains ($g = 370$ nm, 480 nm, 520 nm and 560 nm). The chains are made up of oblate spheroids with $d = 120$ nm and $h = 30$ nm. 102

4.9 Calculated S-factor of four different pitches, g, of silver particle chains ($g = 370$ nm, 480 nm, 520 nm and 560 nm). The chains are made up of oblate spheroids with $d = 120$ nm and $h = 30$ nm. 103

4.10 S-factor calculated extinction cross-section per particle showing the contribution of the different field components to the extinction spectrum. Calculation is of 480 nm pitch square array of silver discs ($d = 120$ nm, $h = 30$ nm). 105

5.1 Modified long-wavelength approximation calculated extinction cross-section (left axis) and phase of polarizability (right axis) with respect to the incident electric field of a single silver disc ($d = 85$ nm, $h = 30$ nm). 110

5.2 Scanning-electron micrographs of one-particle basis square arrays with four different pitches, g. The particles were silver discs with $d = 85$ nm and $h = 30$ nm. 112

5.3 Measured extinction cross-section per particle vs. wavelength of four different pitches, g, square arrays ($g = 350$ nm, 400 nm, 450 nm and 500 nm) with a one-particle basis. The particles were silver discs ($d = 85$ nm and $h = 30$ nm). 113

5.4 Simple coupled-dipole model calculated (a) extinction cross-section per particle and (b) $\varepsilon_0 S$ for four different pitch square arrays ($g = 350$ nm, 400 nm, 450 nm and 500 nm) with a one-particle basis. 114

5.5 Scanning-electron micrographs of four different pitch, g, square arrays with a two-particle basis. The basis consisted of two discs ($d = 85$ nm and $h = 30$ nm) with a 150 nm centre-to-centre separation. 116

5.6 Measured extinction cross-section per pair vs. wavelength of four different pitches, g, of two-particle basis square arrays of silver discs ($d = 85$ nm and $h = 30$ nm). The particle centre-to-centre in the basis was 150 nm. 118

5.7 Simple coupled-dipole model calculated extinction cross-section per particle pair vs. wavelength of four different pitches, g, of two-particle basis square arrays. The basis consisted of two silver oblate spheroids with $d = 85$ nm and $h = 30$ nm. 120

5.8 (a) simple coupled-dipole model extinction cross-section per pair vs. wavelength and (b) $\varepsilon_0 S$ of four different pitches, g, of two-particle basis square arrays with $g = 350$ nm, 400 nm, 450 nm and 500 nm. The basis comprised of two silver discs with $d = 85$ nm and $h = 30$ nm and a centre-to-centre separation of 150 nm. 121

5.9 (a) Pinchuk effective polarizability and (b) coupled-dipole approximation calculated extinction cross-section per particle of a single particle pair (both particles have $d = 85$ nm, $h = 30$ nm) with a centre-to-centre separation 150 nm. 124

5.10 Comparison of S-factors and calculated extinction cross-sections of a 400 nm pitch square array with a two-particle basis. In (a) retardation of the scattered electric field between particles in the pair was included and in (b) ignored. 126

5.11 Comparison between the (a,b) measured and (c,d) S-factor calculated extinction cross-section per pair of a 400 nm pitch square array with a two-particle basis. The optical response of the two-particle basis array was described as two particles, each particle with their own polarizability (α_1 and α_2) - hence retardation of the scattered electric field between the particles in the pair was included. 127

5.12 Scanning-electron micrographs of 500 nm pitch square arrays with a two-particle basis of silver discs (d = 115 nm and h = 30 nm) with different centre-to-centre separations, l. 129

5.13 Measured extinction cross-section per particle pair vs. wavelength of 500 nm pitch square arrays with a two-particle basis of silver discs (d = 115 nm and h = 30 nm). Extinction spectra are shown for four different centre-to-centre separations, l = 160 nm, 180 nm, 200 nm and 220 nm. . 130

5.14 Simple-coupled dipole model calculated extinction cross-section per particle pair vs. wavelength of 500 nm pitch square arrays with a two-particle basis of silver discs (d = 115 nm and h = 30 nm). Extinction spectra are shown for four different centre-to-centre separations of l = 160 nm, 180 nm, 200 nm and 220 nm. 131

5.15 Simple coupled-dipole model calculated (a) extinction cross-section per particle pair and (b) $\varepsilon_0 S$ for 500 nm pitch square arrays with a two-particle basis (d = 115 nm and h = 30 nm). Spectra are shown for three different centre-to-centre separations (l = 120 nm, 185 nm and 250 nm) with the incident electric field perpendicular to the particle-pair axis. . . 132

6.1 Diagram indicating r_j and θ_j that are used to calculate S, which is the contribution of the scattered electric fields from the same particle type in the pair and r'_f and θ'_f that are used to calculate S', which is the contribution of the scattered electric fields from the different particle type in the pair. 137

6.2 (a) Modified long-wavelength approximation calculated extinction cross-section of single particles (d = 85 nm and d = 115 nm, both with height of 30 nm) and (b) coupled-dipole approximation calculated extinction cross-section of a single asymmetric particle pair (d_1 = 85 nm and d_2 = 115 nm, both with 30 nm height). 139

6.3 Scanning-electron micrographs of different pitches, g, of square array with an asymmetric-two-particle basis: (a) $g = 350$ nm, (b) $g = 400$ nm, (c) $g = 450$ nm and (d) $g = 500$ nm. The centre-to-centre separation of the particle pair was 150 nm. 141

6.4 Measured extinction cross-section per pair vs. wavelength of different pitches, g, of square arrays with asymmetric-two-particle basis with a 150 nm centre-to-centre separation. The dimensions of particle 1 were $d_1 = 85$ nm, $h_1 = 30$ nm and the dimensions of particle 2 were $d_2 = 115$ nm, $h_2 = 30$ nm. 142

6.5 Simple coupled-dipole model calculated extinction cross-section per pair vs. wavelength for different pitch, g square arrays with a two-particle asymmetric basis. The particles were silver discs ($d_1 = 85$ nm, $h_1 = 30$ nm and $d_2 = 115$ nm, $h_2 = 30$ nm) with a 150 nm centre-to-centre separation. 143

6.6 (a,b) measured and (c,d) finite-element model calculated extinction cross-section per particle pair vs. wavelength of a 350 nm pitch square array with an asymmetric two-particle basis ($d_1 = 85$ nm and $d_2 = 115$ nm). The particles have a centre-to-centre separation of 150 nm and both have a height of 30 nm. 145

6.7 Spatial distribution of electric fields for a 350 nm pitch square array with an asymmetric two-particle basis of silver discs ($d_1 = 85$ nm and $d_2 = 115$ nm). 146

6.8 S-factor calculated extinction cross-section per particle pair of 450 nm pitch square arrays with an asymmetric two-particle basis ($d_1 = 85$ nm and $d_2 = 115$ nm, both with 30 nm height). The calculations were performed for three different centre-to-centre separations, l, of the pair ($l = 150$ nm, 190 nm and 225 nm). 148

6.9 Coupled-dipole approximation calculated extinction cross-section per particle pair of different single asymmetric pairs. For each of the particle pairs, $d_1 = 90$ nm while d_2 is varied. 150

6.10 Scanning-electron micrographs of 500 nm pitch square arrays with different asymmetric two-particle bases of silver discs with a 150 nm centre-to-centre separation and 30 nm height. 151

6.11 Measured extinction cross-section per pair vs. wavelength of 500 nm pitch square arrays with a two-particle basis of silver discs with a centre-to-centre separation of 150 nm and height 30 nm. The diameter of particle 1 in the pair was kept constant ($d_1 = 90$ nm) while the diameter of particle 2 was increased from smaller to larger than particle 1. 153

6.12 Finite-element model calculated (a,b) extinction spectra and (c-g) spatial distribution of electric fields for a symmetric basis ($d_1 = d_2 = 90$ nm) and asymmetric basis ($d_1 = 90$ nm and $d_2 = 110$ nm) in a 500 nm pitch square array. 154

List of Tables

3.1 Spectral positions and magnitudes of surface lattice resonances from experiment and different modelling approaches: S-factor, the coupled-dipole approximation and finite-element method. 72

3.2 Experimental and S-factor calculated extinction cross-sections for square, hexagonal and honeycomb geometries. 87

4.1 Experimental and S-factor calculated extinction cross-sections for rectangular arrays with different values of g_x but all with g_y=480 nm. Also added for comparison is S-factor calculated extinction cross-sections for particle chains with the same values of g_x as the rectangular arrays. . . 104

5.1 Experimental and S-factor calculated extinction cross-sections for one- and two-particle basis square arrays with the incident electric field either parallel (x-pol) or perpendicular (y-pol) to the pair axis). 122

List of Tables

Chapter 1

Introduction

1.1 Introduction

In this chapter, the concept of particle plasmons, which are also know as a localized-surface plasmon resonances (LSPRs) [1–3], are introduced. A particle plasmon is the result of the motion of conduction electrons in a metallic nanoparticle oscillating in response to an applied harmonic electric field [4]. A logical starting point is to describe how a metal responds to an applied electric field. The optical response of materials is dominated by their electrons, but for metals their optical response is dominated by their conduction electrons. The response of the electrons can be described via a frequency dependent permittivity by considering the induced dipole moments resulting from the applied field. The frequency dependent permittivity of materials gives rise to the phenomenon of dispersion where by different frequencies of light travel at different velocities in a medium. In this chapter, to model the permittivity, the Lorentz and Drude models are introduced. The difference between the Lorentz and Drude models is that the Lorentz model includes a restoring force, whilst the Drude model does not, which is like the free conduction electrons for metals at optical frequencies.

In the remainder of the chapter, the current relevant literature is reviewed in parallel with the background physics in order to develop an understanding of the physical concepts. Previous studies show that the size, shape and dielectric environment of a nanoparticle influence the spectral position and width of the particle plasmon resonance. The absorbed and scattered light from the particle is normally expressed in the form of a cross-section, where the amount of absorbed or scattered light is normalized with

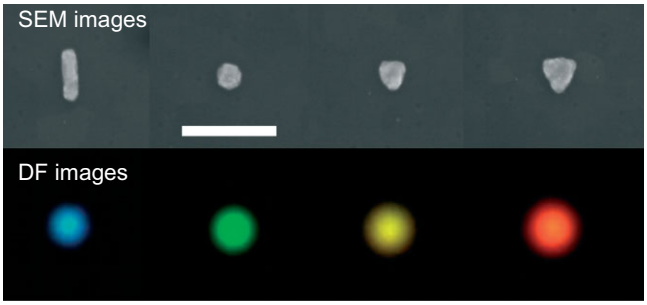

Figure 1.1: Scanning-electron micrographs (top) and dark-field images (bottom) of several isolated silver nanoparticles made by electron-beam lithography. From left to right the shapes are, a rod, a disc, and two triangles (the right hand one being the larger of the two). The thickness of these particles is 30 nm and the substrates are silica glass coated with 20 nm of Indium Tin Oxide (scale bar: 300 nm). Images taken from Ref. [5].

the intensity of the incident electric field.

Following the review of the plasmonic properties of an isolated single particle, the interactions between particle plasmon resonances in single pairs and periodic arrays in previous investigations are reviewed. The chapter concludes with a thesis overview, containing a description of each chapter.

1.2 Introduction to particle plasmons

The resonant nature of a plasmon mode supported by a metallic nanoparticle can be probed by collecting the light scattered by the particle in question (by dark-field spectroscopy). Different shapes and sizes of particle resonantly scatter light at different wavelengths, thereby giving rise to different colours, this is illustrated in Figure 1.1. The physics behind this is as follows. When an electric field (light) is incident upon a metallic nanoparticle, the field forces the mobile conduction electrons in the particle to oscillate. These accelerating charges in turn radiate light, this process is known as scattering. The collective motion of the oscillating charges results in an oscillating dipole moment. The strength of the scattered light depends on the magnitude of the dipole moment, $|\vec{p}|$, which is related to the incident electric field $\vec{E}$ by the polarizability of the particle, α, see Equation 1.1:

$$\vec{p} = \varepsilon_0 \alpha \vec{E}, \tag{1.1}$$

where ε_0 is the permittivity of free space. The scattering cross-section σ_{sca} is related

to the polarizability by,

$$\sigma_{\text{sca}} = \frac{k^4}{6\pi}|\alpha|^2, \tag{1.2}$$

where k is the wave number in the surrounding medium. The σ_{sca} is defined as the area that must block the beam to remove the same amount of power from the incident beam as the scattering particle. Cross-sections for gold and silver particles can be larger than their geometric cross-section.

1.2.1 Quasi-static approximation: spherical particles

The quasi-static approximation, also known as Rayleigh approximation, is valid when the dimensions of the particle are much smaller than the wavelength (when $a/\lambda \leq 0.01$, where a is the radius of the sphere) [6] and thus the polarization field can be considered to be uniform throughout the volume of the particle, i.e. retardation can be ignored. For a sphere small enough that the Rayleigh approximation holds, the polarizability of the sphere is given by the *Clausius-Mossotti* relation [7],

$$\alpha(\omega) = 4\pi a^3 \frac{\varepsilon_m(\omega) - \varepsilon_s}{\varepsilon_m(\omega) + 2\varepsilon_s}, \tag{1.3}$$

where a is the radius of the sphere, $\varepsilon_m(\omega)$ is the frequency dependent relative permittivity of the metal sphere and ε_s is the relative permittivity of the surrounding medium. The polarizability of the particle describes the response of the collective electron oscillation to an external electric field when subjected to a different charge distribution enforced by the shape of the particle [4]. The phase of the polarizability indicates the phase of the collective electron motion with respect to the incident electric field. From inspection of Equation 1.3, it is seen that the polarizability takes a maximum value when the denominator is minimized. When this occurs the *Fröhlich* condition is met,

$$\Re[\varepsilon(\omega)] = -2\varepsilon_s, \tag{1.4}$$

where $\Re[\varepsilon(\omega)]$ refers to the real part of the relative permittivity of the metal. The permittivity of the metal describes the response of the electrons in a bulk metal to an applied electric field, and is frequency dependent. The frequency dependence of the

material permittivity gives rise to dispersion - different frequencies of light will have different phase velocities in such a medium. Silver and gold have a high density of free electrons, and therefore have a negative real part of their permittivity at optical frequencies (approximately 10^{15} Hz), making them good plasmonic materials. Particle plasmon resonances have also been observed in aluminium triangular particles [8] and platinum and palladium discs [9].

1.3 Lorentz model

The response of materials, especially metals, to an electromagnetic field is dominated by the response of its constituent electrons and gives rise to the phenomenon of dispersion. To describe the motion of the electrons to an external electromagnetic field, it is necessary to begin by implementing Newton's second law of motion,

$$\vec{F} = m\frac{d^2\vec{r}}{dt^2} \tag{1.5}$$

where $\vec{F}$ is the *net* force on the electron, m is the mass of the electron and $\vec{r}$ is the displacement of the electron. By considering all of the forces acting on the electron an equation of motion can be constructed,

$$m\frac{d^2\vec{r}}{dt^2} = -\xi\frac{d\vec{r}}{dt} - \eta\vec{r} - e\vec{E}, \tag{1.6}$$

where ξ is a damping constant, η is the effective spring constant arising from the Coulomb restoring force, e is the absolute charge of an electron and $\vec{E}$ is the local electric field. The first term on the right-hand side of Equation 1.6 describes the damping force from the scattering of the electrons, the second term describes the Coulomb restoring force from the positive ionic cores and the third term gives the force provided by the applied electric field. The damping term has a negative sign because the frictional force always opposes the velocity of the electron and the restoring force term has a negative sign because the restoring force is always opposite to the displacement of the electron. The driving electric field has a harmonic time dependence and can be written as $\vec{E} = \vec{E}_0 \exp(-i\omega t)$. An assumption of the Lorentz model is that the displacement of the electron will oscillate at the same frequency as the applied electron field, so a guess of the form of the displacement can be made as $\vec{r} = \vec{r}_0 \exp(-i\omega t)$. Using the harmonic

time dependent forms of the electric field and displacement yields,

$$-m\omega^2\vec{r} = i\omega\xi\vec{r} - \eta\vec{r} - e\vec{E}. \tag{1.7}$$

Equation 1.7 can be rearranged to make $\vec{r}$ the subject,

$$\vec{r} = \frac{e\vec{E}}{m\omega^2 + i\omega\xi - \eta}, \tag{1.8}$$

and can be written in the following form,

$$\vec{r} = \frac{e\vec{E}/m}{\omega^2 + i\omega\xi/m - \eta/m}. \tag{1.9}$$

Then the substitutions $\gamma = \xi/m$ and $\omega_0 = \sqrt{\eta/m}$ can be made, where ω_0 is the resonant frequency, to yield,

$$\vec{r} = \frac{e\vec{E}/m}{\omega^2 + i\omega\gamma - \omega_0^2} \tag{1.10}$$

From Equation 1.10 it can be observed that the complex displacement, $\vec{r}_0$ is given by,

$$\vec{r}_0 = \frac{e\vec{E}_0/m}{\omega^2 + i\omega\gamma - \omega_0^2}. \tag{1.11}$$

The complex amplitude of the displacement relates the phase of the electron displacement to the applied electric field. The phase of the displacement is defined as the phase difference between the applied electric field and the electron displacement. Figure 1.2 illustrates the (a) amplitude and (b) phase of the displacement (see Equation 1.11) with $\omega_0 = 3$ Hz and various different damping parameters. As the damping parameter is decreased, the amplitude of the electron oscillation increases and the change in phase of the displacement with respect to the incident field becomes more step like. There are three main regimes in the phase of the electron oscillation as the frequency of the driving field is varied: low frequency, resonance and high frequency. At low frequencies the electron displacement is π rad behind the driving field, corresponding to being in-phase with the driving force (the force is opposite to the field as an electron is being

considered). Here the polarization of the material is in-phase with the electric field. On resonance there is a $\pi/2$ rad phase difference between the electric field and the electron oscillation displacement and the amplitude of oscillation of the electrons is greatest. Near resonance (just above and below) is the region of *anomalous* dispersion where the real part of the permittivity decreases with frequency. On resonance maximum absorption occurs, where a material can in fact be opaque as the electrons have their largest amplitude, and a large amount of energy is being dissipated by the damping mechanism. At high frequencies the displacement and field are in-phase (electron displacement lags the force by π rad) as the electrons can not follow the applied force from the electric field and their displacement tends towards zero and the polarization of the material is in anti-phase with the applied electric field.

The electrons displaced from their equilibrium positions contribute,

$$\vec{P} = -ne\vec{r}, \tag{1.12}$$

to the macroscopic polarization of the material, where n is the number density of electrons. By inserting Equation 1.10 into Equation 1.12, the macroscopic polarization of the material can be expressed in the form,

$$\vec{P} = \frac{-ne^2/m\vec{E}}{\omega^2 + i\omega\gamma - \omega_0^2}. \tag{1.13}$$

The polarization for a linear, homogeneous and isotropic material is related to the applied electric field by the following relation,

$$\vec{P} = \varepsilon_0(\varepsilon - 1)\vec{E}, \tag{1.14}$$

where ε_0 is the permittivity free space and ε is the relative permittivity of the material. By equating Equations 1.13 and 1.14, the permittivity can be found to be,

$$\varepsilon = 1 - \frac{ne^2/m}{\varepsilon_0(\omega^2 + i\omega\gamma - \omega_0^2)}. \tag{1.15}$$

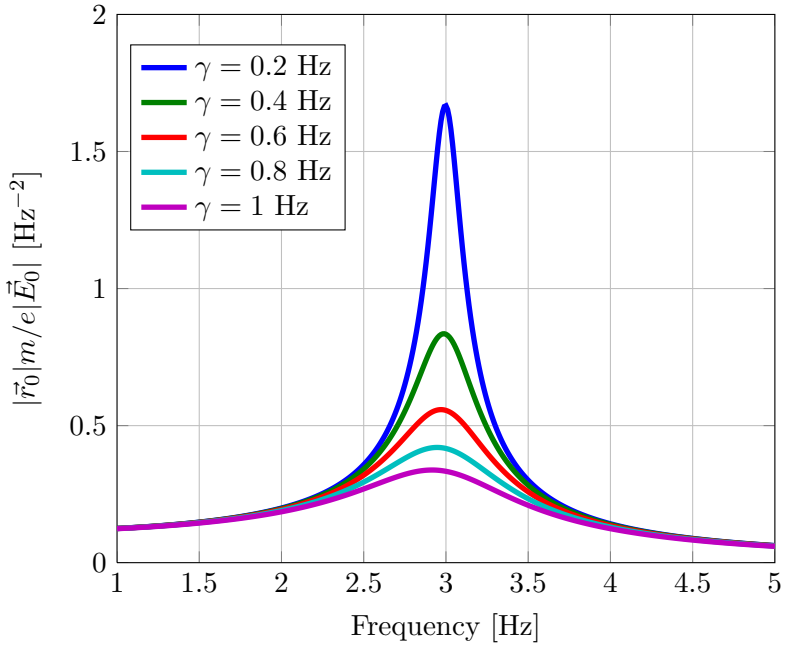

(a) Amplitude.

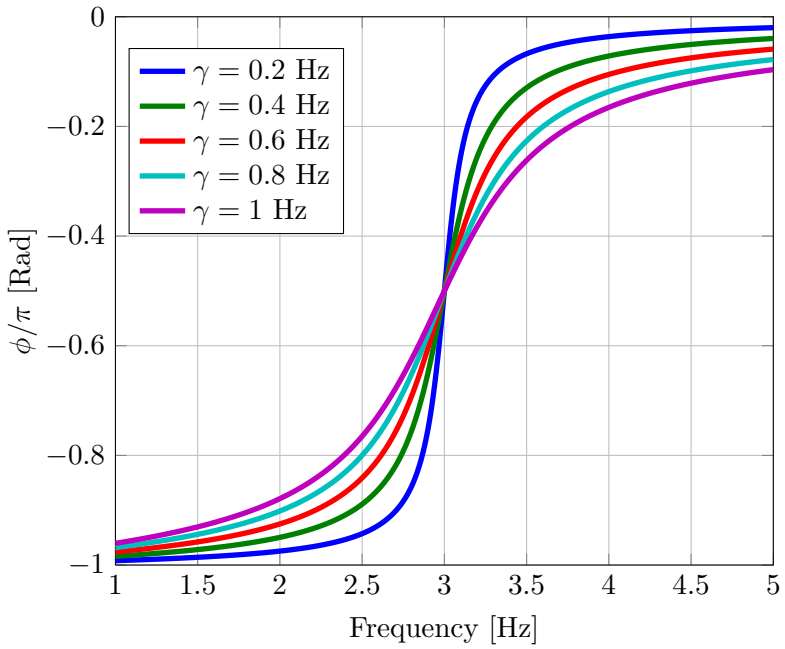

(b) Phase of the amplitude with respect to the electric field.

Figure 1.2: (a) amplitude and (b) phase of the electron oscillation displacement with respect to the incident electric field calculated using the Lorentz model (see Equation 1.11) with $\omega_0 = 3$ Hz and various different damping parameters.

The permittivity is usually expressed in the form,

$$\varepsilon = 1 - \frac{\omega_p^2}{\omega^2 + i\omega\gamma - \omega_0^2} \tag{1.16}$$

where ω_p is the plasma frequency and is given by the following relation,

$$\omega_p = \sqrt{\frac{ne^2}{\varepsilon_0 m}}. \tag{1.17}$$

1.4 Drude model

In the Drude model of the permittivity, the restoring force from the Coulomb interaction between the ionic cores and electrons is neglected, which is equivalent to setting ω_0 to zero in the Lorentz model (see Equation 1.16). This assumption is made because the optical properties of metals are dominated by the response of their free conduction electrons which have a zero restoring force. The permittivity in the Drude model is therefore,

$$\varepsilon(\omega) = 1 - \frac{\omega_p^2}{\omega^2 + i\gamma\omega}. \tag{1.18}$$

Figure 1.3 displays the (a) Lorentz and (b) Drude permittivity for a hypothetical material with the values $\omega_p = 4$ Hz, $\omega_0 = 3$ Hz and $\gamma = 0.6$ Hz. In (a), ω_0 corresponds to when the real part of the permittivity is equal to one and the imaginary part takes its maximum value. The region were the real part of the permittivity is negative (see grey shaded regions in Figures 1.3a and 1.3b) means a wave can not propagate inside the medium and the wave instead decays evanescently.

For an electric field propagating in the x-direction the field can be written as,

$$\vec{E} = \vec{E}_0 \exp i(kx - \omega t), \tag{1.19}$$

where t is time. Since $k = nk_o$, and $n = \sqrt{\varepsilon}$, where n is the refractive index in the

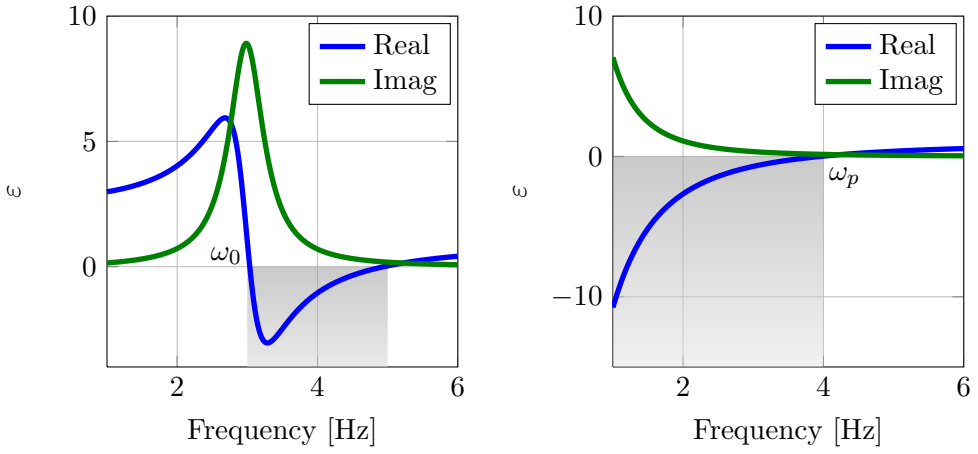

(a) Lorentz. **(b)** Drude.

Figure 1.3: Comparison of the (a) Lorentz (see Equation 1.16) and (b) Drude (see Equation 1.18) model for the permittivity of a material. The calculations have been performed with the values of $\omega_p = 4$ Hz, $\omega_0 = 3$ Hz and $\gamma = 0.6$ Hz.

material and k_0 is the freespace wave number, Equation 1.19 can be expressed as,

$$\vec{E} = \vec{E}_0 \exp i(\sqrt{\varepsilon} k_0 x - \omega t). \tag{1.20}$$

If the real part of the permittivity is negative, then $\sqrt{-\varepsilon} = \sqrt{-1}\sqrt{\varepsilon} = i\sqrt{\varepsilon}$. Equation 1.20 becomes,

$$\vec{E} = \vec{E}_0 \exp i(i\sqrt{\varepsilon} k_0 x - \omega t) = \vec{E}_0 \exp(-\sqrt{\varepsilon} k_0 x) \exp(-i\omega t), \tag{1.21}$$

an evanescently decaying wave, propagating in the x-direction with a complex amplitude of $\vec{E}_0 \exp(-\sqrt{\varepsilon} k_0 x)$. The distance required for the amplitude of the electric field to be reduced to $1/\exp$ of its initial value is defined as the *skin depth*. The skin depth for bulk silver and gold are shown in Figure 1.4. The skin depth for silver and gold is between 25 nm and 45 nm at optical wavelengths.

In the Drude model (see Figure 1.3b) there is no resonant behaviour and the real part of the permittivity becomes negative below the plasma frequency. The frequency at which the real part of the permittivity becomes negative is actually just above the plasma frequency. In the absence of damping, the real part would become negative at frequencies below the plasma frequency.

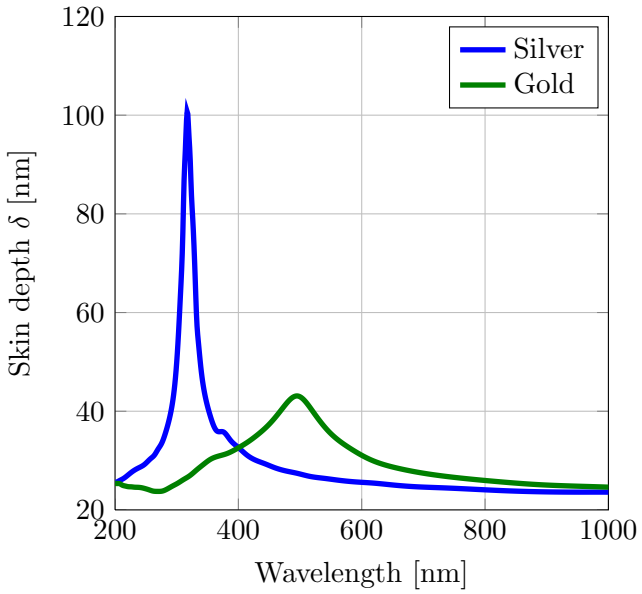

Figure 1.4: Plot of the skin depth vs. wavelength for bulk silver and gold. Skin depth calculated using $\delta = \lambda/2\pi\kappa$ with optical constants taken from Refs. [10] (silver) and [11] (gold).

From Equation 1.4 it is seen that for different surrounding materials (i.e. different ε_s) although the metallic particle is the same, the particle plasmon resonant condition occurs at different wavelengths. For glass the refractive index n equals 1.5, making its relative permittivity $\varepsilon_s = n_s^2 = 2.25$. Figure 1.5 shows the real and imaginary parts of the relative permittivity of bulk gold and silver. The values for bulk gold were determined by reflection and transmission measurements by Johnson and Christy [11], and the silver values were taken from Ref. [10]. In both cases, a spline fit has been used to fit the permittivity between wavelengths of 200 nm and 1000 nm. From Figure 1.5 it can be seen that the particle plasmon resonance condition is satisfied when $\lambda \approx 530$ nm for gold and $\lambda \approx 410$ nm for silver.

1.5 Single particle response

Mock *et al.* [12] experimentally observed a red-shift in spectral position of the particle plasmon resonance with increasing refractive index (1.44–1.56) using dark-field spectroscopy of isolated spherical and triangular silver particles. Murray *et al.* [13] carried out a similar experiment with rods and disc-shaped gold particles and confirmed this red-shifting of the single particle plasmon resonance with an increase of surrounding refractive index.

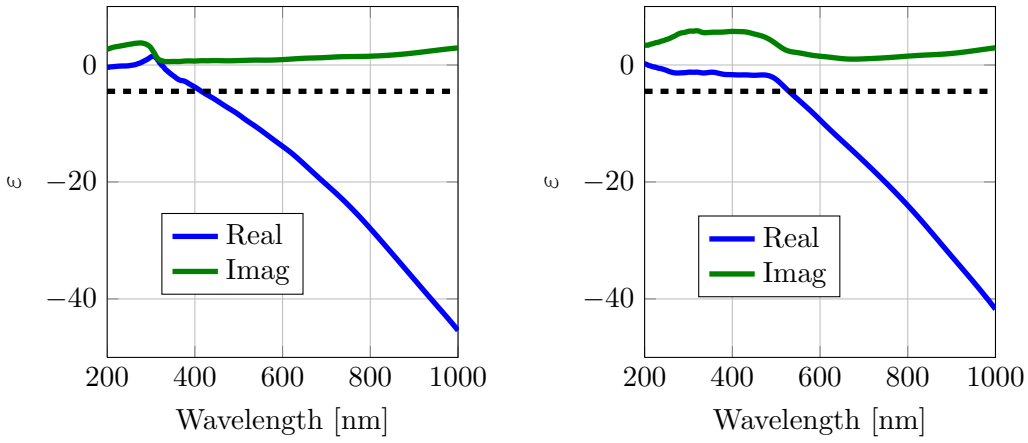

(a) Silver. **(b)** Gold.

Figure 1.5: Plot of the real part of the relative permittivity vs. wavelength for silver and gold. Real part of relative permittivity calculated using $\varepsilon = n^2 - \kappa^2$ with a spline fit of optical constants taken from references [10] (silver) and [11] (gold). Dashed line drawn at a value of -4.5 for the real part of the relative permittivity. This gives $\lambda \approx 530$ nm for gold and $\lambda \approx 410$ nm for silver that satisfy the resonance condition, (see Equation 1.3) when surrounded by glass ($\varepsilon_s = 2.25$).

For spherical particles there only exists one resonant particle plasmon mode when illuminated with unpolarized light at normal incidence. This is different from non-spherical particles, which have two or more resonant modes. A simple non-spherical particle is the nanorod and this will be discussed first. Nanorods have two resonant modes, one corresponding to charge oscillating parallel to the long-axis and one corresponding to charge oscillating parallel to the short-axis [14]. An example of the polarization dependence of the incident light can be seen in the single particle scattering spectra of a silver nanowire by Barbic *et al.* [15] in Figure 1.6. Link *et al.* [16] produced ensembles (300 particles) of gold nanorods using an electrochemical method and measured their absorption as a function of wavelength with unpolarized light.

An example of the absorption spectrum obtained by Link *et al.* of a sample of randomly orientated nanorods with an aspect ratio of 3.3 (75 nm × 25 nm) is presented in Figure 1.7. Evident in Figure 1.7 are two peaks, with one peak corresponding to a particle plasmon resonance of the long-axis (longitudinal) mode (740 nm) and one corresponding to the short-axis (transverse) mode (525 nm). When the aspect ratio (long-axis/short-axis) of the nanorod is increased the short-axis mode blue-shifts and the long-axis mode red-shifts [17, 18]. The blue-shift of the short axis mode is small compared to the red-shift of the long-axis mode, so the long-axis mode is more intensely studied. Funston *et al.* [19] studied the change in spectral position as a function of

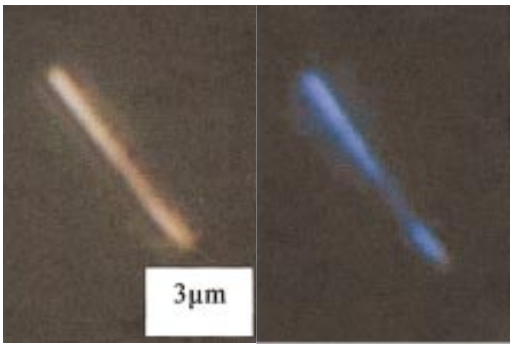

(a) Parallel. **(b)** Perpendicular.

Figure 1.6: Resonant light scattering of light by a silver nanowire with the incident electric field (a) parallel or (b) perpendicular to the long-axis of the nanowire. The violet light corresponds to the short-axis plasmon mode and the orange to the long-axis. Images taken from Ref. [15].

aspect ratio of the long-axis plasmon mode of gold nanorods in air (see Figure 1.7b). For each measurement, Funston *et al.* plot the spectral position of the scattering peak against aspect ratio, observing a linear correlation between the peak plasmon wavelength and aspect ratio (the plasmon mode position red-shifts with increasing aspect ratio). Physically this is due the charge distribution being altered as the shape of the particle is changed. Depending on the orientation of the incident electric field with respect to the nanorod a combination of the two modes (longitudinal and transverse) will be excited. The relative strength of each mode will depend on the magnitude of the electric field component parallel to the relevant axis [20–22].

Mock *et al.* [23] investigated the effect of changing the shape and size of isolated silver nanoparticles on the spectral position of the particle plasmon resonance. They collected dark-field scattering spectra of spheres, pentagons and triangles of different sizes and recorded the peak plasmon wavelength associated with the spectra for each different particle and size (see Figure 1.8). They discovered that spheres have the shortest wavelength particle plasmon resonance, then pentagons and then triangles. Additionally, it can be observed from Figure 1.8 that for each different particle type, the particle plasmon resonance position red-shifted with increasing particle size. This shape and size dependence of the spectral position of the particle plasmon resonance was then verified again later by Anker *et al.* [24]. Mock *et al.* also found that for triangles the resonant frequency is dependent on the sharpness of the tips of the particle (sharper tips have a red-shifted particle plasmon resonance). They found that by rounding off the tips of triangles the resonance peak position blue-shifted from 625 nm to 555 nm.

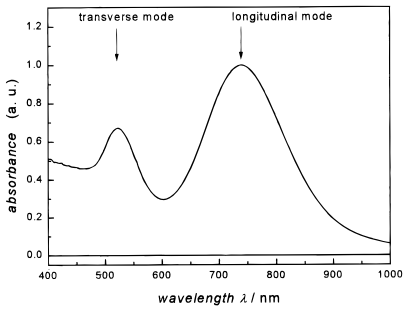

(a) Experimental absorption spectrum of a gold nanorod sample with an average aspect ratio of 3.3 from Ref. [16].

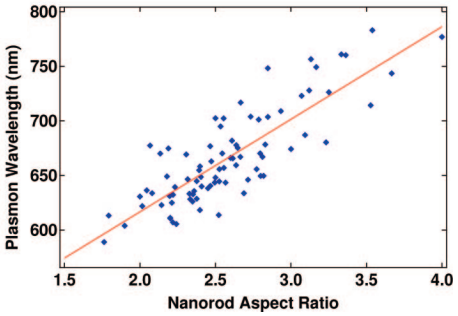

(b) Long-axis mode of gold nanorod as a function of rod aspect ratio (long-axis/short-axis) from Ref. [19].

Figure 1.7: Experimental nanorod data: (a) absorption spectrum illustrating the two resonances (transverse and longitudinal) and (b) the long-axis plasmon mode wavelength as a function of aspect ratio. In (a) the mode at 525 nm is referred to as the short-axis (transverse) mode, while the one centered at 740 nm is called the long-axis (longitudinal) mode. In (b) each data point is corresponds to one rod for which the spectrum and scanning-electron micrograph were measured. The rods were dispersed on Indium-tin-oxide-coated glass in air.

This shifting of the dipole in-plane resonance had been predicted earlier by Jin *et al.* [25]. Jin *et al.* demonstrated the effect of edge rounding via modelling two different isolated triangles immersed in water: the first one with edge length of 100 nm and height 100 nm, and the second one with the same height but with a snip of 12 nm, where the snip is the length of the side of triangle cut from the tip of the original triangle. Each triangle was modelled by dividing up its volume into an array of N dipoles from which the extinction cross-section can then be found. Jin *et al.* found that by taking a snip of 12 nm off each the corner of triangle that the in-plane dipole resonance shifted from 770 nm to 670 nm. More recently Jayabalan *et al.* [26] confirmed the blue-shift of the in-plane dipole resonance with increasing snip size by modelling the extinction of triangles using the same method as Jin *et al.*, but with more variation in snip size (15 nm to 23 nm).

Henson [27] *et al.* fabricated arrays of gold discs with a diameter of 130 nm and various heights by electron-beam lithography (EBL) in order to investigate the influence of nanoparticle height on the spectral position of the particle plasmon resonance. The key point here is that the arrays had small pitches (240 nm) and were hence non-diffracting within the spectral range of the single particle resonance. Additionally they did not index-match the environment of the particles. They found a blue-shift in the single particle resonance from approximately 625 nm to 515 nm by changing the particle

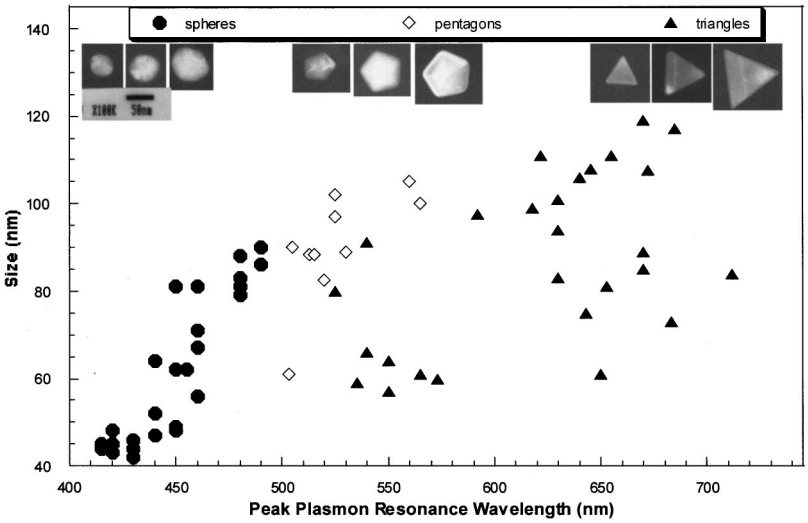

Figure 1.8: Transmission electron microscope (TEM) lateral size vs. the spectral peak wavelength for a diverse collection of individual silver nanoparticles. The size of each particle was assigned using the TEM image taken with the e-beam normal to the sample and by comparing a characteristic dimension to the TEM calibration bar. The characteristic dimension for a spherical particle is the diameter, for a pentagon it is the length between opposite corners and for a triangle it is the length of a side. Representative high-resolution TEM images for three different size particles, of each geometrical shape, are also shown. Figure taken from Ref. [23].

height from 20 nm to 160 nm (see Figure 1.9).

So far the spectral position of the particle plasmon resonance has been discussed, now the factors which determine the width of the resonance will be investigated. This is a good point to reintroduce the equation of motion for one of the conduction electrons, which takes the form of a forced oscillator [7, 28],

$$m\frac{d^2\vec{r}}{dt^2} = -\xi\frac{d\vec{r}}{dt} - m\omega_0^2\vec{r} - e\vec{E}, \tag{1.22}$$

where m is the mass of an electron, $\vec{r}$ is the displacement of the electron, η is the spring constant, e is the elementary charge of an electron, ω_0 is the resonant frequency and E is the applied electric field. The spring constant arrises from the Coulomb force between the conduction electrons and the ionic cores. The resonant frequency is given by,

$$\omega_0 = \sqrt{\frac{\eta}{m}}. \tag{1.23}$$

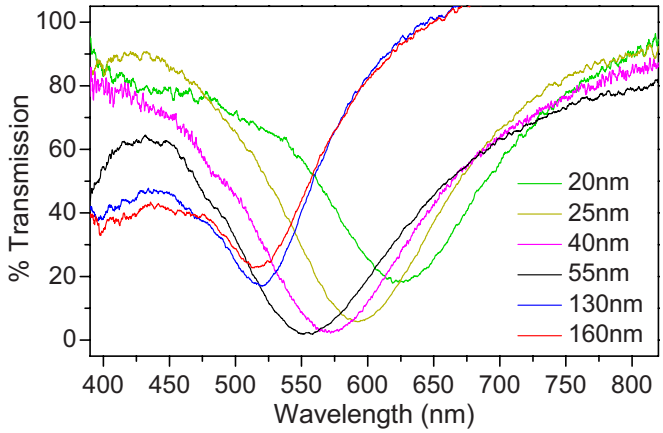

Figure 1.9: Measured transmission spectra of 240 nm pitch square arrays of gold discs with a diameter of 130 nm with various heights. Figure reproduced from Ref. [27].

As mentioned earlier, an applied electric field will displace the conduction electrons of the nanoparticle from their equilibrium positions, which induces a dipole moment. This displacement creates a separation of charge, creating a restoring force. The restoring force of the particle plasmon resonance can be altered by changing the shape or size of particle, which results in a different surface charge distribution. Note: an increase in η (i.e increase in restoring force) will increase (blue-shift) the resonant frequency. Whereas a reduction in η will decrease the restoring force, therefore decrease (red-shift) the resonant frequency. The *quality factor,* Q of a resonator, which is related to the damping of the system, is given by,

$$Q = \frac{\omega_0 m}{\xi} \equiv \frac{\lambda_{\text{res}}}{\Delta\lambda} \equiv \frac{E_{\text{res}}}{\Gamma}, \tag{1.24}$$

where λ_{res} and E_{res} are the resonant wavelength and energy respectively, $\Delta\lambda$ is the full-width half maximum and Γ is the line-width (E_{res} and Γ are illustrated in Figure 1.10). Notice from Equation 1.24 that the line-width is directly related to the damping of the system. Resonators with higher Q-factors have lower damping, a smaller line-widths and a greater amplitude of oscillation than lower Q-factor resonators. The relationship between damping and line-width of the resonance allows the damping of the system to be determined directly from the line-width of the oscillation.

Sherry *et al.* [30] fabricated silver triangles by a photoinduced conversion of colloidal spheres to triangles using the method described elsewhere Ref. [25]. This allowed Sherry *et al.* to produce triangles with a varying degree of tip rounding, so they could perform dark-field scattering measurements. From the scattering measurements they

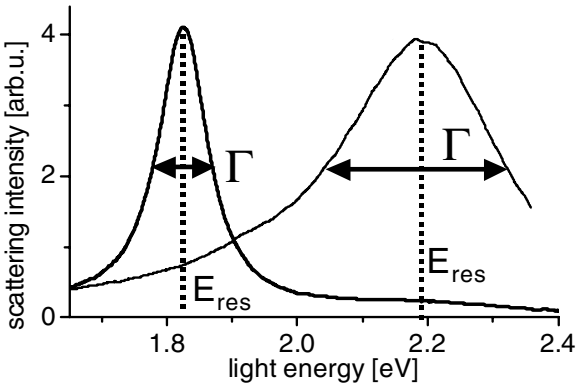

Figure 1.10: Diagram to indicate the resonant energy E_{res} and line-width Γ of the plasmon resonance. The spectrum on the left has a smaller line-width than the one on the right, therefore the resonance has lower damping. Diagram adapted from Ref. [29].

found that the plasmon in-plane dipole resonance line-width is directly related to the sharpness of the corners of the triangle: the sharper the tips of the triangle are the broader the line-width. They confirmed this relationship between tip sharpness and line-width by modelling the different triangles as a volume of single polarizable units. They suggest the tip sharpness and line-width correlation is due to the lightning rod effect which can be understood as roughness-induced momentum matching of surface plasmons to the radiated field.

Sonnichsen *et al.* [29] fabricated individual gold nanoparticles (spheres and rods) chemically in order to investigate the damping of plasmonic resonances. They found that rods have a smaller line-width (hence greater Q values) than spheres with the same resonant energy, E_{res} (see Figure 1.11). They suggest this reduced line-width of the plasmon mode is not due to the reduced radiation damping of the nanorods compared to the spheres: a rod of much smaller volume can support a plasmon mode of the same resonant frequency as a sphere. The reduced damping is due to the resonant energy of plasmon mode of the rod being less than the threshold (1.8 eV) required for inter-band transition in gold. A sphere with a resonant energy less than the threshold would benefit from the reduced non-radiative damping, but to obtain an energy less than the threshold energy, the volume of the sphere would have to be large in comparison to the equivalent rod. This additional radiation damping would provide a large line-width.

Sonnichsen *et al.* also observed a red-shift in the resonant mode of spheres with increasing particle size in agreement with Ref. [23]. This red-shift is not captured by the simple electrostatic approximation (see Equation 1.3), as the approximation assumes

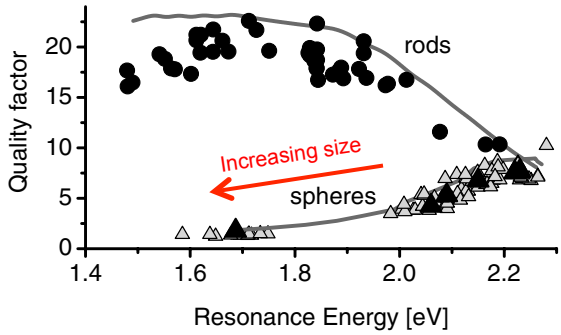

Figure 1.11: Quality factor of single nanorods (dots) and nanospheres (grey triangles) vs resonance energy E_{res}. Black triangles: averages for spherical particles of the same nominal size (150 nm, 100 nm, 80 nm, 60 nm, 40 nm, and 20 nm from left to right) [29].

the electric field is homogeneous (i.e. has constant phase and magnitude) over the volume of the particle. However, this is not the case, due to the finite value of the skin depth and due to retardation effects. At optical wavelengths the skin depth of silver and gold is approximately 30 nm (see Figure 1.4) therefore only the conduction electrons in the outer shell of a large particle will oscillate. An estimate of the retardation for the oscillating electrons to be out of phase by 1/10 of a cycle is as follows; at optical frequencies $\omega \approx 10^{15}$ rad^{-1} so the period T of an oscillation is approximately $1/\omega \approx 10^{-15}$ s. If an arbitrary value of 1/10 of a period is chosen for there to be a noticeable effect of retardation, this gives a time, t of approximately 10^{-16} s. Using the relation $s = d/t$, where s is speed, d distance, and inserting the according values, $d = c \times 10^{-16} = 10^{-8}$ m $= 10$ nm, where c is the speed of light. So for particles with dimensions greater than or equal to 30 nm the electric field does not penetrate the whole of the particle, and for particles with dimensions greater than or equal to 10 nm retardation is significant. Hence the electrostatic approximation only holds for particles with dimensions less than or equal to 10 nm.

1.5.1 Optical cross-sections

A particle can remove energy from an incident beam of light in two ways; by *absorption* or by *scattering*. In the first process, energy is non-radiative and can involve the conversion of energy from the incident beam into heat, for example as the collective motion of the electrons is damped. In the second process, the electrons driven in oscillatory motion elastically scatter a photon, hence this process is radiative [31]. The

absorption and scattering can be expressed as their cross-sections,

$$\sigma_{\text{abs}} = k\Im(\alpha), \tag{1.25}$$

and,

$$\sigma_{\text{sca}} = \frac{k^4}{6\pi}|\alpha|^2, \tag{1.26}$$

where k is the wave number in the surrounding medium. The extinction cross-section is the sum of the absorption and scattering cross-sections and is given by,

$$\sigma_{\text{ext}} = k\Im(\alpha) + \frac{k^4}{6\pi}|\alpha|^2. \tag{1.27}$$

The scattering cross-section can be derived by considering the power radiated by an electric dipole and normalizing with the intensity of the incident electric field. The electric and magnetic fields for a oscillating point dipole in the far field, expressed in spherical coordinates is given by [32],

$$\vec{E} = -\frac{\mu_0 p_0 \omega^2}{4\pi}\left(\frac{\sin\theta}{r}\right)\cos[\omega(t - r/c)]\hat{\theta}, \tag{1.28}$$

and,

$$\vec{B} = -\frac{\mu_0 p_0 \omega^2}{4\pi c}\left(\frac{\sin\theta}{r}\right)\cos[\omega(t - r/c)]\hat{\phi}, \tag{1.29}$$

where r is the distance from the dipole, p_0 is the magnitude of the dipole moment and θ is the angle between the $\vec{p}$ and $\vec{r}$. The energy per unit area, per unit time, radiated by the oscillating dipole can be calculated using the Poynting vector,

$$\vec{S} = \frac{1}{\mu_0}(\vec{E} \times \vec{B}) = \frac{\mu_0}{c}\left\{\frac{p_0\omega^2}{4\pi}\left(\frac{\sin\theta}{r}\right)\cos[\omega(t - r/c)]\right\}^2 \hat{r}. \tag{1.30}$$

The intensity can be obtained by averaging $\vec{S}$ in time over one complete light cycle.

Since the average of $\cos^2\theta = 1/2$, Equation 1.30 becomes,

$$\langle \vec{S} \rangle = \left(\frac{\mu_0 p_0^2 \omega^4}{32\pi^2 c} \right) \frac{\sin^2\theta}{r^2} \hat{r}. \tag{1.31}$$

Equation 1.31 shows the intensity of the dipole falls off as $1/r^2$ and there is no radiated energy along the dipole axis. To calculate the total power radiated from the dipole $\langle \vec{S} \rangle$ must be integrated over a sphere of radius r,

$$\langle P \rangle = \int \langle \vec{S} \rangle \cdot d\vec{a} = \frac{\mu_0 p_0^2 \omega^4}{32\pi^2 c} \int \frac{\sin^2\theta}{r^2} \sin\theta d\theta d\phi = \frac{\mu_0 p_0^2 \omega^4}{12\pi c}. \tag{1.32}$$

The power can be expressed as,

$$\langle P \rangle = \frac{\mu_0 \varepsilon_0^2 |\alpha|^2 E_0^2 \omega^4}{12\pi c}, \tag{1.33}$$

where the substitution of $p_0 = \varepsilon_0 |\alpha| E_0$ has been used. To express Equation 1.33 as the scattering cross section it has to be normalized with respect to the intensity of the incident electric field. An incident monochromatic plane wave has an intensity, $I = 1/2\varepsilon_0 c E_0^2$ and hence the scattering cross-section is,

$$\sigma_{\text{sca}} = \frac{\langle P \rangle}{I} = \frac{\mu_0 \varepsilon_0^2 |\alpha|^2 E_0^2 \omega^4}{6\pi c^2 \varepsilon_0 E_0^2} = \frac{\mu_0 \varepsilon_0 |\alpha|^2 \omega^4}{6\pi c^2} = \frac{k^4}{6\pi} |\alpha|^2, \tag{1.34}$$

where Equation 1.34 has been tided up using $\omega = ck$ and $c^2 = 1/\varepsilon_0 \mu_0$.

It is interesting to note that for particles that do not have a frequency dependent permittivity the scattering cross-section varies as,

$$C_{\text{scat}} \approx \frac{1}{\lambda^4}, \tag{1.35}$$

so blue-light will be scattered more strongly than red light. This is not the case with the metallic particles investigated in this thesis. It is worth mentioning at this point that the absorption and scattering of a sample can not be determined by the transmission alone.

In summary, the optical response of a single isolated particle has been investigated in the literature and in particular how the spectral position of the resonance is altered and broadened. An interesting question is whether the position or width of the resonance changes when another particle is brought into close proximity? This is the focus of the next section.

1.6 Two particles

Is the optical response of two particles in close proximity different from the response of just one isolated particle? This section addresses this question.

It might be expected that there would be a change in their optical response because the electric field produced by one particle will act on the other. Experiments confirm that this is the case. Gunnarsson *et al.* [33] fabricated silver particle pairs with a diameter of 95 nm and height 25 nm by electron-beam lithography. They varied the separation between the particles and probed their polarization response to the incident electric field by collecting the scattered light from the pair. Presented in Figure 1.12 are measured scattering spectra from a number of isolated particle pairs where the separation (edge-to-edge) between the particles has been varied from 10 nm to 250 nm. It is seen that the collective response of two particles (spectra A-E) differs from that of the single isolated particle (spectra F). The shift in the dipolar particle plasmon wavelength also depends on the inter-particle separation, the shift increasing as the particle separation is reduced, the single particle response being retrieved for separations greater than approximately $\lambda/2$. It is also seen that the optical response of the pair depends on the polarization of the incident electric field. When the electric field is parallel to the particle-pair axis, the resonance associated with the pair shifts to longer wavelengths (red-shift) than the single particle response. When the electric field is perpendicular to the particle-pair axis the resonance of the pair shifts, if anything, to shorter wavelengths (blue-shift) than the single particle response.

As discussed in Section 1.5, the resonant frequency is determined by the strength of the restoring force that acts when the charges in the particle are separated. The restoring force arises from the electric field that acts on the charges. For a single particle it is only the field associated with the charges in that particle (internal field) that contributes to the restoring force. In contrast, when two particles are present, the charges on one particle can contribute an extra electric field and it is the net electric field that provides the restoring force. Thus, depending on the relative orientation of internal and external

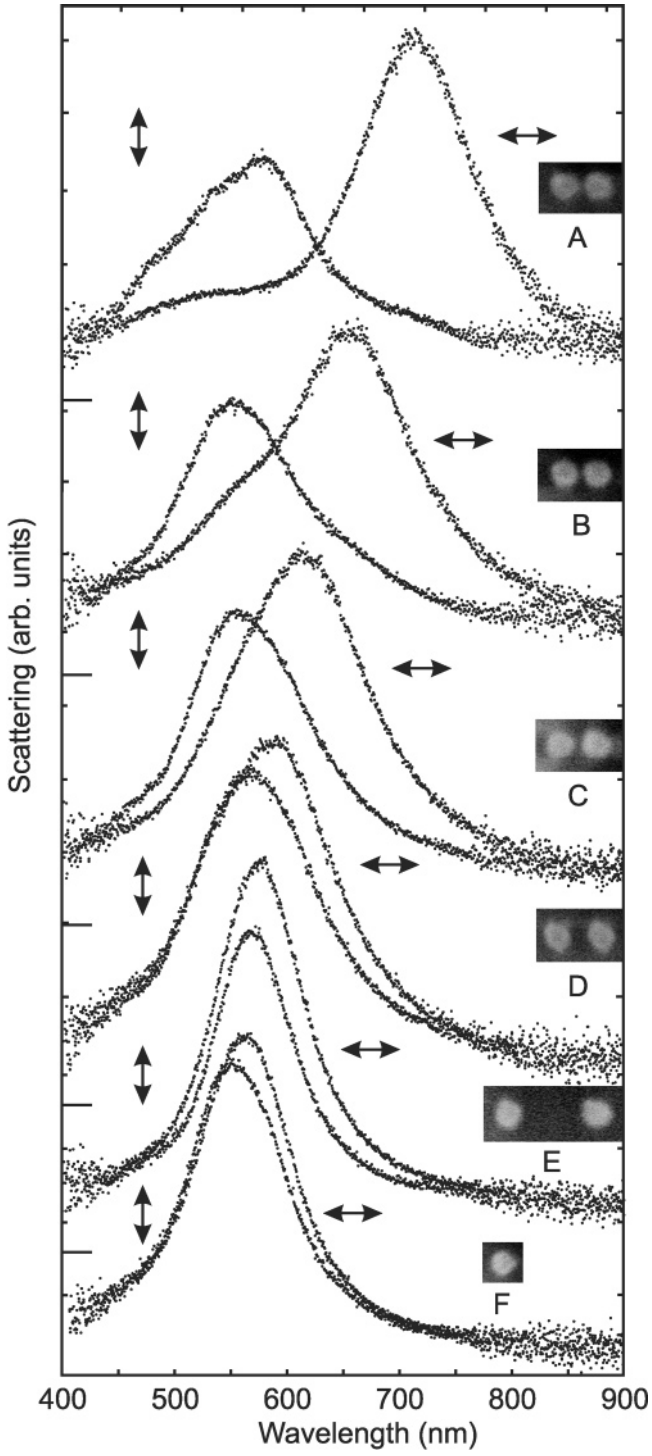

Figure 1.12: Dark-field spectra and scanning-electron micrographs from isolated particles (diameter $D = 95$ nm, height $h = 25$ nm) and particle pairs for varying separations. Data are shown for incident electric fields parallel and perpendicular to the interparticle axis, as indicated by the arrows. The separations (gaps) d between the particles are d $\approx$ 10 nm (A), 15 nm (B), 25 nm (C), 50 nm (D) and 250 nm (E). Spectra F are from a single particle and are included for comparison. The vertical bars indicate the baselines for the different spectra. Figure taken from Ref. [33].

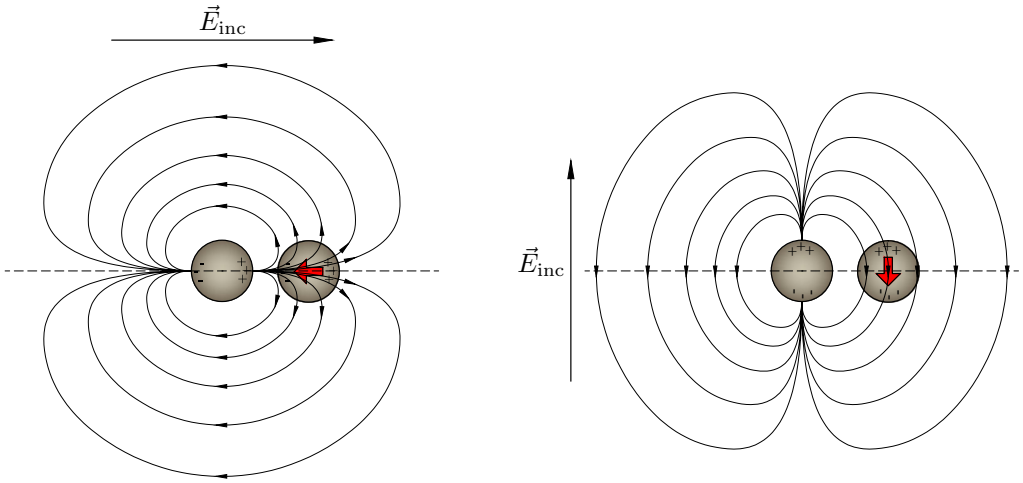

(a) Incident electric field parallel to pair axis.

(b) Incident electric field perpendicular to pair axis.

Figure 1.13: Diagram indicating two possible combinations of near-field coupling for a plasmonic particle pair. When the exciting incident electric field is parallel to the particle-pair axis in (a), the electric field from the neighbouring particle and the internal electric field (red arrow) of the adjacent particle are in *opposite* directions. The net electric field acting on the oscillating electrons is therefore reduced, which leads to a reduced restoring force and a red-shift of the particle plasmon resonance. In (b) the exciting electric field is perpendicular to the particle-pair axis, and the electric field from the neighbouring particle and the internal electric field (red arrow) of the adjacent particle are in the *same* direction: the net electric field acting on the collective electron motion is increased, and the particle plasmon resonance is blue-shifted. Particle-pair axis indicated by dashed line.

fields, the restoring force can either be strengthened or weakened corresponding to blue and red-shifts, respectively, of the resonance.

These red- and blue-shifts can be understood by considering the charge distribution of each particle as a simple electric dipole. An illustration of the electric fields acting on a neighbouring particle in a particle pair are shown in Figure 1.13. As discussed in Section 1.5, when an external electric field is applied to a particle the conduction electrons are displaced from their equilibrium positions creating a dipole moment. With the polarization of the electric field parallel to the particle-pair axis, the electric field from the neighbouring particle and the internal electric field (see red arrow in Figure 1.13a) of the dipole are in *opposite* directions, causing the electric field between the oscillating charges to be reduced. This in turn reduces the restoring force between the oscillating electrons, lowering the resonant frequency, hence red-shifting the particle plasmon resonance (see Equation 1.23). With the electric field orientated perpendicular to the particle-pair axis the net electric field acting on the oscillating electrons is increased, increasing the restoring force and resonant frequency, leading to a blue-

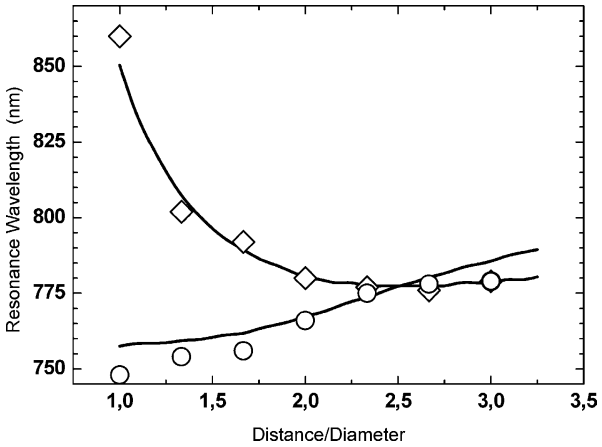

Figure 1.14: Spectral position of the extinction maximum vs. inter-particle distance for seven different particle-pair separations of gold discs with a diameter of 150 nm and height 17 nm. The distance refers to the centre-to-centre separation of the particles in the pair. The polarization directions of the incident electric field is parallel (rhombs) or perpendicular (circles) to the particle-pair axis. Solid lines show the corresponding results of the dipole-pair model calculations. Figure reproduced from Ref. [35].

shifted resonance. In summary, the coupling not only depends on the separation but also on the relative orientation of the dipole moments associated with the two particles. It is seen that the red-shift should be greater than the corresponding blue-shift owing to the electric field being greater at the poles of the dipole than in the equatorial plane.

Gunnarsson *et al.* [33] found that for joined particles, i.e. they have merged to become a nanorod, the resonance associated with the electric field parallel to the particle-pair axis is found at a much longer wavelength than even the closest particle pair that they studied (gap 10 nm). The dramatic red-shift of the dipolar plasmon resonance peak when the particle pair becomes joined has been reported more recently in Ref. [34]. Rechberger *et al.* [35] also explore the plasmonic near-field coupling between particles. They fabricated gold nanodiscs with a diameter of 150 nm and a height of 17 nm, and observed the same trends for the particle plasmon resonance wavelengths of the pair, i.e. a red-shift with decreasing particle separation for the electric field polarized along the particle-pair axis and a blue-shift of the particle plasmon resonance wavelength with decreasing particle separation with the electric field perpendicular to the pair axis. They compared their experimental data to a model based on interacting dipoles and found good agreement, see Figure 1.14.

Interestingly, Fromm *et al.* [36], who fabricated single "Bowtie" structures, observed an initial blue-shift for gaps greater than 75 nm and then a red-shift for gaps less than 75

nm with the electric field polarized along the particle-pair axis, with coupling extending over a greater distance (approximately λ) compared with Gunnarsson *et al.* [33] who only observed coupling for less than $\lambda/2$. One suggestion for this difference is due to the sharp edges of the triangles concentrating the charge into a smaller region, thus increasing the charge density and increasing the projected coupling electric field [37].

This distance-dependent resonance can be exploited to measure the distance between coupled particles as demonstrated by Tabor *et al.* [37], who proposed a "plasmon ruler equation":

$$\frac{\Delta\lambda}{\lambda} = A \exp\left(-\frac{s/D}{\tau}\right), \tag{1.36}$$

where $\Delta\lambda/\lambda$ is the fraction change in the particle plasmon resonance wavelength normalized against the single isolated particle plasmon resonance wavelength, A is the relative strength of the dipole field, s is the gap between the particle pair, D is the particle size parameter and τ is the decay length from the particle surface. In their study they successfully fit Equation 1.36 to spherical nanoparticles, nanodiscs, nanoprisms and nanocubes. The distance-dependent relationship is also confirmed by Jain *et al.* [38] who fit Equation 1.36 to gold nano disc pairs and by Su *et al.* [39] who fit Equation 1.36 to gold elliptical discs with an aspect ratio (long-axis/short-axis) of 1.55. Funston *et al.* [19] find at short distances (less than a few nanometers separation) the plasmon ruler equation for Au dimers did not hold.

So far the focus has only been on the spectral position of the particle plasmon resonance, this section will be concluded by discussing the effect of inter-particle coupling on the line-width of the collective resonance of a particle pair. Dahmen *et al.* [40] provided an analysis based on the coupling of two 80 nm diameter gold nanospheres, using Mie theory to calculate the scattering spectra of a particle pair as a function of particle separation. The results of their calculation are shown in Figure 1.15.

Their results (see Figure 1.15) show how the line-width and the resonance energy of the particle pair oscillates around the single particle values as the separation increases. These oscillations have a period of approximately 400 nm and decay in amplitude with increasing particle separation. The oscillations decay more rapidly when the electric field is parallel to the particle-pair axis than when perpendicular (the line-width decreases with increasing separation). This oscillatory behaviour of the line-width with particle separation has been confirmed experimentally by Olk *et al.* [41] where they collected the back scattered light from a pair of gold nanospheres of the same dimen-

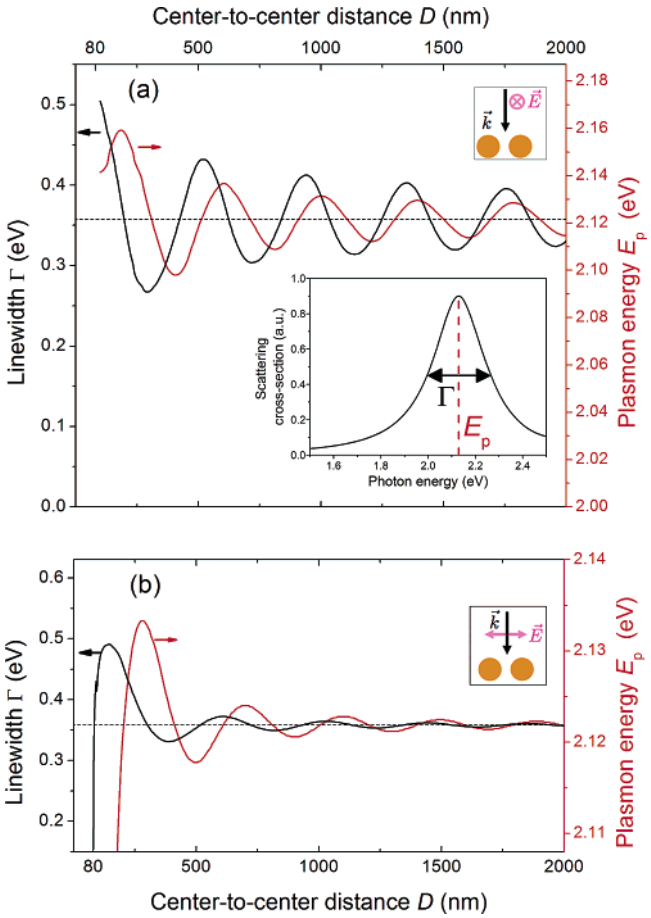

Figure 1.15: Calculated plasmon line-widths (FWHM, left axis) and plasmon energies (right axis) of a pair of 80 nm diameter gold nanospheres as functions of the centre-to-centre inter-particle distance D. Every datapoint is extracted from a light-scattering spectrum (central inset: light-scattering spectrum calculated for $D = 290$ nm, transverse polarization). (a) is for transverse polarization of the incident electric field and (b) is for longitudinal polarization (see top right insets). In both figures, the horizontal dashed lines indicate the plasmon line-width and plasmon energy of an isolated 80 nm gold sphere. Figure taken from Ref. [40].

sions as Dahmen and coworkers. Olk and coworkers observed a periodic modulation of the line-width with a period of approximately 350 nm, but over smaller distances (approximately λ for parallel and approximately 3λ for perpendicular) than theoretical predicted by Ref. [40]. Ref. [41] suggest that shorter distance of line-width modulation is related to the bandwidth-limited coherence length of their light source. Dahmen and coworkers observe an increase in resonant energy when the electric field is parallel to the pair axis as the particle separation is increased for distances less than $\lambda/2$, which is in agreement with the gap sizes investigated Gunnarsson *et al.* [33] (see spectra (A-D) in Figure 1.12). However, when the electric field is perpendicular to the pair and for distances less than $\lambda/3$, they predict an increase in resonant energy with increasing particle separation which disagrees with Gunnarsson and coworkers.

As noted above for the single particle, the line-width is related to how heavily the oscillation is damped. Again, as with the single particle, there are two possible damping mechanisms: radiative and non-radiative. In this instance it is the collective radiative damping of the pair that is altered. For distances greater than $\lambda/2$ the simple electrostatic model is no longer valid and the finite speed of light needs to be accounted for. Accordingly, retardation of the electric field, depends upon the particle separation. The particle pair in Figure 1.15 has been modelled in a medium with refractive index of 1.51 (the resonant wavelength of an isolated 80 nm diameter gold sphere is 387 nm in this medium) [40]. When the particles are separated by a distance of a multiple of $n\lambda/2$ (where $n = 1, 2, 3...$) destructive interference takes place. This leads to reduced collective radiation and lower resonant energy of the pair. When the separation is $n\lambda$ constructive interference takes place and the pair radiate more light and have a higher resonant energy.

Does the optical response of particles arranged in a periodic array differ from that of two coupled particles? Yes, the response can be very different from that of a single isolated particle, as will now be demonstrated.

1.7 Array of particles

Haynes *et al.* [42] fabricated square and hexagonal arrays by electron-beam lithography in order to investigate the plasmonic coupling between particles. They measured the extinction spectra of arrays with different pitches d (where $d < \lambda_{\mathrm{PPR}}/2$, where λ_{PPR} is the particle plasmon resonant wavelength). Figure 1.16a shows a scanning-electron micrograph of an example of one of the structures that was fabricated (in this case

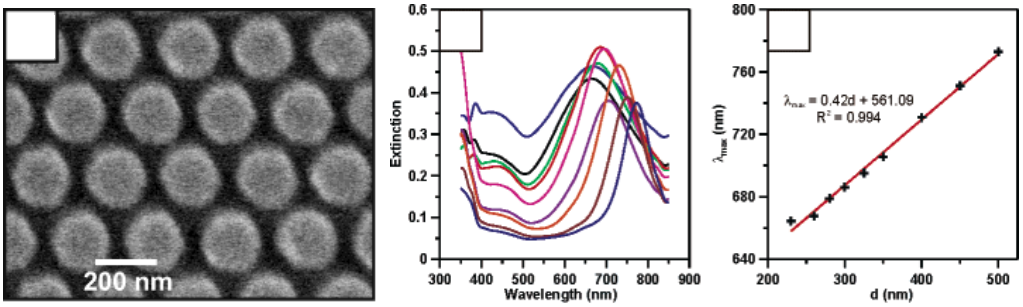

(a) Scanning-electron micrograph of representative nanoparticle array. Shown are cylindrical nanoparticles with diameter (D) of 200 nm, height (h) 35 nm in hexagonal arrangement, pitch 260 nm.

(b) Measured extinction spectra of Au cylinders in hexagonal arrays (D = 200 nm, h = 35 nm) with variety of pitches.

(c) Corresponding plot of particle plasmon peak wavelength as a function of pitch (d).

Figure 1.16: (a) scanning-electron micrograph of cylindrical particles in a hexagonal arrangement, (b) measured extinction spectra of the same arrangement but with a variety of array pitches and (c) dependence of the particle plasmon peak wavelength as a function of pitch d for the arrays in (b). Coloured lines in (b) correspond to array pitches: 230 nm (black), 260 nm (blue), 280 nm (green), 300 nm (red), 325 nm (pink), 350 nm (purple), 400 nm (orange), 450 nm (brown) and 500 nm (navy). Figures taken from Ref. [42].

cylindrical nanoparticles in a hexagonal arrangement). Shown in Figure 1.16b are the extinction spectra of gold cylinders with $D = 200$ nm, $h = 35$ nm in a hexagonal array with a variety of array pitches (230 nm–500 nm). The corresponding plot of particle plasmon peak wavelength (nm) vs. pitch, d, is exhibited in Figure 1.16c. Haynes *et al.* [42] observed a red-shift of the particle plasmon resonance peak wavelength with increasing pitch of square and hexagonal arrays for both types of shapes (discs and trigonal prisms) of nanoparticles.

Lamprecht *et al.* [43] also explored the coupling between particles in an array. They fabricated periodic arrays of gold discs by electron-beam lithography with various array pitches but over a larger range ($d > \lambda_{\mathrm{PPR}}/2$) than Haynes *et al.* [42]. They found that for small pitches ($d < \lambda_{\mathrm{PPR}}/2$) a red-shift of the particle plasmon resonance peak was displayed with increasing array pitch, see dashed line in Figure 1.17, in agreement with Haynes *et al.* [42]. In both, Refs. [42] and [43], the square and hexagonal arrays exhibit a red-shift in λ_{PPR} with increasing array pitch for pitches $d \leq \lambda_{\mathrm{PPR}}/2$. Focus on thinking about the simpler case of a square array: in a square array there are both types of particle-pair interactions that were described in Section 1.6. Refer back to Figure 1.14, from which it is seen that the red-shift for polarization of the incident

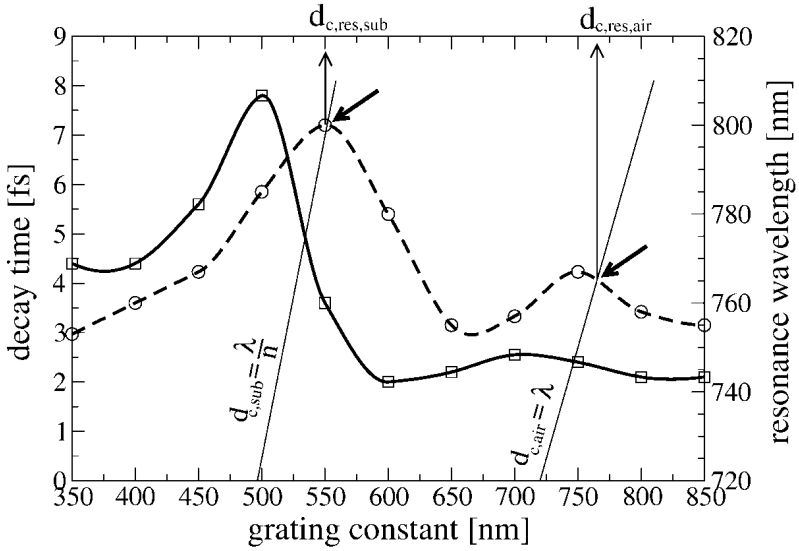

Figure 1.17: Plasmon decay time (solid line) and particle plasmon resonance wavelength (dashed line) vs. pitch (350–850 nm) of different square arrays. The particles were gold discs with a diameter of 150 nm and height 14 nm giving an isolated particle plasmon resonance of approximately 775 nm. Plasmon decay time was determined from FWHM of the measured extinction spectra. Figure taken from Ref. [43].

electric field parallel to the particle-pair axis is much stronger than the blue-shift for the perpendicular polarization - this is different to what is observed in an array. For pitches greater than $d = \lambda_{\mathrm{PPR}}/2$ an oscillatory dependence of the λ_{PPR} with pitch was found, with the oscillation amplitude decreasing with increasing pitch.

Lamprecht *et al.* [43] also investigated the resonance lifetime which, as discussed in Section 1.5, is equivalent to the inverse resonance line-width $1/\Gamma$. For pitches of approximately λ the plasmon lifetime is found to take its greatest value (see solid line in Figure 1.17) leading to the narrowest resonance ($\Gamma \approx 30$ nm, $Q \approx 26$).

Auguié and Barnes [44] fabricated square arrays of gold nanorods by electron-beam lithography and varied the pitch of the arrays from 480 nm to 560 nm. They performed the transmittance measurements of these arrays with the incident electric field parallel to the long-axis of the nanorods, and the particles immersed in an index-matching fluid to provide a homogeneous optical environment. In each of the spectra (see upper panel in Figure 1.18), a strong dip in transmittance is observed at a longer wavelength than isolated single particle plasmon resonance (approximately 710 nm), which red-shifts with increasing pitch of the array. This extra feature, i.e. the largest dip in each of the transmittance spectra, is due to the periodic nature of the array and results from coherent interaction of dipoles associated with the single particle resonances. This was

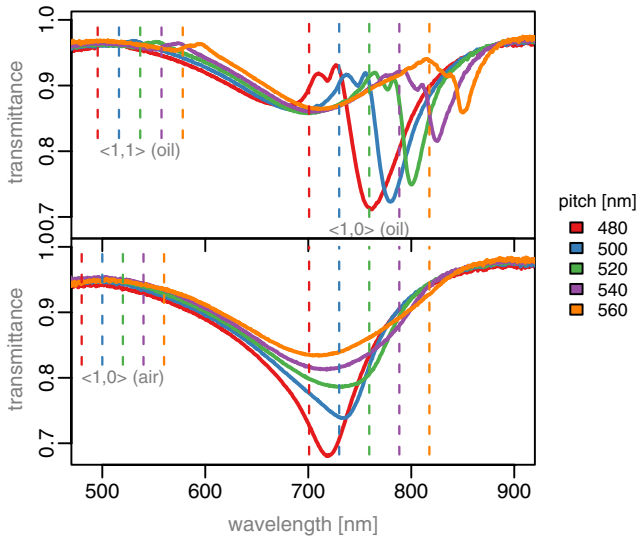

Figure 1.18: Transmittance spectra for gold nanorod arrays in homogeneous index environment (top, oil immersion $n = 1.46$) and asymmetric refractive index configuration (bottom, incident light in air) for five array pitches. Nominal particle sizes: 100 nm × 90 nm × 35 nm (top), 120 nm × 90 nm × 35 nm (bottom). The vertical lines indicate the position of the $\langle 1, 0\rangle$ and $\langle 1, 1\rangle$ diffraction edges for the two refractive index environment configurations. Figure taken from Ref. [44].

not seen by Lamprecht *et al.* [43] and Haynes *et al.* [42] as they did not index-match the surrounding environment of the array with the substrate. A non-index-matched environment leads to two different interference conditions: one for the substrate and one for the surrounding environment of the array. The overall effect of this is blurring of the dip, as shown in the bottom panel in Figure 1.18.

Chu *et al.* [45] demonstrated that by selecting the appropriate size of particle and pitch a narrower resonance could be produced. They fabricated gold nanodiscs by electron-beam lithography. The nanodiscs had a diameter, D, of 180 nm and a height, h, of 40 nm and were arranged in a square array (see Figure 1.19a). The arrays were immersed in water ($n = 1.327$) and the spectra obtained (see Figure 1.19c). The spectra show two important trends: a red-shift in λ_{PPR} with increasing pitch (in agreement with Lamprecht *et al.* [43] and Haynes *et al.* [42]) and a narrowing of the line-width with increasing pitch. It is interesting to compare the single isolated particle line-width (see black line in Figure 1.19c) with the narrowest resonance (corresponding to a pitch of 660 nm), see pink line in Figure 1.19c. The line-width of a single isolated particle, $\Gamma = 311.6$ nm with $Q \approx 3$ compared to an array of the same particles giving a line-width, $\Gamma = 26.6$ nm and $Q \approx 38$.

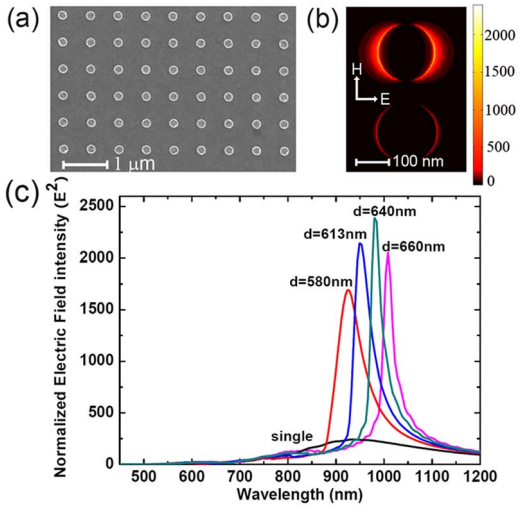

Figure 1.19: (a) scanning-electron micrograph of gold disc array. (b) intensity ($\langle|E|^2\rangle$) distribution on the surface of single gold disc at $\lambda = 930$ nm (bottom). Intensity distribution on the surface of gold disc of an array with a grating pitch $d = 640$ nm at $\lambda = 982$ nm (top). Polarization of plane wave illumination is shown, which is along one axis of the square array. (c) near-field intensity enhancement ($\langle|E|^2\rangle$) spectra for a single isolated gold disc and for gold discs in 2D arrays of different grating pitches (d). Figure taken from Ref. [45].

Zhou and Odom [46] fabricated arrays of gold nanoparticles using a template-stripping nano-fabrication technique in order to investigate out-of-plane plasmon modes. An out-of-plane plasmon mode is one in which the conduction electrons oscillate in the z-dimension (height dimension) of the particle, instead of in the x-direction as with the in-plane mode (see Figure 1.20). The gold nanoparticles that Zhou and Odom studied have a diameter of 160 nm and were arranged in a 400 nm pitch square array. Zhou and Odom considered four different particle arrays, each with a different particle height ($h = 65$ nm, 100 nm, 120 nm and 170 nm), and measured their transmittance spectra as a function of wavelength (see Figure 1.21a). The arrays were illuminated with $\vec{k}$ at an angle of incidence, θ of 15°, to provide a component of the incident electric field in the z-direction so an out-of-plane plasmon mode could be excited. An illustration of the two different configurations of the incident electric field (TM and TE) are shown in Figure 1.20.

For both TM and TE polarizations (see Figure 1.20) of the incident electric field, a broad resonance associated with the in-plane plasmon mode is seen at approximately 750 nm, which blue-shifts with increasing particle height in agreement with Ref. [27]. The main difference between the two polarizations is that for TM-polarization (see Figure 1.21a) there is a sharp dip in the transmittance spectra that shifts to longer wavelengths with

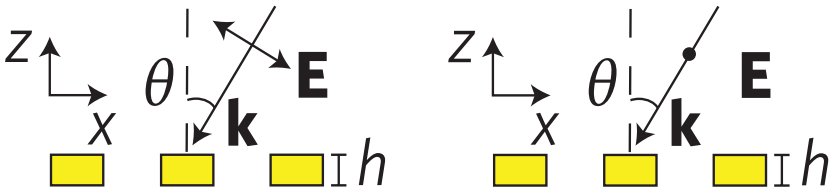

(a) TM-polarized. **(b)** TE-polarized.

Figure 1.20: Schematic illustrating the two different polarizations of the incident electric field: (a) TM and (b) TE-polarized light. TM-polarized light at an angle of incidence, $\theta = 15°$ provides a component of the incident electric in the z-direction allowing excitation of an out-of-plane plasmon mode. Figures adapted from Ref. [46].

increasing particle height (from $\lambda \approx 720$ to $\lambda \approx 860$ nm). This sharp dip corresponds to an out-of-plane plasmon mode and is exhibited at different wavelengths for different particle heights: approximately 710 nm for height 65 nm; approximately 730 nm for height 100 nm; approximately 755 nm for height 120 nm; and approximately 860 nm for height 170 nm. This feature is not observed with TE-polarization (see Figure 1.21b) as there is no component of the incident electric field in the z-direction of the particles, so an out-of-plane resonance can not be excited. $\Gamma \approx 5$ nm, $Q \approx 146$, cf. single particle where $Q \leq 10$.

Kravets *et al.* [47, 48] have probed out-of-plane resonances of single particles and particle pairs and more recently Thackray *et al.* [49] have studied out-of-plane resonances by fabricating particles with a non-trivial geometry and measuring their normal-incidence transmission spectra as a function of wavelength. The non-trivial geomery allows an out-of-plane dipole moment to be excited. In this thesis, only in-plane resonances are investigated, as all the measurements are performed at normal incidence, and the particles have a height of 30 nm, so an out-of plane particle plasmon mode can not be excited.

1.8 Conclusion

It was demonstrated that the interaction of light with a metallic particle leads to the collective oscillation of the free conduction electrons that constitute the particle. This collective surface charge oscillation of a particle is known as a particle plasmon resonance and results in enhanced absorption and scattering of light at certain visible frequencies for silver. To understand the physics behind particle plasmons, the electro-

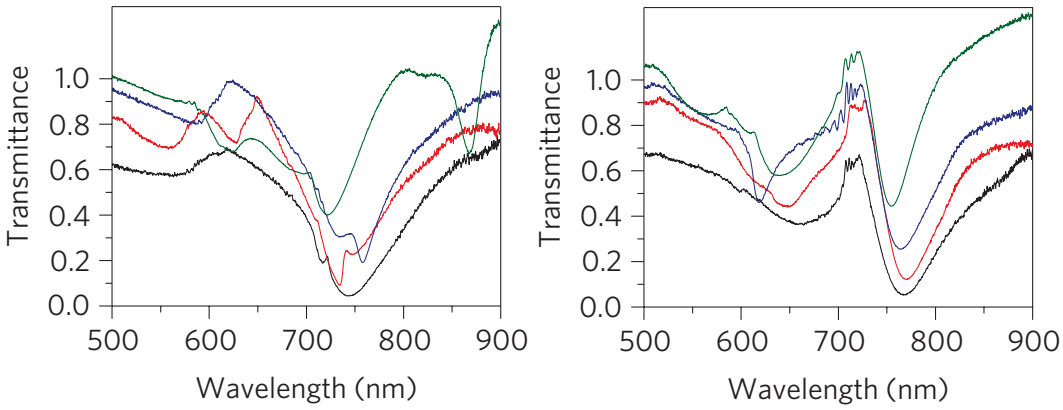

(a) TM-polarized light. **(b)** TE-polarized light.

Figure 1.21: Measured transmittance spectra of 400 nm pitch square arrays of gold nanoparticles with heights of $h = 65$ nm (black), 100 nm (red), 120 nm (blue) and 170 nm (green) under (a) TM- and (b) TE-polarized light. Incident angle, $\theta = 15°$. The individual spectra have been displaced by 10% for clarity. Figures taken from Ref. [46].

magnetic response of the bulk metal must be first described. The optical response of metals at optical frequencies is dominated by their conduction electrons, which can be described using the Drude model for the permittivity. The permittivity is frequency dependent and below the plasma frequency the real part becomes negative meaning that waves decay evanescently, their amplitude falling to a value of $1/\exp$ after approximately 30 nm in gold and silver at optical frequencies.

In previous studies, it was found that the size, shape and dielectric environment of the single particle changes the particle plasmon resonant wavelength. Changing the size and shape of the particle changes the charge distribution of the electrons, and the restoring force between the electron and ionic cores. For an interacting particle pair, the spectral position of the particle plasmon resonance red-shifts when the incident electric field is parallel to the particle-pair axis and blue-shifts when perpendicular. The red-shift of the resonance occurs because when the incident electric field is parallel to the pair axis, the internal electric field of the particle and the electric field from the the neighbouring particle are in opposite directions, so the electric field between the electrons and ionic cores are reduced. A reduced restoring force results in a lower resonant frequency, i.e a red-shift. When the incident electric field is perpendicular to the pair, the internal field of the particle and electric field from the neighbouring particle are in the same direction and add to make a stronger restoring force, i.e. a blue-shift in the resonance.

Previous investigations on particle arrays showed that when the particles are roughly separated by the wavelength, illuminated by normal-incidence light, and the environment of the particles was homogeneous that sharp spectral features were observed. The normal-incidence light excites an in-pane dipole plasmon mode, where the electron oscillation in the particle is parallel to the plane of the array. These sharp spectral features are the result of the of coherent interaction of the scattered light in the plane of the array by each one of the particles. The strength and width of this coherent resonance is an interplay between the single particle resonance and the pitch of the array.

Further studies showed that by exciting the particles by oblique angle of incidence light that an out-of-plane plasmon mode could be excited. An out-of-plane plasmon mode is one in which the electrons collectively oscillate parallel to the height dimension of the particles, normal to the plane of the array. These were only observed for TM-polarized light, as TE-polarized light does not supply a component of the electric field in the height direction of the particle.

The results discussed above show that the optical response of an array can be controlled by appropriate array design. Plasmonic arrays offer the opportunity to confine light to dimensions less than the diffraction limit [50], with a high field enhancement [51] and can be used for example for strong coupling [52, 53] and lasing [54, 55].

The work reported in this thesis, through experiment and theory, explores the electromagnetic interaction between in-plane particle plasmon resonances in periodic arrays of nanoparticles. Periodic arrays, which have a pitch comparable to the particle plasmon resonance wavelength, may exhibit narrow resonances known as surface lattice resonances (SLRs). In the first part of this thesis, these SLRs are studied in different array geometries with a one-particle basis and in the second part, SLRs are investigated in square arrays with a two-particle basis. The details are provided below in Section 1.9.

1.9 Thesis overview

Chapter 2: Single particle response

In Chapter 2, a polarizability with retardation and radiation terms is introduced to describe the interaction of light with an isolated silver spheroidal nanoparticle. A discussion on how the spectral position of the particle plasmon resonance of spheroids

shifts by changing the axes is presented. Mie theory is discussed and used to describe the main features of the absorption and scattering of light from spherical particles. Fabrication of isolated single particles by electron-beam lithography (EBL) is described and their optical characterization by dark-field spectroscopy is introduced. Comparison is made between experimental and simulated scattering spectra of isolated single silver discs.

Chapter 3: Response of regular arrays of plasmonic particles

In Chapter 3, different array geometries of plasmonic particles that exhibit sharp spectral features from the coherent scattering of light in the plane of the particles is studied. The optical response of these arrays is modelled as coupled point dipoles using the polarizability introduced in Chapter 2 to describe the interaction of light with an isolated particle. The coupled-dipole calculated extinction spectra are compared to finite-element method calculations. Square, hexagonal and honeycomb arrays are fabricated by EBL, and extinction measurements are described and presented. Finally, the polarization sensitivity of the optical response of square, hexagonal and honeycomb arrays is investigated - finding that due to their high symmetry they are insensitive to the polarization of the incident light.

Most of the results presented in this chapter appear in the publication:

> Humphrey, A.D. and Barnes, W.L. Plasmonic surface lattice resonances on arrays of different lattice symmetry. *Phys. Rev. B*, **90**, 075404, (2014). Ref. [56].

Chapter 4: Optical response of rectangular arrays

In Chapter 4, rectangular arrays are fabricated to explore the coupling between plasmonic particles over large distances (greater than lambda). The polarization dependence of rectangular arrays of silver nanoparticles is probed by normal incidence extinction measurements as in Chapter 3. The coupled-dipole model introduced in Chapter 3 is used to calculate the extinction cross-section of rectangular arrays and chains of particles. Experimental observations of the rectangular array are explained by considering the interaction between particles in chains. Lastly, the nature of the coupling between particles is examined by isolation of the different components of the scattered field. Coupling between particles is found to be dominated by far-field interaction.

Most of the results presented in this chapter appear in the publication:

> Humphrey, A.D. and Barnes, W.L. Plasmonic surface lattice resonances on arrays of different lattice symmetry. *Phys. Rev. B*, **90**, 075404, (2014). Ref. [56].

Chapter 5: Symmetric two-particle basis square arrays

Chapter 5 is concerned with the polarization dependence of square arrays with a two-particle basis. The measured extinction of one-particle basis square arrays of varying pitch are compared with two-particle basis square arrays of the same pitch. Two-basis particle square arrays show a polarization dependence in their measured extinction, unlike one-particle basis arrays. SLRs observed in the extinction spectra of both one-particle basis and two-particle basis square arrays are explained using the coupled-dipole model used in Chapters 3 and 4. Presented is a discussion on whether a two-particle basis can be treated as a single polarizable unit, concluding that the basis must be treated as two separate particles. Extinction measurements are performed on two-particle basis square arrays with varying centre-to-centre separation between the two particles that form the basis. Centre-to-centre separation variation of the basis shows when approximately the $\lambda/2$ condition is met, destructive interference of the scattered light from the particles results and the SLR is wiped out.

Results from this chapter were presented at Nanometa 2015 in a poster entitled:

> 'Narrow Surface Lattice Resonances on Arrays of Plasmonics Particle Pairs'.

Chapter 6: Asymmetric two-particle basis square arrays

Chapter 6 investigates surface lattice resonances of bright (symmetric) and dark plasmonic (anti-symmetric) modes of a two-particle basis. In Chapter 5 the coupling of the bright modes of the basis were investigated, as the dark mode of the symmetric pair could not be coupled to by a normal-incidence light. The dark mode can be coupled to by breaking the symmetry of the system, either by either oblique angle of incidence excitation or by inducing asymmetry into the basis itself. In the work reported here, the asymmetry is introduced by fabricating particle pairs with different diameters and probing their optical response using normal-incidence-extinction measurements. The

optical response of the arrays will then be compared to a modified simple-coupled dipole model to accept two different particle polarizabilities. The nature of the observed SLRs will be studied using finite-element modelling to determine their spatial electric field distributions.

Results from this chapter were presented at Nanometa 2015 in a poster entitled:

> 'Asymmetric dot dimers - optical properties and interactions'.

Chapter 7: Conclusions and future work

In Chapter 7, a summary of each chapter is presented with an overall summary of the thesis. Following are suggestions for future work and a list of publications and presentations of the work in this thesis.

Chapter 2

Single particle response

2.1 Introduction

It was shown in Chapter 1 that light incident on a single metallic nanoparticle causes its conduction electrons to oscillate, resonantly absorbing and scattering light at optical frequencies. A polarizability for a spherical particle with dimensions much smaller than the incident wavelength was introduced. The polarizability of describes how the collective electron oscillation in a particle responds to an applied electric field. In this chapter, a polarizability that is applicable to non-spherical particles is introduced to model the optical response of discs that are fabricated and charaterized in this thesis. The polarizability for non-spherical particles is modified with additional terms that take into account particle size effects, i.e. retardation and radiation damping. Mie theory calculations are presented to discuss general features of the absorption and scattering of light from an isolated spherical particle. A comparison is made between the quasi-static approximation (QSA), the modified long-wavelength approximation (MLWA), Kuwata empirical polarizability, and Mie theory of the extinction cross-section of different radii of spheres. A description of the the electron-beam lithography (EBL) fabrication of isolated silver discs is presented, and dark-field scattering microscopy is introduced. Finally, experimentally determined scattering spectra of single isolated discs are compared with MLWA calculated spectra.

2.2 Modelling techniques

It is often more informative to work with analytical expressions to get a grasp of the physical concepts, therefore, in this thesis the quasi-static (QS) model is used with additional terms added to approximate the optical response of discs. To describe the optical response of a metallic nanoparticle, a polarizability is used.

2.2.1 Quasi-static approximation: non-spherical particles

The QSA assumes that electric field is uniform over the complete volume of the particle [6] and is therefore only valid for particles much smaller than the resonant wavelength. The polarizability within the QS regime can be extended for ellipsoids and is given by [7],

$$\alpha_{\text{static}} = 4\pi abc \frac{\varepsilon_m - \varepsilon_s}{3\varepsilon_s + 3L(\varepsilon_m - \varepsilon_s)}, \tag{2.1}$$

where a, b and c are the semi-axes of the particle, ε_s is the relative permittivity of the surrounding medium, ε_m is the relative permittivity of the material from which the particle is made and L is a geometrical factor. Each axis of the ellipsoid has an associated geometrical factor, where $L_a \leq L_b \leq L_c$ and $L_a + L_b + L_c = 1$. L in Equation 2.1 is chosen by selecting the geometrical factor that corresponds to axis of the ellipsoid which the incident electric field is parallel to. L_a can be calculated using [7],

$$L_a = \frac{abc}{2} \int_0^\infty \frac{dq}{(a^2+q)\sqrt{(q+a^2)(q+b^2)(q+c^2)}}. \tag{2.2}$$

To calculate the absorption and scattering cross-sections, Equation 2.1 is inserted into Equation 1.25 or 1.26. From Equation 2.1 it is seen that the particle plasmon resonance condition depends on the geometrical factor L. Physically this is because the surface charge distribution changes the internal and external electric fields of the particle.

Three cases will be considered; a *sphere*, a *prolate* spheroid and an *oblate* spheroid. Spheroids are special cases of ellipsoids having two axes of the same length: a prolate spheroid has two minor axes of the same length ($b = c$), and is therefore cigar-shaped (see Figure 2.1a), and an oblate spheroid (see Figure 2.1b) has two major axes of the same length ($a = b$), and is therefore pancake-shaped. The aspect ratio, R, of a spheroid

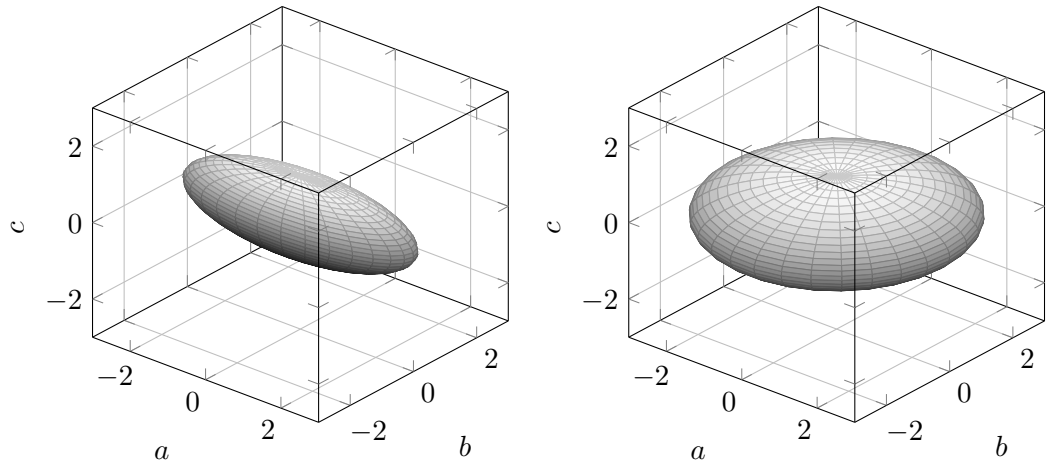

(a) Prolate spheroid ($a > b = c$). **(b)** Oblate spheroid ($a = b > c$).

Figure 2.1: 3:1 aspect ratio spheroids: (a) prolate and (b) oblate. The aspect ratio of a prolate spheroid is given by a/b and the aspect ratio of an oblate spheroid is given by a/c.

is given by $R = a/b$ for prolate and $R = a/c$ for oblate.

For a sphere $a = b = c$ & $L_a = L_b = L_c = 1/3$ and Equation 2.1 reduces to Equation 1.3.

The geometrical factor relating to the major axis (a) of a prolate spheroid is given by [7],

$$L_a = \frac{1-e^2}{e^2}\left(-1 + \frac{1}{2e}\ln\frac{1+e}{1-e}\right) \qquad e^2 = 1 - \frac{b^2}{a^2}, \tag{2.3}$$

where e is the *eccentricity*.

The geometrical factor relating to the two major axes ($a = b$) of an oblate spheroid is evaluated from [7],

$$L_a = \frac{g(e)}{2e^2}\left[\frac{\pi}{2} - \tan^{-1} g(e)\right] - \frac{g^2(e)}{2}, \tag{2.4}$$

and,

$$g(e) = \left(\frac{1-e^2}{e^2}\right)^{1/2}; \qquad e^2 = 1 - \frac{c^2}{a^2}. \tag{2.5}$$

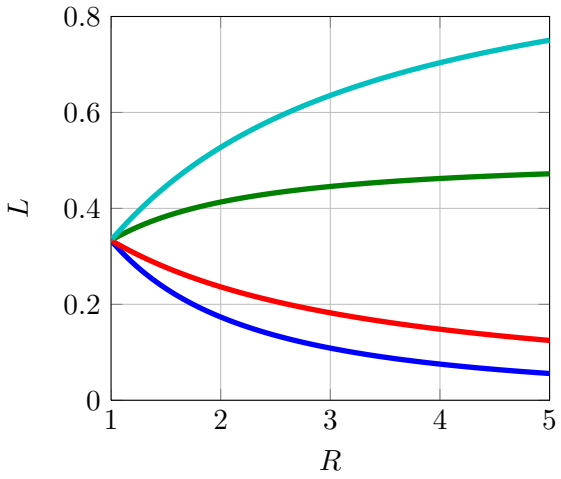

Figure 2.2: Geometrical factors L_a, L_b and L_c of prolate and oblate spheroids plotted against aspect ratio R. $R = a/b$ for a prolate spheroid and $R = a/c$ for an oblate spheroid. L_a prolate major axis (blue line), L_b and L_c prolate minor axes (green line), L_a and L_b oblate main axes (red line) and L_c oblate minor axis (cyan line). Geometrical factors calculated using Equations 2.3–2.5.The geometrical factors are related via $L_a + L_b + L_c = 1$.

Figure 2.2 shows the relationship between the geometrical factors and aspect ratio of prolate and oblate spheroids. Several observations can be made from Figure 2.2: the geometrical factors associated with their major axes of both prolate (blue line) and oblate (red line) spheroids decrease with increasing aspect ratio R, and the geometrical factors associated with their minor axes (prolate (green line) and oblate (cyan line)) increase with aspect ratio. It is of experimental advantage to produce particles with high aspect ratios (greater than 4) as for a small variation in particle dimensions the geometrical factor will change less than with lower-aspect-ratio particles (compare gradient of L vs. R between aspect ratios of 1 and 2 and 4 and 5 in Figure 2.2). Notice that L only changes depending on the aspect ratio and not on the overall particle size: the QSA is independent of particle size. The typical discs fabricated in this thesis are oblate spheroids, have a diameter of 120 nm and a height of 30 nm, giving an aspect ratio of 4 with a corresponding L_a of 0.1482.

The dipole particle plasmon resonance will occur when the denominator of Equation 2.1 vanishes, this can be approximated to [7, p. 343],

$$\Re[\varepsilon_m] = \varepsilon_s \left(1 - \frac{1}{L}\right), \tag{2.6}$$

providing that the imaginary part of the permittivity of the metal is small compared

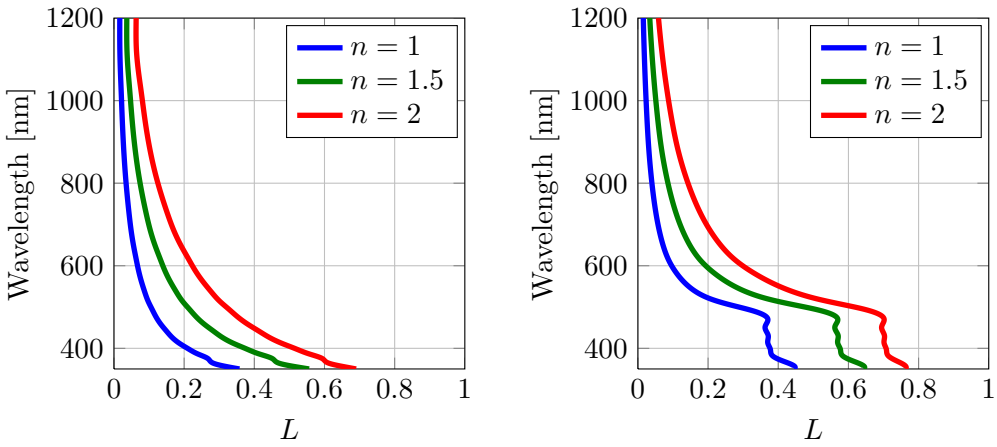

(a) Silver. **(b)** Gold.

Figure 2.3: Variation of dipole particle plasmon wavelength with geometrical factor L with three different surrounding media of different refractive index (permittivity of silver taken from Ref. [10] and gold from Ref. [11]). An increase in geometrical factor will result in a blue-shift of the dipolar particle plasmon mode, and an increase in surrounding refractive index will cause a red-shift.

to the real part. Again, L corresponds to the geometrical factor of the ellipsoid axis which the incident electric field is parallel to. The particle plasmon resonant wavelength dependence of the geometrical factor can then be plotted (see Figure 2.3). The particle plasmon resonance position as a function of geometrical factor has been evaluated for (a) silver and (b) gold using measured optical constants from the literature [10, 11].

From comparison of Figure 2.2 and Figure 2.3, is it is seen that the aspect ratio, R is related to the position of the particle plasmon resonance wavelength corresponding to each axis of the spheroid. As the aspect ratio of prolate and oblate spheroids is increased, the geometrical factor associated with their major axes decreases (see Figure 2.2), therefore the particle plasmon wavelength associated with their major axes red-shifts (see Figure 2.3). The case is opposite for their minor axes. The increase of aspect ratio, thus decrease of L_a, of an oblate spheroid would be equivalent to increasing disc diameter and then measuring the particle plasmon resonance associated with the charge oscillation in the plane of a and b of the particle and observing a red-shift. It is also observed that for prolate spheroids, e.g. nanorods, the long-axis mode is more sensitive to a change in aspect ratio than the short-axis mode (gradient of L vs. R plot greater). This is in contrast to oblate spheroids where the short-axis mode is more sensitive to changes in aspect ratio. It is also noted that for the same aspect ratio spheroid, the two resonances for silver will occur at shorter wavelengths than gold and increasing the host refractive index will red-shift the particle plasmon resonance (see Figure 2.3). The

red-shifting of the resonance can be understood by realising that if the surrounding refractive index is increased, Equation 2.6 will be satisfied at a different wavelength for the metal, as the permittivity of the metal is frequency dependent (see Figure 1.5).

As previously mentioned, the QSA resonance position is independent of particle size, however this does not reflect reality (see Equation 2.1). This is because the full electrodynamic response of the particle has been ignored. The Modified long-wavelength approximation puts some of these key retardation features back into the QSA to extend the range of particle sizes it can be applied to.

2.2.2 Modified long-wavelength approximation

For particles that are comparable to the wavelength of incident light, the polarizability has to be modified to take into account radiation damping [57] and retardation [58]. These are incorporated into the MLWA [59]. The MLWA polarizability is given by

$$\alpha_{\mathrm{MLWA}} = \frac{4\pi\alpha_{\mathrm{static}}}{4\pi - \frac{2}{3}ik^3\alpha_{\mathrm{static}} - \frac{k^2}{a}\alpha_{\mathrm{static}}}, \tag{2.7}$$

where k is the wavenumber in the surrounding medium, a is the semi-axis of the particle parallel to the incident electric field and α_{static} is the QS polarizability. The radiation damping term, $i\frac{2}{3}\alpha_{\mathrm{static}}k^3$, arises from the damping of the dipole by photon emission, i.e. the dipole produces a field which acts back on itself [60]. This radiation reaction causes weakening and broadening of the plasmon resonance with particles of large volumes ($a \geq 20$ nm). The dynamic depolarization term, $\alpha_{\mathrm{static}}\frac{k^2}{a}$, arises from the finite speed of light, causing retardation of the internal and external electric fields of the particle [61]. The retardation causes a red-shift of the particle plasmon resonance for large particles.

2.2.3 Kuwata: empirical polarizability

In 2003, Kuwata *et al.* [62] determined a simple analytical formula that can be used to calculate the polarizabilty of the dipolar plasmon mode of non-spherical particles with dimensions that fall outside the Rayleigh regime (see Section 1.2.1). The empirical formula was verified by comparing it with experimental scattering spectra of the long-axis

mode of gold nanorods. The Kuwata polarizability is given by [62],

$$\alpha_{\text{Kuwata}} \approx \frac{V}{L + \frac{\varepsilon_s}{\varepsilon_m - \varepsilon_s} + A\varepsilon_s x^2 + B\varepsilon_s^2 x^4 - i\frac{4\pi^2\varepsilon_s^{3/2}}{3}\frac{V}{\lambda_0^3}}, \tag{2.8}$$

where V is the volume of the particle, λ_0 is wavelength in vacuum and x is a size parameter corresponding to the half-axis of the direction that incident light is polarized along, and is evaluated from,

$$x = \frac{2\pi a}{\lambda_0}. \tag{2.9}$$

The experimentally determined material independent parameters by Kuwata *et al.* are,

$$A(L) = -0.4865L - 1.046L^2 + 0.8481L^3, \tag{2.10}$$

and,

$$B(L) = 0.01909L + 0.1999L^2 + 0.6077L^3. \tag{2.11}$$

2.2.4 Mie: exact solution for spherical particles

In 1908, Gustav Mie [63] solved the Maxwell equations in spherical polar coordinates by expansion of the incident, internal, and scattered plane waves using vector spherical harmonics [7]. Using this approach the absorption, scattering, and extinction cross sections of a sphere of arbitrary size can be calculated. The scattering cross-section can be found by evaluating,

$$\sigma_{\text{sca}} = \frac{2\pi}{k^2}\sum_{u=1}^{\infty}(2u+1)(|a_u|^2 + |b_u|^2), \tag{2.12}$$

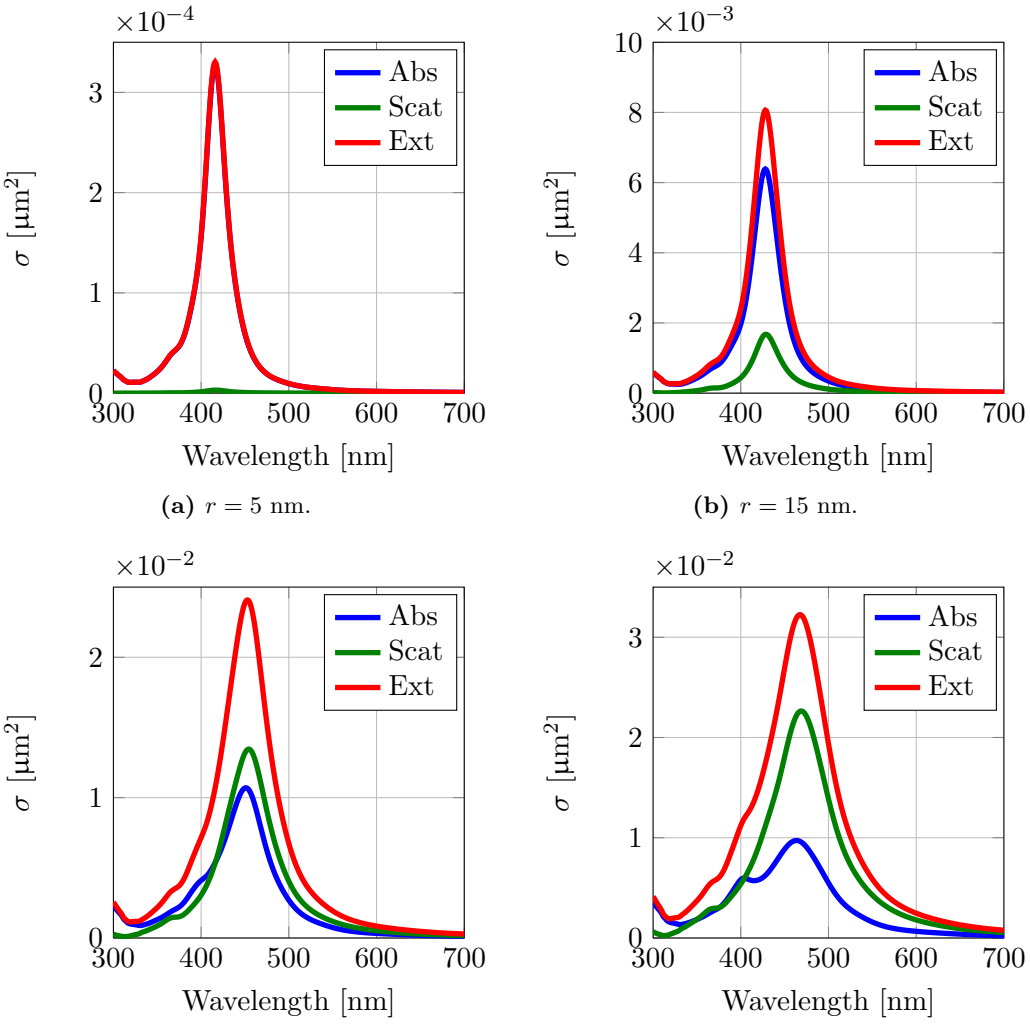

(a) $r = 5$ nm. **(b)** $r = 15$ nm.

(c) $r = 25$ nm. **(d)** $r = 30$ nm.

Figure 2.4: Mie calculated absorption, scattering and extinction cross-sections of four different radii silver spheres embedded in a refractive index of $n = 1.5$. Permittivity of silver taken from Ref. [10]. Extinction of a 5 nm radius particle is dominated by absorption, whereas the extinction of a 30 nm radius particle is dominated by scattering. The feature seen in all spectra at approximately 380 nm is attributed to the permittivity taken from the literature.

and the extinction cross-section by,

$$\sigma_{\text{ext}} = \frac{2\pi}{k^2}\sum_{u=1}^{\infty}(2u+1)\Re\{a_u + b_u\}, \tag{2.13}$$

and the absorption cross-section by,

$$\sigma_{\text{abs}} = \sigma_{\text{ext}} - \sigma_{\text{sca}}, \tag{2.14}$$

where u is the order of the partial wave and corresponds to $u = 1$ for dipole field, $u = 2$ for quadrupole field and $u = 3$ for octupole field etc., and a_u and b_u are scattering coefficients. The scattering coefficients can be obtained from,

$$a_u = \frac{m\psi_u(mx)\psi_u'(x) - \psi_u(x)\psi_u'(mx)}{m\psi_u(mx)\xi_u'(x) - \xi_u(x)\psi_u'(mx)}, \tag{2.15}$$

and,

$$b_u = \frac{\psi_u(mx)\psi_u'(x) - m\psi_u(x)\psi_u'(mx)}{\psi_u(mx)\xi_u'(x) - m\xi_u(x)\psi_u'(mx)}, \tag{2.16}$$

where m is the *relative refractive index* given by $m = n_1/n$, where n_1 and n are the refractive indices of the particle and medium respectively, x is a *size parameter* given by $x = k/a = 2\pi na/\lambda$, where a is the radius of the sphere and $\psi_u(\rho) = \rho j_u(\rho)$ and $\xi_u(\rho) = \rho h_u^{(1)}(\rho)$ are Riccati-Bessel functions. For the Mie calculations of the cross-sections of spheres in this chapter, MATLAB code from the SPlaC package from Ref. [64] was used. For more information on Mie theory, the reader is directed to Ref. [7].

Figure 2.4 shows the calculated absorption (blue line), scattering (green line) and extinction (red line) cross-sections of various different radii of a silver sphere in $n = 1.5$ calculated using Mie theory. From these spectra, it is seen that the plasmon resonance peak for a 5 nm radius particle is at approximately 410 nm, red-shifting to approximately 480 nm for a 30 nm radius particle as the phase of the incident electric field varies more over the volume of the particle. The width of the particle plasmon resonance becomes broader as the particle dimensions are increased, due to the increased radiation damping. For a sphere of radius of 5 nm or less, the extinction of the particle

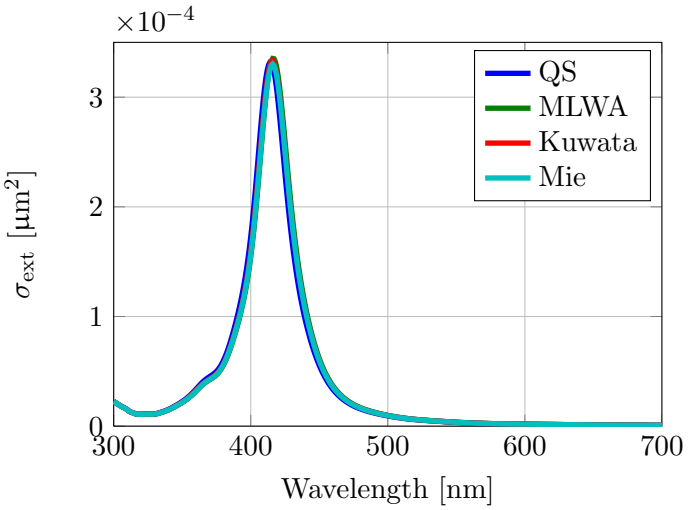

(a) $r = 5$ nm.

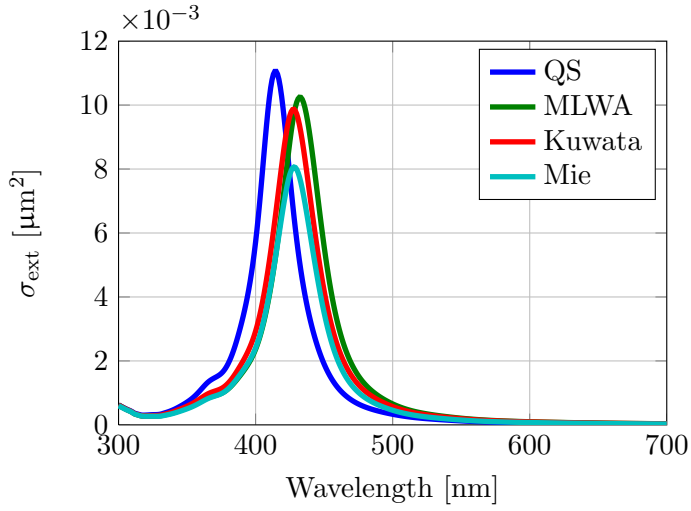

(b) $r = 15$ nm.

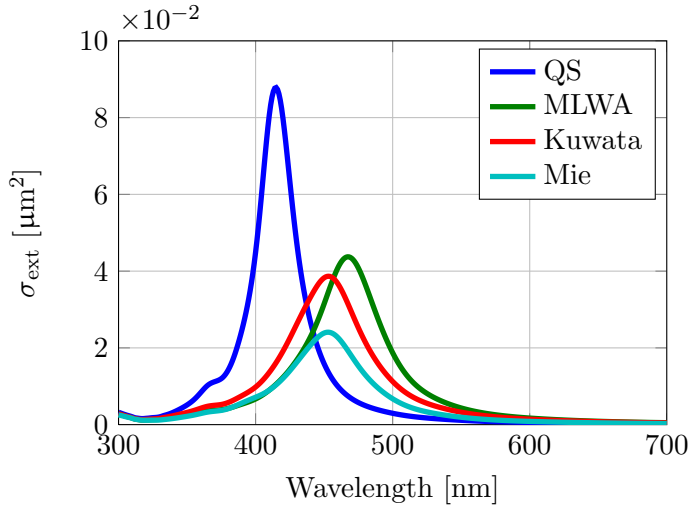

(c) $r = 25$ nm.

Figure 2.5: Comparison of extinction cross-sections calculated by quasi-static, modified long-wavelength approximation, Kuwata and Mie for three different radii of silver spheres.

is almost completely due to absorption; for a sphere of 25 nm radius the absorption and scattering are comparable; and for a 30 nm radius sphere scattering dominates: in the QS limit σ_{abs} scales with a^3 (see Equation 1.25) and σ_{sca} scales with a^6 (see Equation 1.26) and explains why the extinction of small particles is dominated by absorption. A further observation is that the extinction cross-section of a 25 nm radius sphere is two orders of magnitude greater than that of a 5 nm radius sphere. This increase in extinction is attributed to the additional scattering of light by the particle and demonstrates why it is difficult to measure the scattering of light by particles with dimensions of less than 5 nm.

Figure 2.5 shows a comparison between commonly used modelling approaches to calculate the extinction cross-section of a spherical particle [60]. The spheres were modelled in a refractive index of $n = 1.5$ and the permittivity for silver was taken from Ref. [10]. All of the methods show the dipole plasmon resonance at approximately 410 nm for a 5 nm radius particle (see Figure 2.5a). The particle can be considered to be in the QS regime, since it is small compared to the wavelength of the incident light. The feature seen at approximately 380 nm in all of the spectra is attributed to the permittivity taken from Ref. [10]. Moving to a 15 nm radius particle, the position of the QS peak remains in the same spectral position as for a 5 nm radius particle and its magnitude increases as the polarizability is scaled by the volume ($proportional to a^3$) of the particle. Red-shifting of the particle plasmon peak is seen with the MLWA, Kuwata, and Mie theory, as retardation effects are now important. The MLWA and Kuwata agree well with Mie theory on the spectral position of the resonance, but both give a larger extinction cross-section. If the particle radius is increased to 30 nm, the QS approximation strongly overestimates the strength of the resonance and remains at the same spectral position as for the 5 nm radius sphere, as expected from Equation 2.1. The MLWA and Kuwata have red-shifted and give a similar position of the plasmon resonance peak as Mie, but both give a larger extinction cross-section.

2.3 Electron-beam lithography

The process of EBL involves passing an electron beam over the surface of a resist to trace the desired shape. The interaction of electrons with the resist change the resist's solubility and allows the exposed or unexposed regions to be removed with solvent, depending on whether a positive or negative resist has been used. EBL is a fundamental nanoscale fabrication technique allowing the production of structures with sub-10 nm dimensions [65]. With EBL, nanostructures can be produced with

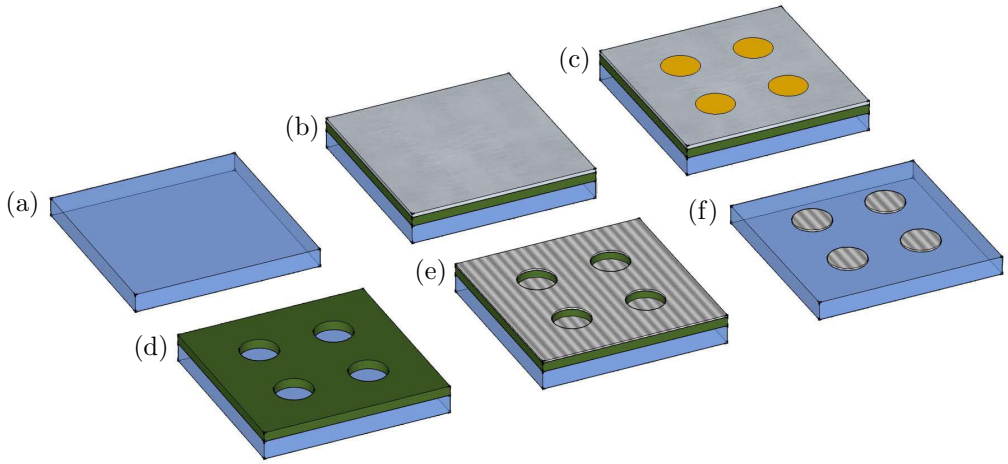

Figure 2.6: Schematic of electron-beam lithography process outlining the key steps involved. The steps are (a) substrate preparation, (b) spin coating of substrate with resist (indicated in green) and addition of conductive layer, (c) exposure of resist (indicated with yellow areas), (d) removal of conductive layer and development, (e) evaporation and (f) lift-off.

precise control over particle size and position, with the resolution limited by the forward scattering of electrons in the resist and by back scattering from the substrate [66, 67]. Electrons entering the resist perform a series of elastic collisions that act to broaden the beam - this forward scattering increases with resist thickness. Back scattering arises where electrons pass through the resist and penetrate deeply into the substrate and are scattered at large angles and re-enter the resist at a distance (greater than 1µm) from where they first entered. A schematic of the key steps of the EBL process are illustrated in Figure 2.6 and are described below.

1. **Substrate preparation.** The particle arrays were fabricated on fused-quartz silica substrates with dimensions of 25 mm × 25 mm. Initially, the substrates were cleaned with acetone and cotton buds to remove any large dust particles and foreign particles from the surface. This is the only stage at which cotton buds are used as they can leave fibres on the surface of the substrate. Then the substrates were sonicated hot in acetone (50°C–70°C) for 10 min followed by 2 min hot in Propan-2-ol (50°C–70°C). Acetone is used to remove any organic contaminants and Propan-2-ol (IPA) to remove the residue left from the acetone. After each stage the sample was dried in a stream of nitrogen.

2. **Spin coating of substrate with resist and addition of conductive layer.** Substrates were spin-coated with 950k A4 poly(methyl methacrylate) (PMMA) positive photo resist at a spin speed of 4000 rpm for 50 s to produce a resist layer

of 200 nm (950k refers to the molecular weight of the PMMA and A4 refers to the concentration (i.e. 4%) of the PMMA in solvent (the A in A4 is for anisole)). The resulting thickness of the resist is an interplay between the concentration of the PMMA (the more viscous the PMMA the thicker the layer) and the rotation speed of the spinner. After the application of the resist to the substrate, the sample is baked for 20 mins on a hotplate at 160°C to evaporate any remaining solvent. A 20 nm aluminium film is then deposited on top of the resist layer by thermal evaporation to provide a continuous conductive layer to prevent charge accumulation and thus defection of the beam in the lithography process. If the conductive layer is too thick, there will be a small amount of electrons transmitted and if it is too thin the metal will not form a continuous conducting film.

3. **Exposure of resist.** The substrate was placed into a scanning-electron microscope chamber, where a focussed electron beam was passed through the conductive layer and resist, drawing the required pattern. In this process, inelastic collisions of the electrons with the long chain polymer resist produce smaller more soluble fragments. A positive resist was used so that the exposed regions of the resist become more soluble and can be removed in the development stage and that is advantageous because the area coverage of structures to substrate is tiny.

4. **Removal of conductive layer and development.** Prior to development the conductive layer of aluminium was etched by placing the sample in tertamethylammonium hydroxide. The removal of the layer allows the developer to surround the fragments of the resist. The sample was rinsed twice by placing it in two separate beakers of de-ionized water and agitating it. The exposed regions of the resist now consist of smaller more mobile fragments and can be removed by diffusion into the developer (mixture of 3:1 Methyl isobutyl ketone (MIBK) to IPA). This stage involves placing the sample in the developer for 10 s, then 20 s into IPA and finally drying with a stream of nitrogen. This produces a template of the desired pattern in the resist, through which the metal can pass and adhere to the substrate, forming the silver particles.

5. **Evaporation.** The sample is placed in a vacuum chamber where 30 nm of silver was deposited by thermal evaporation at a rate of 1-2 $Å s^{-1}$ and pressure of 2×10^{-6} mbar. The mass of silver deposited was then measured by the change in frequency of a quartz crystal microbalance, which can then be converted to the thickness. After the evaporation of the metal, the sample is left for 30 min to cool down before bringing the chamber up to atmospheric pressure.

6. **Lift-off.** The remaining resist and excess metal was removed by immersion of the

sample in warm (less than 50°C) acetone for 2-10 min. The acetone dissolves the PMMA and lifts the metal film away from the sample, leaving only the patterned metal arrays behind.

The single particle plasmon resonance of each fabricated disc can then be measured by collecting the resonantly scattered light by dark-field spectroscopy.

2.4 Dark-field scattering measurements

Dark-field spectroscopy is a common technique used for obtaining the scattering of *single* particles [23, 68–72], but is limited to the detection of 20 nm or larger particles [73, 74]. This is the result of the optical response of particles with dimensions less than 20 nm being dominated by absorption (see Figure 2.4). The advantage of dark-field scattering measurements is the reduced background signal over conventional transmission measurements; only the weak scattering from the substrate, in comparison to the large background of the incident light source in the transmission geometry. The substrate must be thoroughly cleaned as any dust on it will scatter more light than the particle in question, reducing the contrast of the measurement. The key to dark-field scattering measurements is for the numerical aperture (NA) (Equation 2.17) of the condenser to be greater than the collection objective, so that no directly transmitted light is collected [75], see Figure 2.7. Alternatively, the scattering of a single particle can be measured by total-internal reflection (TIR), by placing the particle in an evanescent field produced by a prism [76]. In Ref. [76] they claim by using TIR as the excitation method, particles with dimensions less than 10 nm can be detected. Particle plasmon resonance of single particles with dimensions of 5 nm have been measured using an interferometric detection technique [77]. The NA is defined as [31],

$$NA = n \sin \theta, \tag{2.17}$$

where n is the refractive index of the surrounding medium and θ is the half-angle of the cone of light that can enter or exit the lens. In this instance, $n = 1.515$ for the immersion oil and the $NA = 0.5$ for the collection lens, meaning the half-angle of the collection lens is 19.3°.

The condenser contains a block that stops small angles of light being transmitted thus producing a hollow cone of light (in this case 53°–72°) that is focussed onto the sample.

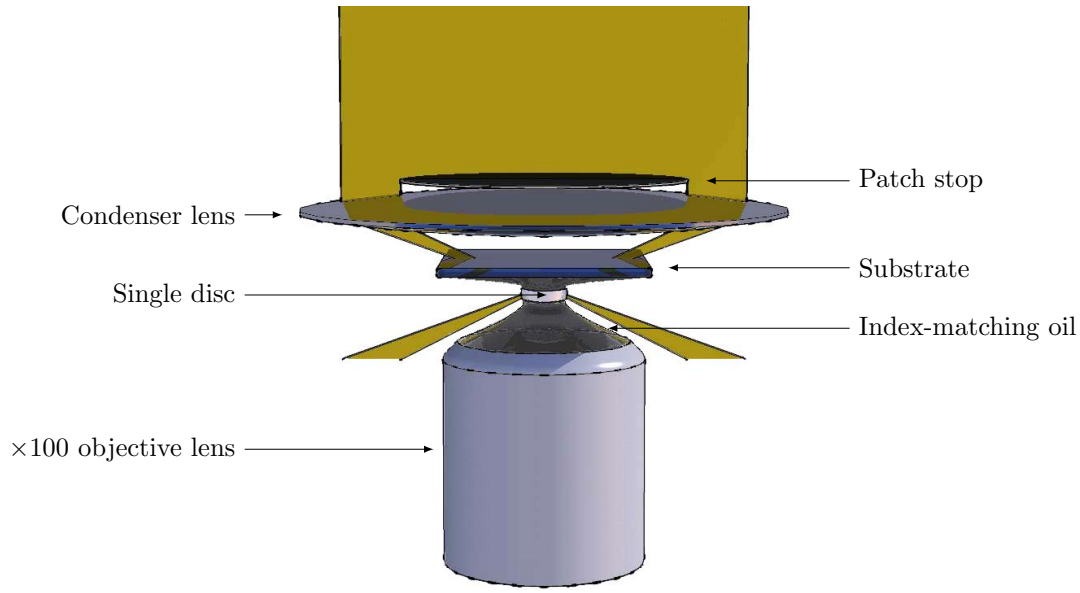

Figure 2.7: Schematic of experimental dark-field setup. The numerical aperture of the collection objective must be smaller than the condenser, so no directly transmitted light is collected. Light scattered by an isolated single nanoparticle is measured over the collection angle of the objective lens.

To obtain the scattering from one nanoparticle, the slit of the spectrometer is centered and then opened or closed to isolate one row of particles in the square array, see Figure 2.8. The pitch of the square array is 2 μm to avoid particle interactions. Scattered light from each disc is seen using an optical microscope, as the scattering cross-section is larger than the geometric cross-section of the particle. By choosing the different strips of the CCD, the scattering spectrum of an individual particle can be measured. To normalize the scattering spectra of a particle, the dark-field intensity is calculated by,

$$I_{\mathrm{DF}} = \frac{I_{\mathrm{signal}} - I_{\mathrm{ref}}}{I_{\mathrm{lamp}} - I_{\mathrm{dark}}}, \tag{2.18}$$

where I_{signal} is the spectrum obtained of a single particle, I_{ref} is the spectrum of a blank portion of the substrate, I_{lamp} is the lamp spectrum (which is the same as I_{ref} in this case) and I_{dark} is the dark counts from the CCD.

An example of the dark-field processing of spectra is shown in Figure 2.9. Firstly, the lamp spectrum (see Figure 2.9a) is obtained by finding a blank portion of the substrate away from the location of the particles. This lamp spectrum is the same one used for the reference. Notice that the intensity of the halogen lamp source is highest

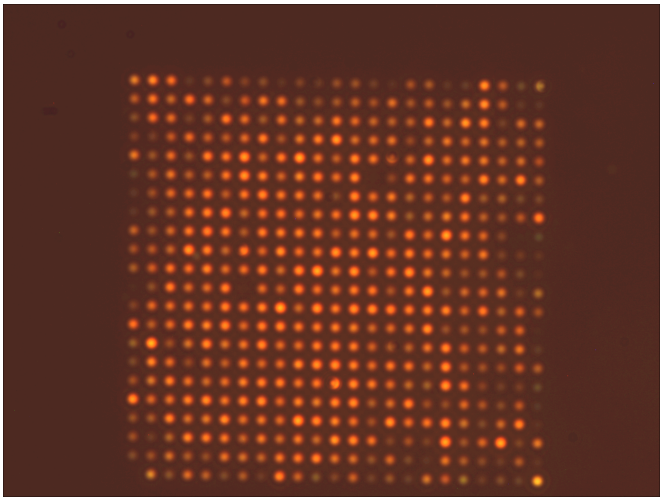

Figure 2.8: Colour image taken using a CCD coupled to an optical microscope illustrating the resonantly scattered light from silver nanoparticles. The scattered light can be observed using an optical microscope as the scattering cross-section of each disc is larger than its geometric cross-section. Particles are arranged in a 50 µm × 50 µm square array with a 2 µm pitch to avoid particle interactions.

between wavelengths 500 nm to 900 nm. The shutter of the CCD is closed for the same integration time to obtain the dark counts (see Figure 2.9b) from the CCD. The array is imaged and the slit on the spectrometer centered and closed to isolate just one row of the array of particles (see Figure 2.9c). Equation 2.18 is computed by subtracting the spectrum of lamp (see Figure 2.9a) from the spectrum of the particles (see Figure 2.9c) and dividing this by the lamp spectrum (see Figure 2.9a) minus the background (see Figure 2.9b).

An example of the measured scattering spectra of one row of silver discs ($d = 110$ nm, $h = 30$ nm) is shown in Figure 2.10. (a) is a CCD image of the dispersed light from one row of particles in the square array; and (b) scattering spectra from six selected discs in the row by choosing strips corresponding to the spectrum of each disc (bright regions in (a)). Inset top of (b) is a SEM of a typical disc in the row. From (b) it is seen that there is variation in the scattering spectra (spectral position and strength) from the discs that have been designed with the same dimensions. Due to the EBL fabrication process each particle is not a symmetric disc: it has jagged edges and a rough surface from the polycrystalline domains formed from the evaporation of silver. Any change to the shape of the particle will change the way light is scattered from it and will result in different scattering spectrum.

Plotted in Figure 2.11 are (a) experimental and (b) MLWA calculated scattering spectra

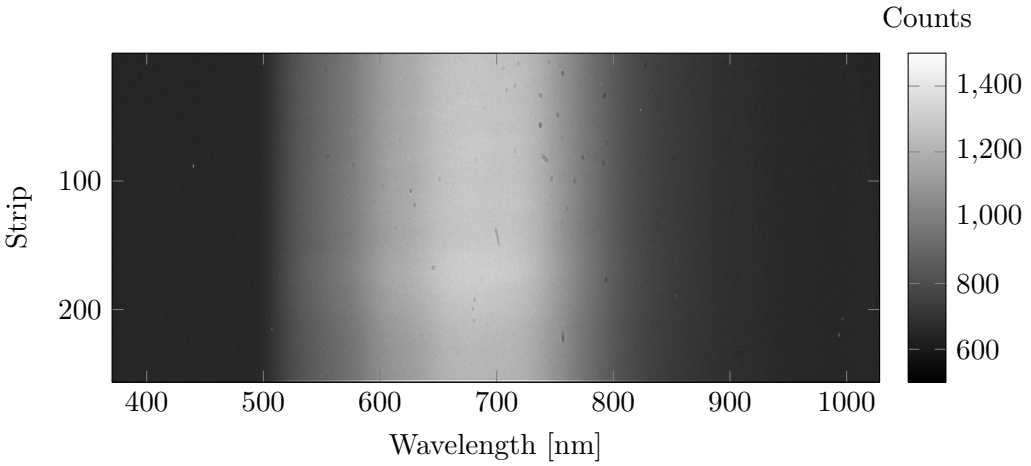

(a) Lamp spectrum.

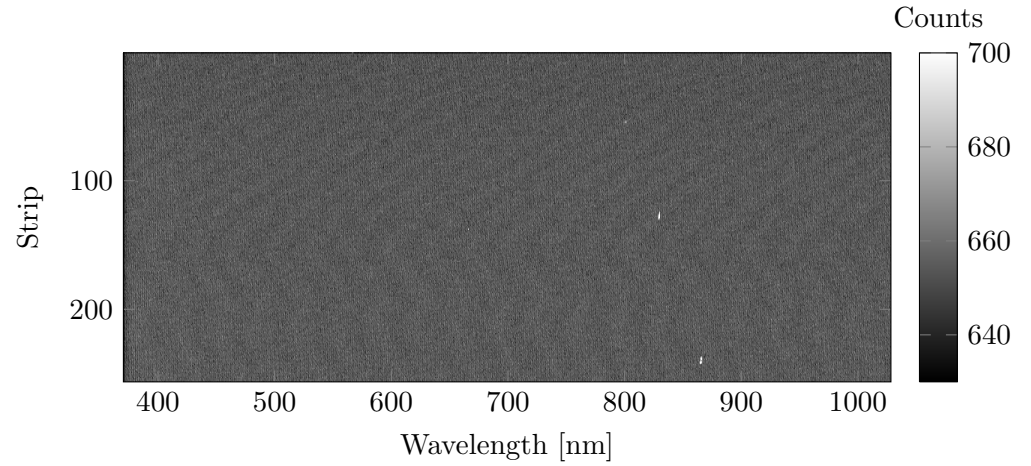

(b) Dark spectrum (CCD dark counts).

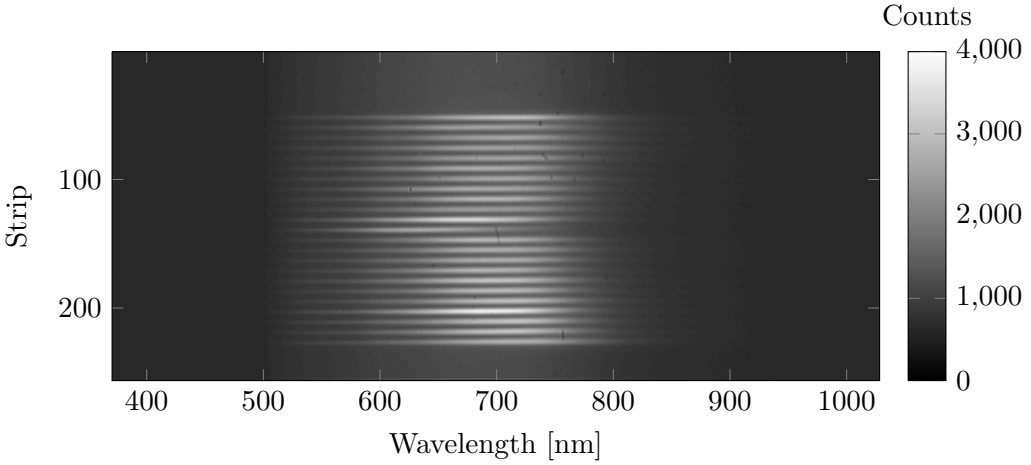

(c) Signal spectrum (scattering from a single Silver disc with 110 nm diameter and 30 nm height).

Figure 2.9: CCD images of the dispersion of the (a) lamp, (b) dark and (c) signal spectra. The dark-field intensity is calculated by [(c)-(a)]/[(a)-(b)].

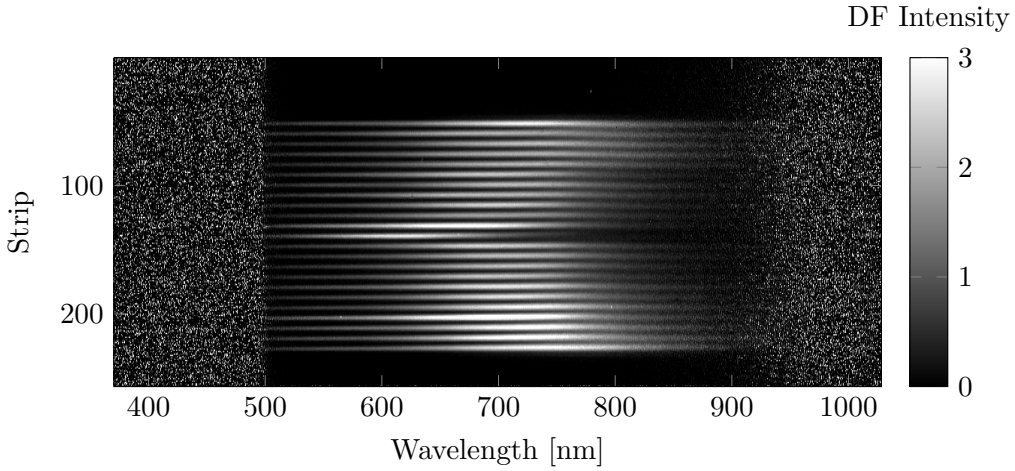

(a) CCD dispersion of one row of particles.

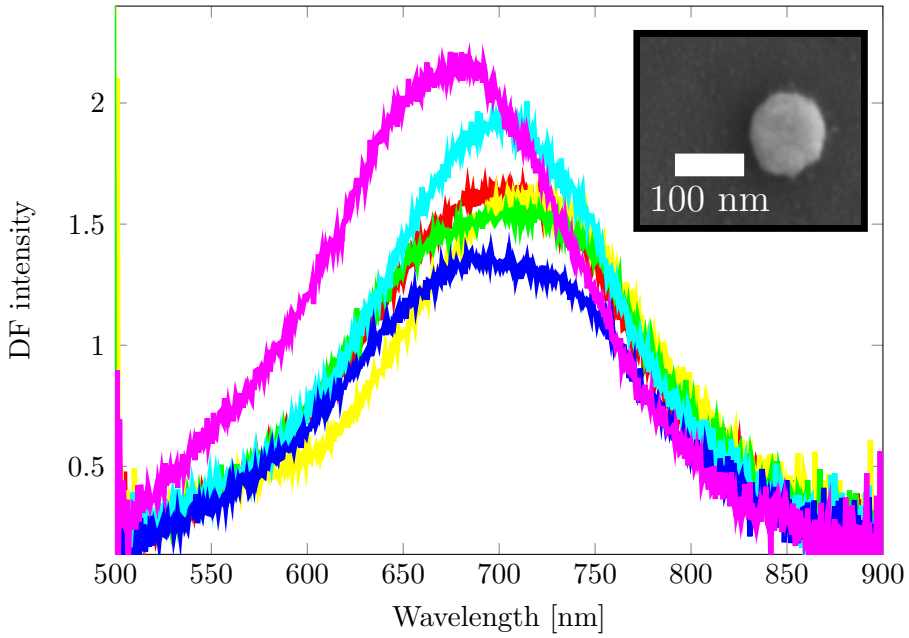

(b) Dark-field spectra.

Figure 2.10: Dark-field scattering spectra of silver discs (d = 110 nm, h = 30 nm) arranged in a 2 µm pitch square array. (a) image from CCD corresponding to the dispersion of one row of discs from the square array and (b) six scattering spectra by choosing different strips from (a). Inset top right in (b) is a scanning-electron micrograph of an example of one of the particles from the row.

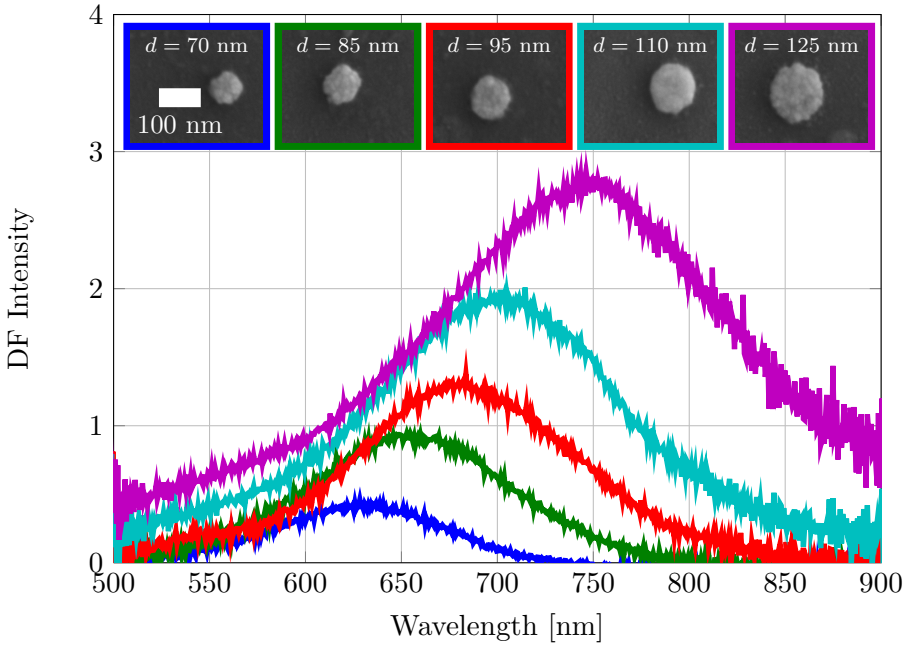

(a) Experiment.

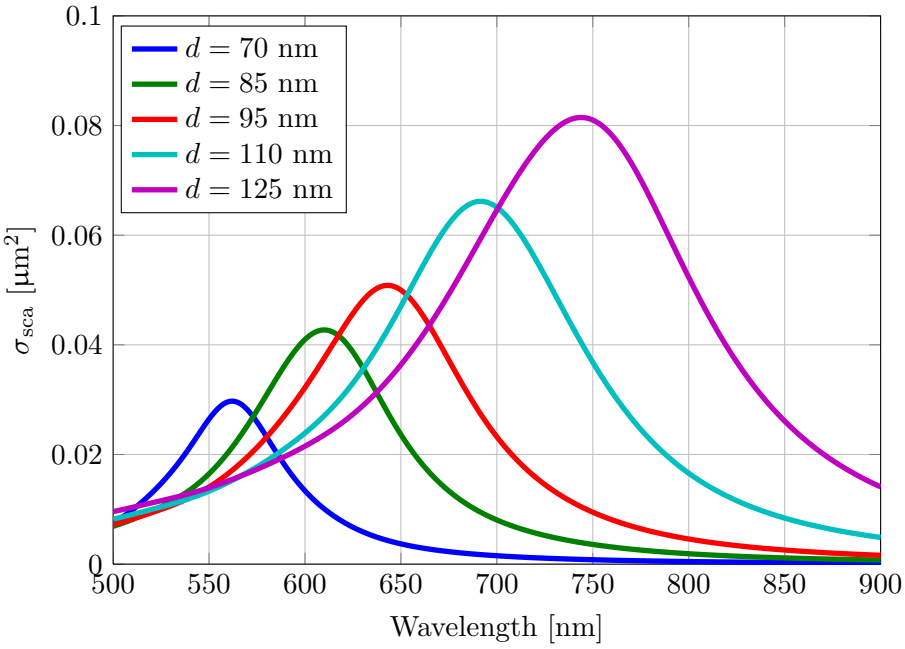

(b) Model.

Figure 2.11: (a) measured and (b) Modified long-wavelength approximation calculated scattering spectra of single silver discs with various diameters (d = 70 nm, d = 85 nm, d = 95 nm, d = 110 nm and d = 125 nm). Each disc has a height of 30 nm and is surrounded by an environment with n = 1.515. As the disc diameter is increased, retardation effects become important and the dipolar plasmon mode red-shifts.

from five different diameter particles ($d = 70$ nm, $d = 85$ nm, $d = 95$ nm, $d = 110$ nm and $d = 125$ nm) of silver discs. The discs have a height of 30 nm and the surrounding medium has $n = 1.515$ to index-match with the substrate. In the experiment (see Figure 2.11a), for each different disc diameter a peak is observed in each scattering spectrum, corresponding to the dipolar particle plasmon resonance of the disc. The particle plasmon resonance wavelength red-shifts as the disc diameter is increased as the phase of the incident electric field varies more over the volume of the particle. As the particle diameter is increased, the strength of the scattering increases and the particle plasmon resonance broadens. The strength of the scattering increases with particle size as there are more electrons in the particle collectively oscillating (scattering scales with the volume of the particle). Broadening is the result of radiative loss from the accelerating charges and as the particle volume increases there are simply more charges. These trends are also displayed in the calculated spectra (see Figure 2.11b). There is poor agreement between the experiment and model for the spectral position of the particle plasmon resonance for the smaller diameters of the disc ($d = 70$ nm, $d = 84$ nm and $d = 93$ nm) - it is not obvious why this is the case and has also been observed elsewhere [33]. Two possible suggestions are: there is variation in particle height between each one of the arrays or in relation to their size the imperfections that change the scattering are more dominant for smaller particles. It is important to note, there are several differences between the experiment and model: (i) the particles have been modelled as oblate spheroids, in the experiment they are in fact discs with jagged edges (not symmetric); (ii) the illumination optics provide a range of k vectors and polarization states which are unknown; (iii) unpolarized light will cause multiple plasmon modes in each particle, and as the discs are not symmetric this will change the width of the resonance; (iv) the immersion oil may not exactly match the dispersion of the substrate.

2.5 Conclusion

In Chapter 1 it was demonstrated that light incident on a metallic nanoparticle displaces its conduction electrons from their equilibrium positions inducing a dipole moment. The dipole moment of a particle is related to its polarizabilty, which describes the response of the collective charge oscillation to an applied electric field. Introduced in this chapter was a polarizability that is applicable to non-spherical particles outside the quasi-static limit to model the isolated single particle response of discs to incident light. Using Mie theory, it was shown the extinction of a small sphere ($r = 5$ nm) is dominated

by absorption; scattering increases with particle volume; and for a $r = 25$ nm sphere the absorption and scattering are comparable. Comparison was made between the quasi-static (QS), modified long-wavelength approximation (MLWA), Kuwata and Mie calculated extinction cross-section of spheres: there is good agreement for a $r = 5$ nm sphere, but as the radius of the sphere is increased the QS, MLWA and Kuwata predict a larger magnitude cross-section, with the MLWA and Kuwata red-shifting more than Mie theory. Isolated single particles were fabricated by electron-beam lithography and their scattering measured and compared to calculated scattering spectra. There was good agreement between the model and experiment for larger dimension discs ($d = 110$ nm and $d = 125$ nm), but poor agreement with smaller ($d = 70$ nm, $d = 85$ nm, $d = 95$ nm). A discussion on differences between the model and the experimental setup were presented to account for this discrepancy. The fact that plasmonic particles can resonantly scatter light, means they can couple together over long distances (greater than λ). By an appropriate choice of array pitch, the scattered fields from the particles can interfere together constructively, giving rise to surface lattice resonances (SLRs). The content of Chapter 3 explores theoretically and experimentally SLRs on different array geometries.

Chapter 3

Response of regular arrays of plasmonic nanoparticles

3.1 Introduction

In Chapter 2, it was shown that plasmonic silver nanoparticles resonantly scatter light at optical wavelengths. For particles with dimensions greater than approximately 30 nm, their extinction is dominated by scattering over absorption. The fact that plasmonic particles scatter light means they can couple over large distances (greater than the incident wavelength). When such particles are separated by roughly the particle plasmon resonance wavelength, the scattered light from all the particles can interfere constructively, resulting in sharp (FWHM $<$ 10 nm) spectral features. This chapter investigates the collective array response of particles via experiments and modelling of square, hexagonal and honeycomb arrays, which possess a high degree of symmetry.

Firstly, three methods used in this thesis to model the extinction of arrays of plasmonic metallic nanoparticles will be introduced: the coupled-dipole approximation (CDA), a semi-analytical coupled-dipole model and the finite-element method (FEM). Next, fabrication and extinction measurements on square, hexagonal and honeycomb arrays are discussed, and the semi-analytical model will be compared to experimental extinction spectra. Lastly, the polarization sensitivity of different array geometries will be investigated. Previous work has involved studying square arrays but initially without the conditions needed (unsuitable particle size, illumination angle and an asymmetric optical environment etc.) [43, 78, 79] to observe narrow surface lattice resonances (SLRs).

It was not until 2008 that narrow SLRs were observed experimentally [44, 45, 47]. More recently, Rodriguez *et al.* [80] have studied the number of particles that contribute to this collective behaviour, i.e. they addressed the question when does an array become infinite. They modelled the extinction of square arrays of nanoparticles by treating the particles as coupled point dipoles and compared the Q-factor of the SLR peak. They found for a square array of 30×30 particles the Q-factor approached that of an infinite array. The effect of disorder and particle size dispersion on the SLR has been studied by Auguié and Barnes [81]. They fabricated square arrays of particles and varied both particle position and size separately. Upon a gradual transition from a regular to a disordered array, the SLR broadened, weakened and eventually disappeared, whereas varying the particle size only caused broadening and weakening of the SLR. Out-of-plane SLRs have been investigated by Zhou and Odom [46] using oblique angle of incidence excitation, and more recently by Thackray *et al.* [49]. Out-of-plane resonances occur where the electrons of the particle collectively oscillate parallel to the height dimension. In Ref. [49] they fabricated arrays of particles with a non-trivial geometry, allowing normally incident light to couple to out-of-plane dipole moment. In Ref. [46] they fabricated square arrays of gold discs (65–170 nm tall) and measured their transmission and reflection at a range of incident angles (10–60°) for TE and TM polarized light. Up until now, a direct comparison of the optical response of three different array geometries (square, hexagonal and honeycomb) has not been made - this is the essence of this chapter. This chapter begins by introducing modelling techniques to predict the optical response of the arrays.

3.2 Modelling of array response

3.2.1 Coupled-dipole approximation

The coupled-dipole approximation (CDA), also known as the discrete-dipole approximation (DDA), is a versatile and useful modelling technique used to calculate the scattering and absorption of particles. It was first used to study interstellar dust grains by Purcell and Pennypacker [82] in 1973. The CDA can be used to model either a particle of arbitrary geometry for which Maxwell's equations can not be solved exactly, or for an ensemble of particles that are small enough to only support a dipolar mode [83]. For an array of particles, each particle is approximated as a dipole and given a polarizability. The CDA code used in this thesis is a modified version of the one produced by Burrows in Ref. [84]. The code has been modified by Dr. N. Meinzer to

accept polarizabilities of non-spherical particles.

Here the incident electric field at the position of each particle f is a plane wave of the form $\vec{E}_{\mathrm{inc},f} = \vec{E}_0 \exp(i(\vec{k}\cdot\vec{r} - \omega t))$, where $\vec{E}_0$ is the amplitude, $\vec{k}$ is the wavevector in the medium, $\vec{r}$ is a position vector, ω is angular frequency and t is time. Each particle can be considered as an oscillating dipole moment and, ignoring the time dependence the electric field, can be written as [85],

$$\vec{E}_{\mathrm{dipole}} = \frac{1}{4\pi\varepsilon_0}\exp(i\vec{k}\cdot\vec{r})\left\{\frac{k^2}{r}[(\hat{r}\times\vec{p})\times\hat{r}] + \left(\frac{1}{r^3} - \frac{ik}{r^2}\right)[3\hat{r}(\hat{r}\cdot\vec{p}) - \vec{p}]\right\}, \tag{3.1}$$

where $\vec{r}$ is the distance from the dipole to the point of observation, $\vec{p}$ is the dipole moment and ε_0 is the permittivity of free space. The electric field at the site of each particle f is the sum of the incident electric field at position f plus the scattered field from the other j particles and can be expressed as,

$$\vec{E}_f = \vec{E}_{\mathrm{inc},f} - \sum_{f\neq j}\vec{E}_{fj}, \tag{3.2}$$

where the term $-\sum_{f\neq j}\vec{E}_{fj}$ is the contribution of the electric field from the other j dipoles at point f, and can be written as [86],

$$-\sum_{f\neq j}\vec{E}_{fj} = -\sum_{f\neq j}\frac{1}{4\pi\varepsilon_0}\frac{\exp(i\vec{k}\cdot\vec{r}_{fj})}{r_{fj}^3}\left\{k^2[\vec{r}_{fj}\times(\vec{r}_{fj}\times\vec{p}_j)] + \frac{(1-ikr_{fj})}{r_{fj}^2}[r_{fj}^2\vec{p}_j - 3\vec{r}_{fj}.(\vec{r}_{fj}\cdot\vec{p}_j)]\right\} \tag{3.3}$$

Equation 3.2 can be rewritten as,

$$\vec{E}_f = \vec{E}_{\mathrm{inc},f} - \sum_{f\neq j}A_{fj}\vec{p}_j, \tag{3.4}$$

where A_{fj} is the interaction sub-matrix and is given by,

$$A_{fj} = \frac{1}{4\pi\varepsilon_0}\frac{\exp(ikr_{fj})}{r_{fj}}\left\{k^2(\hat{r}\otimes\hat{r} - I_3) + \left(\frac{ikr_{fj}-1}{r_{fj}^2}\right)(3\hat{r}\otimes\hat{r} - I_3)\right\}, \tag{3.5}$$

where I_3 is a 3×3 identity matrix. The interaction sub-matrix is a 3×3 matrix that contains the cartesian components of the electric field at point f due to the dipole moment at point j [84]. A simplification can be made, by relating the electric field at point f to the polarizability of particle f by $\vec{E}_f = \vec{p}_f/\alpha_f\varepsilon_0$. This allows Equation 3.4 to be rewritten as,

$$\vec{E}_{\text{inc},f} = A_{ff}\vec{p}_f + \sum_{f\neq j} A_{fj}\vec{p}_j, \tag{3.6}$$

where A_{ff} is a 3×3 matrix and is given by,

$$\begin{pmatrix} \frac{1}{\varepsilon_0\alpha_{f,x}} & 0 & 0 \\ 0 & \frac{1}{\varepsilon_0\alpha_{f,y}} & 0 \\ 0 & 0 & \frac{1}{\varepsilon_0\alpha_{f,z}} \end{pmatrix}$$

where $\alpha_{f,x}$, $\alpha_{f,y}$ and $\alpha_{f,z}$ are the polarizabilities associated with the three different axes of the ellipsoid. For the discs modelled in this thesis, $\alpha_{f,x}$ and $\alpha_{f,y}$ are the polarizabilities related to the two major axes and $\alpha_{f,z}$ is the polarizability corresponding to the height dimension of the particle. Equation 3.6 can be reduced to the following equation for a system of N particles,

$$\vec{E}_{\text{inc},f} = \sum_{j=1}^{N} A_{fj}\vec{p}_j. \tag{3.7}$$

Column vectors $\boldsymbol{P}$ and $\boldsymbol{E}_{\text{inc}}$ of length $3N$ can be constructed containing the dipole moments and the incident electric field. The dipole moment of each particle f can be found by solving the matrix equation,

$$\boldsymbol{P} = \boldsymbol{A}^{-1}\boldsymbol{E}_{\text{inc}}. \tag{3.8}$$

The absorption cross-section per particle and scattering cross-section per particle can then be calculated by substituting $\frac{1}{N}\vec{E}^*_{\text{inc},f} \cdot \vec{p}_f$ for the single particle polarizability into Equations 1.25 and 1.26, giving the following formulae,

$$\sigma_{\text{abs}} = \frac{k}{|\vec{E}_0|^2} \sum_{f=1}^{N} \Im(\frac{1}{N}\vec{E}^*_{\text{inc},f} \cdot \vec{p}_f), \tag{3.9}$$

and,

$$\sigma_{\text{sca}} = \frac{k^4}{6\pi|\vec{E}_0|^2} |\sum_{f=1}^{N} |\frac{1}{N}(\vec{E}^*_{\text{inc},f} \cdot \vec{p}_f)|^2, \tag{3.10}$$

where N is the number of particles modelled in the CDA calculation, $\vec{p}_f$ is the dipole moment at position f, $|\vec{E}_0|$ is the magnitude of the incident field and $\vec{E}^*_{\text{inc},f}$ is the complex conjugate of the incident electric field at position f.

3.2.2 S-factor: a semi-analytical coupled-dipole model

For an infinite 2D array of identical dipoles, the CDA model can be simplified leading to an useful approximation in the context of this chapter [42, 44, 49, 80, 87, 88]. It was introduced in Chapter 1 that the dipole moment, $\vec{p}_{\text{isolated}}$ of an isolated metallic particle is related to an applied electric field, $\vec{E}_{\text{inc}}$, by its polarizability, α,

$$\vec{p}_{\text{isolated}} = \varepsilon_0 \alpha \vec{E}_{\text{inc}}. \tag{3.11}$$

In an array, the total field experienced by each particle is the sum of the incident field plus the scattered fields from the other particles,

$$\vec{E}_{\text{total}} = \vec{E}_{\text{inc}} + \sum \vec{E}_{\text{other}}. \tag{3.12}$$

The dipole moment of a particle in the array can be expressed by using Equation 3.12,

$$\vec{p}_{\text{array}} = \varepsilon_0 \alpha (\vec{E}_{\text{inc}} + \sum \vec{E}_{\text{other}}). \tag{3.13}$$

If the array is assumed to be infinite, which is equivalent to each point dipole having the same magnitude and direction [88], the electric field scattered from the other particles can be written as,

$$\sum \vec{E}_{\text{other}} = S\vec{p}_{\text{array}}, \tag{3.14}$$

where the array factor, S, only depends on the geometry of the array. Substitution of Equation 3.14 into Equation 3.13 with rearrangement yields,

$$\vec{p}_{\text{array}} = \varepsilon_0 \frac{1}{1/\alpha - \varepsilon_0 S}\vec{E}_{\text{inc}}. \tag{3.15}$$

By comparison of Equation 3.15 with Equation 3.11, it is seen that the modified polarizability, α^*, of a particle in the array is given by,

$$\alpha^* = \frac{1}{1/\alpha - \varepsilon_0 S}. \tag{3.16}$$

For $\vec{r}_j$ and $\vec{p}_j$ in the same plane, and noting that in Equation 3.3 it is the projection of $(\vec{r}_j \cdot \vec{r_j})$ and $(\vec{r}_j \times \vec{r_j})$ along $\vec{p}_j$ that is needed [89, p. 126],

$$\hat{p}_j \cdot (\vec{r}_{fj} \times (\vec{r}_{fj} \times \vec{p}_j)) = -r_{fj}^2 p_j \sin^2\theta_{fj}, \tag{3.17}$$

and,

$$\hat{p}_j \cdot (\vec{r}_{fj}(\vec{r}_{fj} \cdot \vec{p}_j)) = r_{fj}^2 p_j \cos^2\theta_{fj}, \tag{3.18}$$

where θ_{fj} is the angle between $\vec{p}_j$ and $\vec{r}_{fj}$. Substitution of Equation 3.17 and Equation 3.18 into Equation 3.3 gives,

$$\sum \vec{E}_{\text{dipole}} = -\sum_j \frac{1}{4\pi\varepsilon_0}\frac{\exp(i\vec{k}\cdot\vec{r}_j)}{r_j^3}\left\{[-k^2 r_j^2 \vec{p}_j \sin^2\theta_j] + \frac{(1-ikr_j)}{r_j^2}[r_j^2\vec{p}_j - 3r_j^2\vec{p}_j\cos^2\theta_j]\right\} \tag{3.19}$$

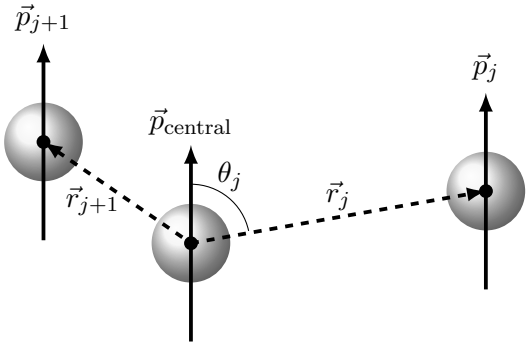

Figure 3.1: The total electric field on the central particle in the array is the sum of the incident electric field plus the scattered field from the other particles. $|\vec{r}_j|$ is the distance from the central particle to particle j and θ_j is the angle between the dipole moment of the central particle, $\vec{p}_{\text{central}}$, and $\vec{r}_j$.

where $\vec{r}_j$ is the vector from the central particle to particle j and θ_j is the angle between $\vec{r}_j$ and $\vec{p}_{\text{central}}$ (see Figure 3.1). After rearranging, Equation 3.19 can be expressed as,

$$\sum \vec{E}_{\text{dipole}} = \sum_j \frac{\vec{p_j}}{4\pi\varepsilon_0} \exp(i\vec{k}\cdot\vec{r}_j) \left\{ \left[\frac{k^2 \sin^2\theta_j}{r_j} \right] + \frac{(1-ikr_j)}{r_j^3} [3\cos^2\theta_j - 1] \right\}. \quad (3.20)$$

Assuming $\vec{p}_j = \vec{p}$ for each j, then,

$$\sum \vec{E}_{\text{dipole}} = S\vec{p}, \quad (3.21)$$

and,

$$S = \frac{1}{4\pi\varepsilon_0} \sum_j \exp(ikr_j) \left[\frac{(1-ikr_j)(3\cos^2\theta_j - 1)}{r_j^3} + \frac{k^2 \sin^2\theta_j}{r_j} \right]. \quad (3.22)$$

It should be noted that, for a given k, S only depends on the particle separation and arrangement. Once the polarizability has been calculated, the absorption σ_{abs} and scattering σ_{sca} cross-section per particle can be calculated by the substitution of Equation 3.16 into the expressions for the cross-sections expressed in Chapter 1 (see Equations 1.25 and 1.26).

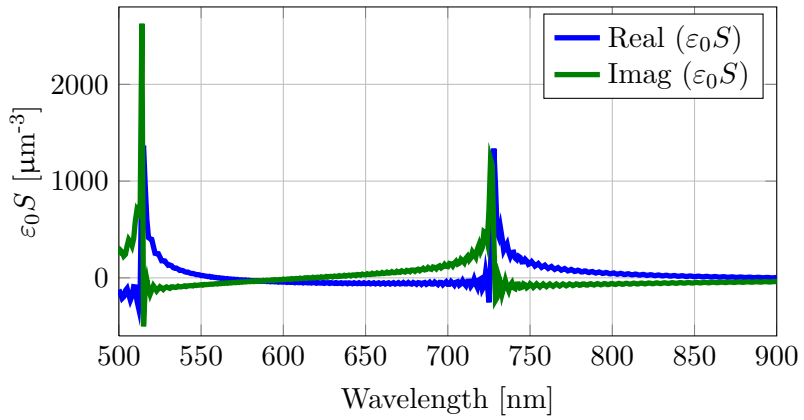

(a) Un-smoothed S-factor.

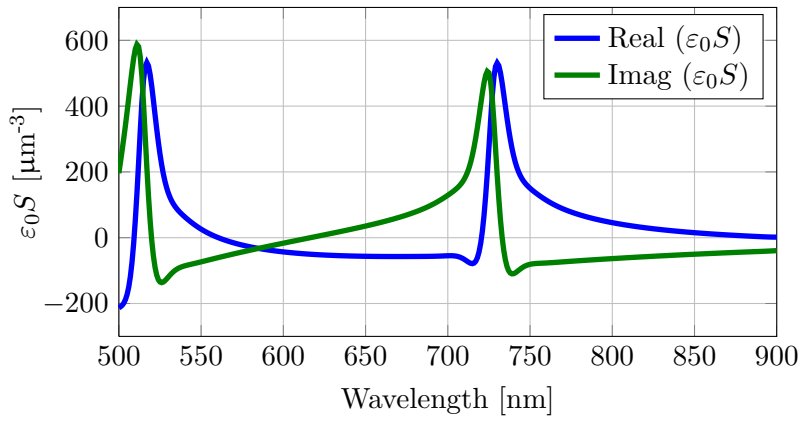

(b) Smoothed S-factor.

Figure 3.2: Comparison of (a) un-smoothed and (b) smoothed S-factor (see Equation 3.22) of a 480 nm pitch square array. Smoothing was carried out using MATLAB function "csaps" with a smoothing parameter of 0.01.

The S-factor (see Equation 3.22) is plotted in Figure 3.2a. As a finite number of particles (400×400) are modelled, the real (blue line) and imaginary (green line) parts of the S-factor shows rapid oscillations [90]. Before substitution of S into Equation 3.16 to perform the calculations, the S-factor data was smoothed using the MATLAB function "csaps" with a smoothing parameter of 0.01 to remove the oscillations (see Figure 3.2b).

As seen in Chapter 1, particle plasmon resonances occur when the denominator of Equation 1.3 is minimized (for a sphere in the QS regime when the real part of the permittivity of the metal equals -2). When the particles, are placed in an array the modified polarizability is given by Equation 3.16 and again, similar to the single particle, resonances occur when the denominator is minimized (when Re $(1/\alpha = \varepsilon_0 S)$). For

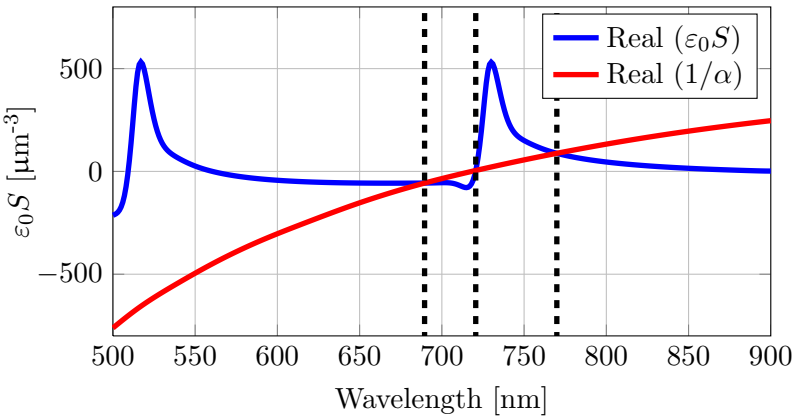

(a) Real parts of $1/\alpha$ and $\varepsilon_0 S$.

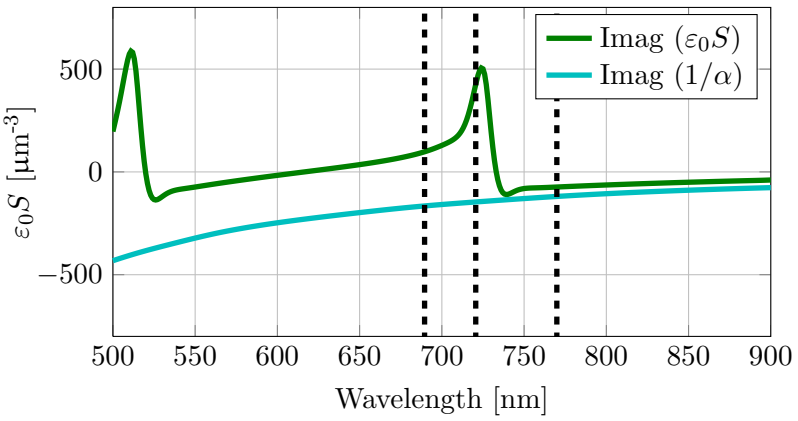

(b) Imaginary parts of $1/\alpha$ and $\varepsilon_0 S$.

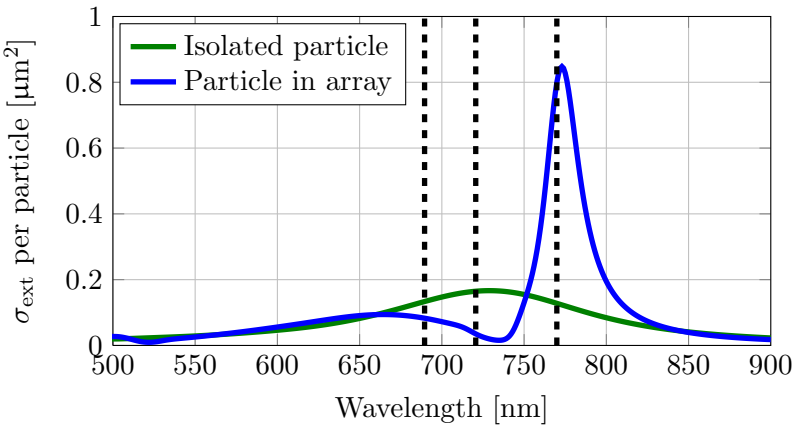

(c) Extinction cross-section per particle.

Figure 3.3: Calculated (a) real and (b) imaginary parts of $1/\alpha$ and $\varepsilon_0 S$ and (c) calculated extinction cross-section per particle for an oblate spheroid ($d = 120$ nm, $h = 30$ nm) in a square array with a pitch of 480 nm. The interceptions of the real part of $1/\alpha$ and $\varepsilon_0 S$ indicate the position of the surface lattice resonances and the difference between the imaginary parts of $1/\alpha$ and $\varepsilon_0 S$ the width and strength. The particles have been modelled in a homogeneous medium with $n = 1.515$. The electric field is in the plane of the particles. Dashed lines indicate the crossing points of the real parts of $1/\alpha$ and $\varepsilon_0 S$ (690 nm, 721 nm and 770 nm).

particles in an array, however, these collective resonances describe SLRs and not particle plasmon resonances.

It will now be discussed how the real and imaginary parts of S are related to the SLR. Presented in Figure 3.3 are the results of an S-factor calculation for a square array of silver discs ($d = 120$ nm and $h = 30$ nm) with a 480 nm pitch. The real parts of $1/\alpha$ (red line) and $\varepsilon_0 S$ (blue line) are plotted in (a) and their accompanying imaginary parts ($1/\alpha$ (cyan line) and S (green line)) are in (b). The crossing points of the real parts of $1/\alpha$ and $\varepsilon_0 S$ are illustrated with black dashed lines. The calculated extinction cross-section per particle of the square array of discs (blue line) and isolated single particle (green line) are shown in (c). The MLWA (see Equation 2.7) has been used to calculate the single particle polarizability.

In Figure 3.3a three crossing points of the real parts of $1/\alpha$ and $\varepsilon_0 S$ (690 nm, 721 nm and 770 nm) are seen, so three SLRs would be predicted in the extinction spectrum (see Figure 3.3c). The extinction spectrum exhibits only two SLRs (at approximately 660 nm and 773 nm) where the real part of $1/\alpha$ and $\varepsilon_0 S$ intersect [91]. Two SLRs are seen because the strength and width of the SLR depends on the difference between the imaginary parts of $1/\alpha$ and $\varepsilon_0 S$ [87]: the difference between $1/\alpha$ and $\varepsilon_0 S$ is largest at the crossing point at 721 nm, so a SLR is not expected to occur, in contrast to the crossing point at 770 nm where the difference between the imaginary parts of $1/\alpha$ and $\varepsilon_0 S$ are small. The SLR at 773 nm does not occur at the crossing point of 770 nm due to the smoothing of the extinction spectrum: the smoothing causes the spectrum to shift to longer wavelengths. In this particular square array example, the SLRs are observed when the real parts of $1/\alpha$ and $\varepsilon_0 S$ intersect, but in different arrays, which are studied later in this thesis, the SLRs can occur on the closest approach of $1/\alpha$ and $\varepsilon_0 S$ [49] as SLRs occur when the denominator of Equation 3.16 is minimized (not necessarily vanishing).

3.2.3 Finite-element modelling

Throughout this thesis the CDA code has been used to explore the responses of arrays metallic nanoparticles; however, in some circumstances the finite-element method (FEM) was employed. This method was used to verify the results of the CDA and S-factor model.

FEM is a widely used technique for calculating the electromagnetic properties of a wide range of structures [92]. Since its inception, FEM has been used to simulate the EM

responses of electronic and antenna components [93], and more recently, researchers used it to investigate a number of different EM effects, for example in the fields of plasmonics [94, 95] and metamaterials [96, 97].

The FEM simulations presented in this thesis were performed by Dr. T. Starkey using Ansys's High Frequency Structure Simulator (HFSS) [98] FEM software. HFSS is a three-dimensional full wave EM field simulation package that solves electric field components. A brief description of this full FEM is given in Ref. [99].

Building and solving a model takes several steps: first, a unit cell that represents the structure is created and assigned material properties. Second, boundary conditions and excitation conditions are applied to the unit cell. Following this, a mesh of small elements to represent the structures in the unit cell is generated. Finally, the electric field components associated with each mesh element are calculated in order to obtain reflectance, transmittance and other field information.

For structures with regular periodicities, like the arrays of metallic nanoparticles simulated in this thesis, a unit cell is first created. The geometries can be drawn using the built-in CAD interface or imported from other software. For designs with regular shapes the three-dimensional CAD tool is ideal. Using the in-built CAD tools first a particle is rendered as a cylinder, and then surrounded with a dielectric volume (other structures, such as a membrane can be incorporated at this stage). Once the geometries are rendered each component is assigned their associated optical constants i.e. material. Here, the permittivity parameters of silver were taken from Ref. [10].

Since the arrays are large compared to the incident radiation periodic boundary conditions (BCs) can be assigned. Periodic BCs enable a unit cell to be repeated throughout space to allow the EM modelling of periodic planes, using Bloch-Floquet expansion theory [100].

In addition to these periodic BCs, further BCs need to be imposed on the top and bottom of the unit cell in order to excite and terminate the electric fields in the model. To achieve this excitation and termination, Floquet ports are assigned. Floquet ports allow the excitation of the arrays with different polarization, incident angle and frequency parameters, and importantly allow the calculation of the optical response for different diffracted orders.

To simulate the response of a structure, the model is first 'meshed'. The meshing process involves subdividing the model unit cell into smaller spatial volumes in which the electric fields are later solved. This is done by adding mesh elements, which are

tetrahedra, to approximate the rendered structure and surrounding space in which the electric field is later interpolated. HFSS's solution is then calculated by numerically solving using Maxwell's equations in vector potential form [101] for every individual element. The electric fields can be interpolated at any point in each mesh element using the field components at the vertices and midpoints of the connecting lines. At the start of the solution process, an initial guess is made for the matrix of unknowns that describes Maxwell's equations [101]. This matrix is recursively updated, during which the adaptive mesh process takes place, until an error tolerance has been reached.

A convergence process decides when an acceptable tolerance, defined by the user, has been achieved. This is determined by using the percentage change in the local energy of each tetrahedron between each solution iteration. As this relative change decreases between solutions, the model is assumed to have converged. Once converged, the electric fields are then solved for the frequency range defined.

Once the model is solved, the reflectance and transmittance can be obtained from the scattering matrix for each diffracted order, typically the transmitted specular diffracted order is extracted for the metallic-particle arrays considered here.

3.2.4 Comparison of methods used to model the optical response of arrays

A comparison of the three different methods used in this thesis to calculate the optical response of a square array (480 nm pitch) of silver particles is shown in Figure 3.4. In this example, the particles are silver discs with $d = 120$ nm and $h = 30$ nm. All of the extinction spectra (see Figure 3.4) have been smoothed using a Gaussian to mimic the 7 nm resolution of the spectrometer: the MATLAB "filter" function has been used with 7-points with $a = 1$ and $b = [0.054; 0.123; 0.203; 0.240; 0.203; 0.123; 0.054]$, where a and b are weighting coefficients. This smoothing has been applied to all of the modelled extinction spectra with the filter function run from shorter to longer wavelengths. For the S-factor and CDA calculations the MLWA has been used for the single particle polarizability to allow direct comparison between the two methods. The MLWA polarizability has been used in the remainder of this thesis for all of the following extinction cross-section calculations.

In the S-factor calculation (see Figure 3.4a), two SLRs are seen at approximately 660 nm and 773 nm; in the CDA calculation (see Figure 3.4b) approximately 665 nm and 774 nm and in the FEM calculation (see Figure 3.4c) approximately 670 nm and

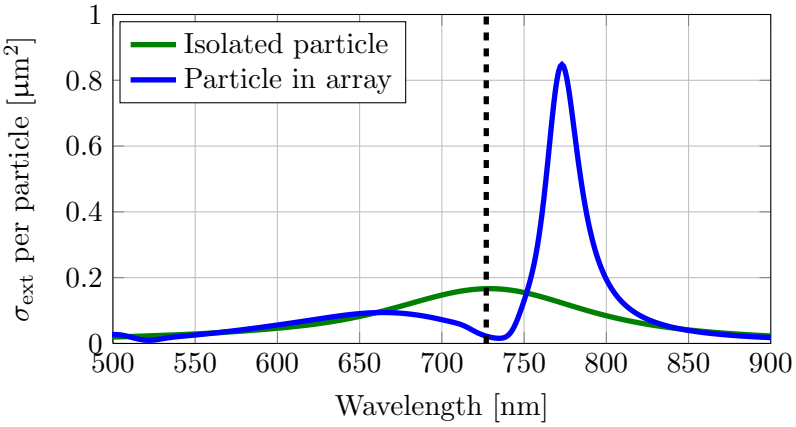

(a) S-factor calculated extinction cross-section per particle.

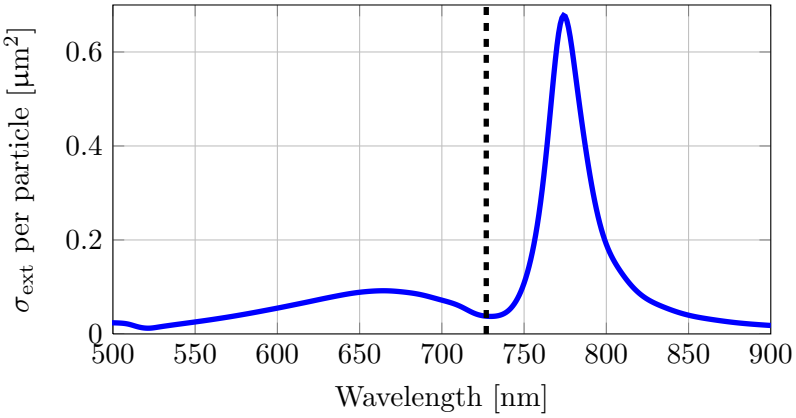

(b) Coupled-dipole approximation calculated extinction cross-section per particle.

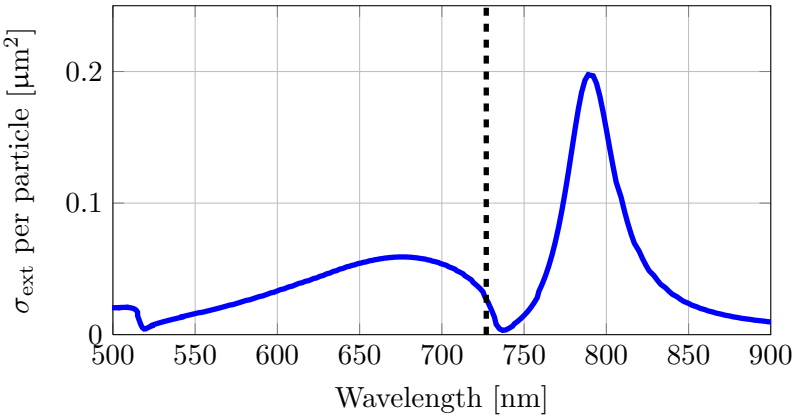

(c) Finite-element model calculated extinction cross-section per particle.

Figure 3.4: Comparison of the three different methods used in this thesis to calculated the optical response (extinction cross-section per particle) of a square array (480 nm pitch) of silver discs ($d = 120$ nm, $h = 30$ nm). (a) S-factor calculated extinction cross-section per particle; (b) CDA calculated extinction cross-section per particle; and (c) FEM calculated extinction cross-section per particle. Surface lattice resonances are observed at 773 nm in (b), 774 nm in (b) and approximately 790 nm in (c). In (a) 400×400 particles have been modelled and in (b) 30×30. In all of the calculations, the surrounding environment of the particles is $n = 1.515$ and the incident electric field is in the plane of the particles. The modified long-wavelength approximation has been used for the single particle polarizability in (a) and (b).

	Expt.	S-factor	CDA	FEM
Res.	λ_{peak} (nm) (Mag. (μm^2))	λ_{peak} (nm) (Mag. (μm^2))	λ_{peak} (nm) (Mag. (μm^2))	λ_{peak} (nm) (Mag. (μm^2))
SLR1	650 (0.05)	660 (0.10)	665 (0.09)	670 (0.06)
SLR2	Not visible	Not visible	Not visible	Not visible
SLR3	755 (0.11)	773 (0.85)	774 (0.68)	790 (0.20)

Table 3.1: Spectral positions and magnitudes of surface lattice resonances from experiment and different modelling approaches: S-factor, the coupled-dipole approximation and finite-element method. An experimental extinction spectrum is not shown, but the data has been added to the table for comparison.

approximately 790 nm. The SLR at 773 nm in the S-factor calculation has an extinction cross-section of approximately 0.85 μm^2, the SLR at 774 nm in the CDA calculation has an extinction cross-section of approximately 0.7 μm^2 and the SLR at approximately 790 nm in the FEM calculation has an extinction cross-section of approximately 0.2 μm^2. A summary of the spectral position and magnitude of the SLRs, calculated by the three different methods along with experimental data (spectrum not displayed), is presented in Table 3.1. There is a 3-fold difference in the extinction cross-section between the S-factor and CDA calculations with the FEM calculation. The difference in spectral position and strength (extinction cross-section per particle) of the SLRs between the S-factor calculation and CDA calculation is due to the S-factor model treating the array as infinite: each point dipole has the same magnitude and direction whereas in the CDA model each dipole moment can be different. In the S-factor calculation, the incident electric field and scattered field is simply summed at the position of the centrally located particle in the array, which is different to the CDA model where the electric field is summed at the position of each dipole. The spectral position of the SLRs in the S-factor model are closer to the experimental values than those predicted by the FEM, but there is an 8-fold difference in the magnitude of the extinction cross-section instead of 2-fold with the FEM when both are compared to experiment. In this thesis, the S-factor model has been implemented as the primary method since it broadly predicts the spectral position of the SLRs and it takes approximately 10 min to calculate the extinction cross-section of 400×400 particles which is a lot faster in comparison to the CDA (approximately 1 hr for 30×30 particles) and FEM (approximately 10 hr).

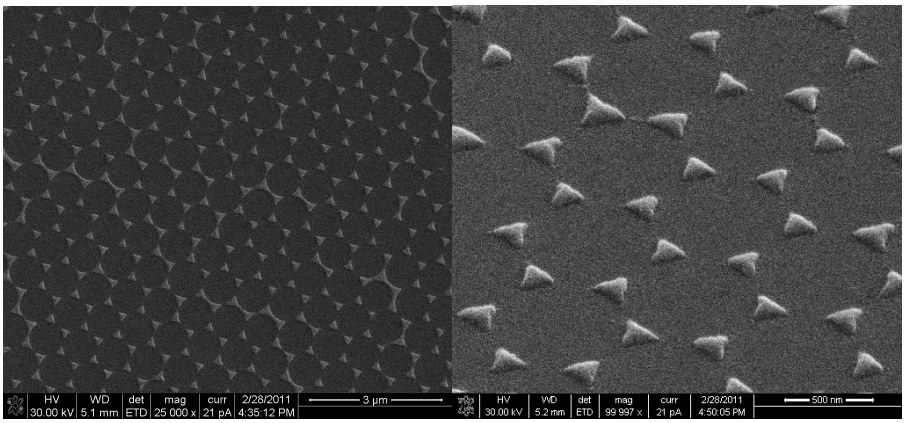

(a) SEM taken normal to array. **(b)** SEM taken at 52° to array.

Figure 3.5: Scanning electron micrographs of examples of arrays made by nanosphere lithography. 780 nm diameter nanospheres were used to produce triangular silver particles with an in-plane width of 180 nm and an out-of-plane height of 100 nm.

3.3 Array fabrication

Regular arrays of metallic particles can be fabricated by common methods such as nanoshere lithography [102–104] (NSL), nano imprint lithography or electron-beam lithography (EBL). An example of an array made by NSL is shown in Figure 3.5. By selecting different diameters of the nanospheres the period of the structure can be varied. The advantage of this method is the high throughput and the large footprint of the array that can be made. In this thesis, the regular arrays of metallic nanoparticles have been fabricated by EBL (see Section 2.3 where the whole process is described). EBL has a greater degree of freedom and more precise control over the nanostructures that can be produced. The drawback with the Nova 600 (FEI) system or any older system used to produce the particles is that at the extremities of the write-field, i.e. in the corners, the particles become distorted. An example of the distortion of the particles in a 50 µm × 50 µm is shown in Figure 3.6. Distortion of the particles occurs because only the centre of the write-field is optimized for the stigmation and focus of the electron beam. A way around this edge distortion would be to chose a larger write-field, but this would decrease the resolution of the particles designed. A write-field of 50 µm × 50 µm was chosen as the beam spot for the extinction measurements has a diameter of 30 µm: the spot can be located centrally on the array for the measurement. The added complication of producing arrays of particles with smaller pitches is the proximity effect. The electron beam of the SEM has a finite size with a Gaussian distribution function centered at the focus, but this isn't the limitation on the resolution. The

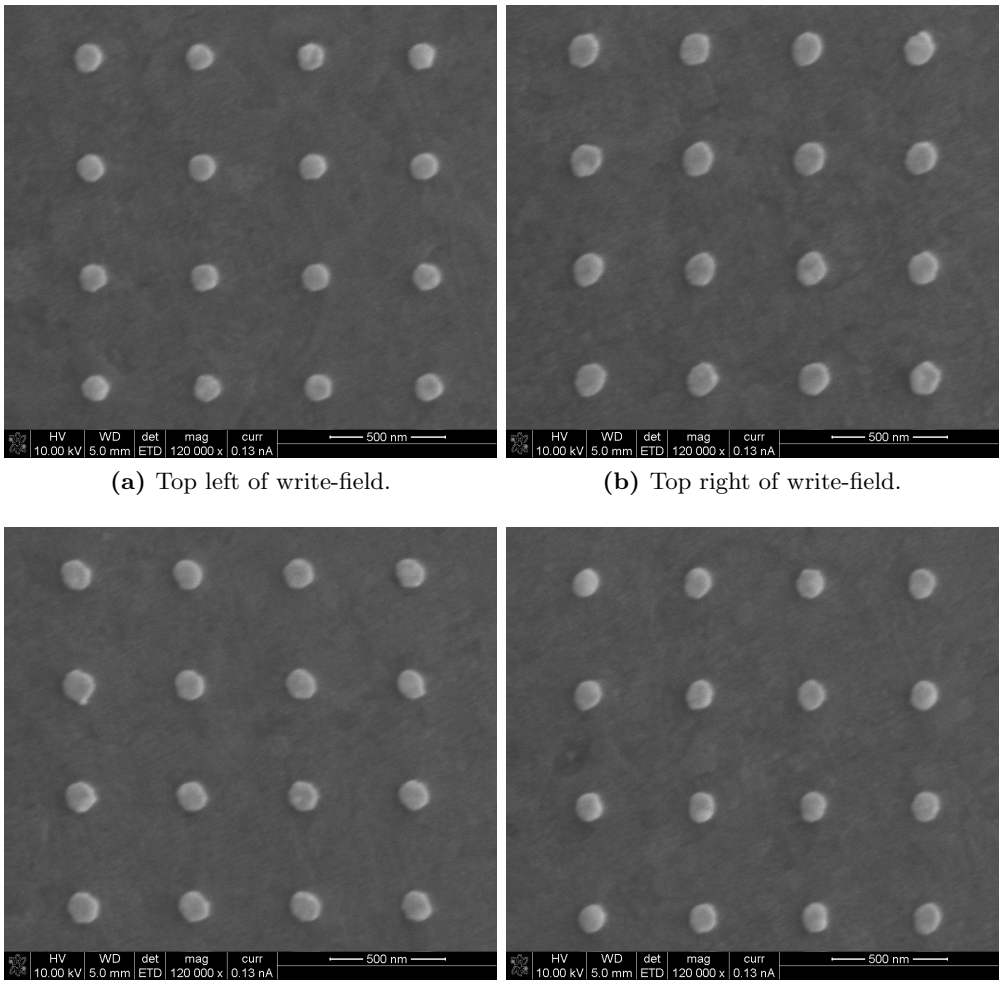

(a) Top left of write-field.

(b) Top right of write-field.

(c) Bottom left of write-field.

(d) Bottom right of write-field.

Figure 3.6: Scanning-electron micrographs of different regions of one 50 µm × 50 µm write-field illustrating particle variation attributed to distortion of the electron-beam at the extremities. (a) top left of write-field, (b) top right of write-field, (c) bottom left of write-field and (d) bottom right of write-field.

limitation of the feature size (resolution) is down to the forward scattering of electrons with the resist, and the proximity is dictated by the back scattered electrons. Back scattered electrons originate from passing through the resist and into the substrate. The electrons are then scattered at a large angle back into the resist at distance from where they first entered. This means for dense arrays, particles in close proximity receive an additional dose. The overall outcome for the particle is that the more close neighbours a particle has the higher dose the particle will receive. The greater the dose, the larger the final particle will be - this will be seen as a redshift in the single particle response. The area dose used was 1450 $\mu Ascm^{-2}$ and this was varied between $(0.9 - 1.1) \times$ Area dose depending on the pitch of the array (smallest dose for the most dense array). When the arrays for the single particle scattering measurements were fabricated for Chapter 2, the dose did not have to be varied as the pitch of the arrays was much larger (2 μm).

3.4 Optical charaterization techniques

The optical response of the arrays was determined by measuring their normal-incidence extinction spectrum. The setup consisted of an inverted microscope (Nikon ECLIPSE TE2000-U) coupled to an Acton Research Corporation Spectra Pro-2500i spectrometer with a 1056 × 256 pixel CCD. In all of the measurements described here, the sample was index-matched using immersion oil ($n = 1.515$) and an oil objective was used. A 30 μm pin-hole aperture was inserted in the light path between the lamp and collector lens (see Figure 3.7) to reduce the beam-spot diameter on the sample and to reduce the in-plane component of the incident wavevector. The illumination beam spot diameter was 30 μm to ensure it was smaller than the size of the array (50 μm × 50 μm), and the beam divergence was estimated to be around 1°. A long-pass filter (500 nm cut-off) was placed in the optical path after the objective and before the spectrometer to eliminate second order diffraction from the grating in the spectrometer.

Köhler illumination (see Figure 3.7) was adopted to provide bright and uniform illumination of the sample. The collimating lens focusses the illumination light rays at infinity, in effect defocussing the light source [75].

The optical extinction was calculated from $1-T$, where T is the measured transmittance

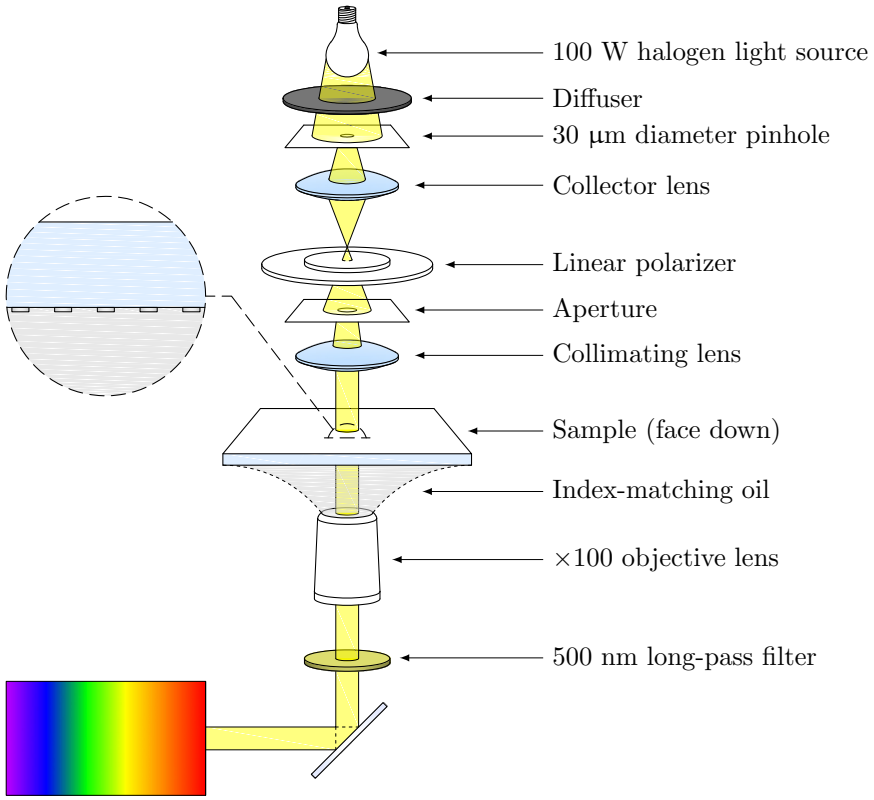

Figure 3.7: Schematic of setup to measure the transmission of arrays of particles. The array was index-matched with the substrate to provide a homogeneous environment for the particles. The array was illuminated by a 30 µm diameter beam spot with a beam divergence of less than 1°. Light collected by the objective was then fed to the spectrometer where the light is dispersed and collected by the CCD camera.

and is given by:

$$T = \frac{\text{signal} - \text{background}}{\text{reference} - \text{background}}, \tag{3.23}$$

where signal is the spectrum of the particle array and substrate, background refers to the dark counts from the CCD and reference refers to the spectrum of a blank portion of the substrate. To compare experiment with theory, the calculated transmission was converted to extinction cross-section per particle using,

$$\sigma_{\text{ext}} = A(1 - T), \tag{3.24}$$

where A is the area per particle. Equation 3.24 is valid because the array footprint is much larger (by about 60 %) than the illumination spot. To directly compare measured and calculated extinction is hard due to the objective lens in any optics experiment collecting light over a small finite angle range around the forward direction. Consequently, the measured extinction cross-section will be smaller than that predicted by theory.

To obtain a transmission spectrum, the 30 µm diameter beam spot is aligned centrally with the array in question. Due to the size of the beam spot not all of the CCD is illuminated, so for each measurement only the central strips (100–150) are selected. Figure 3.8a displays an image of the dispersion of the transmission of the square array shown in Figure 3.9 across the CCD. The strips 100–150 are the translation of a line along the sample which has a finite thickness. Here each strip (y-dimension) corresponds to a different spatial position of the array in one-dimension, and the x-dimension corresponds to wavelength. The narrow SLR is shown as the thick black strip at approximately 760 nm and does not vary with spatial position of the array. For the smaller array periods of smaller particles proximity effects means that the variation in particle size is greater. Figure 3.8b shows the dispersion of the transmission spectrum of a 350 nm pitch square array of silver discs ($d \approx 85$ nm, $h = 30$ nm). The SLR ranges from approximately 560 nm to approximately 660 nm from strip 50 to 200. This is caused by increasing particle size across the array, which - for this sample - was due to proximity effects in the EBL fabrication process.

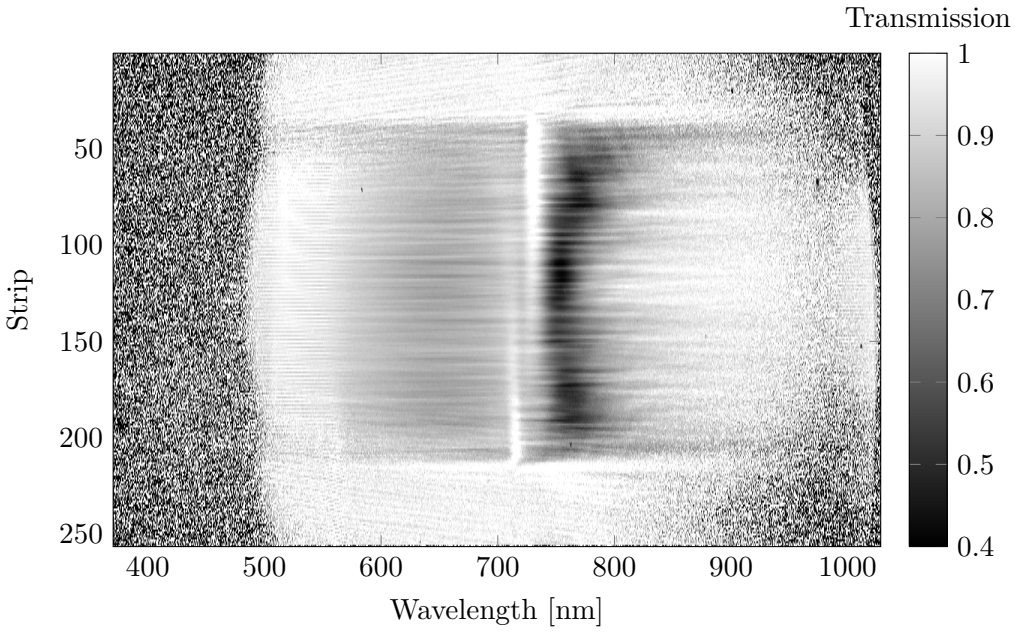

(a) Dispersion of the transmission spectrum of a 480 nm pitch square array of silver discs ($d = 120$ nm, $h = 30$ nm).

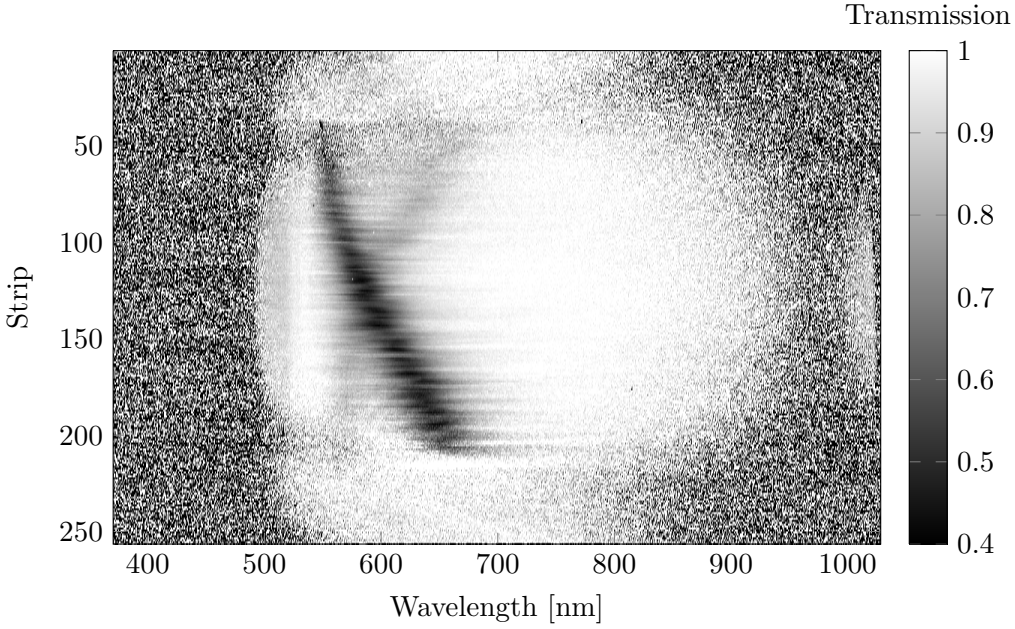

(b) Dispersion of the transmission spectrum of a 350 nm pitch square array of silver discs ($d \approx 85$ nm, $h = 30$ nm).

Figure 3.8: CCD image of the dispersion of the transmission from two square arrays with different pitches: (a) 480 nm and (b) 350 nm. The surface lattice resonance (SLR) of the array corresponds to a minimum in transmission, as light is absorbed and scattered at that particular wavelength. In (a) the SLR occurs at approximately 760 nm and in (b) at approximately 560 nm to approximately 660 nm. For smaller pitches, proximity effects between particles change the particle size such that the spectral position of the SLR changes with spatial position of the array. Particles that receive a higher dose are larger and this is seen as a red-shift in their optical response.

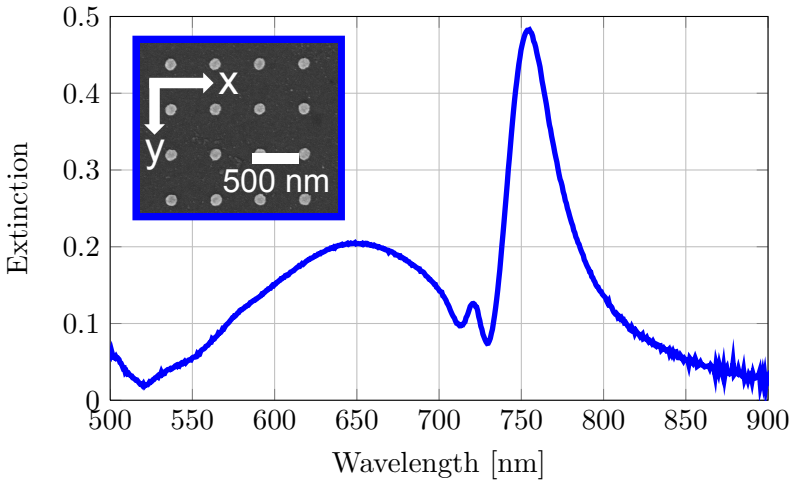

Figure 3.9: Measured extinction spectrum of a 480 nm pitch square array of silver discs ($d = 120$ nm, $h = 30$ nm) with the incident electric field parallel to the y-axis of the array (see inset top left for scanning-electron micrograph of the array). Surface lattice resonances are observed in the extinction spectrum at approximately 650 nm and 755 nm. The extra feature at approximately 520 nm is due to $< 1, 1 >$ diffraction edge, and the feature at approximately 720 nm is attributed to the divergence of the incident beam.

3.5 Extinction measurements of square, hexagonal and honeycomb arrays

The focus of this section, using experiment and theory, is to investigate the factors that dictate the spectral position and width of SLRs in different array geometries. Square, hexagonal and honeycomb arrays are studied with their diffraction edge in the same spectral position, but as they possess different symmetries their nearest neighbour separation is different. The work reported here directly compares SLRs in square, hexagonal and honeycomb arrays in contrast to earlier work, which has involved studying the different array geometries separately. A short summary of earlier investigations is given below. Haynes *et al.* [42] have experimentally studied hexagonal arrays of gold particles, but because of their inappropriate choice of particle size, relative to the diffraction edge and an inhomogeneous optical environment for the particles, they failed to observe sharp SLRs. Following the work of Haynes and coworkers, hexagonal [87] and honeycomb [105] arrays have been modelled using a coupled-dipole model, predicting sharp SLRs. These sharp SLRs have been experimentally confirmed in honeycomb arrays in Ref. [106], but the majority of observations of SLRs have been reported on square arrays [44, 45, 47, 81].

As mentioned above, in order to observe the phenomenon of SLRs, square, hexagonal

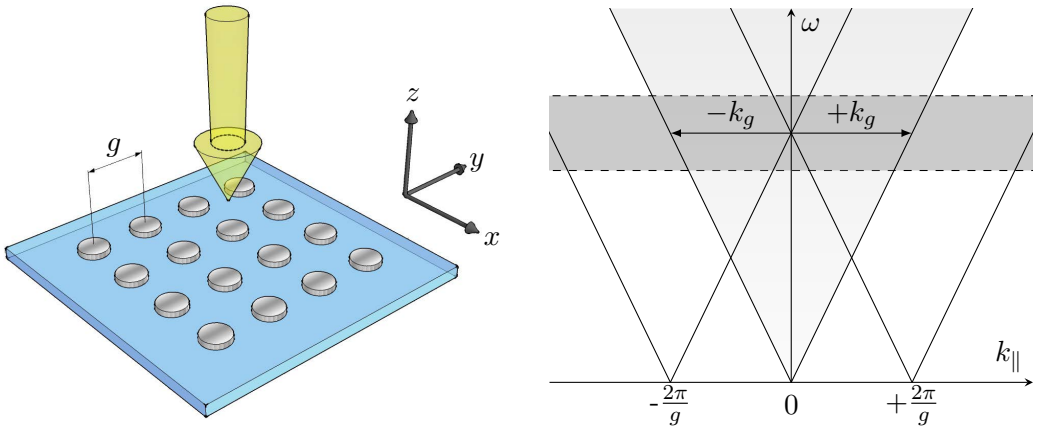

(a) Square array. **(b)** Dispersion diagram.

Figure 3.10: (a) schematic example of a square array and (b) dispersion diagram of the square array with the single particle resonance illustrated as grey shaded band. The particle array acts as a diffraction grating so that light of the same wavelength as the single particle resonance (grey band) is diffracted in the plane of the array. The resonantly scattered light from each of the particles arrives in phase with the collective electron oscillation (plasmon) of each of its neighbours. The electric field experienced by each particle in the array is the sum of the incident electric field plus the scattered field from the other dipoles.

and honeycomb arrays with their diffraction edge (727 nm) in the same spectral position were fabricated. The diffraction edge corresponds to when a diffractive order changes from evanescent to radiative and emerges at grazing along the grating [107, 108]. In the literature, the diffraction edge is also referred to as the Rayleigh anomaly [109–111]. A schematic example of a square array is shown in Figure 3.10a. The dispersion diagram of the square array with the dispersion-less broad single particle resonance [112] added as a dark grey shaded band [90] is shown in Figure 3.10b. The light cone (light grey shaded region) is the radiative region, corresponding to the dispersion of free space radiation. The diffraction edge occurs in Figure 3.10b where the first diffracted order light lines intersect each other. All of the measurements in this thesis were performed at normal incidence, i.e.$k_\parallel = 0$, which corresponds to probing along the frequency axis in Figure 3.10b. Normal incidence light can scatter off the grating and gain or lose integer multiples of k_g, where k_g is the grating lattice vector. For frequencies lower than the diffraction edge the additional in-plane momentum gained by the light means it lies outside the light cone. Light with $k_\parallel > \omega/c$ can not couple to free space radiation and decays as an evanescent wave. For the experiments, the pitch, g, of the square array was specifically chosen so its diffraction edge coincides with the spectral position of the single particle resonance. This causes incident light of the same frequency as the particle plasmon resonance to gain or lose k_g and be diffracted in the plane of the

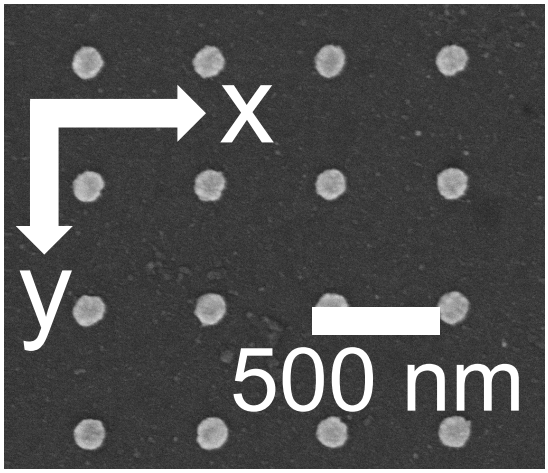

(a) Square array (480 nm pitch).

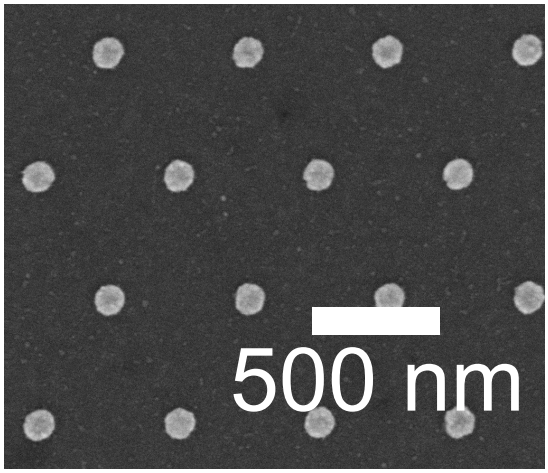

(b) Hexagonal array (555 nm nearest neighbour separation).

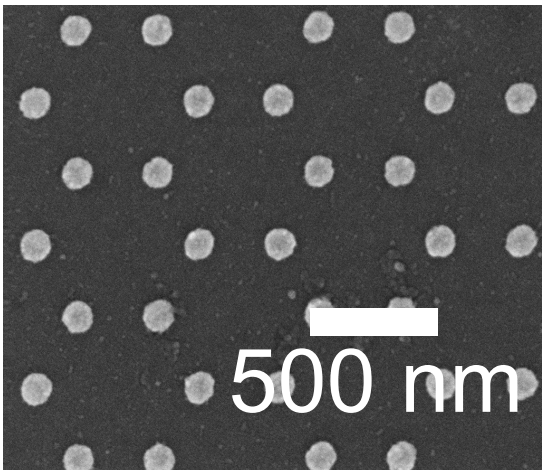

(c) Honeycomb array (320 nm nearest neighbour separation)

Figure 3.11: Scanning-electron micrographs of different array geometries of silver discs ($d = 120$ nm, $h = 30$ nm). (a) square array with 480 nm pitch; (b) hexagonal array with 555 nm nearest neighbour separation, and; (c) honeycomb array with 320 nm nearest neighbour separation. Each of the structures has a diffraction edge of 727 nm when surrounded by immersion oil with $n = 1.515$.

particles. Resonantly scattered light from each one of the metallic particles arrives in phase with the collective electron oscillation (plasmon) of each one of the neighbouring particles. The array response is now the sum of the incident electric field and scattered electric fields from the other particles. Because these narrow spectral features rely on constructive interference, it is paramount that the particles are surrounded by a homogenous medium. Early studies [43, 113] failed to observe in-plane SLRs due to an asymmetric optical environment. In the present case, the particle environment was index-matched with the substrate by the application of immersion oil ($n = 1.515$).

SLRs are now investigated in different array geometries by first examining the optical response of a square array. For ease of comparison, Table 3.2 includes experimental and S-factor data for the three different array geometries. For the square array measurement, the linearly-polarized electric field is parallel to the y-axis, (see Figure 3.11a). Figure 3.12 shows the (a) measured extinction cross-section per particle, (b) S-factor calculated extinction cross-section per particle and (c) $1/\alpha$ (real part red line and imaginary part cyan line) and $\varepsilon_0 S$ (real part blue line and imaginary part green line) for a 480 nm pitch square array of silver discs ($d = 120$ nm, $h = 30$ nm). From the measured extinction vs. wavelength [nm] spectrum (see Figure 3.12a), two SLRs are observed at approximately 650 nm and 755 nm. Also in the extinction spectrum is a peak at approximately 720 nm which is due to divergence of the illuminating beam [80] and a dip at approximately 520 nm which is caused by the $< 1, 1 >$ diffraction edge of the square array. The S-factor calculated extinction cross-section per particle of the square array (see Figure 3.12b) displays two SLRs at approximately 660 nm and 773 nm, which are both at longer wavelengths than the experiment. The dashed lines in (b) and (c) illustrate the crossing points of the real parts of $1/\alpha$ and $\varepsilon_0 S$. The SLR in the calculation at 773 nm corresponds to where the real parts of $1/\alpha$ and $\varepsilon_0 S$ intersect, (see Figure 3.12c). The second SLR shown in the calculated spectrum occurs at a shorter wavelength (at approximately 660 nm) than the crossing points of $1/\alpha$ and $\varepsilon_0 S$ (690 nm). This is due to the difference between the imaginary parts of $1/\alpha$ and $\varepsilon_0 S$ being small but not negligible, thus causing a shift in the SLR position. There is a third crossing point at 721 nm but no resonance is seen because the difference between the imaginary parts of $1/\alpha$ and $\varepsilon_0 S$ is now significant, so this SLR vanishes attributed to high damping. It is noted the SLR at 773 nm (calculated) and at 755 nm (measured) is sharper and stronger than the SLR at approximately 660 nm (calculated) and at approximately 650 nm (measured) due to the difference between the imaginary parts $1/\alpha$ and $\varepsilon_0 S$ being smaller. In the first case, for the larger wavelength SLR there is a factor of 8 difference between the calculated and measured extinction cross-section per particle because the MLWA for these particle dimensions and incident wavelengths, the

limit of the validity of this approximation is reached. Although the MLWA does not correctly predict the magnitude of the extinction cross-section, it does broadly predict the spectral position and shape of the measured extinction cross-section per particle of the fabricated arrays. Because only an analytical expression can be used to describe the polarizabilty of the particle in the S-factor model, the MLWA is used. The MLWA is a suitable single particle polarizability that includes terms that correct the QSA for retardation effects.

SLRs on a hexagonal array will now be discussed. In the measurement, the incident electric field is polarized along the y-axis of the array (see Figure 3.11b). The hexagonal array studied here has a nearest neighbour separation of 555 nm. The (a) measured extinction cross-section per particle, (b) S-factor calculated extinction cross-section per particle and (c) $1/\alpha$ (real part red line and imaginary part cyan line) and $\varepsilon_0 S$ (real part blue line and imaginary part green line) of a hexagonal array of silver discs ($d = 120$ nm, $h = 30$ nm) is shown in Figure 3.13. From the measured extinction spectrum (see Figure 3.13a), three features are seen at approximately 635 nm, approximately 720 nm and 760 nm. The small peak at approximately 720 nm is due to beam divergence, similar to the square array. The features at approximately 635 nm and 760 nm are SLRs as in the case of the square array. These SLRs are present at different spectral positions compared to the calculated spectra (see Figure 3.13b) in which they occur at approximately 650 nm and 781 nm. Again, the position of the SLRs are determined by where the real parts of $1/\alpha$ and $\varepsilon_0 S$ cross (providing the difference between the imaginary parts of $1/\alpha$ and $\varepsilon_0 S$ is small), which are found at 679 am and 778 nm (Figure 3.13c).

Lastly, SLRs on a honeycomb array will be studied. The nearest neighbour separation is 320 nm and the polarization of the electric field is parallel to the y-axis of the array, (see Figure 3.11c). Presented in Figure 3.14 is the (a) measured extinction cross-section per particle, (b) calculated extinction cross-section per particle and (c) $1/\alpha$ (real part red line and imaginary part cyan line) and $\varepsilon_0 S$ (real part blue line and imaginary part green line) for a honeycomb array of silver discs ($d = 120$ nm, $h = 30$ nm). As with the square and hexagonal arrays, two SLRs (approximately 650 nm and 743 nm) are seen in the measured extinction spectrum, (see Figure 3.14a). These two SLRs occur at different positions (at approximately 665 nm and 756 nm respectively) in the calculated spectra, (see Figure 3.14b). When real part of $1/\alpha$ intercepts the real part of $\varepsilon_0 S$ (683 nm, 753 nm) (see Figure 3.14c). Table 3.2 displays experimental and modelled extinction-cross section data for the SLRs on each of the different array geometries for comparison.

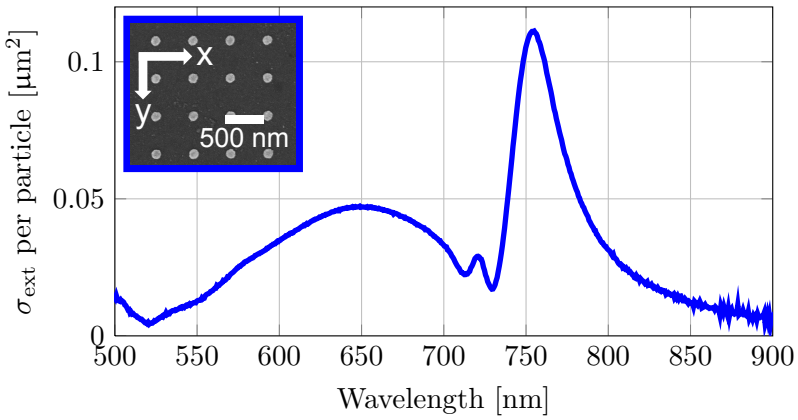

(a) Measured extinction cross-section per particle.

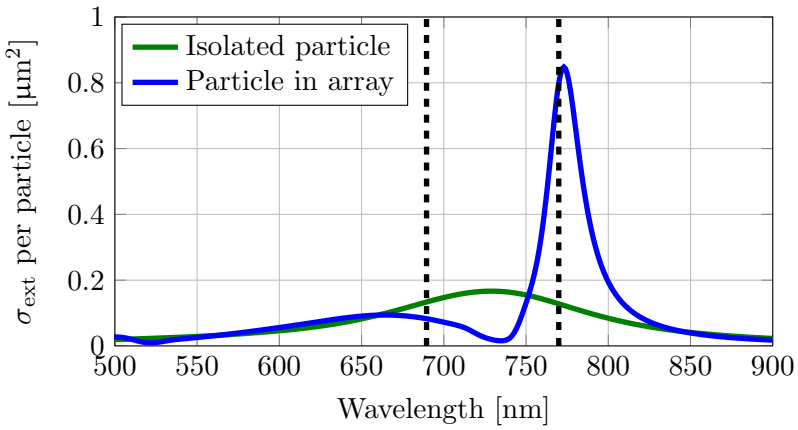

(b) Calculated extinction cross-section per particle.

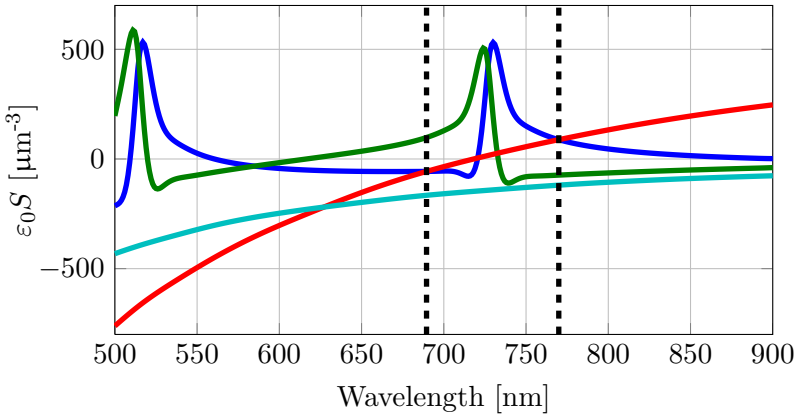

(c) Real and imaginary parts of $1/\alpha$ and $\varepsilon_0 S$: real ($\varepsilon_0 S$) (blue line), imag ($\varepsilon_0 S$) (green line), real ($1/\alpha$) (red line) and imag ($1/\alpha$) (cyan line).

Figure 3.12: (a) measured extinction cross-section per particle; (b) calculated extinction cross-section per particle and; (c) S-factor for a square array (480 nm pitch) of silver discs (d = 120 nm, h = 30 nm). Inset top left in (a) is a scanning-electron micrograph of the square array. The particles were illuminated with linearly-polarized light at normal incidence with the electric field parallel to the y-axis of the array, see Figure 3.11a. The environment of the array is index-matched by immersion oil with $n = 1.515$ meaning that the diffraction edge is at 727 nm. Dashed lines in (a) and (b) indicate the intersection of the real parts of $1/\alpha$ and $\varepsilon_0 S$.

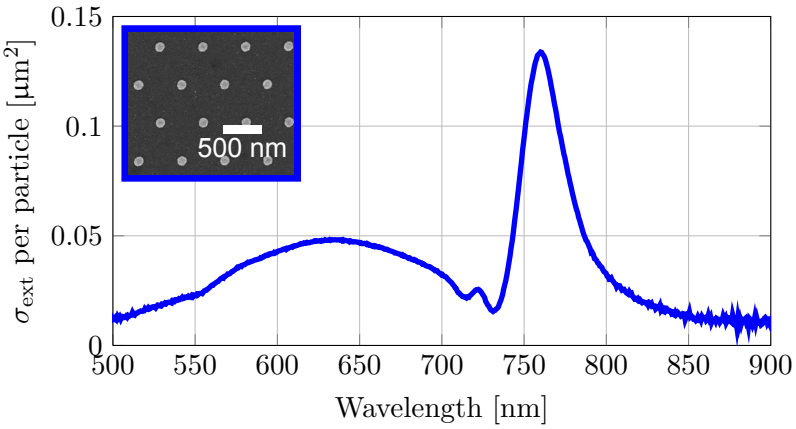

(a) Measured extinction cross-section per particle.

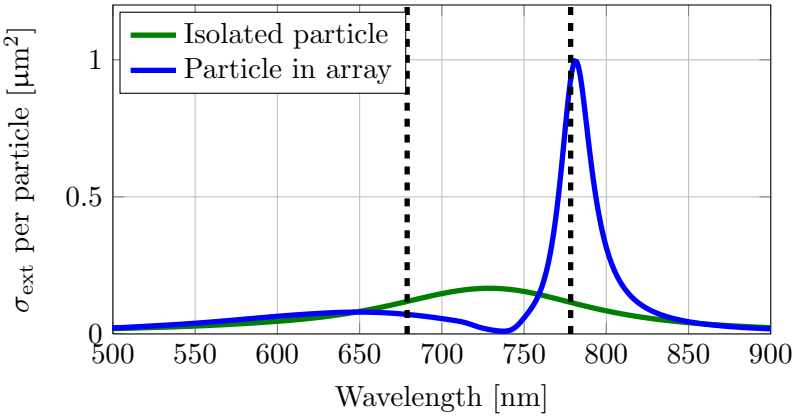

(b) Calculated extinction cross-section per particle.

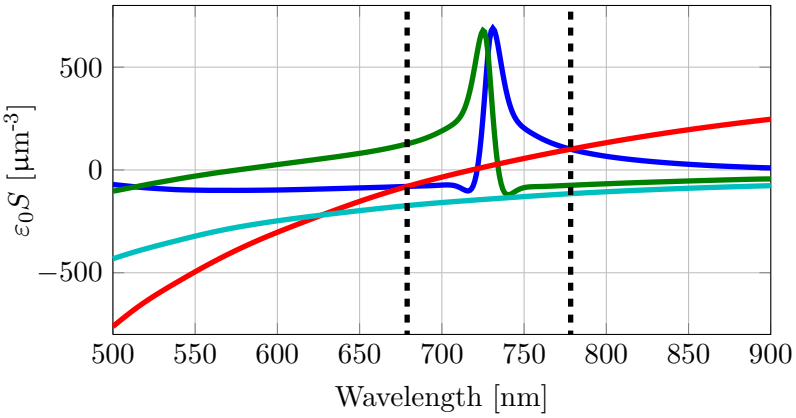

(c) Real and imaginary parts of $1/\alpha$ and $\varepsilon_0 S$: real ($\varepsilon_0 S$) (blue line), imag ($\varepsilon_0 S$) (green line), real ($1/\alpha$) (red line) and imag ($1/\alpha$) (cyan line).

Figure 3.13: (a) measured extinction cross-section per particle; (b) calculated extinction cross-section per particle and; (c) S-factor for a hexagonal array (555 nm nearest neighbour separation) of silver discs (d = 120 nm, h = 30 nm). Inset top left in (a) is a scanning-electron micrograph of the hexagonal array. The particles were illuminated with linearly-polarized light at normal incidence with an electric field parallel to the y-axis of the array, see Figure 3.11b.

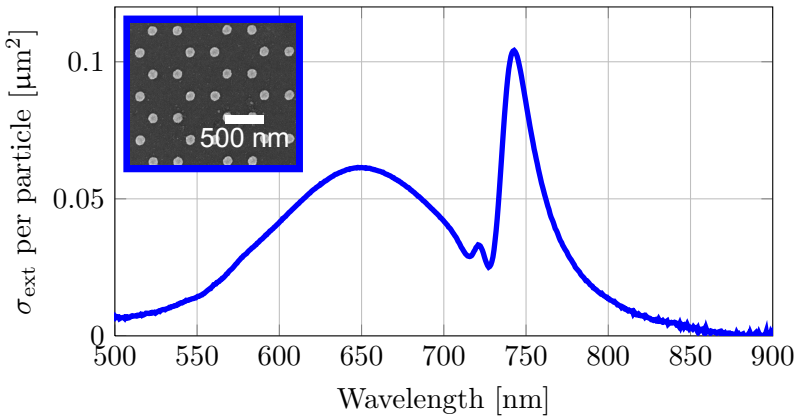

(a) Measured extinction cross-section per particle.

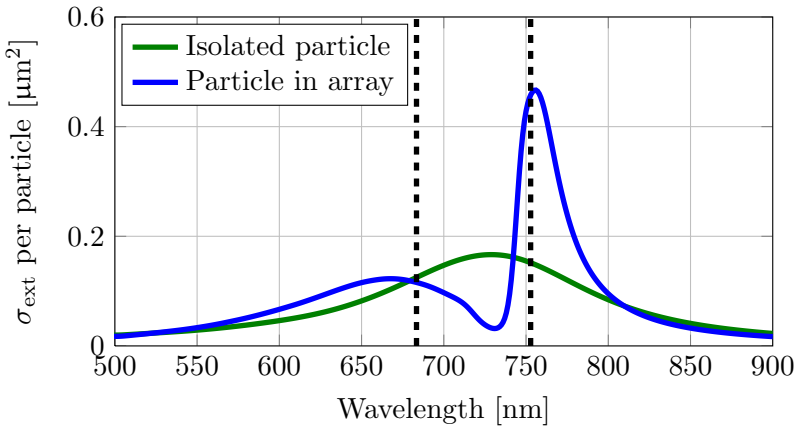

(b) Calculated extinction cross-section per particle.

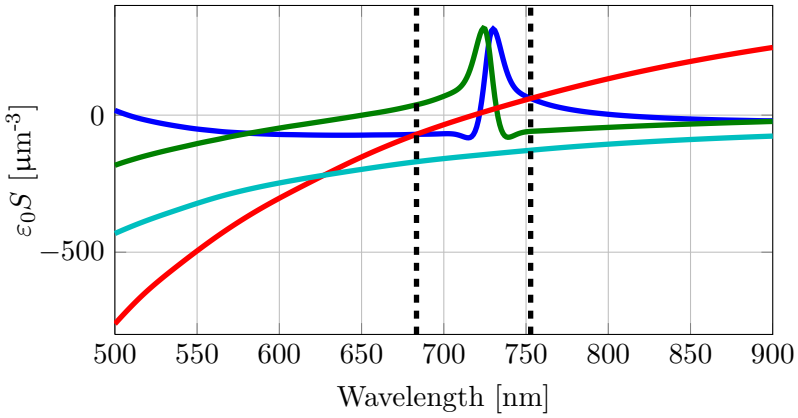

(c) Real and imaginary parts of $1/\alpha$ and $\varepsilon_0 S$: real ($\varepsilon_0 S$) (blue line), imag ($\varepsilon_0 S$) (green line), real ($1/\alpha$) (red line) and imag ($1/\alpha$) (cyan line).

Figure 3.14: (a) measured extinction cross-section per particle; (b) calculated extinction cross-section per particle and; (c) S-factor for a honeycomb array (320 nm nearest neighbour separation) of silver discs (d = 120 nm, h = 30 nm). Inset top left in (a) is a scanning-electron micrograph of the honeycomb array. The particles were illuminated with linearly-polarized light at normal incidence with the electric field parallel to the y-axis of the array, see Figure 3.11c.

	σ_{ext}	Experiment		Model		
Res.	Geometry	λ_{peak} (nm) (Mag. (μm^2))	FWHM (S,M,B)	λ_{peak} (nm)	Re $(1/\alpha = \varepsilon_0 S)$	|Im $(1/\alpha - \varepsilon_0 S)$|
SLR1	Square	650 (0.05)	Broad	660	No	237
	Hexagonal	635 (0.05)	Broad	650	No	279
	Honeycomb	650 (0.06)	Broad	665	No	199
SLR2	Square	Not visible	N/A	Not visible	Yes	585
	Hexagonal	Not visible	N/A	Not visible	Yes	739
	Honeycomb	Not visible	N/A	Not visible	Yes	439
SLR3	Square	755 (0.11)	Medium	773	Yes	45
	Hexagonal	760 (0.13)	Medium	781	Yes	41
	Honeycomb	743 (0.10)	Medium	756	Yes	68

Table 3.2: Experimental and S-factor calculated extinction cross-sections for square, hexagonal and honeycomb geometries.

It has been demonstrated that square, hexagonal and honeycomb arrays all exhibit SLRs, but with their SLRs occurring at slightly different wavelengths relative to each other (see Figure 3.15a). To see why this is the case, the real parts of $1/\alpha$ and $\varepsilon_0 S$ as a function of wavelength of the square (blue line), hexagonal (green line) and honeycomb (red line) arrays were plotted in Figure 3.15b. Even though each one of the arrays has its diffraction edge in the same spectral position (727 nm), the narrowest SLR for each one of the different geometries does not occur at the same spectral position. This can be explained by comparing where the real part of the inverse polarizability intercepts the real part of $\varepsilon_0 S$. In Figure 3.15b it is seen that the real part of $1/\alpha$ crosses the real part of $\varepsilon_0 S$ in different positions for the different arrays: 753 nm for honeycomb, 770 nm for square and 778 nm for hexagonal. The square array has an additional feature due to the $< 1, 1 >$ diffraction edge.

Square, hexagonal and honeycomb arrays possess a high degree of symmetry. Therefore it is expected that normal-incidence extinction measurements of square, hexagonal and honeycomb arrays of symmetric discs will be independent of the orientation (polarization) of the incident electric field. To check if this is the case, the orientation of the electric field was swept in 15° increments from 0° (parallel to y-axis) to 90° (parallel to x-axis) of the three different array geometries (see Figure 3.16). The optical response of the three array types is seen to be insensitive to the orientation of the incident electric field as expected. The honeycomb array has a larger measured extinction than the square and hexagonal arrays because it has a larger particle density.

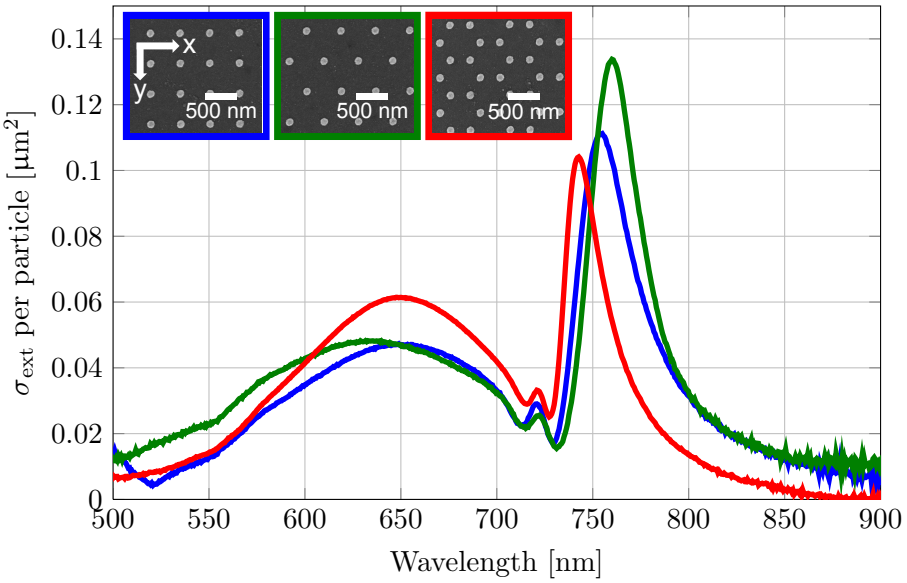

(a) Measured extinction cross-section per particle.

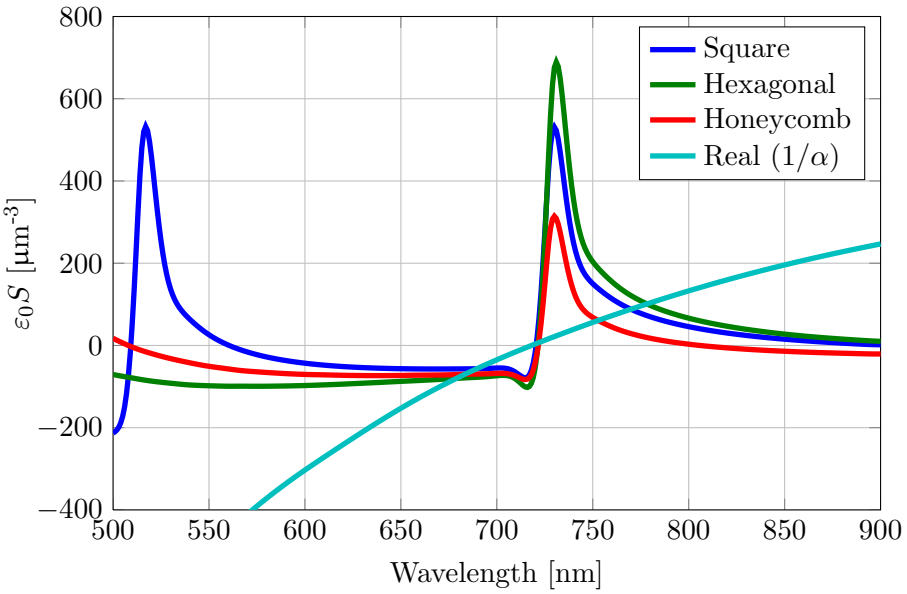

(b) Real parts of $1/\alpha$ and $\varepsilon_0 S$.

Figure 3.15: (a) measured extinction cross-section per particle of square array (see Figure 3.11a); hexagonal array (See Figure 3.11b) and honeycomb array (See Figure 3.11c) with corresponding real parts of $1/\alpha$ and $\varepsilon_0 S$ shown in (b).

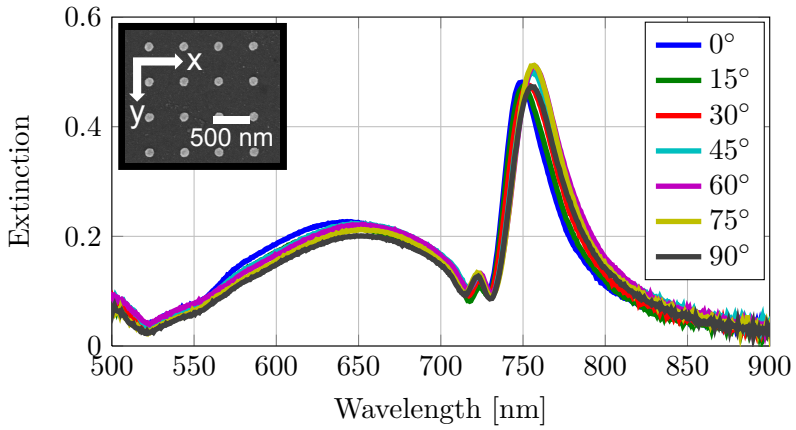

(a) Square array (480 nm pitch).

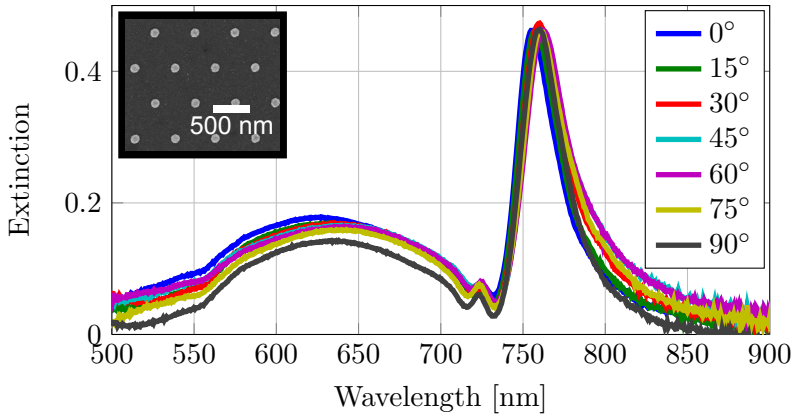

(b) Hexagonal array (555 nm nearest neighbour separation).

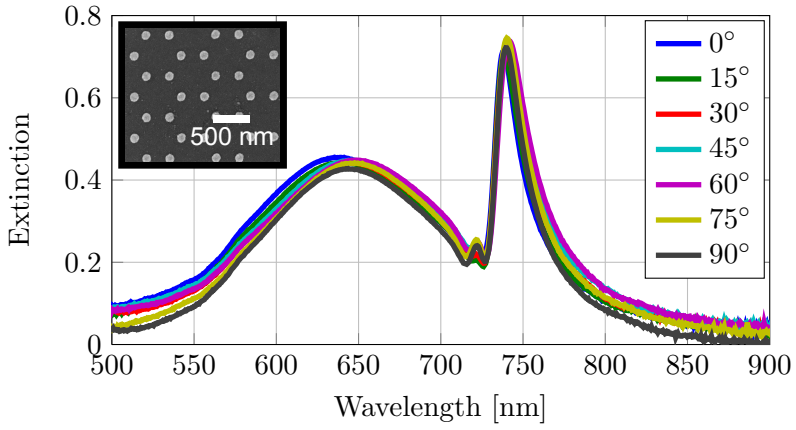

(c) Honeycomb array (320 nm nearest neighbour separation).

Figure 3.16: Measured extinction vs. wavelength [nm] of the three different array geometries: (a) square, (b) hexagonal and (c) honeycomb. In each case, the incident electric field polarization is swept in 15° increments from 0° (parallel to the x-axis of the arrays) to 90° (parallel to the y-axis).

3.6 Conclusion

In this chapter, various modelling techniques to describe regular arrays of nanoparticles have been discussed. Fabrication methods and extinction measurements have been described. It has been shown that regular arrays of nanoparticles, when of a similar period as the single particle resonance exhibit surface lattice resonances (SLRs). Square, hexagonal and honeycomb arrays display these narrow SLRs at slightly different spectral positions even when they all have the same diffraction edge. A semi-analytical coupled-dipole model has been used to explain and demonstrate why these SLRs occur in different spectral positions: SLRs occur where the real parts of $1/\alpha$ and $\varepsilon_0 S$ intersect, and because of the different particle positions for each array geometry $\varepsilon_0 S$ is simply different. For the different array geometries considered, at each point where the real parts of $1/\alpha$ and $\varepsilon_0 S$ cross, the difference between the imaginary parts of $1/\alpha$ and $\varepsilon_0 S$ are similar, so the width of their SLRs are comparable. It has been verified experimentally that SLRs exhibited by square, hexagonal and honeycomb arrays of discs are polarization insensitive to the incident electric field. To gain a greater understanding of how the particles couple together over long distances (greater than λ), an array with lower symmetry needs to be investigated. A useful example is the rectangular array, and this is the focus of Chapter 4.

Chapter 4

Optical response of rectangular arrays

4.1 Introduction

In order to understand the nature of the constructive coupling between particle resonances in arrays of plasmonic particles, it is helpful to examine the optical response of a lower symmetry array, and a useful example is the rectangular array. In this chapter rectangular arrays of silver discs (d = 120 nm and h = 30 nm) were fabricated by electron-beam lithography (EBL) and their extinction as a function of wavelength was measured. The environment of the particles was index-matched with the substrate to provide a homogeneous optical environment to observe constructive interference effects, known as surface lattice resonances (SLRs) [44, 52, 53, 114–119]. The polarization dependence of the rectangular array is studied and comparison made between the rectangular array and chain. The experimental spectra are compared with the S-factor model, the coupled-dipole approximation (CDA) and finite element modelling (FEM). Lastly, the near-, intermediate- and far-field terms of the S-factor are investigated for their effect in the modelling of extinction spectra.

4.2 Polarization dependence of rectangular arrays

One example of a fabricated rectangular array is shown in Figure 4.1. In this instance, the array has a pitch of 370 nm in the x-direction, g_x, and 480 nm in the y-direction, g_y.

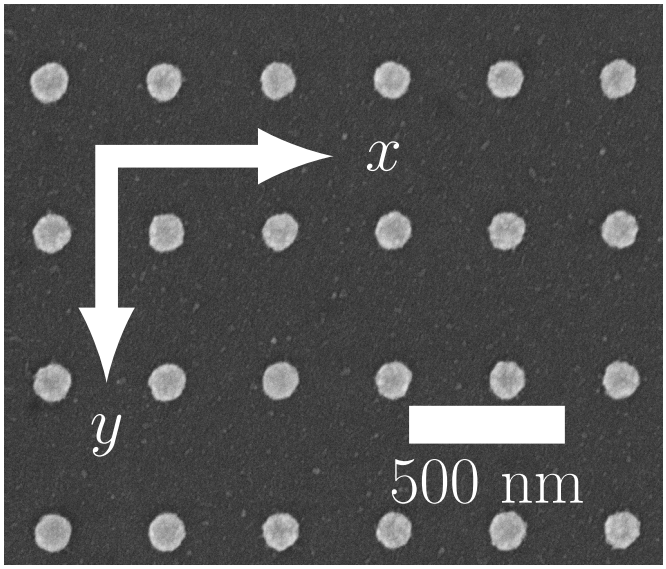

Figure 4.1: Scanning-electron micrograph of a rectangular array with $g_x = 370$ nm and $g_y = 480$ nm, where g_x and g_y are the pitches in the x- and y-directions respectively. The particles are silver discs with $d = 120$ nm and $h = 30$ nm.

The particle dimensions are the same as used in Chapter 3 (silver discs with $d = 120$ nm and $h = 30$ nm). Discs have been chosen because their polarizability (particle plasmon resonance) is independent of the polarization of the incident electric field in the plane of the particles. This means that the polarization dependence of the measured extinction cross-section is due to the array only. For each S-factor array calculation, consisting of 160,000 particles, each of the identical particles was assigned a polarizability, α_{MLWA}, calculated from the modified long-wavelength approximation (see Equation 2.7). The modified polarizability, α^*, which takes into account the scattered field from the neighbouring particles in the array is given by,

$$\alpha^* = \frac{1}{1/\alpha_{\mathrm{MLWA}} - \varepsilon_0 S}, \tag{4.1}$$

where S is given by,

$$S = \frac{1}{4\pi\varepsilon_0} \sum_j \exp\left(ikr_j\right) \left[\frac{(1 - ikr_j)(3\cos^2\theta_j - 1)}{r_j^3} + \frac{k^2 \sin^2\theta_j}{r_j} \right], \tag{4.2}$$

where r_j is the distance from the central particle to particle j, and θ_j is the angle

between $\vec{r}_j$, and the dipole moment of particle j (Equations 4.1 and 4.2 are a repeat of Equations 3.16 and 3.22). S is simply the sum of the scattered electric fields from the particles in the array evaluated at the position of the central particle of the array, and only depends on the geometry of the array. The absorption and scattering cross-sections per particle in the array can then be calculated from insertion of Equation 4.1 into the cross-sections (see Equations 1.25 and 1.26). The extinction cross-section can then be found by addition of σ_{abs} and σ_{sca}. All the modelled extinction spectra have been convolved with a suitable Gaussian to reproduce the 7 nm resolution of the spectrometer in the experiment, as described in Section 3.2.4.

The optical response of the arrays was measured by normal-incidence extinction measurements as outlined Section 3.4. The incident electric field was linearly-polarized either parallel to the x-axis or y-axis of the array. Figure 4.2 shows the (a) measured extinction cross-section per particle and (b) S-factor calculated extinction cross-section per particle of the array in Figure 4.1 with the isolated single particle response. The two different polarizations of the incident electric field yield different extinction cross-section spectra in contrast to the square, hexagonal and honeycomb arrays (see Figure 3.16): when the electric field is parallel to the x-axis of the array, two SLRs are observed (at approximately 620 nm and 752 nm) - a similar extinction spectrum is seen with the square array with 480 nm pitch (see Figure 3.12). A somewhat different response is seen for the orthogonal electric field polarization - a single SLR is seen in the spectrum (at approximately 685 nm). The optical response of the array is now polarization dependent and this has also been observed elsewhere [120]. In Ref. [120] they fabricated rectangular arrays of gold spheres with pitches of 655 nm and 649 nm and investigated the incident electric field polarization dependence of the SLR. Because the difference between the array pitch dimensions they studied was small (6 nm), the change in the observed SLRs between the two orthogonal polarizations of the incident electric field was not as pronounced as reported here.

The S-factor calculated extinction cross-section per particle (see Figure 4.2b) correctly predicts two SLRs (at approximately 640 nm and approximately 780 nm) with the electric field parallel to the x-axis of the array and one SLR (at approximately 740 nm) with the electric field parallel to the y-axis of the array. The SLRs are at longer wavelengths in the model than in the experiment. The position and strength of these SLRs can be explained from Figure 4.3b, which shows the real and imaginary parts of $\varepsilon_0 S$ of the array and the real and imaginary parts of the inverse polarizability of a silver disc with $d = 120$ nm and $h = 30$ nm. Figure 4.2b has been reproduced in Figures 4.3 and 4.4 to allow easier comparison with the modelled extinction spectra.

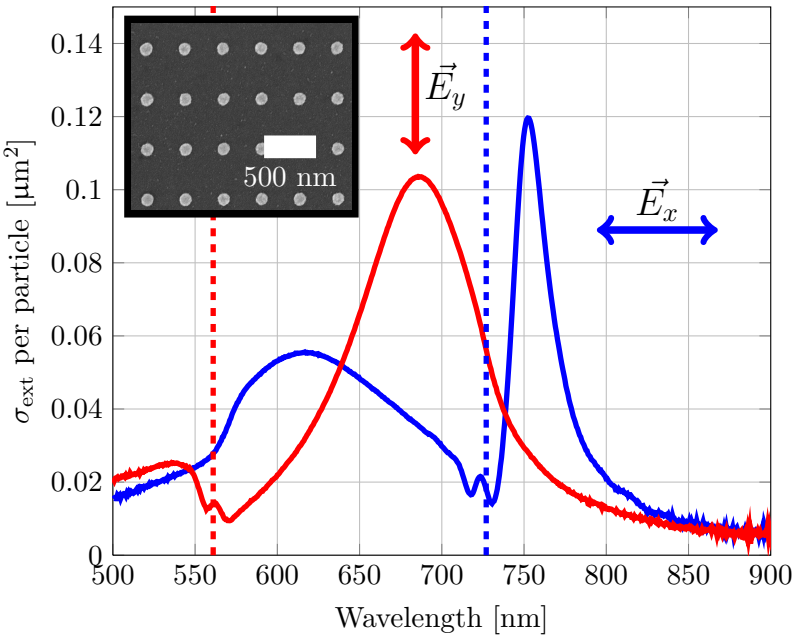

(a) Measured extinction cross-section per particle.

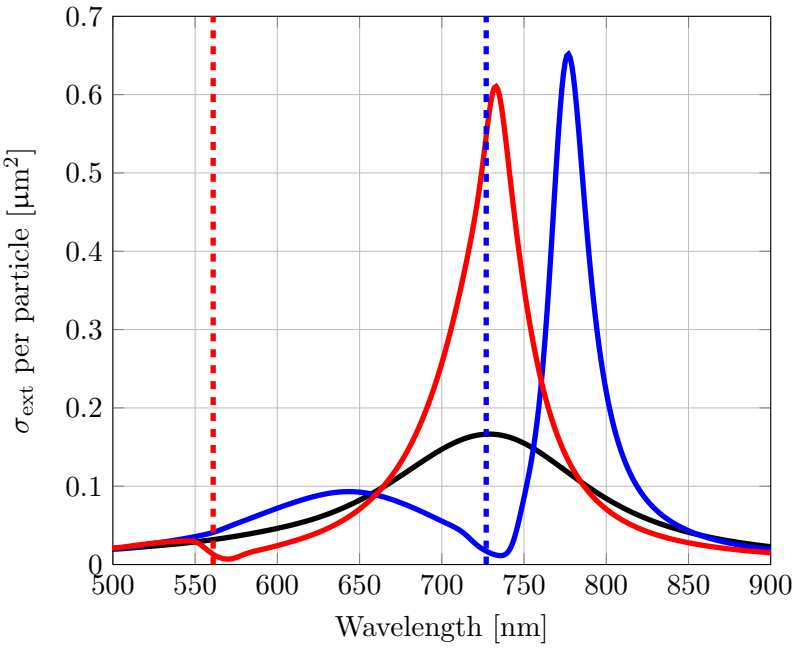

(b) Calculated extinction cross-section per particle.

Figure 4.2: (a) measured extinction cross-section per particle and (b) calculated extinction cross-section per particle for a rectangular array with $g_x = 370$ nm and $g_y = 480$ nm, where g_x and g_y are the pitches in the x- and y-directions respectively. The particles are silver discs ($d = 120$ nm, $h = 30$ nm) and were illuminated with linearly-polarized light at normal incidence. The incident electric field was parallel to either the x-axis (blue solid line) or y-axis (red solid line) of the array, see Figure 4.1 for scanning-electron micrograph. The optical environment of the array was index-matched using immersion oil with $n = 1.515$. The two diffraction edges occur at 561 nm (red dashed line) and 727 nm (blue dashed line).

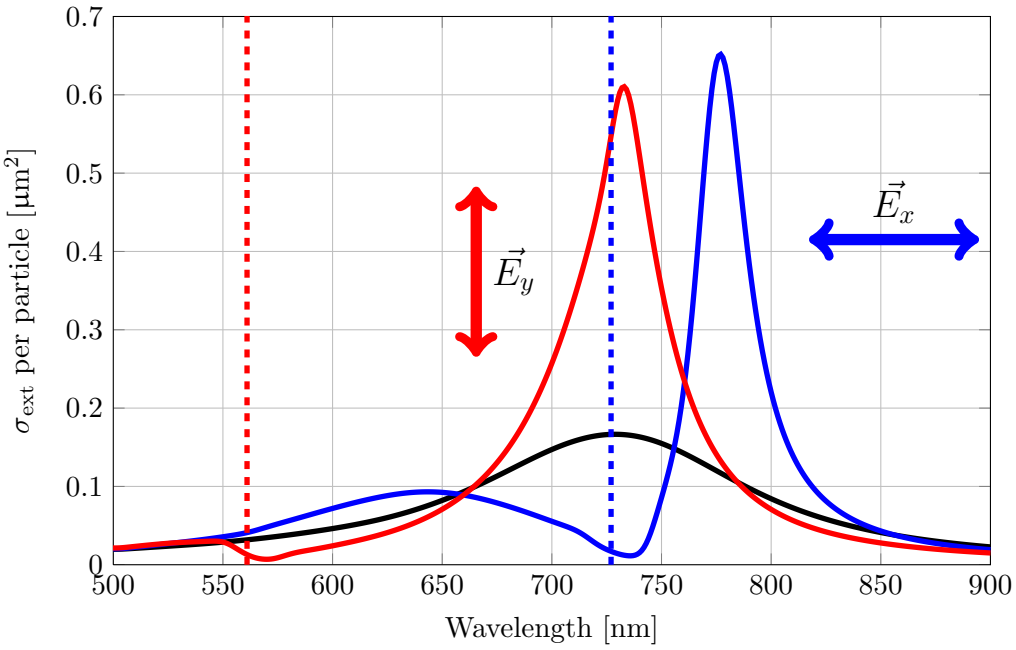

(a) Calculated extinction cross-section per particle.

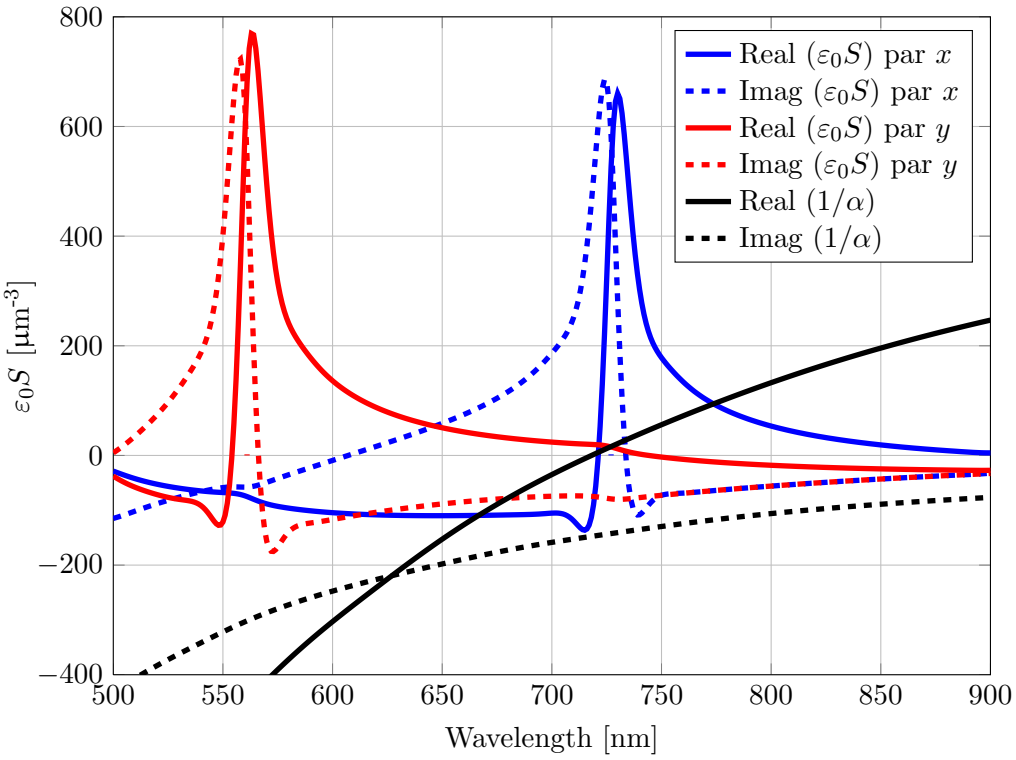

(b) S-factor.

Figure 4.3: (a) extinction cross-section per particle (this is a repeat of Figure 4.2b, for ease of comparison) and (b) S-factor for a rectangular array of silver discs ($d = 120$ nm, $h = 30$ nm), together with the calculated inverse polarizability of an isolated particle. $g_x = 370$ nm and $g_y = 480$ nm for the rectangular array, were g_x and g_y are the pitches in the x- and y-directions respectively. The electric field is parallel to either the x-axis or y-axis of the array, see Figure 4.1 for a scanning-electron micrograph. The array was modelled in $n = 1.515$. The two diffraction edges occur at 561 nm (red dashed line) and 727 nm (blue dashed line).

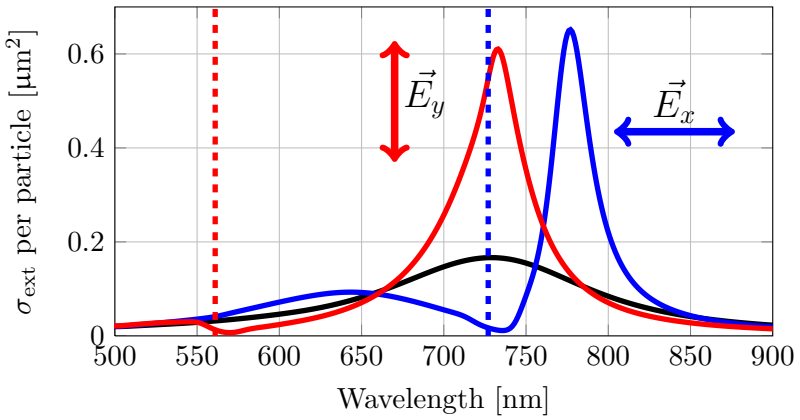

(a) S-factor calculated extinction cross-section per particle.

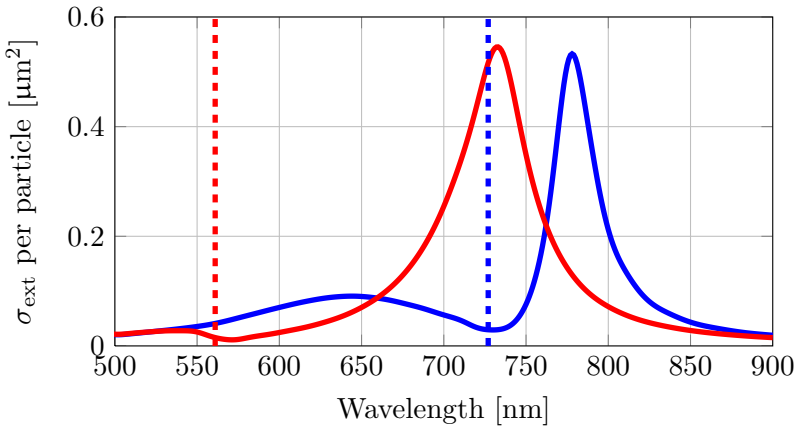

(b) CDA calculated extinction cross-section per particle.

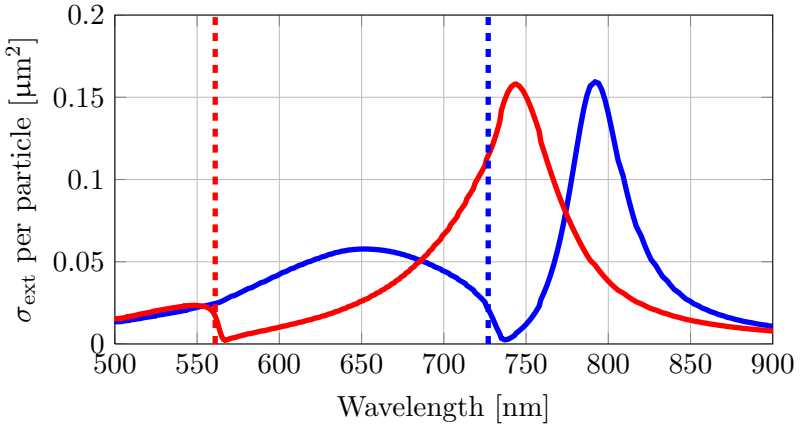

(c) FEM calculated extinction cross-section per particle.

Figure 4.4: (a) S-factor (this is a repeat of Figure 4.2b, for ease of comparison), (b) CDA and (c) FEM calculated extinction cross-section per particle of silver discs ($d = 120$ nm, $h = 30$ nm) in a $g_x = 370$ nm and $g_y = 480$ nm rectangular array, where g_x and g_y are the pitches in the x- and y-directions respectively. The electric field was either parallel to the x-axis (blue solid line) or y-axis (red solid line) of the array, see Figure 4.1 for scanning-electron micrograph. The array was surrounded by a refractive index of $n = 1.515$ meaning the two diffraction edges occur at 561 nm (red dashed line) and 727 nm (blue dashed line). 30×30 particles were modelled in the CDA model.

Two different S-factors are seen (blue) electric field parallel to the x-axis of the array and (red) parallel to the y-axis of the array. These SLRs occur when the denominator of Equation 4.1 is minimised. This occurs where the real part of $\varepsilon_0 S$ and $1/\alpha$ intersect, providing that the difference in imaginary parts of $\varepsilon_0 S$ and $1/\alpha$ are small. This is the case for the SLR at approximately 780 nm with the incident electric field parallel to x-axis of that array and with the SLR at approximately 740 nm when the electric field is parallel to the y-axis of the array. The SLR at approximately 640 nm does not occur exactly at the crossing points of the real parts of $\varepsilon_0 S$ and $1/\alpha$ as the difference between their imaginary parts is large. SLRs occur when the denominator of Equation 4.1 are minimized.

Figure 4.4 shows the modelled extinction cross-section per particle vs. wavelength spectra of the array in Figure 4.1 calculated by three different methods: (a) S-factor, (b) CDA and (c) FEM. For consistency all of the calculated extinction spectra have been convolved with a Gaussian as described before. For the CDA calculation 30×30 particles have been modelled with the MLWA polarizability given by Equation 2.7. The S-factor and CDA calculations give almost identical results apart from the spectrum associated with the electric field is parallel to the x-axis of the array, going to nearly zero at the diffraction edge (blue dashed line). This difference could be due to the S-factor calculation assuming that the array is infinite, therefore, each particle has the same dipole moment, unlike the CDA where the dipole moment of each particle can have different magnitude or direction. The FEM model gives extinction cross-section per particle values that are comparable with the experiment, but the spectral position of the SLRs are at longer wavelengths than the S-factor and CDA models.

4.3 Coupling in regular arrays of plasmonic particles

From the results of the rectangular array it is seen that the pitch associated with the x-axis and y-axis of the rectangular array and the incident electric field polarization affects how the particles couple together. To investigate this further, arrays with $g_y = 480$ nm and four different values of g_x were fabricated: $g_x = 370$ nm, $g_x = 480$ nm (square array), $g_x = 520$ nm and $g_x = 560$ nm (see Figure 4.5). Figure 4.6 shows the measured normal-incidence extinction spectra of these arrays with the electric field (a) parallel to the x-axis and (b) parallel to the y-axis. The corresponding S-factor calculated extinction spectra of these arrays is shown in Figure 4.7. In the measurements when the electric field is parallel to the x-axis of the arrays, a single strong SLR is seen at approximately 750 nm in each extinction spectrum. A different response is found

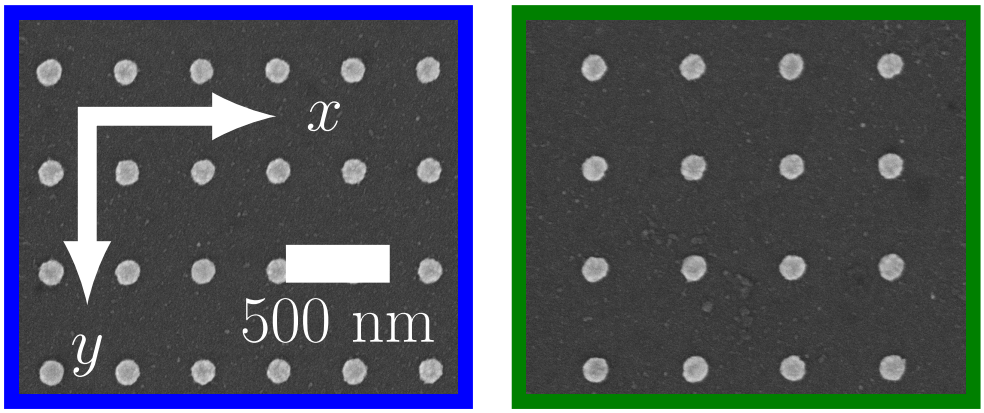

(a) $g_x = 370$ nm.

(b) $g_x = 480$ nm.

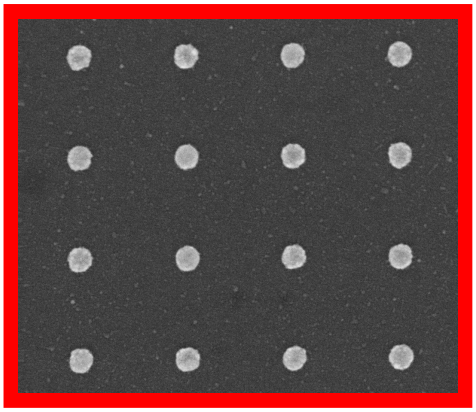

(c) $g_x = 520$ nm.

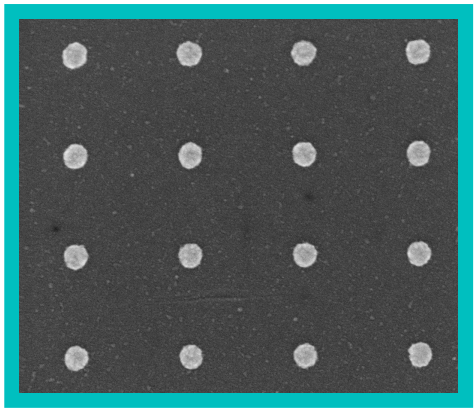

(d) $g_x = 560$ nm.

Figure 4.5: Scanning-electron micrographs of silver particle arrays with different x-pitches, g_x, and same y-pitches, g_y. For the arrays $g_y = 480$ nm. (a) $g_x = 370$ nm, (b) $g_x = 480$ nm (square array), (c) $g_x = 520$ nm and (d) $g_x = 560$ nm. All arrays consist of silver discs with a diameter of 120 nm and height of 30 nm.

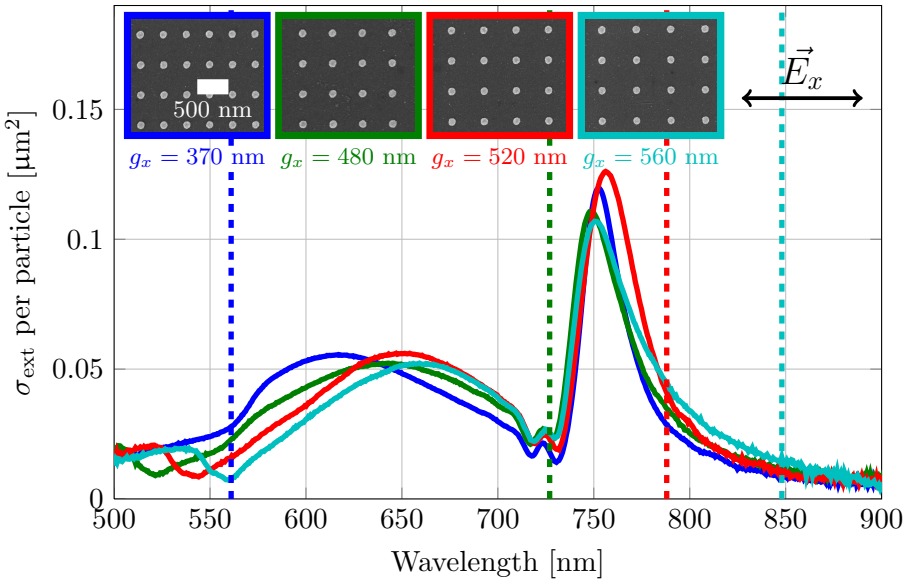

(a) Electric field parallel to x-axis.

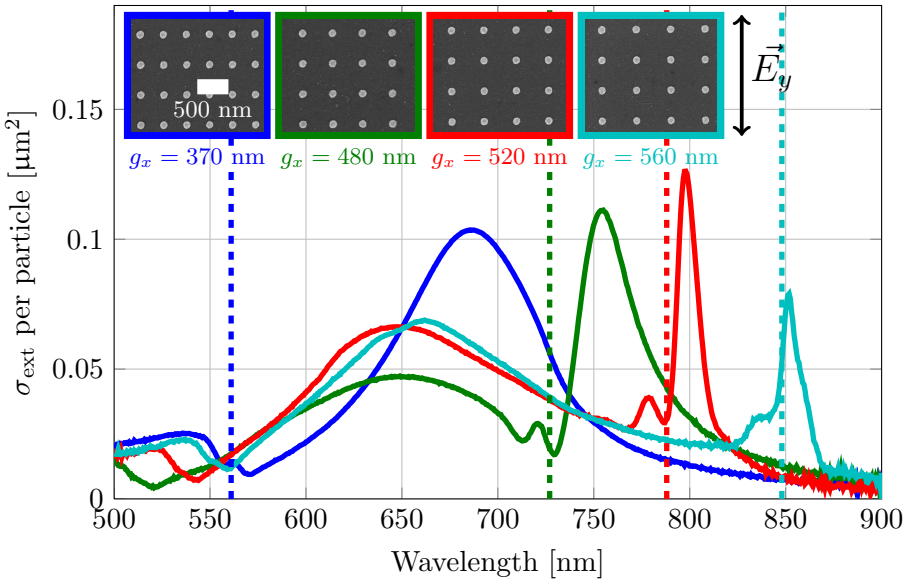

(b) Electric field parallel to y-axis.

Figure 4.6: Measured extinction cross-section per particle as a function of wavelength of arrays with different x-pitches, g_x, and same y-pitches, g_y. $g_y = 480$ nm for all of the arrays. Arrays have $g_x = 370$ nm, $g_x = 480$ nm (square array), $g_x = 520$ nm and $g_x = 560$ nm, see Figure 4.5 for scanning-electron micrographs. All the arrays consist of silver discs with a diameter of 120 nm and height of 30 nm. (a) is with electric field parallel to the x-axis of the array and (b) parallel to the y-axis. The diffraction edges relating to g_y of the four arrays are shown as dashed lines at 561 nm (blue), 727 nm (green), 788 nm (red) and 848 nm (cyan).

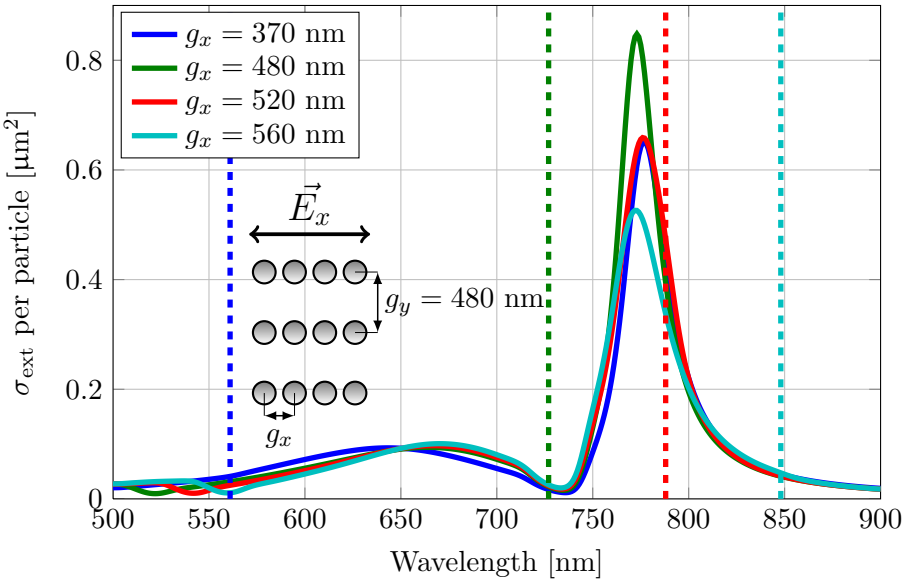

(a) Electric field parallel to x-axis.

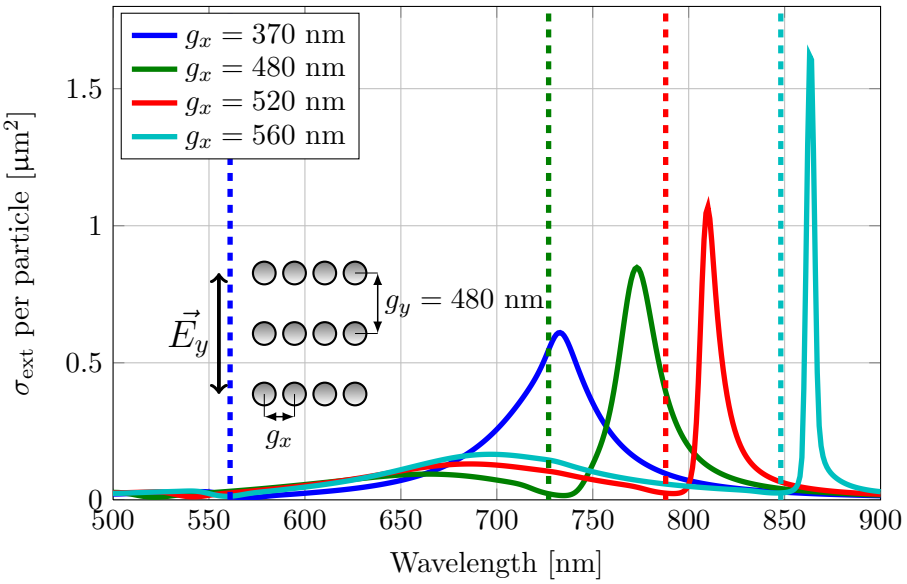

(b) Electric field parallel to y-axis.

Figure 4.7: S-factor calculated extinction cross-section per particle as a function of wavelength of arrays with different x-pitches, g_x, and same y-pitches, g_y. For all of the arrays $g_y = 480$ nm. Arrays have $g_x = 370$ nm, $g_x = 480$ nm (square array), $g_x = 520$ nm and $g_x = 560$ nm. All the arrays consist of silver discs with a diameter of 120 nm and height of 30 nm. (a) is with electric field parallel to the x-axis of the array and (b) parallel to the y-axis. The diffraction edges relating to g_y of the four arrays are shown as dashed lines at 561 nm (blue), 727 nm (green), 788 nm (red) and 848 nm (cyan).

when the electric field is parallel to the y-axis: each array has a strong SLR associated with the x-pitch, but these now occur at different spectral positions (approximately 685 nm, 755 nm, 798 nm and 852 nm) for each different array pitch. As the diffraction edge of g_x is increased, the SLR increases in strength and sharpens until at $g_x = 560$ nm it starts to weaken. The spectral position of the diffraction edge is located in the long-wavelength tail of the single particle resonance, so the SLR is weak. For both polarizations of the electric field, the S-factor calculated extinction spectra broadly predict the experimental spectra with all of the SLRs occurring at longer wavelengths. However there are two main exceptions for the perpendicular polarization: the difference between the experiment and model in the spectral position of the SLR for the $g_x = 370$ nm array is much greater than for the rest of the arrays, and the strength of the SLR of the $g_x = 560$ nm array is stronger relative to the $g_x = 370$ nm, 480 nm and 520 nm arrays. From the spectra, it appears that the particles couple together in the direction that is orthogonal to the applied electric field in agreement with recent literature [114, 121, 122]. To confirm this coupling mechanism, chains with the same pitches as g_x of the rectangular arrays were modelled using the S-factor approach.

Figure 4.8 presents calculated extinction spectra of chains of silver discs ($d = 120$ nm and $h = 30$ nm) with pitches $g = 370$ nm, 480 nm, 520 nm and 560 nm. The incident electric field is parallel to the chain axis in (a) and perpendicular in (b). Since SLRs are sensitive to the particle number, chains were modelled with the same total number of particles (160,000) as for the arrays described above. The accompanying real and imaginary parts of $\varepsilon_0 S$ and inverse polarizability of a single isolated particle ($d = 120$ nm with $h = 30$ nm) are shown in Figure 4.9. The optical response of the chain depends on the polarization of the incident electric field. As illustrated in Figure 4.8a, when the incident electric field is parallel to the chain, the extinction spectra of the chains is similar to the single particle plasmon resonance with a small change in strength and spectral position relative to the perpendicular case.

Equation 4.2 can be split up into the three separate field components: near-, intermediate- and far-fields. The separated-field version of S is given by Equation 4.3,

$$S = \frac{1}{4\pi\varepsilon_0} \sum_j \exp\left(ikr_j\right) \left[\underbrace{\frac{(3\cos^2\theta_j - 1)}{r_j^3}}_{\text{near-field}} + \underbrace{\frac{-ik(3\cos^2\theta_j - 1)}{r_j^2}}_{\text{intermediate-field}} + \underbrace{\frac{k^2\sin^2\theta_j}{r_j}}_{\text{far-field}} \right], \quad (4.3)$$

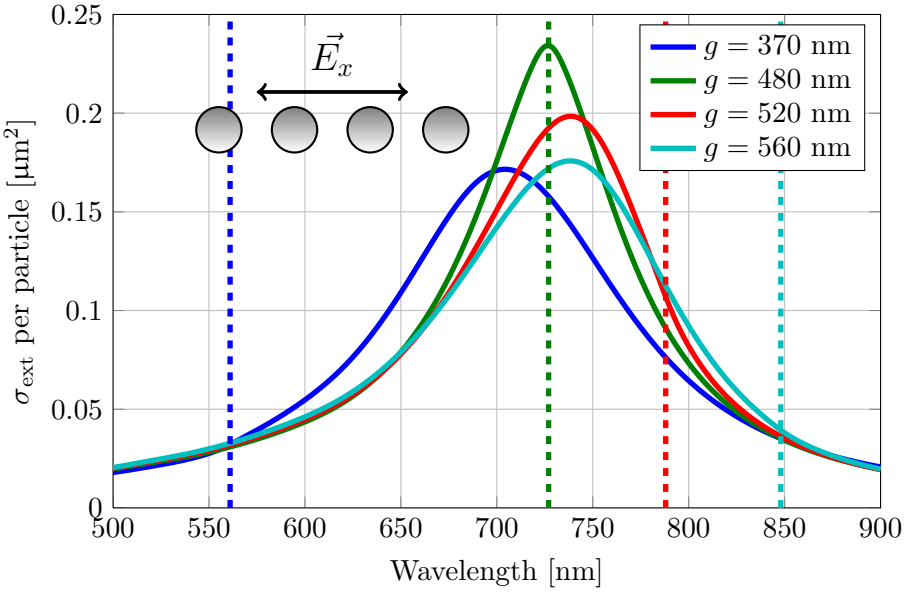

(a) Electric field parallel to chain axis.

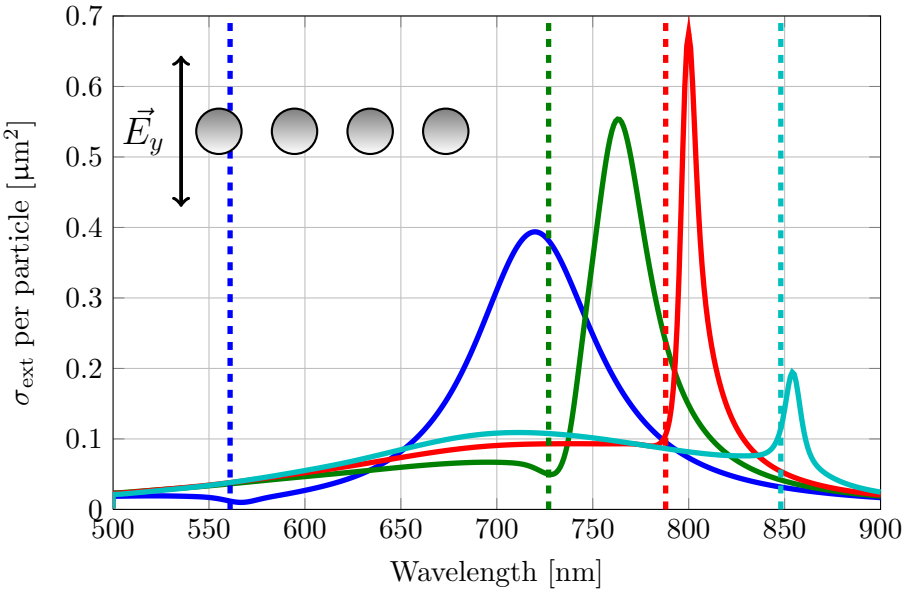

(b) Electric field parallel perpendicular to chain axis.

Figure 4.8: *S*-factor calculated extinction cross-section per particle as a function of wavelength of four different pitches, g, of silver particle chains (g = 370 nm, 480 nm, 520 nm and 560 nm). The chains are made up of oblate spheroids with d = 120 nm and h = 30 nm. (a) is with electric field parallel to the chain axis and (b) perpendicular. The diffraction edges relating to the period of the four chains are shown as dashed lines at 561 nm (blue), 727 nm (green), 788 nm (red) and 848 nm (cyan). The colours in (b) correspond to the legend in (a).

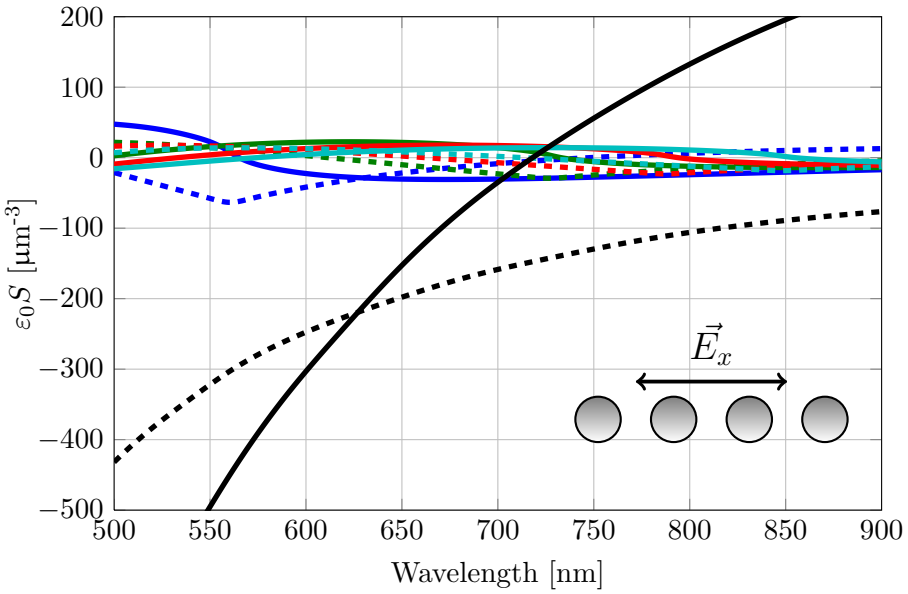

(a) Electric field parallel to chain axis.

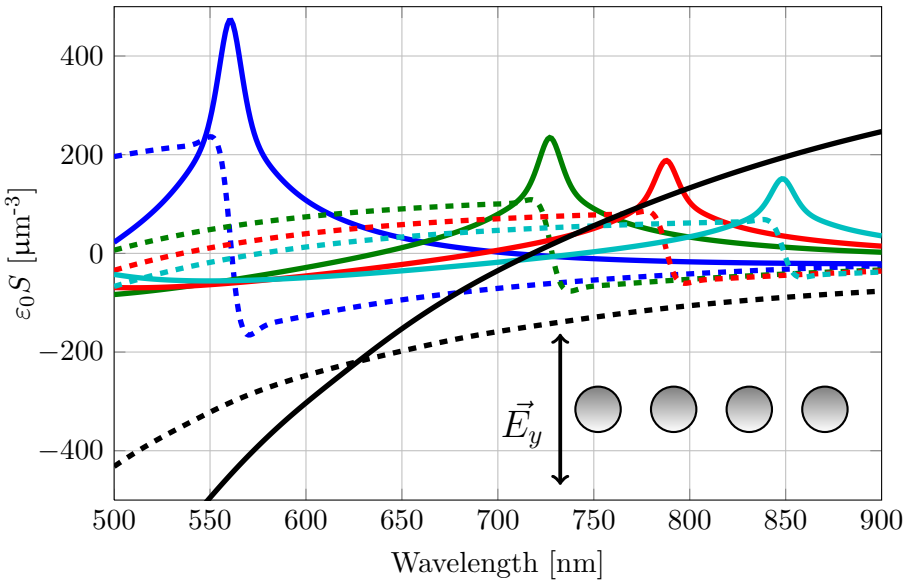

(b) Electric field perpendicular to chain axis.

Figure 4.9: Calculated S-factor of four different pitches, g, of silver particle chains (g = 370 nm (blue), 480 nm (green), 520 nm (red) and 560 nm (cyan)). Solid lines correspond to the real part of S and dashed lines the imaginary part. The real (solid line) and imaginary (dashed line) parts of the inverse polarizability of an oblate spheroid with $d = 120$ nm and $h = 30$ nm have been added as a black line. (a) is with electric field parallel to the chain axis and (b) perpendicular.

σ_{ext}	Rectangular Expt.		Rectangular Model		Chain Model		
g_x (nm)	λ_{peak} (nm) (Mag. (μm^2))	FWHM (S,M,B)	λ_{peak} (nm) (Mag. (μm^2))	FWHM (S,M,B)	λ_{peak} (nm) (Mag. (μm^2))	Re ($1/\alpha = \varepsilon_0 S$)	|Im ($1/\alpha - \varepsilon_0 S$)|
370	685 (0.10)	Broad	733 (0.61)	Broad	720 (0.39)	Yes	83
480	755 (0.11)	Medium	773 (0.85)	Medium	763 (0.55)	Yes	60
520	798 (0.13)	Sharp	810 (1.07)	Sharp	800 (0.68)	Yes	47
560	852 (0.08)	Sharp	863 (1.62)	Sharp	854 (0.19)	No	47

Table 4.1: Experimental and S-factor calculated extinction cross-sections for rectangular arrays with different values of g_x but all with g_y=480 nm. Also added for comparison is S-factor calculated extinction cross-sections for particle chains with the same values of g_x as the rectangular arrays. In all the spectra the incident electric field is parallel to the y-axis.

There can be no far-field interaction in the parallel case as the far-field term is zero i.e. $\sin 0^\circ = 0$ (see Figure 3.1 and Equation 4.3). The interaction is only due to the near and intermediate fields, which are weak due to the particle separation (approximately λ), meaning that the real and imaginary parts of $\varepsilon_0 S$ are small (see Figure 4.9a). Therefore there is no SLR as far-field coupling is required.

When the electric field is perpendicular to the chain axis (see Figure 4.8b) an SLR is seen in each extinction spectrum with the SLRs closer to the diffraction edge than with the rectangular array calculation (see Figure 4.7b). The response is similar to the rectangular array calculation apart from the strength of the $g = 560$ nm chain being weaker (relative to the other chains) than for the corresponding rectangular one. The extinction cross-section per particle is less for each chain SLR than the corresponding rectangular array result, since in a rectangular array there are contributions to the scattered electric field from diagonal particles, which are not present in the chain. Rather surprisingly, the perpendicular chain result is a closer match to the experiment - this is the subject for future investigation. Again, these SLRs occur where the real parts of $\varepsilon_0 S$ and $1/\alpha$ intersect except for the $g = 560$ nm chain where it is the closest approach, resulting in a weak SLR (see Figure 4.9b). Displayed in Table 4.1 is experimental and S-factor calculated results extracted from the data of Figures 4.6b, 4.7b, 4.8b and 4.9b. The data in the table compares the SLRs of rectangular arrays and chains when the incident electric field is parallel to the y-axis of the array (perpendicular to the chain axis).

The relative contribution of the near, intermediate and far-fields can be seen by plotting the different terms of Equation 4.3. Figure 4.10 shows the S-factor calculated extinction

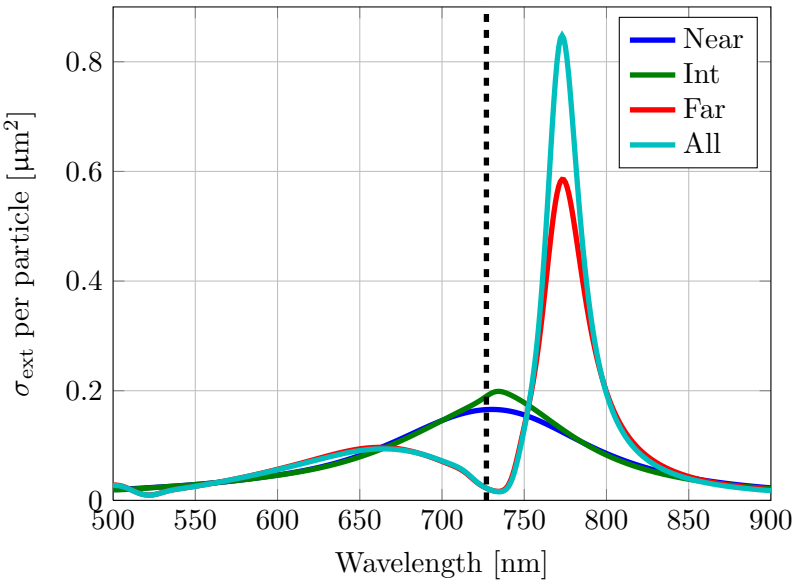

Figure 4.10: S-factor calculated extinction cross-section per particle showing the contribution of the different field components to the extinction spectrum. Calculation is of 480 nm pitch square array of silver discs (d = 120 nm, h = 30 nm). The electric field is in the plane of the particles and the particles are embedded in a homogeneous medium with $n = 1.515$.

cross-section per particle as a function of wavelength for a square array of silver discs (d = 120 nm and h = 30 nm) for each different component of the field. It is seen that the near and intermediate field make little difference to the extinction spectra and that the far-field term is responsible for the coupling between particles. Because S is a complex quantity, $\sigma_{\text{near}} + \sigma_{\text{int}} + \sigma_{\text{far}} \neq \sigma_{\text{all}}$.

4.4 Conclusion

Rectangular arrays of metallic nanoparticles have been fabricated by electron-beam lithography. The collective array response has been characterized by index-matched normal-incidence extinction measurements and experimental results have been compared with the S-factor model, coupled-dipole approximation and finite element modelling. Rectangular arrays have a lower degree of symmetry than square, hexagonal and honeycomb arrays studied previously in Chapter 3, and have shown a clear polarization dependence in their optical response. Further investigation showed that particles coupled together over distances greater then λ in the direction orthogonal to the applied electric field. By modelling the optical response it was found that the dominant

coupling mechanism was due to the far-field interaction.

Chapter 5

Symmetric two-particle basis square arrays

5.1 Introduction

It was shown in Chapter 3, that when the diffraction edge lies within the single particle resonance narrow spectral features, known as surface lattice resonances (SLRs), can be observed. Chapter 3 also presented results showing that SLRs can be observed for different particle geometries (square, hexagonal and honeycomb). The mechanism by which particles couple was investigated in Chapter 4, concluding that particles couple in the direction orthogonal to the applied electric field. A natural question to ask would be, how does the SLR change (with incident electric field perpendicular to the pair-axis) when an extra particle is added to the basis? Kravets *et al.* [48] have experimentally observed SLRs in square arrays of particle pairs at normal incidence, but their work was mainly focused on out-of-plane SLRs (oblique incidence). Their particles were gold nanopillars with height 90 nm (much taller than considered in this thesis). They provide a comprehensive study of the effect that particle size [123] and the presence of a conducting substrate [48] have on SLRs. In Ref. [123] they perform ellipsometry, transmission and reflection measurements on a variety of diameters of gold nano-pillars in square arrays, identifying the plasmonic modes (in-plane, out-of-plane, symmetric or antisymmetric) responsible for the optical response they observe. An in-plane plasmon mode is where the electrons collectively oscillate in the plane of the array, and an out-of-plane mode is where the electrons oscillate parallel to the height dimension of the particles. In Ref. [48] they demonstrate by ellipsometry, transmission and re-

flection measurements that the optical response of particle arrays on conducting and non-conducting substrates is dramatically different. Further differences between their work and the work presented here is that all of their measurements were performed in an asymmetric optical environment (air/glass). They kept the centre-to-centre separation (140 nm) of the particle pair the same and concentrated mainly on one square array pitch (320 nm) throughout their work [47, 48, 123].

To study the electromagnetic interaction of in-plane particle plasmon resonances in a particle pair. Rechberger *et al.* [35] fabricated square arrays of gold discs and varied the centre-to-centre separation between the pairs. Characterization of these samples was performed by normal-incidence extinction measurements in an asymmetric optical environment (air/glass). They chose an array pitch (450 nm) such that their arrays were non-diffracting in the spectral range of the single particle resonance (780 nm in their case), therefore they did not study SLRs. They found when the incident electric field was polarized parallel to the pair axis, a red-shift (compared to the single particle resonance) of the particle plasmon resonance wavelength was observed. A blue-shift of the particle plasmon resonance was observed for the orthogonal polarization.

The work reported in this chapter investigates the coupling between particle pairs, in square arrays that are diffracting within the spectral region of the single particle resonance, rather than simply between particles in a pair, as in Ref. [35], In the extinction measurements presented here, the in-plane plasmon mode was probed, which differs from the work by Kravets and coworkers where they studied the out-of plane mode. The polarization dependence of one- and two-particle basis square arrays of silver nanoparticles fabricated by electron-beam lithography (EBL) will be presented and discussed. The arrays were characterized by normal-incidence extinction measurements and their extinction cross-section compared with a simple coupled-dipole model, i.e. the S-factor model. The simple coupled-dipole model introduced in Section 3.2.2 can be used to explain the main features of the spectra, i.e. the spectral position, strength and width of the SLRs. Extinction spectra of one-particle basis square arrays will be presented first, followed by two-particle basis arrays and finally two-particle basis arrays with different centre-to-centre separations.

The measured transmission (see Equation 3.23) was converted to the extinction cross-section per particle/particle pair using Equation 3.24. The response of the particle arrays was modelled using the S-factor model, where the modified polarizability of the

array is defined by,

$$\alpha^* = \frac{1}{1/\alpha_{\mathrm{MLWA}} - \varepsilon_0 S}, \tag{5.1}$$

where α_{MLWA} (see Equation 2.7) is the modified long-wavelength polarizability, ε_0 is the permittivity of free space and S is given by:

$$S = \frac{1}{4\pi\varepsilon_0} \sum_j \exp\left(ikr_j\right) \left[\frac{(1 - ikr_j), (3\cos^2\theta_j - 1)}{r_j^3} + \frac{k^2 \sin^2\theta_j}{r_j} \right], \tag{5.2}$$

where r_j is the distance from the central particle in the array to particle j and θ_j is the angle between $\vec{r}_j$ and the dipole moment of the central particle (see Figure 3.1). Equations 5.1 and 5.2 are a repeat of Equations 3.16 and 3.22). The function S (see Equation 5.2) was smoothed before insertion into Equation 5.1 (see Section 3.2.2). SLRs occur when the denominator in Equation 5.1 is minimized. In the calculations, the particles (400 × 400 particles for one-particle basis and 280 × 280 pairs for two-particle basis) were approximated as oblate spheroids and given a polarizability calculated from the modified long-wavelength approximation (see Equation 2.7). The calculated extinction cross-section of the particle arrays was convolved following the procedure outlined in Section 3.2.4.

5.2 One-particle basis square arrays

At this point, it is necessary to revisit the square array with a one-particle basis. In this section, the spectral position of the diffraction edge is moved through the single particle resonance by fabricating arrays with pitch g = 350 nm, 400 nm, 450 nm and 500 nm. The extinction cross-section and phase of the polarizability (with respect to the incident electric field) of the single-particle response of a circular silver disc (d = 85 nm, h = 30 nm) with the position of the four different diffraction edges of the arrays (530 nm, 606 nm, 682 nm and 758 nm) are shown in Figure 5.1. The polarizability of the particle describes the response of the conduction electrons in the particle to an applied electric field. In Figure 5.1 the single particle plasmon resonance (black solid line) is observed at approximately 610 nm at which point the phase of the polarizability with respect to the incident field (purple solid line) is $\pi/2$. It is noted that the 530

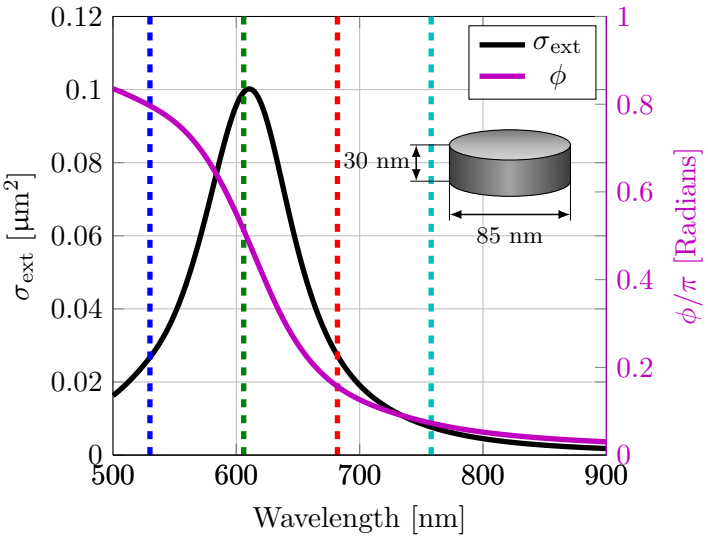

Figure 5.1: Modified long-wavelength approximation calculated extinction cross-section (left axis) and phase of polarizability (right axis) with respect to the incident electric field of a single silver disc ($d = 85$ nm, $h = 30$ nm). The particle was embedded in a homogeneous medium with a refractive index $n = 1.515$ with the incident electric field in the plane of the particle. Diffraction edges for $g = 350$ nm (blue), 400 nm (green) , 450 nm (red) and 500 nm (cyan) square arrays are illustrated by dashed lines. The phase of the polarizability is $\pi/2$ on resonance and decreases for wavelengths longer than the single particle plasmon resonance.

nm diffraction edge (blue dashed line) lies on the short-wavelength side, 606 nm (green dashed line) centrally, 682 nm (red dashed line) and the 758 nm (cyan dashed line) on the long-wavelength side of the single particle resonance. The phase of the polarizability decreases from 0.8π to approximately 0 from wavelengths of 500 nm to 900 nm.

Figure 5.2 shows scanning-electron micrographs (SEMs) of silver discs ($d = 85$ nm and $h = 30$ nm) fabricated by EBL that are arranged in square arrays with $g = 350$ nm, 400 nm, 450 nm and 500 nm. The corresponding extinction spectra per particle for normal incidence as a function of wavelength for two orthogonal polarizations of the electric field ((a) parallel to x-axis or (b) y-axis of the array) are displayed in Figure 5.3. For each different pitch of square array, the corresponding diffraction edge is illustrated by a dashed line of the same colour. In the measured extinction spectra, with the incident electric field parallel (see Figure 5.3a), a peak is seen in each spectrum (at 586 nm, 620 nm, 682 nm and 752 nm) and is attributed to the SLR of the array. These SLRs result from the constructive interference of the scattered light by the particles in the plane of the array. They occur when the real part of $1/\alpha$ equals $\varepsilon_0 S$, provided the difference between their imaginary parts is small. The SLRs occur spectrally closer to the diffraction edge as g, and hence the diffraction edge of the array, is increased. The

phase of the particle polarizability at these wavelengths is smaller (see purple solid line in Figure 5.1) meaning there is less lag in the collective electron motion in response to an applied electric field. The reduced phase difference causes the SLR to occur nearer to the diffraction edge. It is noted that due to the symmetry of the particles and the array, there is negligible difference between the measured extinction spectrum relating to the two orthogonal polarizations of the incident electric field. The differences between the results (see Figures 5.3a and 5.3b) are attributed to the asymmetry of the discs due to the imperfections in the fabrication process. In Figure 5.4 the (a) calculated extinction cross-section per particle and the (b) S-factor of the four different square arrays (see Figure 5.2 for SEMs) are displayed. As with the experimental extinction spectra, the four diffraction edges are illustrated by dashed lines. For a square array of discs, illuminated at normal incidence, the optical response of the array is independent of the orientation of the incident electric field (see Figure 3.16).

A comparison is now made between the experiment (see Figure 5.3a) and model (see Figure 5.4a). In the experiment, a SLR is observed in each extinction spectrum (at 586 nm, 620 nm, 682 nm and 752 nm). These SLRs occur when the real part of $\varepsilon_0 S$ intersects (or most closely approaches) the real part of $1/\alpha$ [49, 105, 124, 125]. There is good agreement between the experiment and model for the spectral positions of the SLRs for $g = 450$ nm (red solid line) and $g = 500$ nm (cyan solid line), but there is an increasing discrepancy for $g = 350$ nm (blue solid line) and $g = 400$ nm (green solid line). This could be due to the MLWA failing at shorter wavelengths, which is attributed to the product of ka becoming larger: the higher powers of ka that have been neglected in the MLWA (see Equation 2.7), which is the lowest order correction the quasi-static polarizability [126], become important.

The relative strengths and widths of the SLRs will now be discussed: in the model (see Figure 5.4a), when $g = 450$ nm (red solid line) the SLR has a smaller FWHM and greater magnitude because the real part of $1/\alpha$ and $\varepsilon_0 S$ intersect perpendicularly (see black solid line and red solid line in Figure 5.4b) and the difference between the imaginary parts of $1/\alpha$ and $\varepsilon_0 S$ is small (see black dashed line and red dashed line in Figure 5.4b). The strength of the SLR is determined by the difference between the imaginary parts of $1/\alpha$ and $\varepsilon_0 S$ and whether the real part of $1/\alpha$ crosses the real part of $\varepsilon_0 S$. The width of the SLR is determined by the difference between the imaginary parts of $1/\alpha$ and $\varepsilon_0 S$ and the angle of the interception of the real parts of $1/\alpha$ and $\varepsilon_0 S$ (for an in-depth discussion see Section 3.2.2). The SLRs for $g = 350$ nm (see blue solid line, Figure 5.4a) and $g = 400$ nm pitch (see green solid line, Figure 5.4a) square arrays are similar in strength and width as their real parts of $1/\alpha$ and $\varepsilon_0 S$ intercept (see Figure

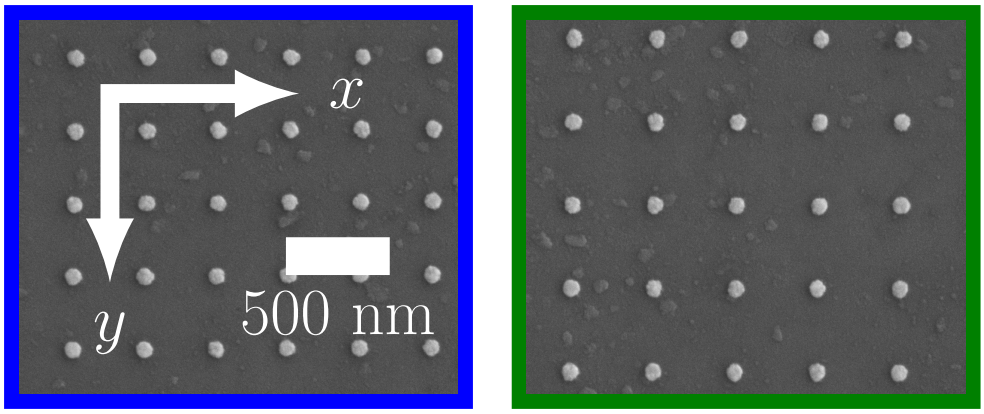

(a) $g = 350$ nm.

(b) $g = 400$ nm.

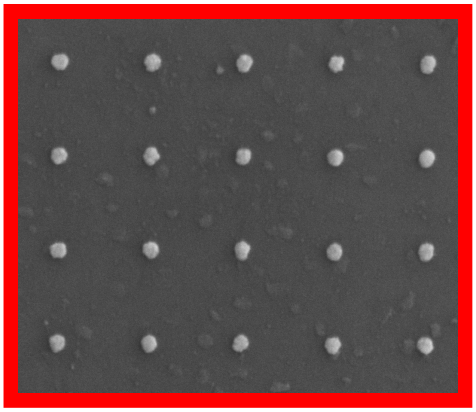

(c) $g = 450$ nm.

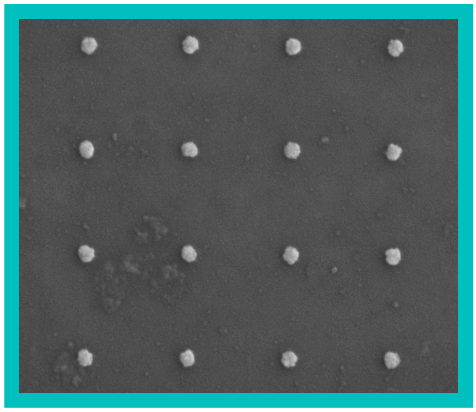

(d) $g = 500$ nm.

Figure 5.2: Scanning-electron micrographs of one-particle basis square arrays with four different pitches, g. The particles were silver discs with $d = 85$ nm and $h = 30$ nm. (a) $g = 350$ nm, (b) $g = 400$ nm, (c) $g = 450$ nm and (d) $g = 500$ nm.

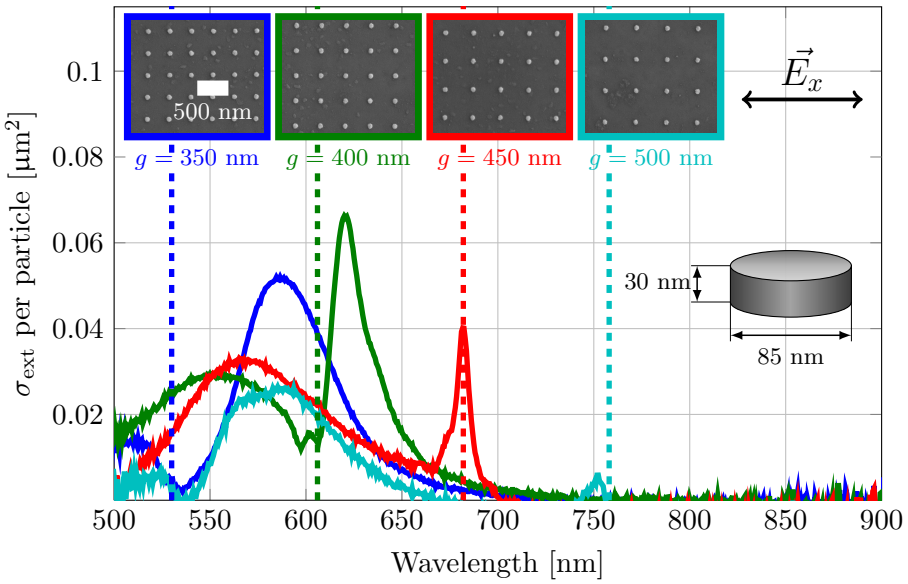

(a) $\vec{E}$ parallel to x-axis of array.

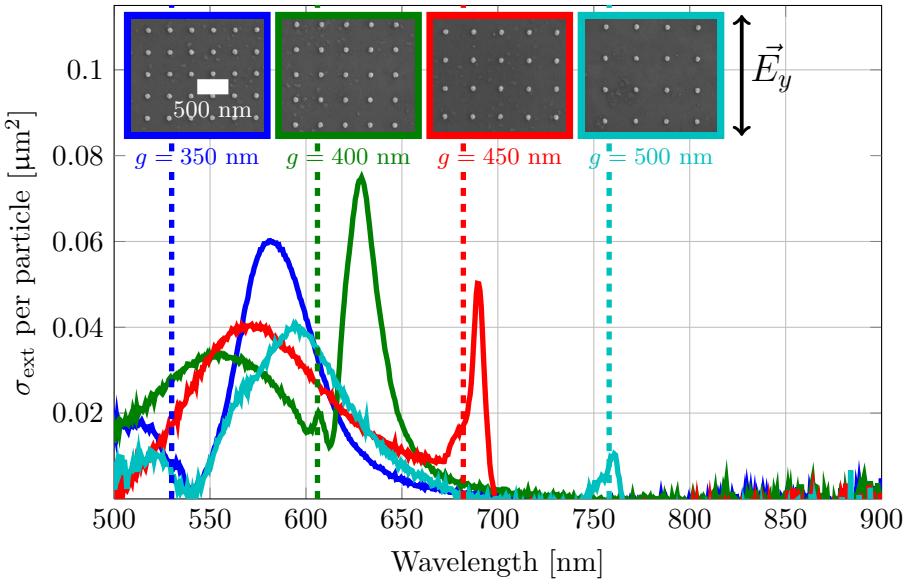

(b) $\vec{E}$ parallel to y-axis of array.

Figure 5.3: Measured extinction cross-section per particle vs. wavelength of four different pitches, g, square arrays (g = 350 nm, 400 nm, 450 nm and 500 nm) with a one-particle basis. The particles were silver discs (d = 85 nm and h = 30 nm), see Figure 5.2 for scanning-electron micrographs of arrays. The incident electric field was parallel to the x-axis of the array in (a) and parallel to the y-axis in (b). The environment of the particles was index-matched with the substrate using oil ($n = 1.515$). The diffraction edge associated with each different array pitch is illustrated by the corresponding coloured dashed line: (530 nm, 606 nm, 683 nm and 758 nm).

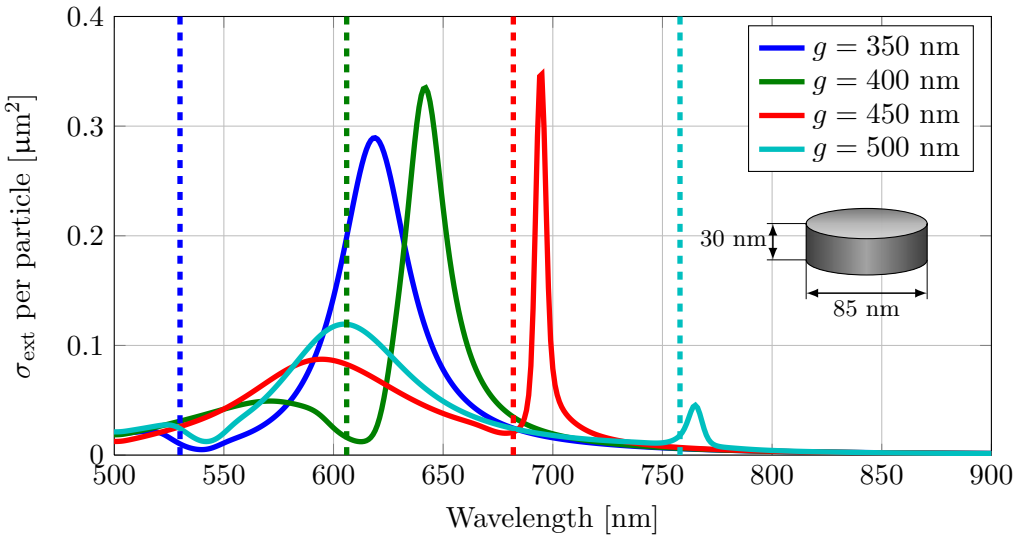

(a) Extinction cross-section per particle.

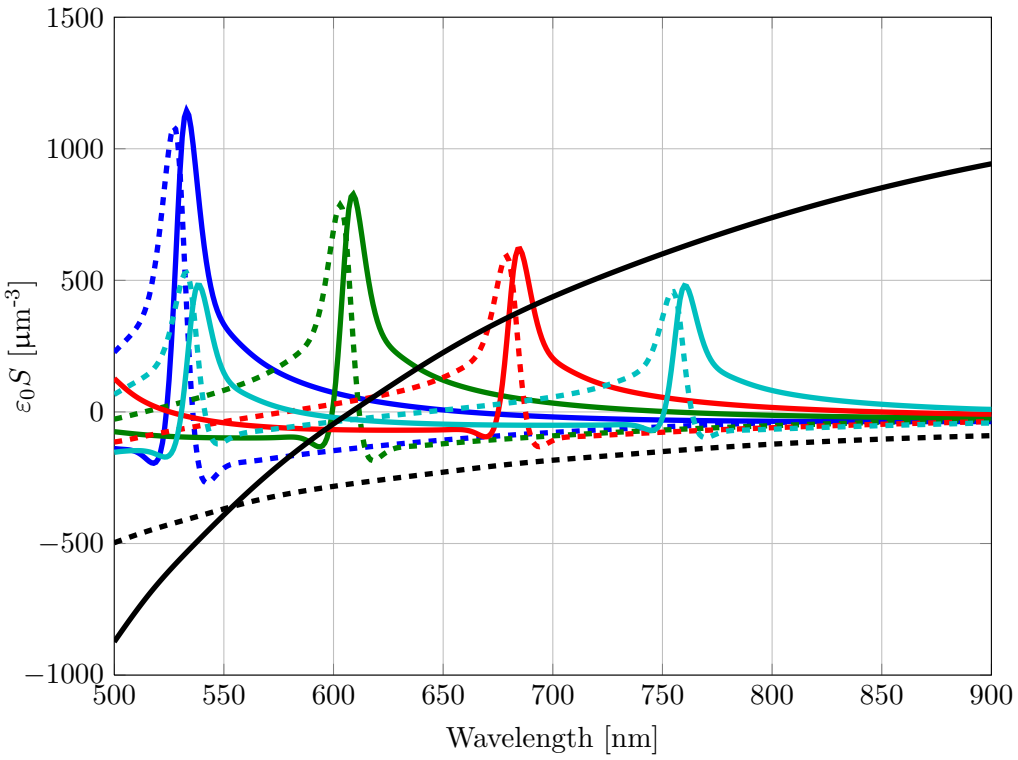

(b) Real (solid lines) and imaginary parts (dashed lines) of $1/\alpha$ (black) and $\varepsilon_0 S$ (see legend in (a) for corresponding colour).

Figure 5.4: Simple coupled-dipole model calculated (a) extinction cross-section per particle and (b) $\varepsilon_0 S$ for four different pitch square arrays (g = 350 nm, 400 nm, 450 nm and 500 nm) with a one-particle basis. Black lines in (b) indicate the real (solid) and imaginary parts (dashed) of the inverse polarizability of a single silver oblate spheroid (d = 85 nm and h = 30 nm). The particles were modelled in a medium with n = 1.515, and the diffraction edge associated with each different array pitch is illustrated by the corresponding coloured dashed line. In each case, 160,000 particles each with its own polarizability, calculated using the modified long-wavelength approximation (see Equation 2.7), was modelled.

5.4b), so the SLR will purely be determined by the difference between their imaginary parts of $1/\alpha$ and $\varepsilon_0 S$, which are similar. The SLR associated with the 500 nm pitch array (see cyan solid line, Figure 5.4a) square array is weak because the real parts of $1/\alpha$ and $\varepsilon_0 S$ do not cross. The relative strengths and widths of the SLRs between the experiment and model show good agreement apart from $g = 450$ nm (compare red solid line in Figures 5.3 and 5.4a). The inhomogeneity of the particles in the experiment could be responsible for the disagreement between the model and experiment regarding the strength of the $g = 450$ nm SLR (the model assumes perfectly uniform particles) [81]. The relationship between particle size variation, and the width and strength of the SLR were studied in Ref. [81]. The authors found by increasing particle size dispersion in square arrays the SLR broadened and weakened. The order of magnitude larger extinction cross-section per particle in the model compared to experiment is due to the polarizability from the MLWA not being an accurate approximation and greatly overestimating the imaginary part of the single-particle polarizability.

5.3 Two-particle basis square arrays

The electric-field polarization dependence of SLRs in two-particle basis square arrays will now be investigated. Figure 5.5 shows SEMs of particle pairs with a centre-to-centre separation of $l = 150$ nm arranged in four different square arrays with $g = 350$ nm, 400 nm, 450 nm and 500 nm. These four different values of g are the same as discussed in Section 5.2, but instead of comprising of a one-particle basis, they have a two-particle basis. The particles are silver discs with ($d = 85$ nm and $h = 30$ nm). The measured extinction cross-section per pair with either the incident electric field (a) parallel or (b) perpendicular to the particle-pair axis of the arrays (see Figure 5.5 for SEMs with array axes indicated) are presented in Figure 5.6. The extinction cross-section per particle pair calculated using the simple coupled-dipole model of the two-particle basis square arrays (see Figure 5.5) is displayed in Figure 5.7. The incident electric field is parallel to the particle-pair axis in (a) or perpendicular in (b). The S-factor for the perpendicular case is set out in Figure 5.8b together with the calculated extinction cross-section per particle pair reproduced to allow easier comparison with $\varepsilon_0 S$.

A small difference is noted in the shape of the measured optical response (extinction cross-section) between the one-particle basis (see Figure 5.3) and two-particle basis square arrays when the incident electric field is parallel to the particle-pair axis (see Figure 5.6a). The main difference is that the SLRs in the two-particle basis arrays for $g = 450$ nm (red solid line) and $g = 500$ nm (cyan solid line) arrays have increased

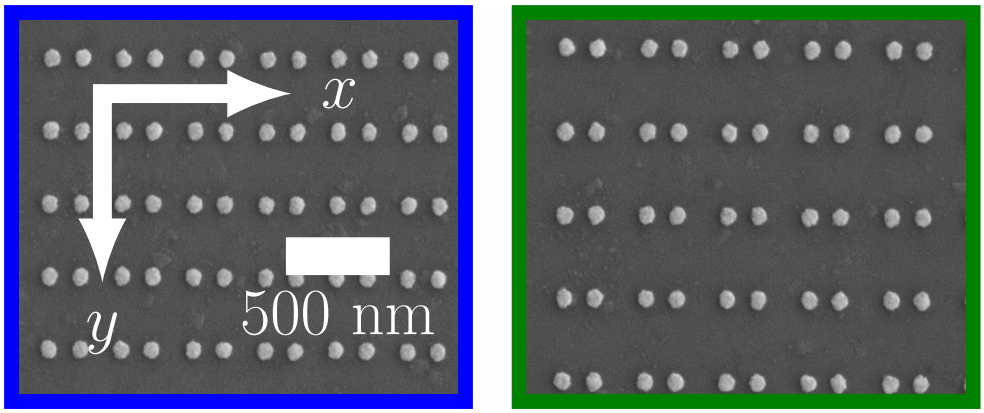

(a) $g = 350$ nm.

(b) $g = 400$ nm.

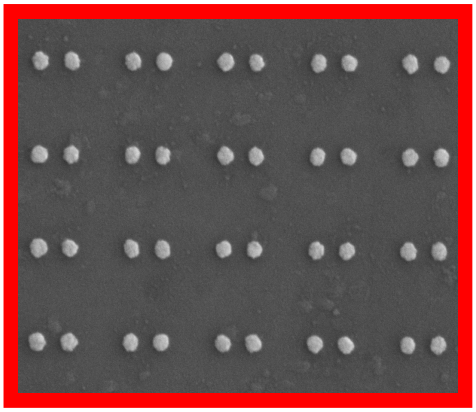

(c) $g = 450$ nm.

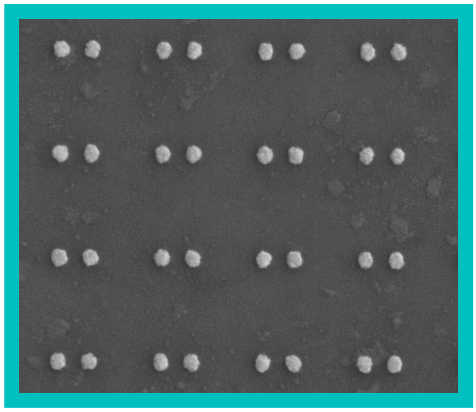

(d) $g = 500$ nm.

Figure 5.5: Scanning-electron micrographs of four different pitch, g, square arrays with a two-particle basis. The basis consisted of two discs ($d = 85$ nm and $h = 30$ nm) with a 150 nm centre-to-centre separation. (a) $g = 350$ nm, (b) $g = 400$ nm, (c) $g = 450$ nm and (d) $g = 500$ nm.

in strength and narrowed relative to the $g = 350$ nm (blue solid line) and $g = 400$ nm (green solid line) square arrays. The similar optical response between the one- and two-particle basis arrays can be explained by considering the direction in which the particles couple together: from Section 4.3 it was found for particles roughly separated by λ that they coupled together in the direction orthogonal to the applied electric field. By further investigation, it was found the coupling was through the far-field component of the scattered electric field (see Equation 4.3) from the other particles. The radiation of an oscillating dipole moment is concentrated in two lobes perpendicular to the dipole moment [127], with no radiation along the dipole axis, explaining why it is the orthogonal direction that is important. The separation between the particles in the y-direction (orthogonal to the applied electric field) of the two-particle basis array is the same as the square array with a one-particle basis, so a similar response would be expected. It might be expected that the SLR could be stronger as there are two particles scattering light in the direction orthogonal to the applied electric field. The neighbouring particle could account for the slight red-shift in the SLR compared to the one-particle basis square array for the parallel electric orientation [33, 35, 38].

The extinction of particle-pair arrays when the incident electric field is perpendicular to the particle-pair axis is now considered. In the measured extinction cross-section per particle pair spectra (see Figure 5.6b), a SLR (at 566 nm, 613 nm, 682 nm and 754 nm) is observed for each different square array. This is surprising as there is an extra particle approximately $\lambda/3$ away adding to the far-field interference condition. Recall from Section 4.3, that the dominant coupling is far-field, therefore particles couple together in the direction perpendicular to the applied electric field. The SLRs for $g = 350$ nm, 450 nm and 500 nm square arrays with a two-particle basis appear similar in spectral shape and strength to the one-particle basis case (compare Figure 5.3 and 5.6b). The largest difference in spectral shape between the one- and two-particle basis square arrays is for $g = 400$ nm (compare green solid line in Figures 5.3 and 5.6b). The shape of the extinction spectra are the most different between the two incident electric field polarizations for the $g = 400$ nm square array with a two-particle basis (compare green solid line in Figures 5.6a and 5.6b).

Comparison is now made between the simple coupled-dipole model (see Figure 5.7) and experimental spectra (see Figure 5.6). The model predicts a SLR at 637 nm for the $g = 350$ nm (blue solid line); 661 nm for $g = 400$ nm (green solid line); 704 nm for $g = 450$ nm (red solid line) and 771 nm for $g = 500$ nm (cyan solid line) when the incident electric field is parallel to the particle-pair axis. These occur at 589 nm, 634 nm, 688 nm and 756 nm respectively in the experiment. The largest difference between

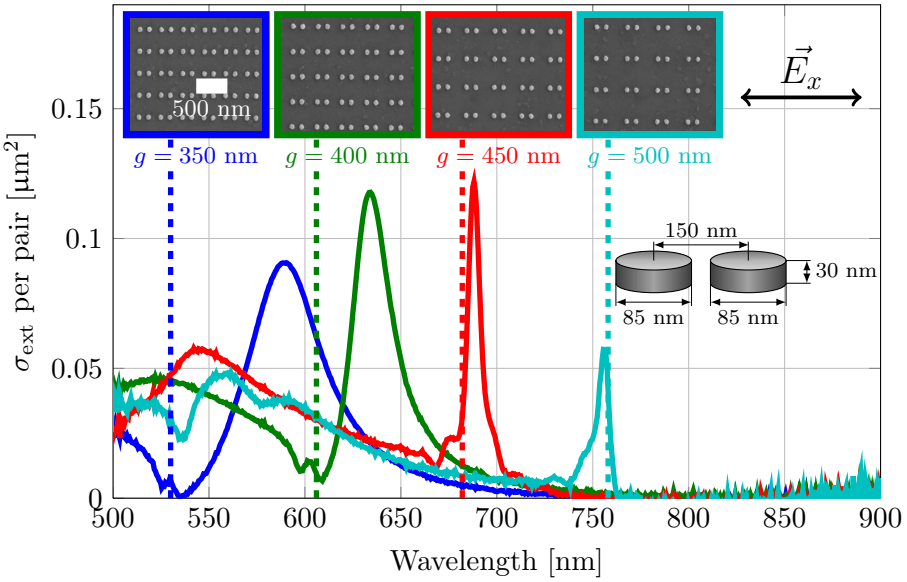

(a) $\vec{E}$ parallel to particle-pair axis.

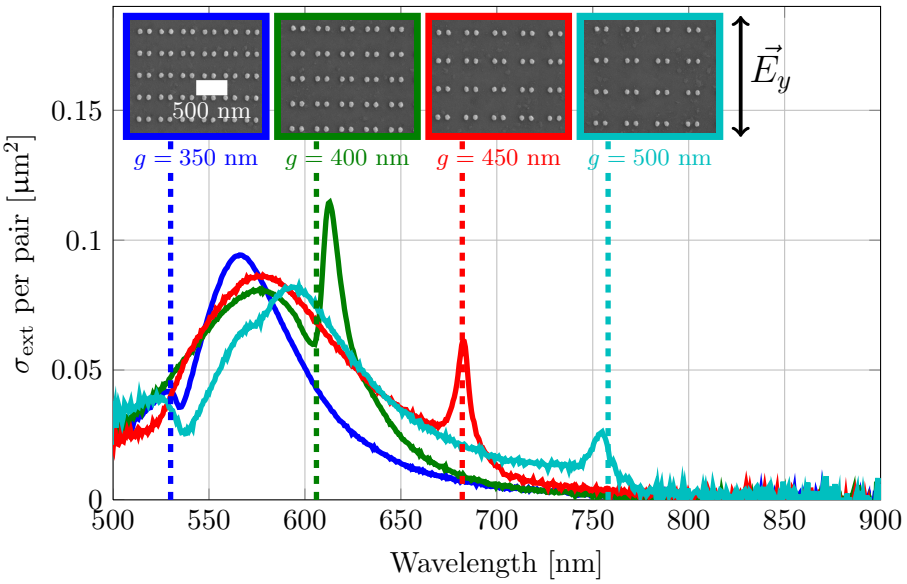

(b) $\vec{E}$ perpendicular to particle-pair axis.

Figure 5.6: Measured extinction cross-section per pair vs. wavelength of four different pitches, g, of two-particle basis square arrays of silver discs ($d = 85$ nm and $h = 30$ nm), see Figure 5.5 for scanning-electron micrographs of arrays. The particle centre-to-centre in the basis was 150 nm. The incident electric field was either (a) parallel to the particle-pair axis or (b) perpendicular. The surrounding environment of the particles was index-matched with $n = 1.515$, and the diffraction edge associated with each different array pitch is illustrated by the corresponding coloured dashed line.

the experiment and model in the spectral positions of the SLRs is for the $g = 350$ nm case (compare blue solid line in Figures 5.6 and 5.7a). Again, this is attributed to validity of the MLWA at large wavevectors (see previous section). The SLR for the $g = 500$ nm (compare cyan solid line in Figures 5.6 and 5.7a) square array is stronger in the model than in the experiment. The weaker SLR in the experiment is due to the variation in particle size attributed to the fabrication process. The strength and width of the SLR is correlated with the distribution in particle size: a greater variation in particle size will broaden and reduce the strength of the SLR [81].

Turning to the perpendicular case, a SLR is seen in the model (see Figure 5.8a) for each different g: 586 nm for $g = 350$ nm (blue solid line); 621 nm for $g = 400$ nm (green solid line); 690 nm for $g = 450$ nm (red solid line) and 763 nm for $g = 500$ nm (cyan solid line). These SLRs occur at 566 nm, 613 nm, 682 nm and 754 nm respectively in the experiment (see Figure 5.6b). The spectral position of the resonance for the $g = 350$ nm array is a much closer match between model and experiment (compare solid blue line in Figures 5.8a and 5.6b) than the parallel polarization (compare blue solid line in Figures 5.7a and 5.6a). These SLRs are seen to occur where the real parts of $1/\alpha$ and $\varepsilon_0 S$ intersect or the closest approach (see Figure 5.8b). The model correctly predicts the relative strength of each SLR associated with each different g. Because the real parts of $1/\alpha$ and $\varepsilon_0 S$ do not intersect for the $g = 450$ nm (black solid line and red solid line in Figure 5.8b) and $g = 500$ nm (black solid line and cyan solid line in Figure 5.8b) square arrays, their associated SLRs are weak compared to the $g = 350$ nm (blue solid line in Figure 5.8a) and $g = 400$ nm (green solid line in Figure 5.8a) arrays. The weakest SLR occurs for the $g = 500$ nm (cyan solid line in Figure 5.8a) array, as the difference between the real parts of $1/\alpha$ and $\varepsilon_0 S$ is greater than for $g = 450$ nm array (compare cyan and red solid lines with black solid line in Figure 5.8b). The strongest SLR is for $g = 400$ nm (green solid line in Figure 5.8a) as the difference between the imaginary parts of $1/\alpha$ and $\varepsilon_0 S$ is smaller than with $g = 350$ nm (compare green and blue dashed lines with black dashed line in Figure 5.8b). Table 5.1 contains experimental and modelled SLR extinction cross-section data for one- and two-particle basis square arrays with different g values. A plot of S-factor data for the two-particle basis arrays when the incident electric field is parallel to the pair axis (x-pol) is not presented, but the data has been added to the table for completeness.

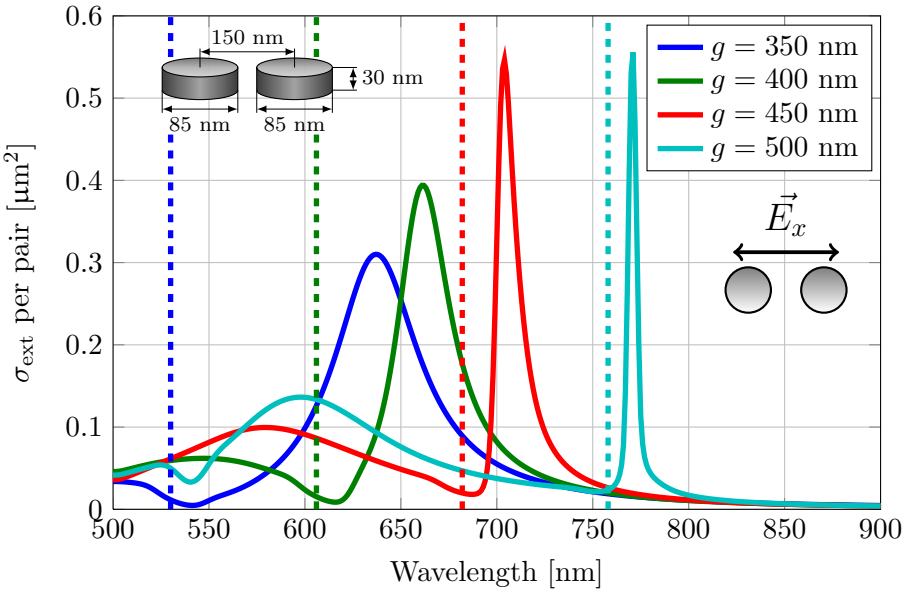

(a) $\vec{E}$ parallel to particle-pair axis.

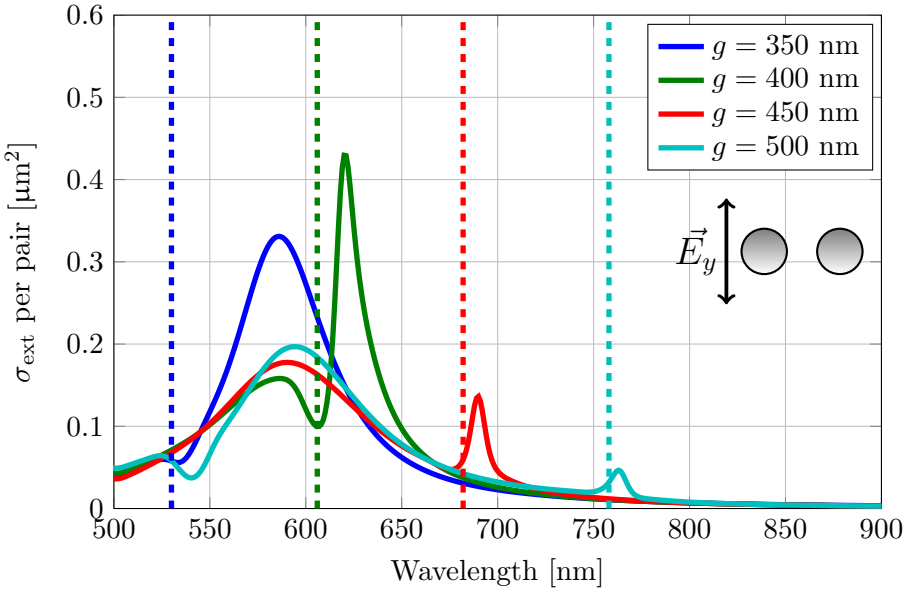

(b) $\vec{E}$ perpendicular to particle-pair axis.

Figure 5.7: Simple coupled-dipole model calculated extinction cross-section per particle pair vs. wavelength of four different pitches, g, of two-particle basis square arrays. The basis consisted of two silver oblate spheroids with $d = 85$ nm and $h = 30$ nm. The electric field was parallel to the particle-pair axis in (a) and perpendicular in (b). The particles in the basis have a centre-to-centre separation of 150 nm, and the particles were modelled in a refractive index of $n = 1.515$. The diffraction edge associated with each different array pitch is illustrated by the corresponding coloured dashed line. 280×280 particle pairs were modelled with each particle given a polarizability calculated using the modified long-wavelength approximation.

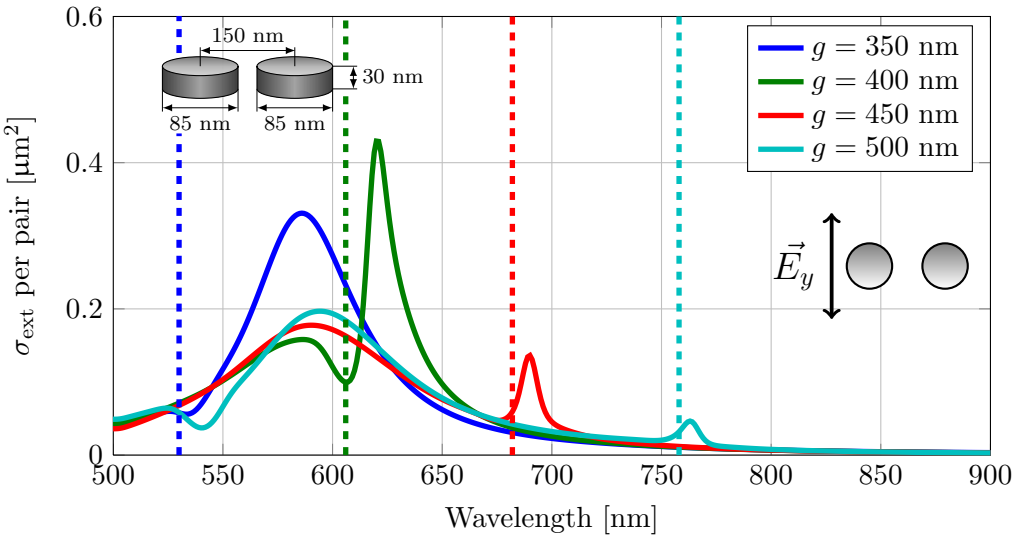

(a) Extinction cross-section per pair.

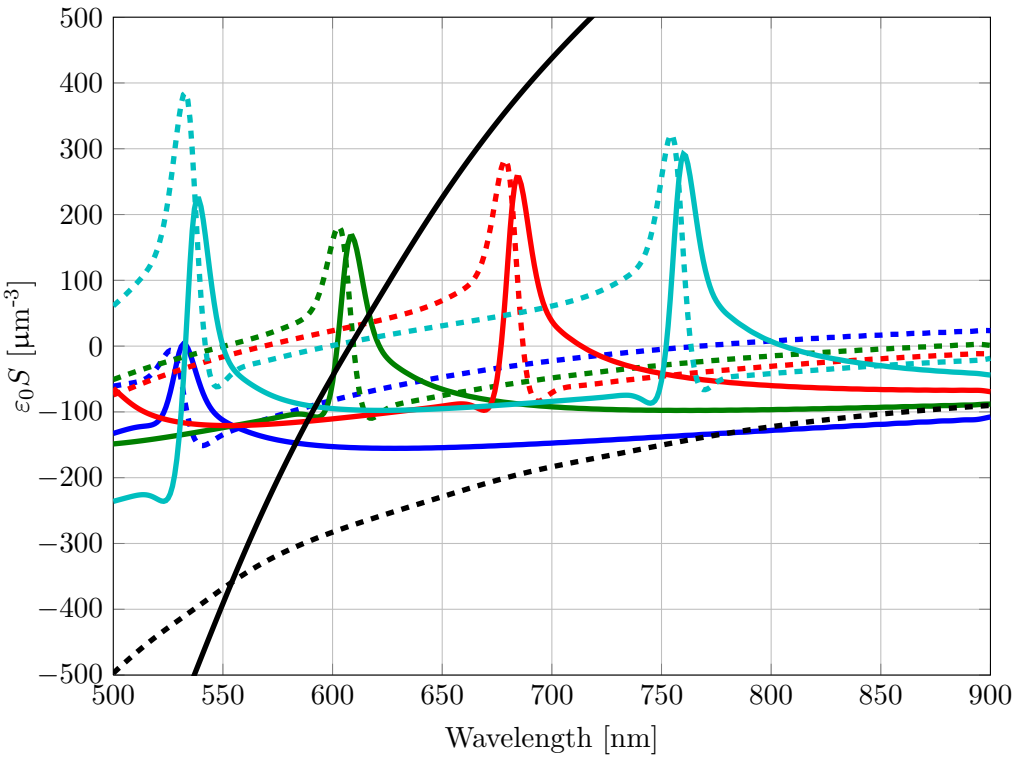

(b) Real (solid lines) and imaginary parts (dashed lines) of $1/\alpha$ (black) and $\varepsilon_0 S$ (see corresponding colour in (a)).

Figure 5.8: (a) simple coupled-dipole model extinction cross-section per pair vs. wavelength and (b) $\varepsilon_0 S$ of four different pitches, g, of two-particle basis square arrays with $g = 350$ nm, 400 nm, 450 nm and 500 nm. The basis comprised of two silver discs with $d = 85$ nm and $h = 30$ nm and a centre-to-centre separation of 150 nm. The real (black solid line) and imaginary part (black dashed line) of the inverse polarizability of a single disc is added to (b). The incident electric field was perpendicular to the particle-pair axis, and the particles were modelled in a homogenous medium with $n = 1.515$. The diffraction edge associated with each different array pitch is illustrated by the corresponding coloured dashed line. An array comprising of 280 × 280 particle pairs was modelled with each particle given a polarizability calculated using the modified long-wavelength approximation.

σ_{ext}		Experiment		Model		
Basis (pol)	g (nm)	λ_{peak} (nm) (Mag. (μm^2))	FWHM (S,M,B)	λ_{peak} (nm)	Re $(1/\alpha = \varepsilon_0 S)$	$\lvert$Im $(1/\alpha - \varepsilon_0 S)\rvert$
One (x-pol)	350	586 (0.05)	Broad	619	Yes	131
	400	620 (0.07)	Medium	642	Yes	111
	450	682 (0.04)	Sharp	695	Yes	57
	500	752 (0.01)	N/A	765	No	89
One (y-pol)	350	581 (0.06)	Broad	619	Yes	131
	400	629 (0.07)	Medium	642	Yes	111
	450	689 (0.05)	Sharp	695	Yes	57
	500	761 (0.01)	N/A	765	No	89
Two (x-pol)	350	589 (0.09)	Broad	637	Yes	187
	400	634 (0.12)	Medium	661	Yes	149
	450	688 (0.12)	Sharp	704	Yes	115
	500	756 (0.06)	Sharp	771	Yes	45
Two (y-pol)	350	566 (0.09)	Broad	586	Yes	206
	400	613 (0.11)	Sharp	620	Yes	100
	450	682 (0.06)	Sharp	690	No	125
	500	754 (0.02)	N/A	763	No	155

Table 5.1: Experimental and S-factor calculated extinction cross-sections for one- and two-particle basis square arrays with the incident electric field either parallel (x-pol) or perpendicular (y-pol) to the pair axis). A plot of the S-factor for the two-particle basis square array when the incident electric field is x-pol is not displayed, but data has been added to the table for completeness.

5.3.1 Retardation between particle pairs

A natural question arises: how does the retardation of the scattered light, between particles in the pair, effect the optical response of the array?

5.3.1.1 Modelling approaches of particle pair

To study this retardation of the scattered electric field between particles in the pair, the optical response of the array was modelled using two different approaches:

1. Two square lattices offset by the centre-to-centre separation, each with a single particle at every lattice point with an associated single particle polarizability.

2. A single square lattice with an effective polarizable unit, which only considers the near-field coupling of the electric field between particles in the pair, at each lattice point.

The difference between approach (1) and (2) is that in (2) only the retardation of the electric field between particle pairs is considered, *not* between particles in the pair. Pinchuk and Schatz [128] provide a derivation of the effective polarizability of two coupled particles and these expressions (Equations 26 and 30 in Ref. [128]) were adopted for the extinction cross-section modelling shown in Figure 5.9a. They consider the local near-field component of the electric field from the induced dipole moment in the neighbouring particle to derive the effective polarizabilities. The equations for the effective polarizability are:

$$\alpha_{\text{par}}^{\text{eff}} = \frac{\alpha_1 + \alpha_2 + \alpha_1\alpha_2/(2\pi l^3)}{1 - 2\alpha_1\alpha_2/(2\pi l^3)^2}, \tag{5.3}$$

and,

$$\alpha_{\text{perp}}^{\text{eff}} = \frac{\alpha_1\alpha_2 - \alpha_1\alpha_2/(2\pi l^3)}{1 - \alpha_1\alpha_2/(4\pi l^3)^2}, \tag{5.4}$$

where l is the centre-to-centre separation of the particles and α_1 and α_2 are the polarizabilities of particle 1 and particle 2 respectively.

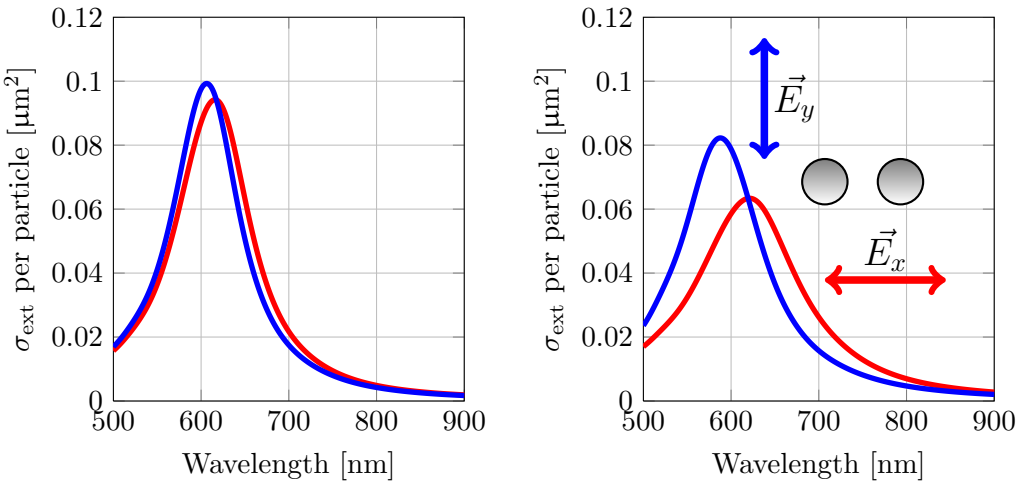

(a) Pinchuk effective polarizability (calculated using Equations 5.3 and 5.4).

(b) Coupled-dipole approximation.

Figure 5.9: (a) Pinchuk effective polarizability and (b) coupled-dipole approximation calculated extinction cross-section per particle of a single particle pair (both particles have $d = 85$ nm, $h = 30$ nm) with a centre-to-centre separation 150 nm. In (a) retardation of the scattered electric field between the particles in the pair was ignored and in (b) it was included. The electric field is in the plane of the particles was oriented either parallel (red solid line) or perpendicular (blue solid line) to the particle-pair axis. Equations 5.3 and 5.4 have been used to calculate the effective polarizability for the calculation in (a).

The calculated extinction cross-section per particle with the incident electric field parallel (red solid line) or perpendicular (blue solid line) to the particle-pair axis of a single pair has been modelled with (a) the Pinchuk effective polarizability and (b) CDA (see Figure 5.9). Equations 5.3 and 5.4 have been used for the effective polarizability, but divided by two - to obtain the extinction cross-section per particle. In this instance, the size of both particles is $d = 85$ nm and $h = 30$ nm with $l = 150$ nm. The diffraction edge for the $g = 400$ nm square array at 606 nm is illustrated with a black dashed line. In Figure 5.9a a single dipolar resonance can be observed in each extinction spectrum. When the electric field is perpendicular to the particle-pair axis, the particle plasmon resonance (at 606 nm) is blue-shifted relative to the single particle case (at 611 nm) and red-shifted when the electric field is parallel to pair, giving a pair plasmon resonance of 616 nm. A description of this near-field coupling for a particle pair is discussed in Section 1.6. The electric field from the neighbouring particle can either increase or decrease the net restoring force acting on the oscillating electrons in the particle, depending on its orientation relative to the internal electric field of the adjacent particle. This red- and blue-shift of the particle plasmon resonance is also observed in the CDA spectra (see Figure 5.9b), but the shift is more pronounced and there is a greater difference in the magnitude of the extinction cross-section between the two polarizations, as retardation of the scattered light between the pair has been included. In the CDA model (see Figure 5.9b), when the incident electric field polarization is pendendicular to the pair (blue solid line), the line-width of the resonance of the pair is reduced relative to the parallel polarization (red solid line), as the collective radiation of the pair is reduced due to interference of the scattered field from each particle.

Figure 5.10a shows $1/\alpha$ and $\varepsilon_0 S$ for approach (1), in this case a $g = 400$ nm square array of silver discs ($d = 85$ nm and $h = 30$ nm). The incident electric field was either parallel to the particle-pair axis (green solid line is $\varepsilon_0 S$ for parallel) or perpendicular (cyan solid line is $\varepsilon_0 S$ for perpendicular). In Figure 5.10b the array has been modelled using approach (2) with the single polarizable unit being a single particle pair with both particles having $d = 85$ nm and $h = 30$ nm with $l = 150$ nm, (single particle pair response shown as black solid line in Figure 5.1). Figure 5.10c displays a comparison of extinction cross-section per particle pair calculated with approach (1) and (2): approach (1) models the array of particles with a single particle polarizability (retardation between the particles in the pair is included) or approach (2) models the array as an array of effective polarizable units (retardation between the particles in the pair has been ignored). From Figure 5.10a it can be seen the S-factor is polarization dependent, attributed to the symmetry of the array, with two different crossing points of the real parts of $1/\alpha$ and $\varepsilon_0 S$ (at 617 nm and 658 nm). Again, these crossing points

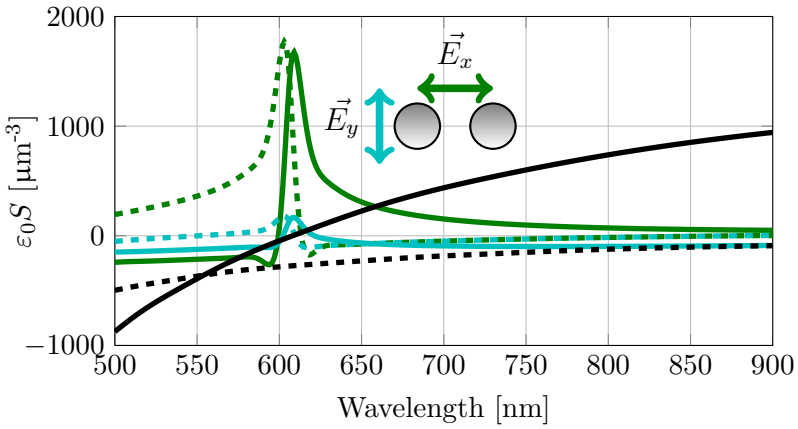

(a) Real (solid lines) and imaginary (dashed lines) parts of $1/\alpha$ (black lines) and $\varepsilon_0 S$ when the two-particle basis was described as two particles, each with their own polarizability, α. The incident electric field was either parallel (green) to the particle-pair axis or perpendicular (cyan).

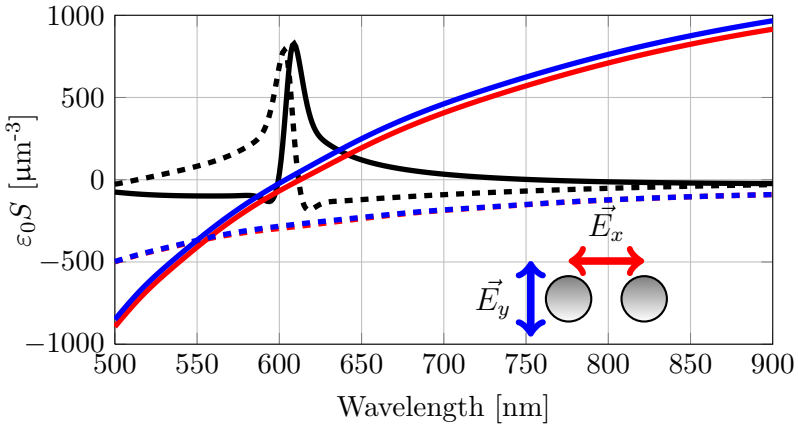

(b) Real (solid lines) and imaginary (dashed lines) parts of $1/\alpha^{\text{eff}}_{\text{par}}$ (red), $1/\alpha^{\text{eff}}_{\text{perp}}$ (blue) and $\varepsilon_0 S$ (black), when the two-particle basis was described with an effective polarizabilty derived by Pinchuk and Schatz (see Equations 5.3 and 5.4).

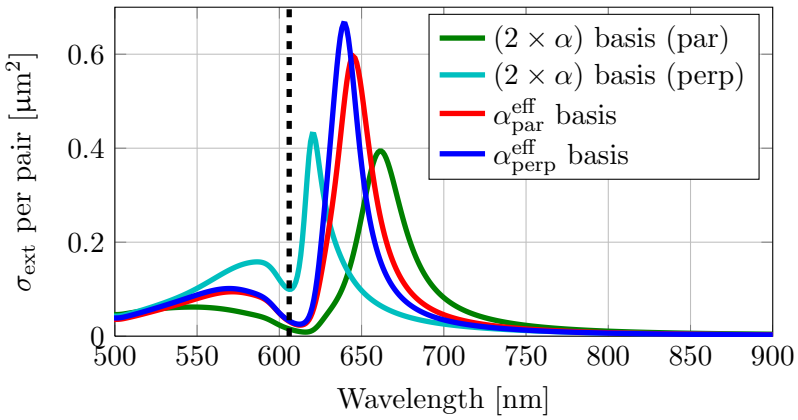

(c) Comparison between the calculated extinction cross-section of a 400 nm pitch square array when modelling the two-particle basis as two particles each with their own polarizability or as a single effective polarizability.

Figure 5.10: Comparison of S-factors and calculated extinction cross-sections of a 400 nm pitch square array with a two-particle basis. In (a) retardation of the scattered electric field between particles in the pair was included and in (b) ignored.

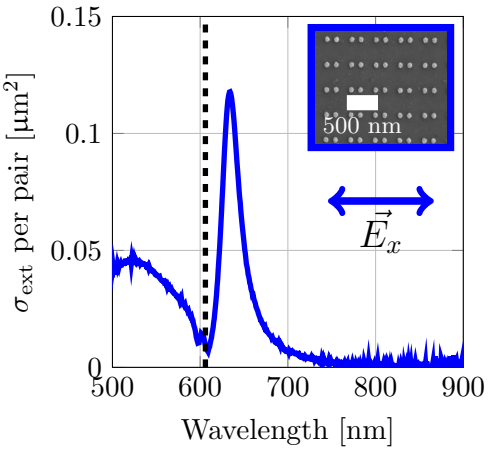

(a) Measured extinction cross-section per pair with the incident $\vec{E}$ field parallel to pair axis.

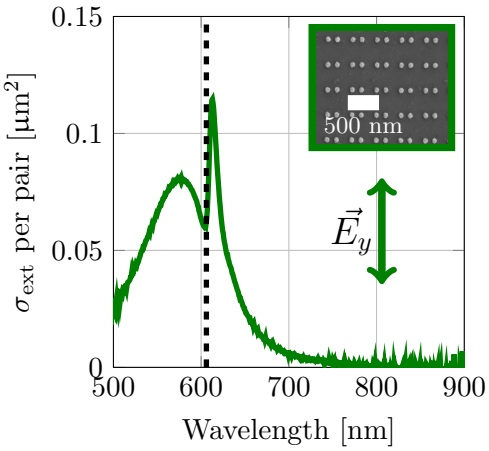

(b) Measured extinction cross-section per pair with the incident $\vec{E}$ field perpendicular to pair axis.

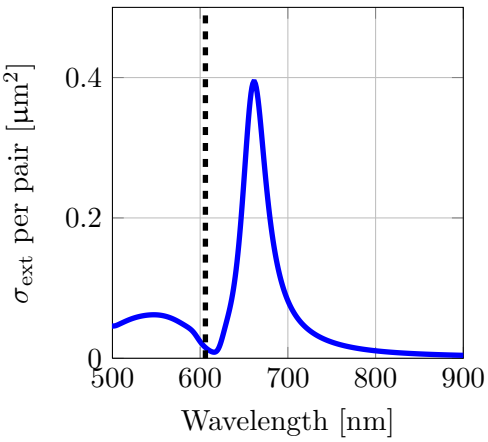

(c) Calculated extinction cross-section per pair with $\vec{E}$ parallel to pair axis. Two-particle basis described as single particles with α_1 and α_2.

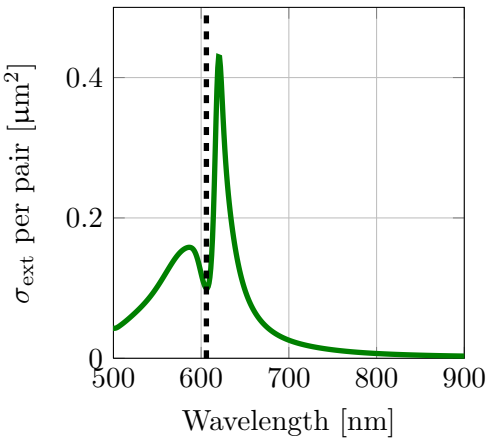

(d) Calculated exticntion cross-section per pair with $\vec{E}$ perpendicular to pair axis. Two-particle basis described as single particles with α_1 and α_2.

Figure 5.11: Comparison between the (a,b) measured and (c,d) calculated extinction cross-section per pair of a 400 nm pitch square array with a two-particle basis. The optical response of the two-particle basis array was described as two particles, each particle with their own polarizability (α_1 and α_2) - hence retardation of the scattered electric field between the particles in the pair was included. Inset top right in (a,b) are scanning-electron micrographs of the arrays. In (a,c) the incident electric field is parallel to the particle-pair axis and in (b,d) perpendicular.

determine the spectral position of the SLRs. In Figure 5.10b the S-factor is polarization independent due to the high symmetry of the square array, but instead there are two polarizabilities (solid red line parallel, solid blue line perpendicular) as the single pair resonance is polarization dependent (see Figure 5.9a). This time the crossings of the real parts of $1/\alpha$ and $\varepsilon_0 S$ occur very near to each other (within 10 nm) meaning that the SLRs for each electric field polarization occur close together. Observation of the calculated extinction spectra in Figure 5.10c show that if the array is modelled using approach (1) there is larger difference in the spectral shape and position of the SLRs (see Figure 5.11a and 5.11b) than modelling the array using approach (2). This is evidence that the distance (approximately $\lambda/3$) between the two particles that make up the pair can not be neglected. Retardation of the scattered light from each particle in the pair is important and must be considered.

Figure 5.11 shows a comparison of the experiment (a,b) and the model (c,d) for the $g = 400$ nm square array with a two-particle basis of silver discs ($d = 85$ nm and $h = 30$ nm). In (a,c) the incident electric field is parallel (solid blue line) to the particle-pair axis and in (b,d) perpendicular (solid green line). By modelling the array using approach (1): an array of single particles each with their own polarizability, which includes retardation of the electric field between the particles in the pair, a greater difference is exhibited in the spectral shape between the two polarizations of the incident electric field, similar to the experiment.

One question remains open: what is the influence of the centre-to-centre separation of the particle pair on the optical response of the array?

5.3.1.2 Extinction measurements on arrays with different particle pair centre-to-centre separations

In this section results from arrays of particle pairs with $l = 160$ nm, 180 nm, 200 nm and 220 nm in a $g = 500$ nm square array are presented. The particles that make up the pair are discs with $d = 115$ nm and $h = 30$ nm (see Figure 5.12 for SEMs). Again, the extinction cross-section per particle pair as a function of wavelength at normal incidence was measured for each one of the different arrays (experimental spectra shown in Figure 5.13). The orientation of the incident electric field is parallel to the particle pair axis in (a) and perpendicular in (b). The diffraction edge is at a wavelength of 758 nm (black dashed line) for all of the arrays in this section. In Figure 5.13a a SLR is observed at 776 nm for $l = 160$ nm; at 770 nm for $l = 180$ nm; at 769 nm for $l = 200$ nm; and at 766 nm for $l = 220$ nm. As l is decreased, the spectral position of the SLR red-shifts and

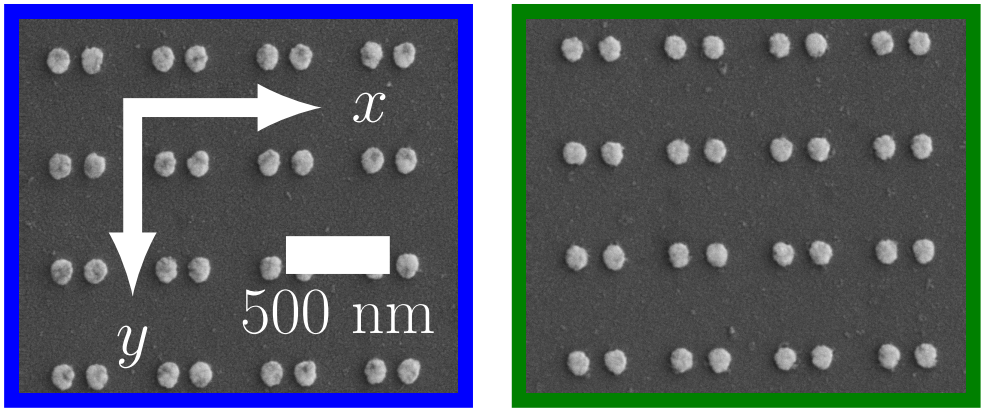

(a) $l = 160$ nm.

(b) $l = 180$ nm.

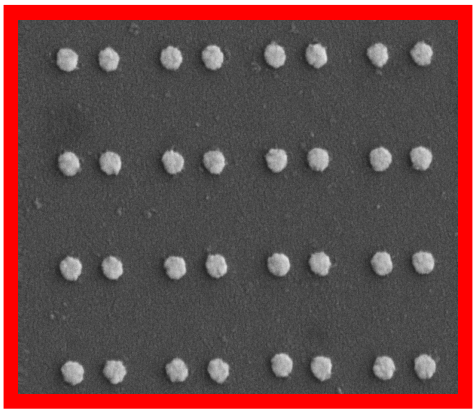

(c) $l = 200$ nm.

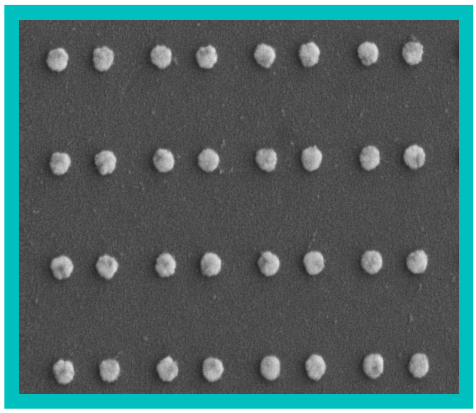

(d) $l = 220$ nm.

Figure 5.12: Scanning-electron micrographs of 500 nm pitch square arrays with a two-particle basis of silver discs ($d = 115$ nm and $h = 30$ nm) with different centre-to-centre separations, l. (a) $l = 160$ nm, (b) $l = 180$ nm, (c) $l = 200$ nm and (d) $l = 220$ nm.

the FWHM increases when the electric field is parallel to the pair axis. This red-shift of the SLR can be explained by considering the shift in resonance position of the single pair response. The electric field from the close neighbouring particle reduces the internal electric field of the other particle in the pair, which reduces the restoring force between the electrons and the positive ionic cores. This near-field coupling is explained in Section 1.6 and is observed in the single pair optical response (red line in Figure 5.9). A different response is obtained when the incident electric field is perpendicular (see Figure 5.13b). SLRs for $l = 160$ nm, 180 nm and 200 nm are observed at 764 nm, 761 nm, 759 nm and approximately 760 nm respectively. The SLR strength decreases with increasing l until at $l = 220$ nm it has nearly vanished.

Figure 5.14 shows the simple coupled-dipole model calculated extinction-cross-section

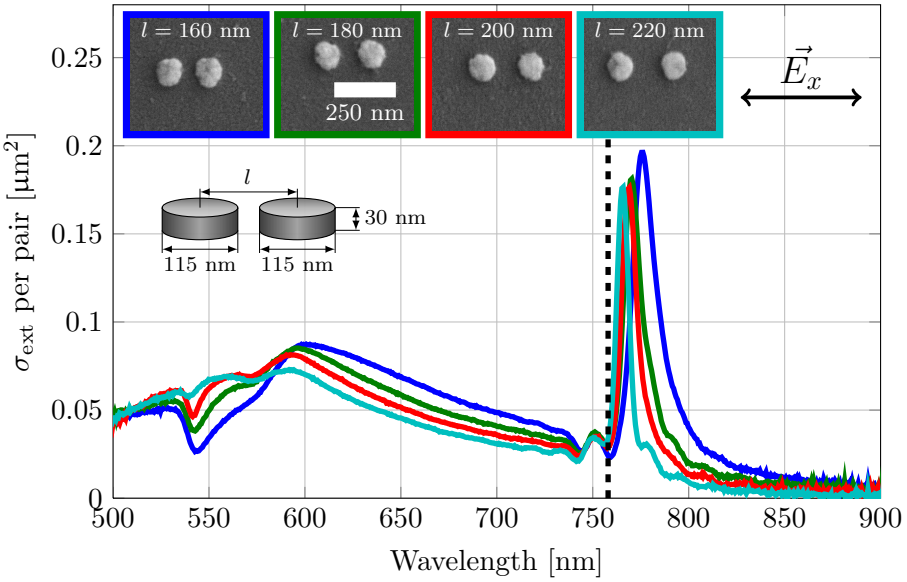

(a) $\vec{E}$ parallel to particle-pair axis.

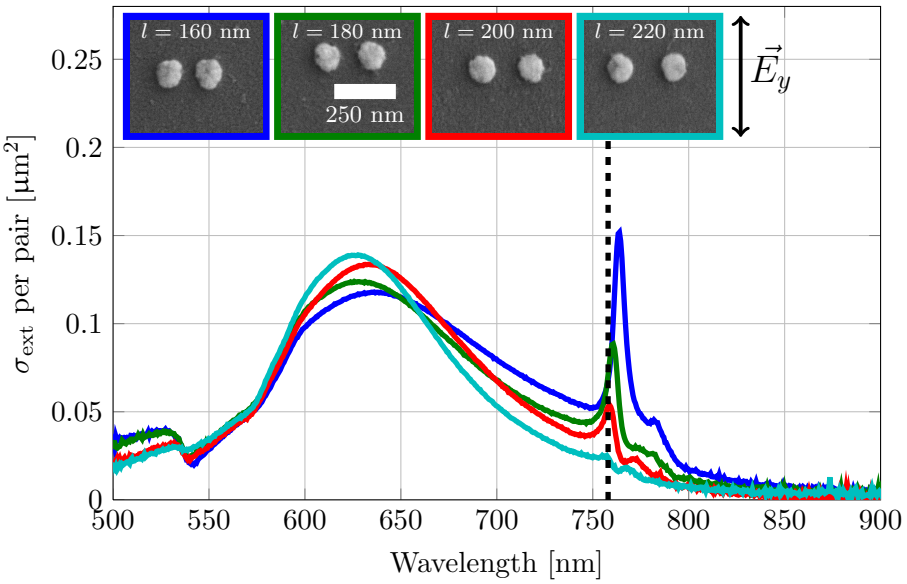

(b) $\vec{E}$ perpendicular to particle-pair axis.

Figure 5.13: Measured extinction cross-section per particle pair vs. wavelength of 500 nm pitch square arrays with a two-particle basis of silver discs ($d = 115$ nm and $h = 30$ nm), see Figure 5.12 for scanning-electron micrographs of the arrays. Extinction spectra are shown for four different centre-to-centre separations, $l = 160$ nm, 180 nm, 200 nm and 220 nm. The incident electric field was (a) parallel or (b) perpendicular to the particle-pair axis. The environment of the particles was index-matched with the substrate with $n = 1.515$ and the diffraction edge is illustrated with a black dashed line.

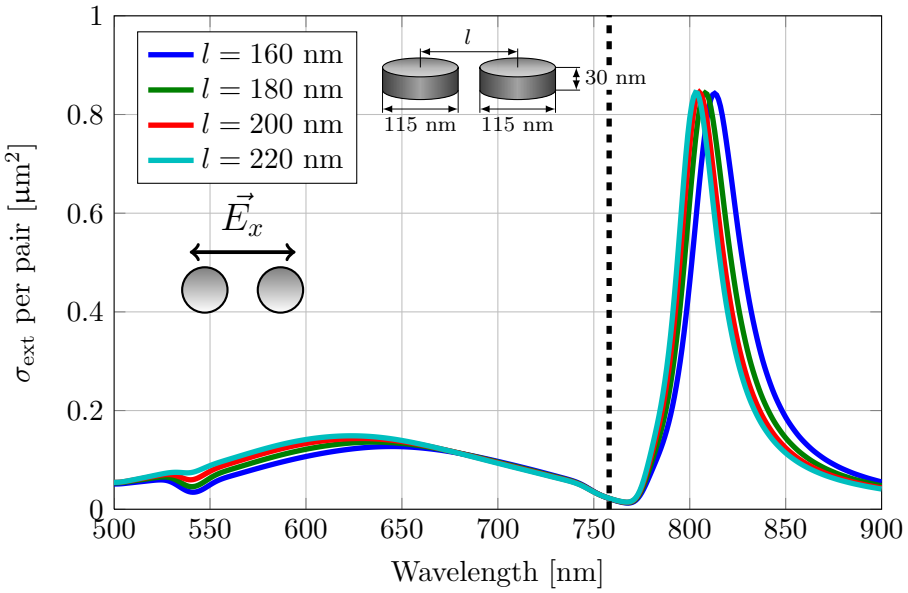

(a) $\vec{E}$ parallel to particle-pair axis.

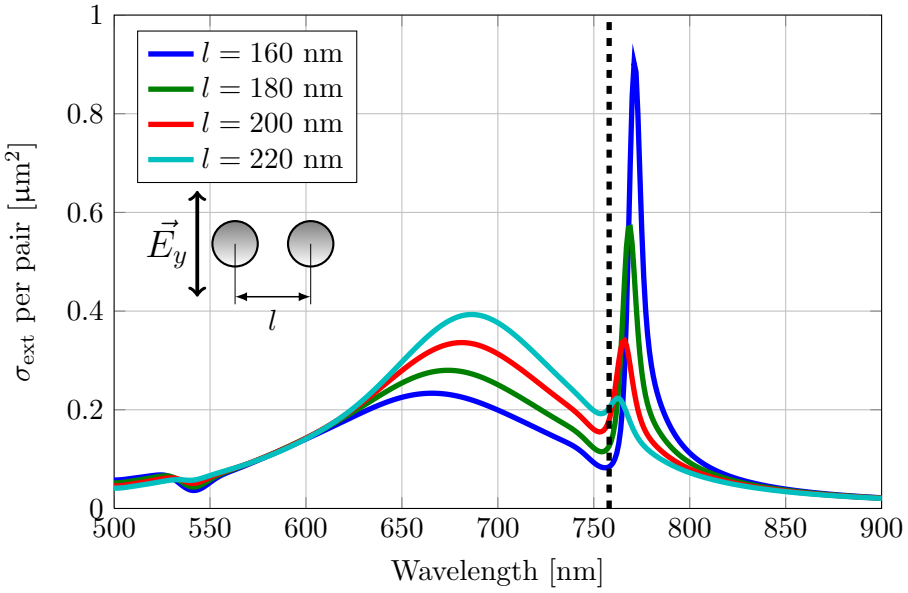

(b) $\vec{E}$ perpendicular to particle-pair axis.

Figure 5.14: Simple-coupled dipole model calculated extinction cross-section per particle pair vs. wavelength of 500 nm pitch square arrays with a two-particle basis of silver discs (d = 115 nm and h = 30 nm). Extinction spectra are shown for four different centre-to-centre separations of l = 160 nm, 180 nm, 200 nm and 220 nm. The incident electric field was (a) parallel to the particle-pair axis or (b) perpendicular. The surrounding environment of the particles had $n = 1.515$. The diffraction edge is illustrated by a black dashed line. An array comprising of 280 × 280 particle pairs was modelled with each particle given a polarizability calculated using the modified long-wavelength approximation.

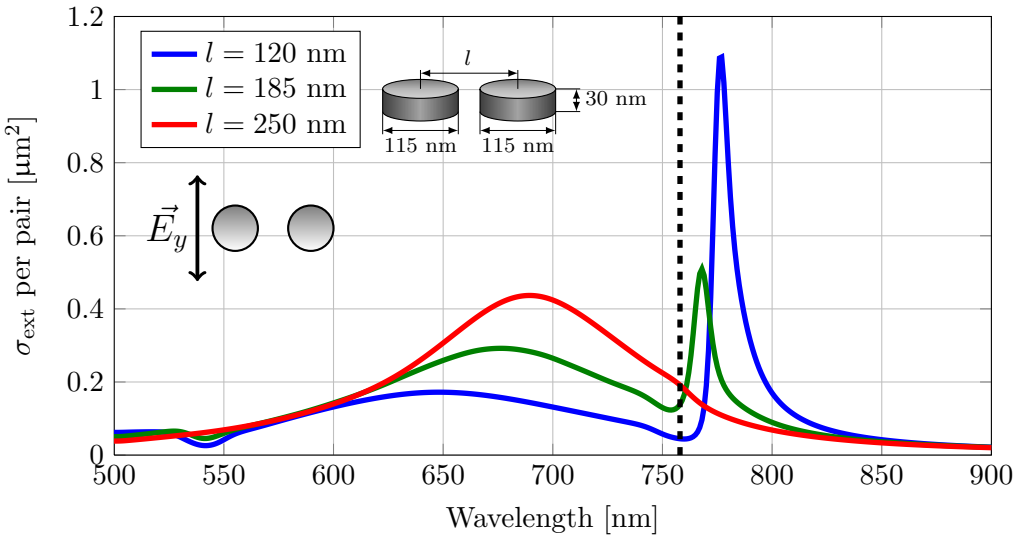

(a) Calculated extinction cross-section per particle pair.

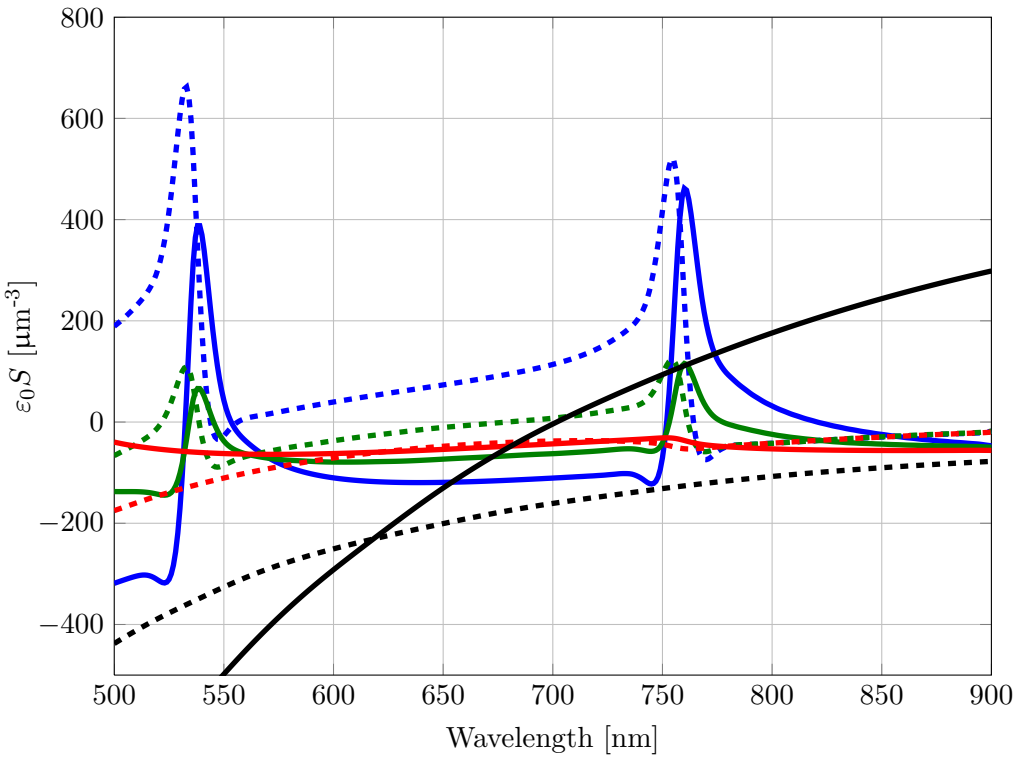

(b) Real (solid lines) and imaginary parts (dashed lines) of $1/\alpha$ (black) and $\varepsilon_0 S$ (see corresponding colour in (a)).

Figure 5.15: Simple coupled-dipole model calculated (a) extinction cross-section per particle pair and (b) $\varepsilon_0 S$ for 500 nm pitch square arrays with a two-particle basis (d = 115 nm and h = 30 nm). The real (black solid line) and imaginary part (black dashed line) of the inverse single particle polarizability is added to (b). Spectra are shown for three different centre-to-centre separations (l = 120 nm, 185 nm and 250 nm) with the incident electric field perpendicular to the particle-pair axis. The surrounding medium of the particles had $n = 1.515$, and the diffraction edge is illustrated with a black dashed line. An array comprising of 280 × 280 particle pairs was modelled with each particle given a polarizability calculated using the modified long-wavelength approximation.

per particle pair of 280 × 280 pairs of oblate spheroids ($d = 115$ nm and $h = 30$) with l of 160 nm, 180 nm, 200 nm and 220 nm. (a) shows the response when the incident electric field is parallel and (b) perpendicular to the particle-pair axis. In the model (see Figure 5.14a), when the electric field is parallel to the pair axis a SLR associated with each different array is seen. These SLRs occur at longer wavelengths (by 30–40 nm) than in the experiment (see Figure 5.13a) and follow the trend of red-shifting as l is decreased. In the model, the extinction cross-section per particle pair at the SLR is a factor of approximately 4 larger, which is attributed to the validity of MLWA for shorter wavelengths (ka is no longer much less than one).

Figure 5.15 shows the calculated (a) extinction cross-section per particle pair and the (b) $1/\alpha$ and $\varepsilon_0 S$ with the electric field perpendicular to the particle pair. These SLRs occur when the real parts of $1/\alpha$ and $\varepsilon_0 S$ intersect or have their closest approach (see Figure 5.15b). The SLRs for $l = 120$ nm and $l = 185$ nm arrays are stronger because the real parts of $1/\alpha$ and the real parts of $\varepsilon_0 S$ intersect, which does not happen with $l = 250$ nm. The $l = 120$ nm is stronger than $l = 185$ nm because the difference between the imaginary parts of $1/\alpha$ and $\varepsilon_0 S$ is smaller than $l = 185$ nm. The SLR with $l = 250$ nm has nearly disappeared because the separation is approximately $\lambda_{\text{res}}/2$ providing almost perfect destructive interference of the light scattered by the nanoparticles.

5.4 Conclusion

One- and two-particle basis square arrays of silver nanoparticles have been successfully fabricated and their optical response (extinction cross-section) modelled using a simple coupled dipole model. It has been shown that the spectral position of SLRs red-shifts with increasing array pitch, along with the diffraction edge, for one- and two-particle basis arrays and these SLRs occur where the real parts of $1/\alpha$ and $\varepsilon_0 S$ intersect or have their closest approach. It has been demonstrated that, when the incident electric field is parallel to the particle-pair axis, the measured extinction cross-section vs. wavelength is similar to that exhibited by the equivalent one-particle basis square array. The perpendicular response of two-particle basis arrays is different from the equivalent one-particle basis arrays for certain pitches of square array (i.e. 400 nm in this instance). The particles couple together in the direction that is orthogonal to the applied electric field, and for the perpendicular polarization, this direction has a particle at approximately $\lambda/3$ away. Two-particle basis square arrays can not be modelled as a single polarizable unit, which ignores retardation of the electric field between the particles in the pair, placed at each lattice point of a single square array. The optical

response of the two-particle basis square arrays were explained due to the differing S-factor. The centre-to-centre separation of the particles is important, and when this is approximately $\lambda_{\text{res}}/2$ the SLR vanishes due to destructive interference. A symmetric two-particle basis can support an anti-symmetric plasmon mode, but this mode can not be coupled to by light at normal incidence, since it has a zero net dipole moment, i.e. it doesn't radiate. However, at normal incidence an asymmetric two-particle basis may support an anti-symmetric mode and this is the content of Chapter 6.

Chapter 6

Asymmetric two-particle basis square arrays

6.1 Introduction

In Chapter 5 it was seen that square arrays with a symmetric two-particle basis, i.e. two identical particles, can support sharp surface lattice resonances (SLRs). It was discovered that, when the incident electric field was parallel to the particle-pair axis, a similar response was obtained to the one-particle basis square arrays; and when the electric field was perpendicular, the response was determined by the pitch of the array and the centre-to-centre separation of the particle in the basis. In this chapter, square arrays with a two-particle-asymmetric basis were fabricated by electron-beam lithography (EBL). An asymmetric two-particle basis, formed for example from two particles of different size, can support both symmetric and anti-symmetric plasmon modes, where the later can have a non-zero net dipole moment when illuminated by light at normal incidence. The electric field polarization dependence of the asymmetric-basis arrays was probed by normal-incidence extinction measurements as a function of wavelength. The simple coupled-dipole model (i.e the S-factor model) introduced in Section 3.2.2 was modified for an asymmetric basis, and the result was compared to experimental spectra.

6.2 Modifications to analytical coupled-dipole model

This section begins by discussing the modifications made to the simple coupled-dipole model to allow the calculation of extinction spectra for an asymmetric two-particle basis. Since the particles in an asymmetric particle pair have different diameters, and hence different polarizabilities, the previously used coupled dipole model (see Section 3.2.2) can not be used. This is because in the simple coupled-dipole model only one polarizability could be specified.

To extend this approach, firstly, the dipole moment of particle type 1, $\vec{p_1}$ is related to the local electric field $\vec{E_1}$ at the position of particle type 1 by its polarizability, α_1, with the following relation,

$$\vec{p_1} = \varepsilon_0 \alpha_1 \vec{E_1}, \tag{6.1}$$

and similarly for particle type 2,

$$\vec{p_2} = \varepsilon_0 \alpha_2 \vec{E_2}, \tag{6.2}$$

where ε_0 is the permittivity of free space. The local electric field at the position of each particle type 1 is a combination of the incident electric field, $\vec{E_0}$, and the electric field from particle type 1 and particle type 2,

$$\vec{E_1} = \vec{E_0} + S\vec{p_1} + S'\vec{p_2}, \tag{6.3}$$

similarly for particle type 2,

$$\vec{E_2} = \vec{E_0} + S'\vec{p_1} + S\vec{p_2}, \tag{6.4}$$

where S is given by,

$$S = \frac{1}{4\pi\varepsilon_0} \sum_{j=2}^{m} \exp\left(ikr_j\right) \left[\frac{(1 - ikr_j)(3\cos^2\theta_j - 1)}{r_j^3} + \frac{k^2 \sin^2\theta_j}{r_j} \right], \tag{6.5}$$

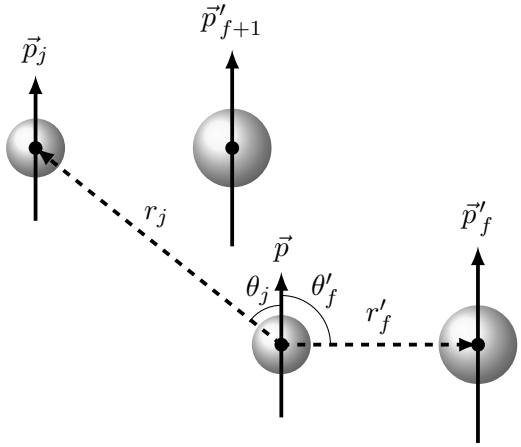

Figure 6.1: Diagram indicating r_j and θ_j that are used to calculate S, which is the contribution of the scattered electric fields from the same particle type in the pair and r'_f and θ'_f that are used to calculate S', which is the contribution of the scattered electric fields from the different particle type in the pair.

where r_j is the distance from the central particle in the array to particle j (same particle type) in a neighbouring pair, m is the number of particle pairs in the array and θ_j is the angle between $\vec{r}_j$ and the dipole moment of particle j. S' is given by,

$$S' = \frac{1}{4\pi\varepsilon_0}\sum_{f=1}^{m}\exp\left(ikr'_f\right)\left[\frac{(1-ikr'_f)(3\cos^2\theta'_f-1)}{r'^3_f}+\frac{k^2\sin^2\theta'_f}{r'_f}\right], \tag{6.6}$$

where r'_f is the distance from the central particle to particle f (different particle type) and θ'_f is the angle between $\vec{r}'_f$ and the dipole moment of particle f (see Figure 6.1). S is the contribution of the scattered electric field from all same particle types in the pair and S' is from all the different particle types. Because one particle in the pair has to be chosen as the central particle in the array, the sum for S starts at $j = 2$, (where $j = 1$ is the central particle). By substitution of Equations 6.1 and 6.2 into Equations 6.3 and 6.4 and rearrangement, the effective dipole moments of particle type 1 and particle type 2 are found to be,

$$p_1 = \varepsilon_0\frac{\alpha_1(1-\alpha_2\varepsilon_0 S+\alpha_2\varepsilon_0 S')}{(1-\alpha_1\varepsilon_0 S)(1-\alpha_2\varepsilon_0 S)-\alpha_1\alpha_2\varepsilon_0^2 S'^2}E_0, \tag{6.7}$$

and,

$$p_2 = \varepsilon_0 \frac{\alpha_2(1 - \alpha_1\varepsilon_0 S + \alpha_1\varepsilon_0 S')}{(1 - \alpha_1\varepsilon_0 S)(1 - \alpha_2\varepsilon_0 S) - \alpha_1\alpha_2\varepsilon_0^2 S'^2} E_0. \tag{6.8}$$

The modified polarizabilities of particle type 1 and 2, using $p = \varepsilon_0 \alpha E_0$, are given by,

$$\alpha_1^* = \frac{\alpha_1(1 - \alpha_2\varepsilon_0 S + \alpha_2\varepsilon_0 S')}{(1 - \alpha_1\varepsilon_0 S)(1 - \alpha_2\varepsilon_0 S) - \alpha_1\alpha_2\varepsilon_0^2 S'^2} \tag{6.9}$$

and,

$$\alpha_2^* = \frac{\alpha_2(1 - \alpha_1\varepsilon_0 S + \alpha_1\varepsilon_0 S')}{(1 - \alpha_1\varepsilon_0 S)(1 - \alpha_2\varepsilon_0 S) - \alpha_1\alpha_2\varepsilon_0^2 S'^2}. \tag{6.10}$$

The cross-sections are calculated from inserting Equation 6.9 and Equation 6.10 into Equation 1.27 and then the cross-section of particle type 1 and 2 are added to obtain the total extinction cross-section of the pair [33]. The modified long-wavelength approximation has been used for the single particle polarizability for the S-factor calculations in this chapter. In each case, the particles (400 × 400 pairs) have been approximated as oblate spheroids embedded in a refractive index of $n = 1.515$. The measured transmission was converted to the extinction cross-section per pair using Equation 3.24.

6.3 Extinction measurements on arrays with an asymmetric basis

This section begins by investigating the polarization dependence as a function of wavelength of square arrays with an asymmetric particle pair basis of silver discs ($d_1 = 85$ nm and $d_2 = 115$ nm). The particle pairs have a centre-to-centre separation of 150 nm and both have a height of 30 nm. The calculated extinction cross-section of single discs ($d = 85$ nm and $d = 115$ nm) that make up the asymmetric basis are shown in Figure 6.2a. The coupled-dipole model calculated extinction cross-section of a single asymmetric silver particle pair with $d_1 = 85$ nm and $d_2 = 115$ nm, both with a height of 30 nm and a 150 nm centre-centre separation is shown in Figure 6.2b. The diffraction edges relating to the four different pitches, g, of square array that will be discussed in this chapter are illustrated by dashed lines: $g = 350$ nm (blue), $g = 400$ nm (green),

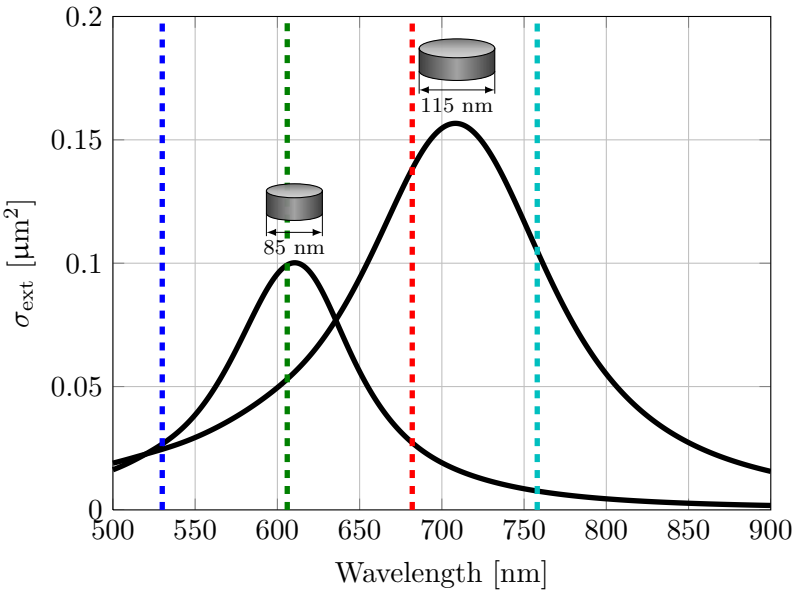

(a) Single particle response.

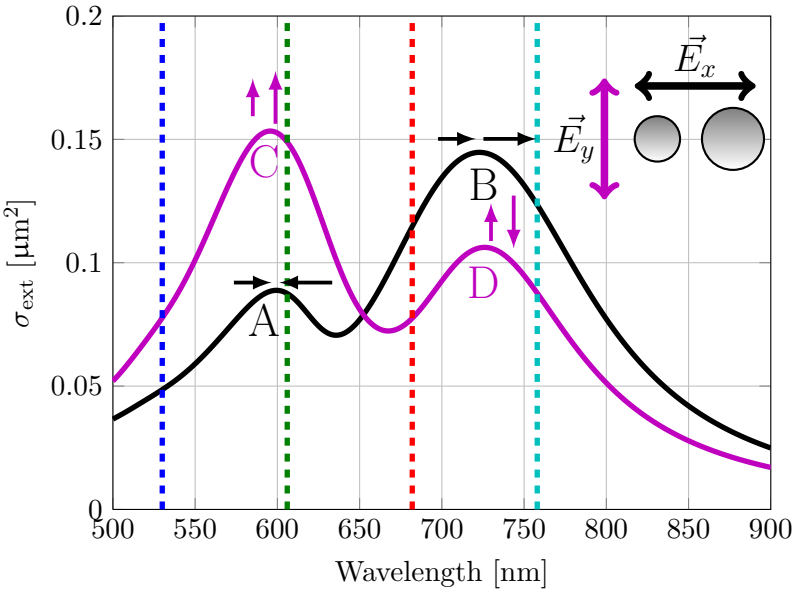

(b) Single pair response.

Figure 6.2: (a) Modified long-wavelength approximation calculated extinction cross-section of single particles (d = 85 nm and d = 115 nm, both with height of 30 nm) and (b) coupled-dipole approximation calculated extinction cross-section of a single asymmetric particle pair (d_1 = 85 nm and d_2 = 115 nm, both with 30 nm height). In (a) the incident electric field was at normal incidence and was linearly-polarized in the plane of the particles and in (b) the incident electric field was either parallel to particle-pair axis or perpendicular. The surrounding medium has n = 1.515. The diffraction edges for the four different pitches of square array considered in this chapter are illustrated by dashed lines of the corresponding colour: 350 nm (blue), 400 nm (green), 450 nm (red) and 500 nm (cyan)

$g = 450$ nm (red) and $g = 500$ nm (cyan). In the extinction cross-section of the single discs (see Figure 6.2a), a single resonance is seen in each extinction spectrum with the particle plasmon resonance of the larger disc occurring at a longer wavelength than that of the smaller disc.

The most noticeable difference between the single particle optical response and the asymmetric pair is that the asymmetric pair exhibits two resonances for each polarization of the incident electric field instead of one (compare Figures 6.2a and 6.2b). The relative strength of the resonances also change when the polarization of the incident electric field is changed: resonance B is stronger than resonance A when the incident electric field polarization is parallel and resonance C is stronger than resonance D for perpendicular. The resonances at B and C are stronger than at A and D because B and C are symmetric modes, where the dipole moments of the particles are parallel. The resonances at A and D are anti-symmetric modes, so the dipole moments of each particle are anti-parallel resulting in a smaller net dipole moment. The smaller net dipole moment results in reduced scattering and this is observed as the reduced extinction cross-section.

It has been observed in Chapters 3 and 4 that when a single particle, with one resonance, is placed in a periodic structure that a single SLR is observed. A single SLR has also been observed in Chapter 5 with the symmetric basis, but with a polarization dependence attributed to the polarization sensitivity of the basis. Here the asymmetric basis not only has a polarization dependence, but possesses two resonances for each incident electric field polarization. It might be expected that there may be two SLRs observed for each electric field polarization. The line-width of an SLR associated with the anti-symmetric mode may have a smaller line-width than the symmetric mode, because of its smaller dipole moment, meaning it will radiate less.

Shown in Figure 6.3 are scanning electron micrographs (SEMs) of square arrays with $g = 350$ nm, 400 nm, 450 nm and 500 nm, where g is the array pitch. The arrays comprise of a basis of asymmetric silver discs with a 150 nm centre-to-centre separation and 30 nm height. Particle 1 in the basis has a diameter of $d_1 = 85$ nm (left) and particle 2 $d_2 = 115$ nm (right). Presented in Figure 6.4 are the normal-incidence extinction spectra of the arrays illustrated in the SEMs in Figure 6.3. The incident linearly-polarized electric field was either (a) parallel to the pair axis or (b) perpendicular. As with all of the previous measurements, the environment of the array was index matched ($n = 1.515$) with the substrate to provide a homogeneous medium for the particles. The diffraction edge associated with g of each different square array is illustrated with a dashed line of the corresponding colour: 530 nm (blue), 606 nm

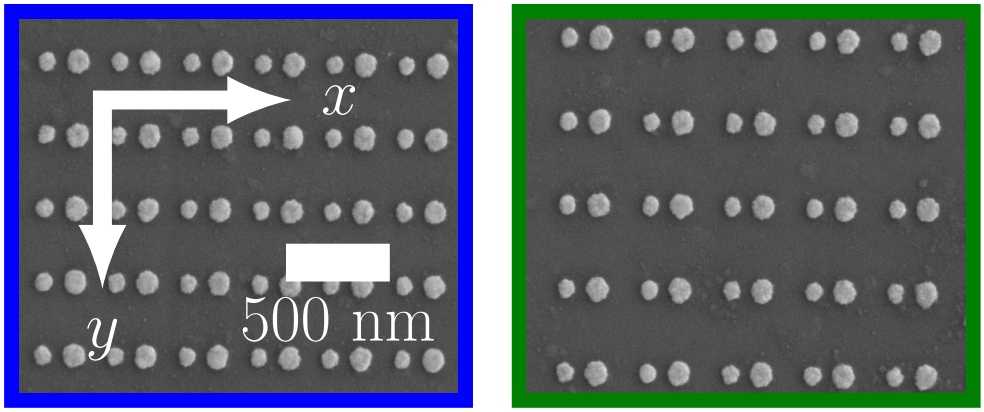

(a) $g = 350$ nm. **(b)** $g = 400$ nm.

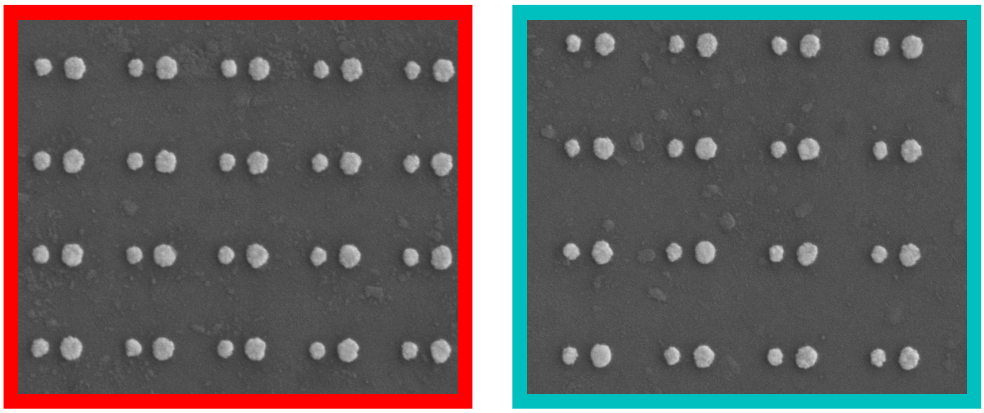

(c) $g = 450$ nm. **(d)** $g = 500$ nm.

Figure 6.3: Scanning-electron micrographs of different pitches, g, of square array with an asymmetric-two-particle basis: (a) $g = 350$ nm, (b) $g = 400$ nm, (c) $g = 450$ nm and (d) $g = 500$ nm. The centre-to-centre separation of the particle pair was 150 nm. The dimensions of particle 1 (left) are $d_1 = 85$ nm, $h_1 = 30$ and the dimensions of particle 2 (right) are $d_2 = 115$ nm, $h_2 = 30$ nm (right).

(green), 682 nm (red) and 758 nm (cyan). The simple coupled-dipole model of the extinction cross-section of the arrays shown in Figure 6.3 are presented in Figure 6.5.

Turning to the measurements (see Figure 6.4a), when the orientation of the incident electric field is parallel to the particle-pair axis, a single strong SLR (at 649 nm (blue solid line), 684 nm (green solid line), 712 nm (red solid line) and 766 nm (cyan solid line)) is observed for each different value of g. As g is increased, the SLR sharpens and increases in strength in agreement with the model (see Figure 6.5a). It is noted that a single strong SLR is displayed for each different value of g, as with the square array of single particles (see Figure 5.3) and the square array of symmetric particle pairs (see Figure 5.6a). In the model (see Figure 6.5a), a strong SLR is also seen for

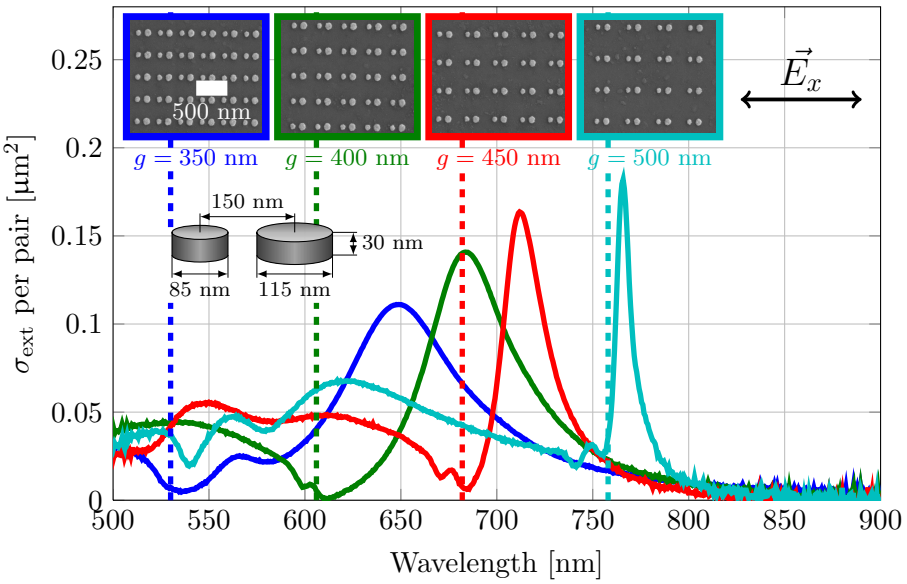

(a) $\vec{E}$ parallel to pair axis.

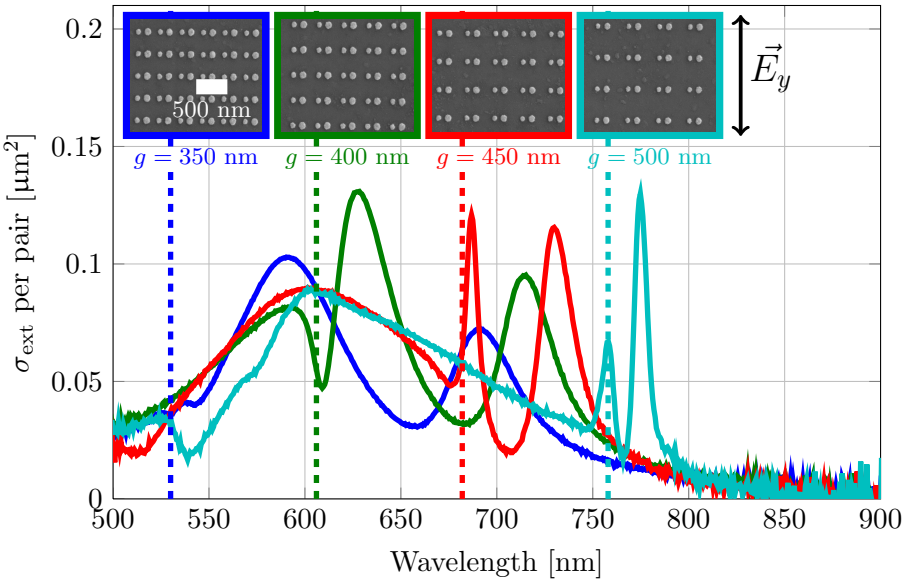

(b) $\vec{E}$ perpendicular to pair axis.

Figure 6.4: Measured extinction cross-section per pair vs. wavelength of different pitches, g, of square arrays with asymmetric-two-particle basis with a 150 nm centre-to-centre separation, see Figure 6.3 for scanning-electron micrographs of the arrays. The dimensions of particle 1 were $d_1 = 85$ nm, $h_1 = 30$ nm and the dimensions of particle 2 were $d_2 = 115$ nm, $h_2 = 30$ nm. The incident electric field was (a) parallel to the pair axis or (b) perpendicular. The environment of the particles was index-matched with the substrate using $n = 1.515$ oil. The diffraction edge associated with each different pitch is illustrated with a dashed line in the corresponding colour.

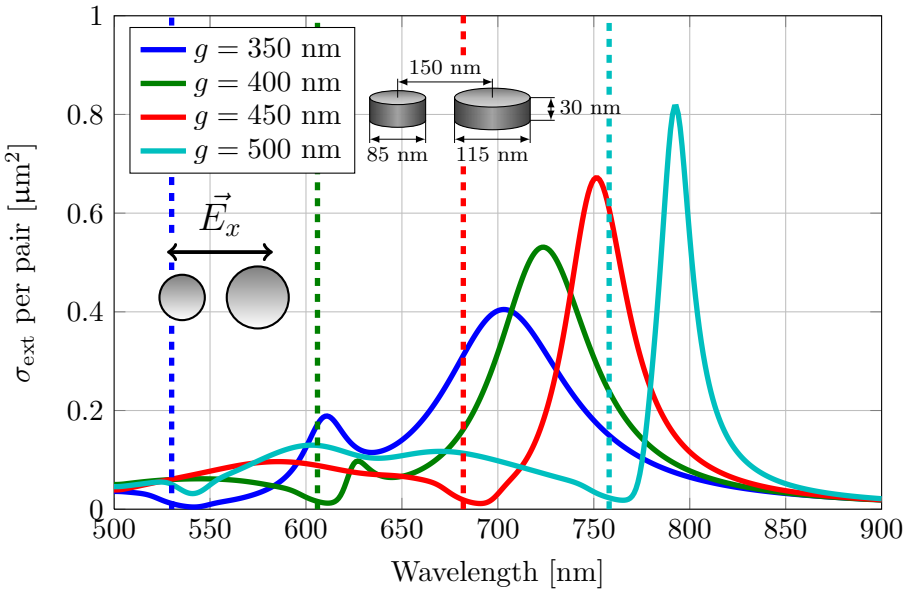

(a) $\vec{E}$ parallel to pair axis.

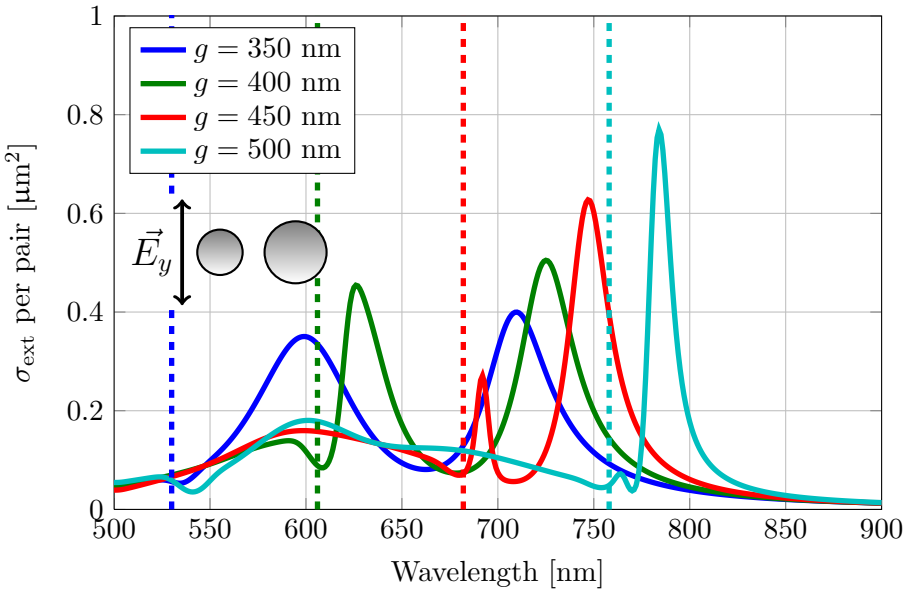

(b) $\vec{E}$ perpendicular to pair axis.

Figure 6.5: Simple coupled-dipole model calculated extinction cross-section per pair vs. wavelength for different pitch, g square arrays with a two-particle asymmetric basis. The particles are silver discs ($d_1 = 85$ nm, $h_1 = 30$ nm and $d_2 = 115$ nm, $h_2 = 30$ nm) with a 150 nm centre-to-centre separation. The incident electric field was (a) parallel to the pair axis or (b) perpendicular. 160000 particle pairs were modelled in a homogenous medium with $n = 1.515$. The diffraction edge associated with each different pitch is illustrated with a dashed line in the corresponding colour.

each different g, but at somewhat longer wavelengths than in the experiment (largest discrepancy approximately 50 nm for $g = 350$ nm (compare blue solid lines in Figures 6.5a and 6.4a). There is good agreement between the model and the experiment in the shape of the spectra across the spectral range, but, as before, the model greatly overestimates the magnitude of the extinction cross-section per particle pair.

Considering the electric field perpendicular to the particle-pair axis, a somewhat different extinction spectrum is measured (see Figure 6.4b). Noticeably, there are two strong SLRs associated with each different value of g instead of one: at 590 nm and 691 nm for $g = 350$ nm; 628 nm and 715 nm for $g = 400$ nm, 687 nm and 730 nm for $g = 450$ nm and 758 nm and 775 nm for $g = 500$ nm. In the model (see Figure 6.5b), as the pitch is increased, both SLRs move to longer wavelengths and move closer together. In the experiment (see Figure 6.4b), the relative strengths of the two SLRs also changes as g is increased: for $g = 350$ nm (blue solid line) and $g = 400$ nm (green solid line) the shorter wavelength SLR is stronger; for $g = 450$ nm (red solid line) the SLRs are comparable in strength and for $g = 500$ nm (cyan solid line), the longer wavelength SLR is stronger. The modelled extinction spectra (see Figure 6.5b) also displays the trend of the shorter wavelength SLR increasing in strength as g is increased, but incorrectly predict the relative strengths for $g = 350$ nm, 400 nm and 450 nm. Compared to the parallel case (compare Figures 6.4a and 6.5a), there is better agreement in the spectral positions of the SLRs and good overall agreement.

In order to understand the nature of these SLR modes, a $g = 350$ nm square array with an asymmetric basis was modelled using finite element modelling (FEM) and compared to experimental spectra (see Figure 6.6). The instantaneous electric field is calculated in a plane that intersects the centre of both particles (i.e. at $h/2$) in the particle pair. In (a,c) the incident electric field is parallel to the particle-pair axis and in (b,d) perpendicular. The spatial distribution of the electric fields at spectral positions A and B in Figure 6.6c and C and D in Figure 6.6d are illustrated in Figure 6.7. By looking at when the electric field is parallel to the particle-pair axis, two SLRs can be seen at positions A and B in the FEM model (see Figure 6.6c) as with the coupled-dipole model (see blue solid line in Figure 6.5a). The SLR at position A in Figure 6.6c is a combination of both symmetric (see Figure 6.7a) and anti-symmetric (see Figure 6.7b) depending at which point in phase, ϕ, the incident electric field is. (Symmetric is when both of the dipole moments are parallel and anti-symmetric when they are anti-parallel). The SLR at position B in Figure 6.6c is symmetric (see Figure 6.7c).

In the model, when the incident electric field orientation is perpendicular to the particle-

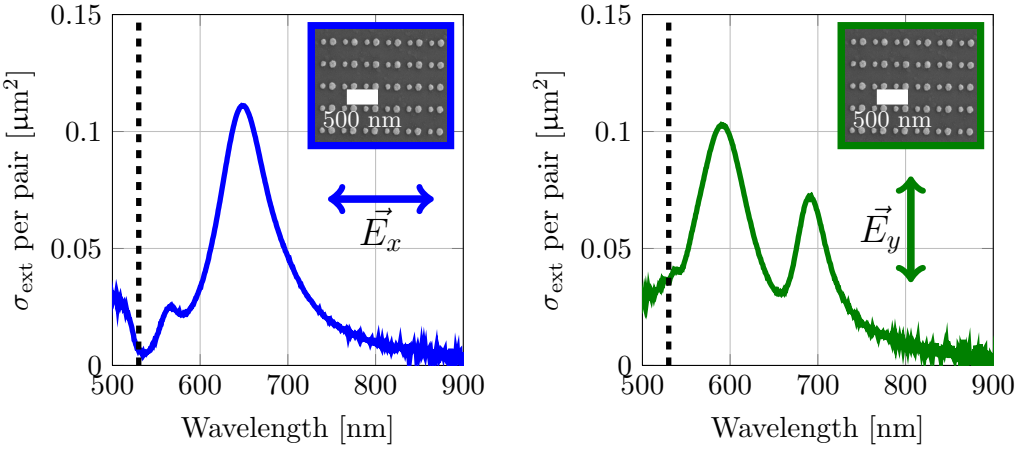

(a) $\vec{E}$ parallel to pair axis (exp).

(b) $\vec{E}$ perpendicular to pair axis (exp).

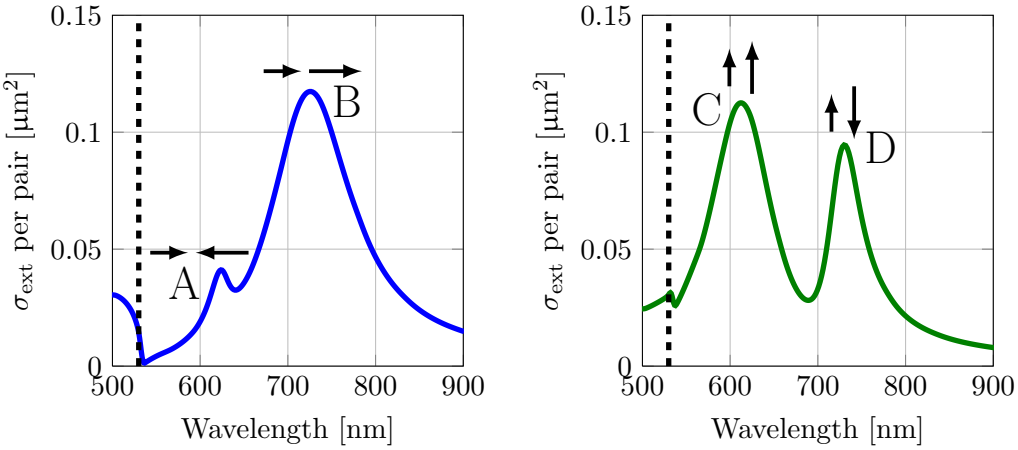

(c) $\vec{E}$ parallel to pair axis (model).

(d) $\vec{E}$ perpendicular to pair axis (model).

Figure 6.6: (a,b) measured and (c,d) finite-element model calculated extinction cross-section per particle pair vs. wavelength of a 350 nm pitch square array with an asymmetric two-particle basis ($d_1 = 85$ nm and $d_2 = 115$ nm), see Figure 6.3a for SEM of array. The particles have a centre-to-centre separation of 150 nm and both have a height of 30 nm. In (a,c) the incident electric field is parallel to the particle-pair axis and in (b) perpendicular. Inset top right in (a,b) are scanning-electron micrographs of the array.

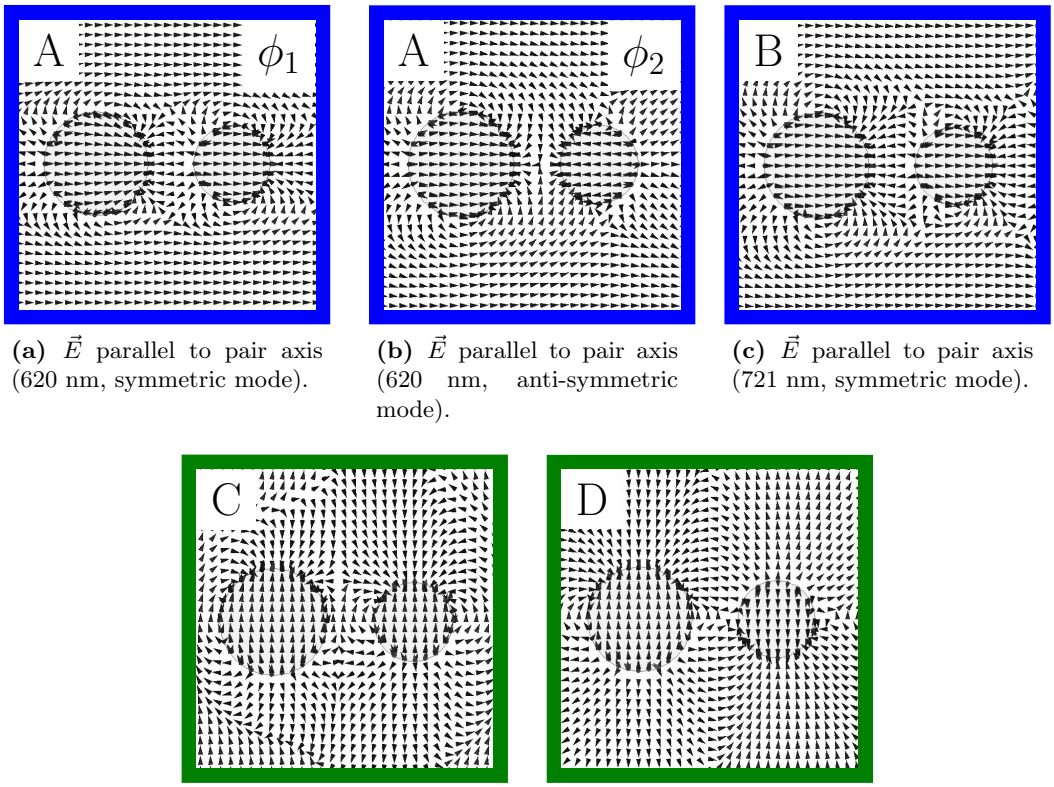

(a) $\vec{E}$ parallel to pair axis (620 nm, symmetric mode).

(b) $\vec{E}$ parallel to pair axis (620 nm, anti-symmetric mode).

(c) $\vec{E}$ parallel to pair axis (721 nm, symmetric mode).

(d) $\vec{E}$ perpendicular to pair axis (610 nm, symmetric mode).

(e) $\vec{E}$ parpendicular to pair axis (725 nm, anti-symmetric mode).

Figure 6.7: Spatial distribution of electric fields for a 350 nm pitch square array with an asymmetric two-particle basis of silver discs (d_1 = 85 nm and d_2 = 115 nm), see Figure 6.3a. The instantaneous electric field was calculated in a plane intersecting the centres of the two particles. In (a,b) the field distribution was calculated at a wavelength of 620 nm, (c) 721 nm, (d) 610 nm and (e) 725 nm. The electric field orientation was parallel to the particle-pair axis in (a-c) and perpendicular in (d,e). The letter inset top left in each figure corresponds to spectral positions in Figure 6.6c and Figure 6.6d.

pair axis, two SLRs can be observed at positions C and D in Figure 6.6d, as with the experiment (see green solid line in Figure 6.6b). The spectral positions of the SLRs from the coupled-dipole model (blue solid line in Figure 6.5b) are a closer match to the experiment than FEM, but again the coupled-dipole model greatly overestimates the magnitude of the extinction cross-section per particle. From the electric field distributions in Figures 6.7d and 6.7e of the two modes (C and D in Figure 6.6d), it is deduced that the mode at C is symmetric and the mode at D is anti-symmetric. When the electric field is parallel to the particle-pair axis the higher energy mode at A is anti-symmetric, which has a smaller net dipole moment than the symmetric mode at B. The opposite is the case when the electric field is perpendicular to the particle-pair axis (higher energy mode at C is symmetric), so the higher energy mode has a larger dipole moment.

Now it is known from the investigations above that the two SLRs, which are observed for certain pitches, for each incident electric field polarization are symmetric and anti-symmetric, similar to the single pair response. The observed SLRs can now be linked to the optical response of the single pair. In the experiment, when the incident electric field is parallel to the particle pair-axis, for the $g = 350$ nm array (blue solid line in Figure 6.4a) the observed optical response is similar to the single pair response (solid black line in Figure 6.2b), as in the spectral region of the particle plasmon resonance the array is non-diffracting. Similarly, because of the spectral position of the diffraction edge, for the perpendicular polarization of the electric field, the single pair response is obtained (compare blue solid line in Figure 6.4b with magenta solid line in Figure 6.2b). Moving on to the $g = 400$ nm array, the diffraction edge is now positioned, spectrally, in the middle of the single pair resonances (see resonances A and C in Figure 6.2b), but the key point here is that the relative strengths of the two modes are different: resonance A is weaker than C. Because of this difference in strength, it would be predicted that for the parallel electric field polarization, the SLR associated with the single pair resonance A will be weak. The SLR associated with the single pair resonance A is not seen in the experiment, but is seen in the model (compare green solid line in Figures 6.4a and 6.5a). For the perpendicular electric field polarization for $g = 400$ nm, the optical response of the array is similar to the single pair response, but with the diffraction edge cutting through the single pair resonance (see resonance C in Figure 6.2b). For the longer pitches ($g = 450$ nm and $g = 500$ nm) when the incident electric field parallel to the particle-pair axis, an SLR associated with the single pair resonance A is not seen (see red and cyan solid lines in Figure 6.4a), because the single pair resonance A is weaker and further away from the diffraction edge than B (see black solid line in Figure 6.2b). For the longer pitches of array, when the electric field

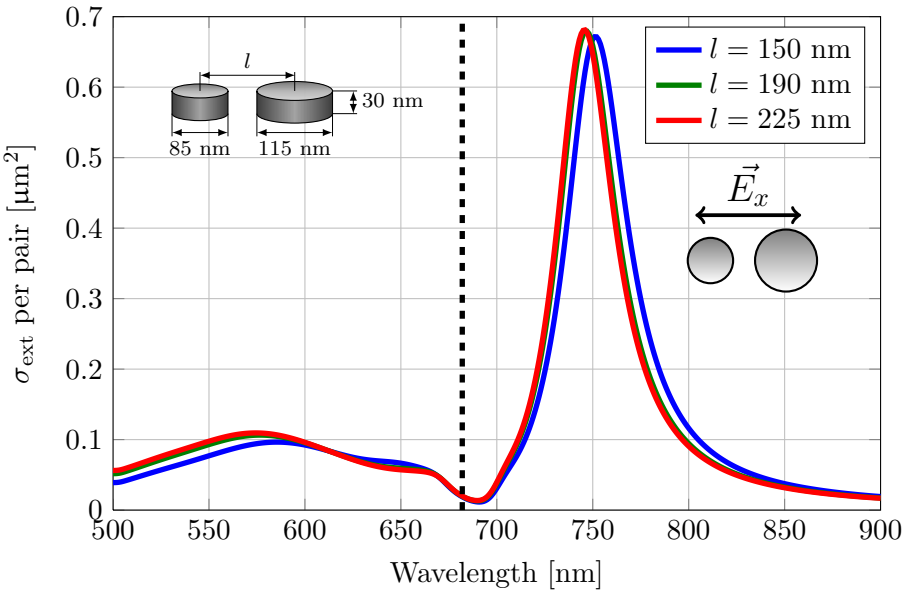

(a) $\vec{E}$ parallel to pair axis.

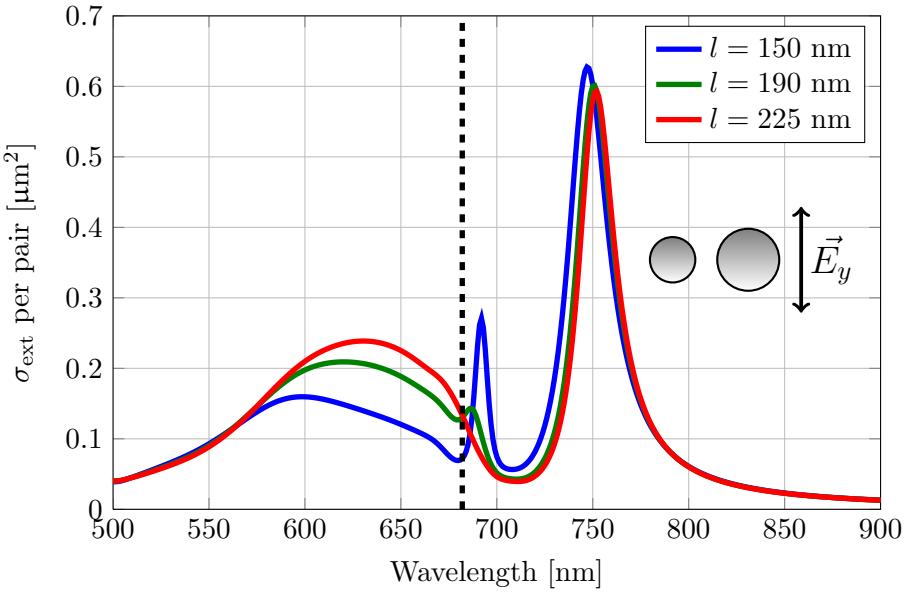

(b) $\vec{E}$ perpendicular to pair axis.

Figure 6.8: S-factor calculated extinction cross-section per particle pair of 450 nm pitch square arrays with an asymmetric two-particle basis (d_1 = 85 nm and d_2 = 115 nm, both with 30 nm height). The calculations were performed for three different centre-to-centre separations, l, of the pair (l = 150 nm, 190 nm and 225 nm). The incident electric field was parallel to the particle-pair axis in (a) and perpendicular in (b).

polarization is oriented perpendicular to the particle-pair axis, the shorter wavelength mode (see resonance C in Figure 6.2b) of the single pair is stronger, so SLRs associated with the shorter wavelength single pair resonance are seen.

Now that the nature of the two modes (symmetric and anti-symmetric) have been confirmed by FEM, it would be interesting to investigate whether the symmetric mode disappears when the centre-to-centre separation is approximately $\lambda/2$, providing destructive interference between the scattered light from the particles. To study the dependence of the symmetric mode on the centre-to-centre separation, l, three different 450 nm pitch square arrays with an asymmetric two-particle basis ($d_1 = 85$ nm and $d_2 = 115$ nm with height 30 nm) were modelled with $l = 150$ nm, 190 nm and 225 nm (see Figure 6.8). In (a) the incident electric field is parallel to the particle-pair axis and in (b) perpendicular. For the parallel electric field orientation only one strong SLR is seen for each different l. The single strong SLR is observed because the single pair resonance A is weak and is, spectrally, further away from the diffraction edge than resonance B (compare resonances A and B with red dashed line in Figure 6.2b). When the incident electric field is perpendicular to the pair (see Figure 6.8b), two strong SLRs are seen for $l = 150$ nm and $l = 190$ nm in the extinction spectra because the single pair resonance C, which is further away from the diffraction than resonance D, is stronger than the single pair resonance A in the parallel case (compare A and C in Figure 6.2b). The longer wavelength SLR in Figure 6.8b is an anti-symmetric resonance and the shorter symmetric. The strength of the symmetric mode reduces as l is increased, until $l \approx \lambda/2$, where the resonantly scattered light between the particles in the pair arrives out-of-phase causing destructive interference.

Next how the degree of asymmetry affects the optical response is investigated. Figure 6.9 shows CDA calculated extinction cross-section of five different particle pairs. The pairs have a centre-to-centre separation of 150 nm and height of 30 nm. Particle 1 is kept constant ($d_1 = 90$ nm) while the diameter of particle 2 was increased from smaller to larger than particle 1: pair 1 has $d_1 = 90$ nm (left) and $d_2 = 55$ nm (right); pair 2 $d_1 = 90$ nm (left) and $d_2 = 80$ nm (right); pair 3 $d_1 = 90$ nm (left) and $d_2 = 90$ nm (right); pair 4 $d_1 = 90$ nm (left) and $d_2 = 105$ nm (right) and pair 5 $d_1 = 90$ nm (left) and $d_2 = 110$ nm (right). In (a) the incident electric field is parallel to the particle-pair axis and in (b) perpendicular. The diffraction edge of a 500 nm pitch square array is illustrated by a black dashed line.

Presented in Figure 6.10 are SEMs of 500 nm pitch square arrays with a two-particle basis. The calculated extinction cross-section of the different bases are shown in Figure 6.9. Normal-incidence extinction spectra of the arrays shown in the SEMs in Figure 6.10

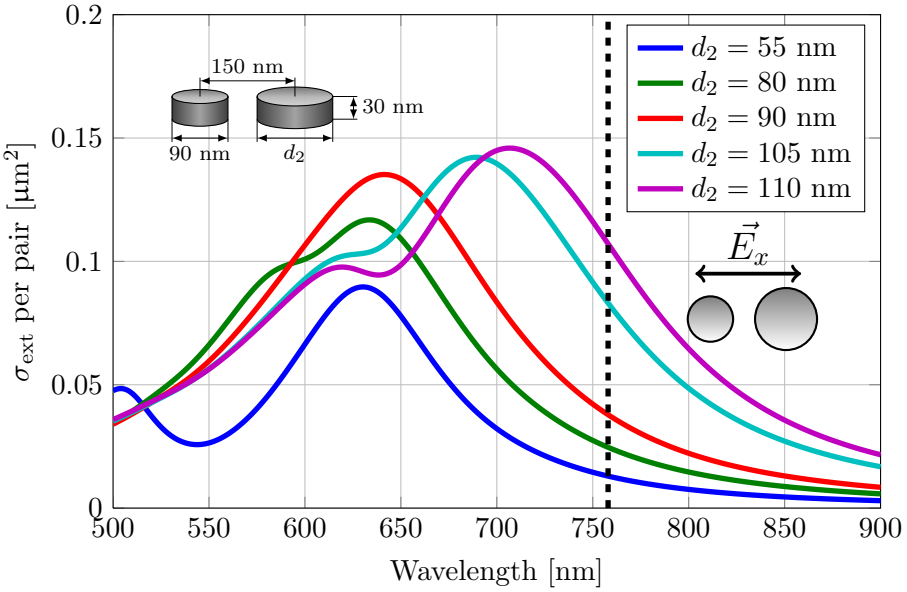

(a) $\vec{E}$ parallel to pair axis.

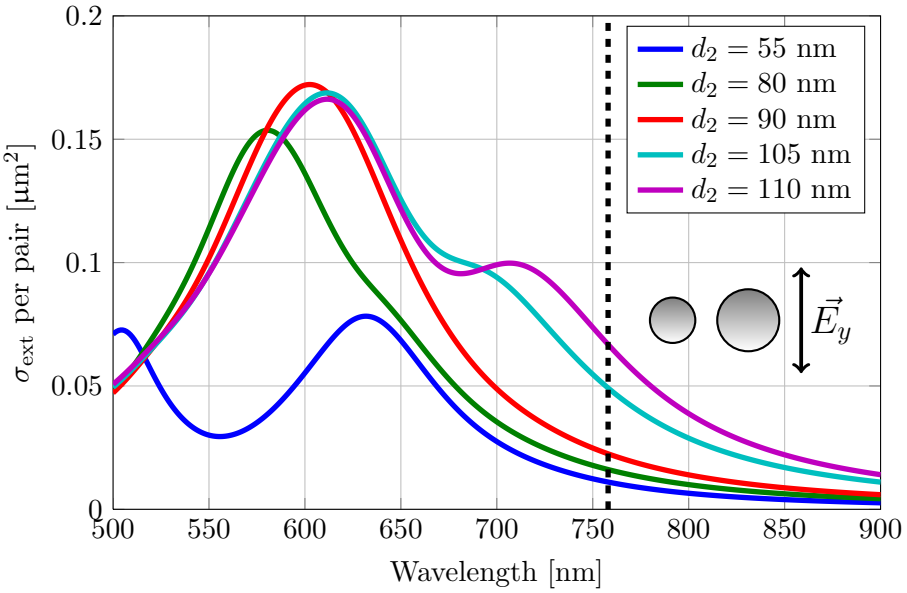

(b) $\vec{E}$ perpendicular to pair axis.

Figure 6.9: Coupled-dipole approximation calculated extinction cross-section per particle pair of different single isolated asymmetric pairs. For each of the particle pairs, $d_1 = 90$ nm while d_2 is varied. In (a) the incident electric field is parallel to the particle-pair axis and in (b) perpendicular. The environment of the particle has $n = 1.515$. The diffraction edge for a 500 nm pitch square array is illustrated by a black dashed line.

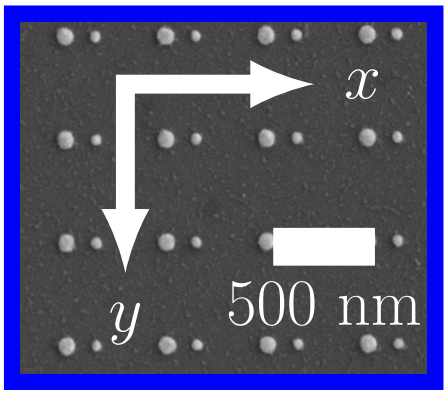

(a) Pair 1: $d_1 = 90$ nm (left) and $d_2 = 55$ nm (right).

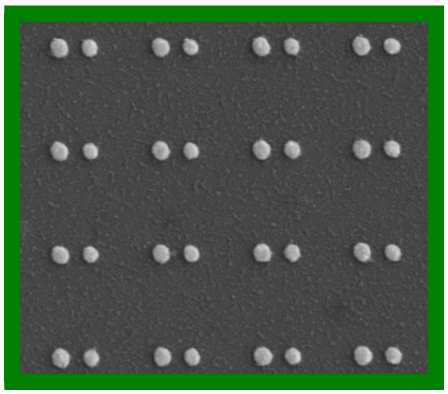

(b) Pair 2: $d_1 = 90$ nm (left) and $d_2 = 80$ nm (right).

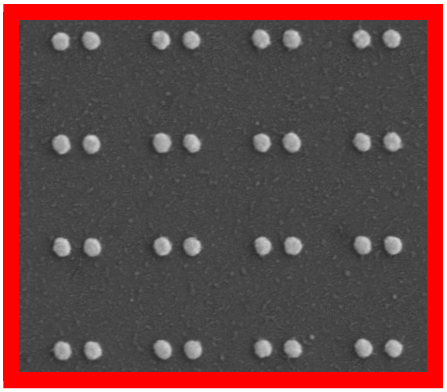

(c) Pair 3: $d_1 = 90$ nm (left) and $d_2 = 90$ nm (right).

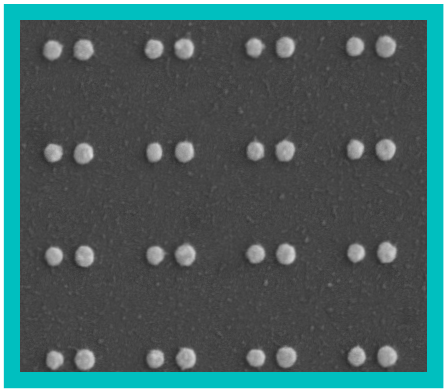

(d) Pair 4: $d_1 = 90$ nm (left) and $d_2 = 105$ nm (right).

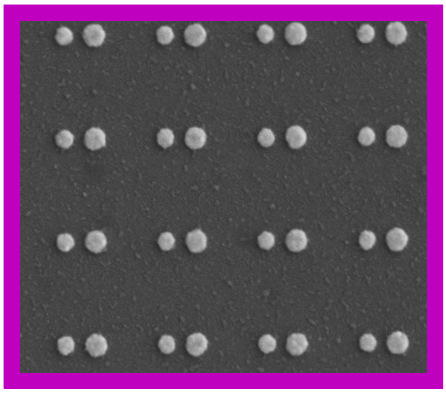

(e) Pair 5: $d_1 = 90$ nm (left) and $d_2 = 110$ nm (right).

Figure 6.10: Scanning-electron micrographs of 500 nm pitch square arrays with different asymmetric two-particle bases of silver discs with a 150 nm centre-to-centre separation and 30 nm height. (a) pair 1: $d_1 = 90$ nm (left) and $d_2 = 55$ nm (right); (b) pair 2: $d_1 = 90$ nm (left) and $d_2 = 80$ nm (right), (c) pair 3: $d_1 = 90$ nm (left) and $d_2 = 90$ nm (right), (d) pair 4: $d_1 = 90$ nm (left) and $d_2 = 105$ nm (right) and (e) pair 5: $d_1 = 90$ nm (left) and $d_2 = 110$ nm (right).

are presented in Figure 6.11. The incident electric field is parallel to the particle-pair axis in (a) and perpendicular in (b). Considering when the electric field is parallel to the particle-pair axis (see Figure 6.11a), each different pair array has a single SLR occurring at approximately 770 nm. The SLR increases in strength and red-shifts with increasing particle 2 diameter ($d_2 = 55$ nm to 110 nm). For the electric field perpendicular to the pair axis (see Figure 6.11b), two SLRs are now exhibited in each extinction spectrum except for the symmetric pair case ($d_1 = d_2 = 90$ nm). Interestingly, the longer wavelength SLR is stronger relative to the shorter wavelength SLR for diameters of particle 2 $d_2 = 55$ nm and $d_2 = 110$ nm.

Again, to verify the nature of the SLRs, FEM was used to find the spatial distribution of the electric fields. Displayed in Figure 6.12 are FEM calculated extinction cross-section per particle pair and spatial electric field distributions for a symmetric basis ($d_1 = d_2 = 90$ nm) and asymmetric basis ($d_1 = 90$ nm, $d_2 = 110$ nm). In (a) the extinction spectra for the symmetric basis are shown for the incident electric field parallel to the pair axis (blue solid line) and perpendicular (green solid line). The electric field distributions for positions A and B in (a) are shown in (c) and (d) respectively. In (b) the extinction spectra for the asymmetric basis are shown for parallel (red solid line) and perpendicular (cyan solid line). The electric field distributions for positions C, D and E in (b) are shown in (e-g) respectively. The letter inset top left in (c-g) corresponds to the spectral positions in (a) and (b). In Figure 6.12a, a single SLR is seen when the electric field is parallel (position A) or perpendicular (position B) to the particle-pair axis. Positions A and B in Figure 6.12a are symmetric modes, as the dipole moments of particle 1 and particle 2 are parallel (see Figures 6.12c and 6.12d). A second mode is not seen in the model (see Figure 6.12a) because the anti-symmetric mode of a symmetric pair has a zero net dipole moment. There is a weak second mode seen in the experiment (see red solid line in Figure 6.11b) due to a residual slight asymmetry between the fabricated particles in the basis. For the asymmetric pair (see Figure 6.12b), only a single SLR is seen when the incident electric field is parallel to the particle-pair axis (position C, red solid line), but two are seen when perpendicular (positions D and E, cyan solid line). The SLR at position C is a symmetric mode (see Figure 6.12e), position D is symmetric mode (see Figure 6.12f) and position E is anti-symmetric mode (see Figure 6.12g).

Again, when the incident electric field polarization is parallel to the particle-pair axis (see Figure 6.9a), for the asymmetric pairs, the short wavelength resonance is weak and is further away from the diffraction edge than the long wavelength resonance, so an SLR associated with the short wavelength resonance is not observed in the experiment (see Figure 6.11a). The symmetric SLR becomes stronger as d_2 is increased, because the

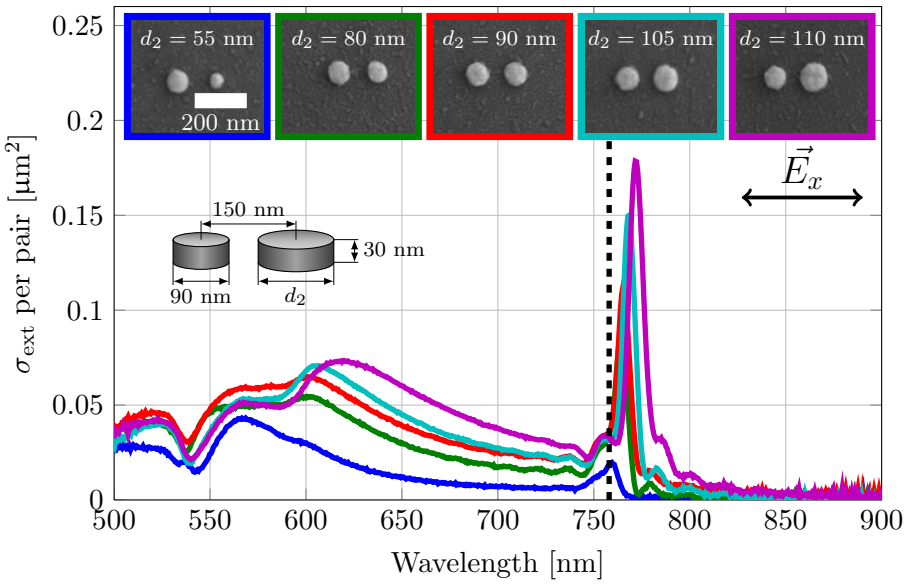

(a) $\vec{E}$ parallel to pair axis.

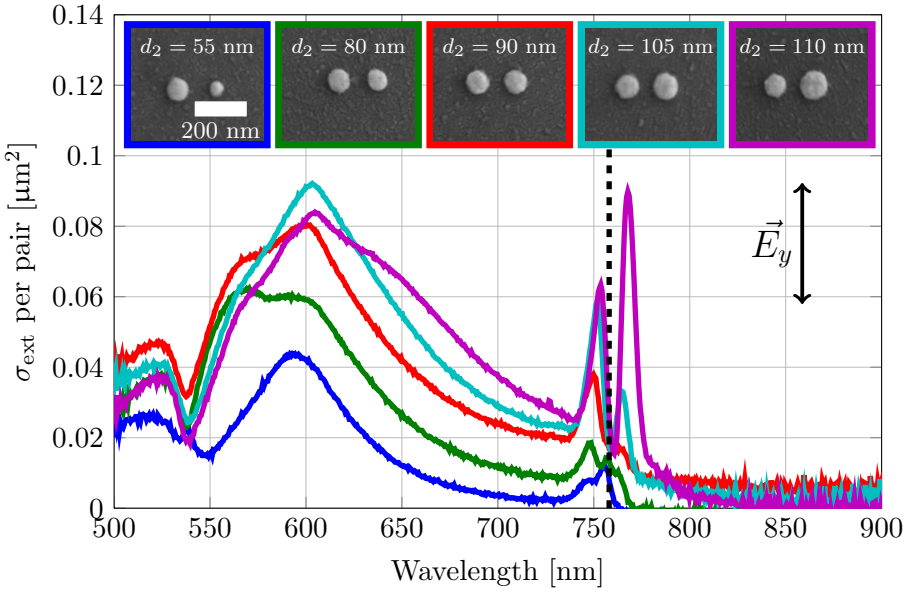

(b) $\vec{E}$ perpendicular to pair axis.

Figure 6.11: Measured extinction cross-section per pair vs. wavelength of 500 nm pitch square arrays with a two-particle basis of silver discs with a centre-to-centre separation of 150 nm and height 30 nm, see Figure 6.10 for scanning-electron micrographs of arrays. The diameter of particle 1 in the pair was kept constant (d_1 = 90 nm) while the diameter of particle 2 was increased from smaller to larger than particle 1. The incident electric field was (a) parallel to the pair axis or (b) perpendicular. The environment of the particles was index-matched with the substrate using oil with n = 1.515. The diffraction edge is illustrated with a black dashed line at 758 nm.

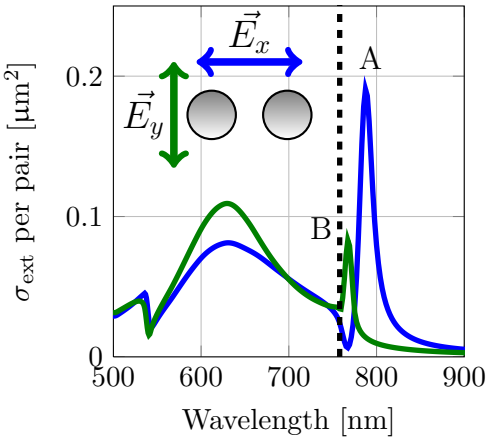

(a) $d_1 = d_2 = 90$ nm.

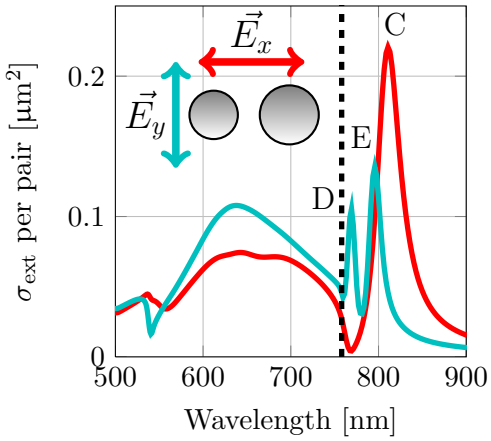

(b) $d_1 = 90$ nm and $d_2 = 110$ nm.

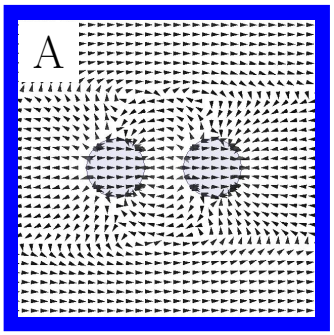

(c) $\vec{E}$ parallel to pair axis (781 nm, symmetric mode).

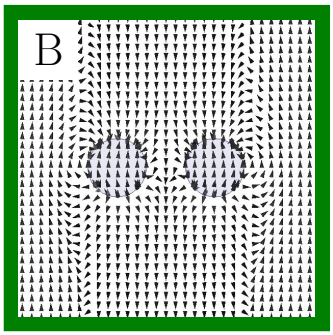

(d) $\vec{E}$ perpendicular to pair axis (761 nm, symmetric mode).

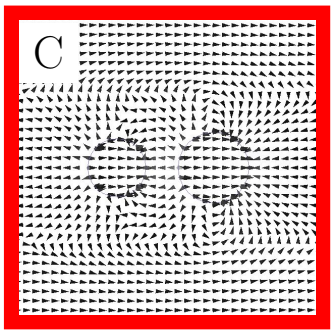

(e) $\vec{E}$ parallel to pair axis (804 nm, symmetric mode).

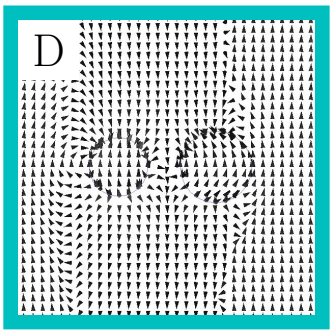

(f) $\vec{E}$ perpendicular to pair axis (761 nm, symmetric mode).

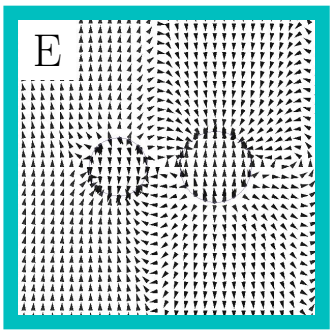

(g) $\vec{E}$ perpendicular to pair axis (790 nm, anti-symmetric mode).

Figure 6.12: Finite-element model calculated (a,b) extinction spectra and (c-g) spatial distribution of electric fields for a symmetric basis ($d_1 = d_2 = 90$ nm) and asymmetric basis ($d_1 = 90$ nm and $d_2 = 110$ nm) in a 500 nm pitch square array. Spatial distribution of electric field for points A and B in (a) are shown in (c) and (d) respectively. Spatial distributions of electric field for points C, D and E in (b) are shown in (e-g) respectively. Inset top left in (c-g) are letters that correspond to the spectral positions in (a,b).

symmetric single pair resonance red-shifts and becomes stronger with increasing d_2.

When the incident electric field is perpendicular to the particle-pair axis (see Figure 6.9b), the short wavelength resonance of the single pair for $d_2 = 80$ nm, 105 nm and 110 nm is stronger than the long wavelength resonance. Two strong SLRs are seen in the experimental spectra (see Figure 6.11b), for $d_2 = 105$ nm (cyan line) and $d_2 = 110$ nm (magenta line) when the electric field is perpendicular to the particle-pair axis. The relative strengths of the symmetric and asymmetric SLRs change between $d_2 = 105$ nm and $d_2 = 110$ nm because the long wavelength (anti-symmetric) resonance of the single pair becomes stronger and red-shifts when d_2 is increased from 105 nm to 110 nm. Notice that the symmetric SLR strength for $d_2 = 105$ nm and $d_2 = 110$ nm in the experiment are similar in strength because the symmetric single pair resonances are similar (compare cyan and magenta lines in Figure 6.9b).

6.4 Conclusion

Arrays with an asymmetric-two-particle basis have been fabricated by electron-beam lithography and their extinction as a function of wavelength measured. An analytical coupled-dipole model has been used to simulate the optical response (extinction cross-section) of these arrays and has shown good agreement with the experimental results. In contrast to the symmetric two-particle basis arrays in Chapter 5, an asymmetric basis exhibits two surface lattice resonances (SLRs) when the incident electric field is perpendicular to the particle-pair axis. The nature of these SLRs was investigated by finite-element modelling, finding that the two SLRs were symmetric and anti-symmetric. In a symmetric mode the dipole moments of both particles in the basis are parallel and in an anti-symmetric mode they are anti-parallel. The anti-symmetric mode is not observed in the symmetric basis in Chapter 5 as the net dipole moment is zero.

Chapter 7

Conclusions and future work

In this chapter, the conclusions of each of the chapters in this thesis are presented, concluding with an overall summary. Following this suggestions for future work, and finally a list of publications and presentations is given.

7.1 Conclusions

In Chapter 1, it was shown that light incident on a metallic nanoparticle causes the particles' conduction electrons to oscillate sinusoidally, inducing an oscillating dipole moment. At certain frequencies, corresponding to particle plasmon resonances, the absorption and scattering of light by a metallic nanoparticle is enhanced. These plasmonic resonances, were found to occur when the denominator of the particle polarizability was minimized, where the polarizability describes the response of the collective charge oscillation to an external electric field. In a particle, the collective motion of the electrons is altered compared to the bulk material by the restraint of the particle boundary, which dictates the surface charge distribution of the particle. The response of the electrons in the bulk metal can be described by the permittivity: for metals their optical response is dominated by their conduction electrons (free electrons), so at optical frequencies they behave as a Drude metal.

Following this was a review of the relevant current literature in the field of plasmonics. Previous studies showed that for different shapes of an isolated single particle light was resonantly scattered at different frequencies, a result of the different restoring force acting on the electrons in the particle from the change in surface charge distribution.

The particle plasmon resonance was also reported to red-shift on an increase in particle size, arising from retardation of the internal and external (applied) electric fields. Previous work demonstrated that for particle pairs in close proximity (less than $\lambda/2$), the electric near-field from the neighbouring particle could either be in the same or opposite direction to the internal field of the adjacent particle. When the incident electric field is parallel to the particle-pair axis, the electric field from the neighbouring particle is in the *opposite* direction to the internal field of the adjacent particle: the net electric field acting on the oscillating electrons in the adjacent particle is decreased, leading to red-shift of the particle plasmon resonance position. When the incident electric field is perpendicular to the particle-pair axis, the electric field from the neighbouring particle and the internal field of the adjacent particle are in the *same* direction, the net electric field acting on the oscillating electrons is increased, and the particle plasmon resonance position is blue-shifted. For greater separations, (approximately greater than λ) there was a modulation in spectral position and FWHM of the combined particle plasmon resonance of the pair via their interaction through the far-field component of the electric field.

In early work it was shown that narrow spectral features can be observed in the extinction spectrum of arrays of plasmonic particles with a separation of roughly the resonant wavelength. Normal-incidence light excites an in-plane dipole moment in each of the particles, which in turn re-radiate (elastically scatters) the light into the far-field. These narrow features are the result of constructive interference of the resonantly scattered light from each of the particles. By changing the pitch of the array and/or particle dimensions the position and width of the collective resonances may be changed. For oblique angle of incidence of light, an out-of-plane dipole moment may be excited: the collective electron oscillation of the surface charge of the particle is then parallel to its height dimension.

In Chapter 2, various modelling techniques were introduced to describe the plasmonic response of a non-spherical particle via its polarizability. First, the quasi-static approximation was introduced to model the response of spherical and non-spherical particles. The change of shape was incorporated into a geometrical factor associated with each axis, which physically arises from the change in surface charge distribution. The geometrical factor of each axis dictates the spectral position of the particle plasmon resonance associated with that axis: as the geometrical factor is reduced the position of the particle plasmon resonance red-shifts for both silver and gold. Optical cross-sections calculated using Mie theory of different radii of silver spheres were presented to discuss the general features of particle plasmon resonances. It was shown for a 5 nm radius

silver particle, the extinction is dominated by absorption; for a 25 nm radius sphere, absorption and scattering are comparable in magnitude; whilst for a 30 nm radius sphere, scattering dominates. The extinction cross-sections of the different modelling techniques (quasi-static approximation, Modified long-wavelength approximation and Kuwata) were then compared with Mie theory for three different radii of silver spheres.

The fabrication of silver particles by electron-beam lithography (EBL) and optical measurements by dark-field spectroscopy were described. Comparison of the experimental scattering spectra of different radii of silver discs was compared to modified long-wavelength calculated spectra. Good agreement was found in the spectral positions of the particle plasmon resonance for larger diameters of disc (d = 100 nm and d = 125 nm), but poor agreement for smaller (d = 70 nm, d = 85 nm, d = 95). There were a number of differences between the experiment and model suggested in the chapter for this discrepancy. The resonantly scattered light by the discs, which was confirmed experimentally, allows them to couple together via their electric fields, and this was investigated in different array geometries in Chapter 3.

Chapter 3 is concerned with the study of surface lattice resonances (SLRs) in different array geometries through theory and experiment. It was demonstrated in the review of current literature in Chapter 1, that narrow spectral features could be observed in arrays with particle separations of approximately λ. In Chapter 3, the in-plane dipole moment of each particle was excited by normal-incident light and the extinction of each array measured. The scattered light from the in-plane dipole moment associated with each particle allows the particles in the array to collectively couple together in the far-field. Methods of modelling the optical response of the array were introduced: the coupled-dipole approximation, a simple-coupled dipole model and the finite-element model. The extinction cross-section per particle calculated using these three different methods was compared and the processing of the calculated spectra to reproduce the resolution of the spectrometer was discussed. EBL fabrication of the particles was discussed, particularly proximity effects and distortion of the particles at the extremities of the write-field. This was followed by a description of the optical characterization techniques implemented on the particle arrays. Extinction measurements on square, hexagonal and honeycomb arrays displaying SLRs were presented and compared to the simple coupled-dipole model. The SLRs were found to occur where the real parts of $1/\alpha$ and $\varepsilon_0 S$ intersected. Good agreement was found between experiment and the simple coupled-dipole model in the shape of the extinction spectra, but the magnitude of the predicted extinction cross-section was found to be much larger than experiment. The polarization sensitivity, to incident light, of the three different array geometries was

then probed by linearly-polarized light: the arrays possess a high degree of symmetry, therefore they were shown to be polarization insensitive.

In Chapter 4, rectangular arrays of silver discs were fabricated by EBL to explore the coupling between particle resonances. The optical response (extinction) of these arrays was measured at normal-incidence, and their extinction cross-section compared with the simple coupled-dipole model introduced in Chapter 3. It was found that the optical response of the rectangular arrays was dependent upon the polarization of the incident electric field, in contrast to the square, hexagonal and honeycomb arrays, which possess a high degree of symmetry, investigated in Chapter 3. Further experimental investigation, revealed that the particles couple together in the direction orthogonal to the applied electric field. By comparison of the simple coupled-dipole extinction cross-section with the experiment, SLRs were found to be stronger and sharper in the model. This difference in strength and width of the SLRs was accounted for by particle size dispersion in the experiment. By modelling the extinction cross-section of different pitches of particle chains, and also by separating the different components of the scattered electric field from the particles, the coupling mechanism between particle resonances was ascertained to be via the far-field component of the electric field.

In Chapter 5, square arrays with a symmetric one- and two-particle basis were fabricated by EBL and their polarization response to the incident electric field measured. The polarization response of the one-particle basis arrays was found to be similar when the incident electric field was parallel or perpendicular to the pair axis, with the difference being attributed to the slight asymmetry of the particles in the EBL process. As the pitch of the square arrays was increased, and hence the diffraction edge shifted, the SLR associated with the array moved to longer wavelengths and occurred spectrally closer to the diffraction edge. This was understood by considering the polarizability of the particle, which includes phase information of the collective oscillation with respect to an applied electric field: at shorter wavelengths than the particle plasmon resonance, the phase is greater than $\pi/2$, increasing as the wavelength is decreased; at resonance, $\pi/2$; and at longer wavelengths than resonance, less than $\pi/2$, decreasing as the wavelength is increased. At wavelengths much longer than resonance, the phase of the electron oscillation is nearly in phase with the electric field, explaining why the SLR occurred close to the diffraction edge.

Measurements on two-particle basis arrays found that for the incident electric field polarized parallel to the particle-pair axis, a similar response was obtained to the one-particle basis of the same dimensions. A different extinction spectrum was found when the electric field was perpendicular to the particle-pair axis. The SLRs occurred when

the real parts $1/\alpha$ and ε_0 intersected or at their closest approach. The largest difference in spectral shape between the two incident electric field polarizations was for the 400 nm pitch array. Following this observation, a 400 nm pitch square array was used to investigate whether the optical response of the particle pair could be modelled as a single polarizable unit, which excluded retardation of the electric field between the particles in the pair, instead of two separate particles each with their own polarizability. It was found that the particles must be modelled as separate particles; the separation between the particles is important due to retardation of the scattered electric field between them. This finding led to additional measurements on particle pairs with different separations between particles in the pair. In the experiment, when the incident electric field was polarized perpendicular to the particle-pair axis, for the smallest centre-to-centre separation of 160 nm, the strongest SLR was observed. The SLR was found to reduce in strength as the centre-to-centre separation was increased from 160nm to 220 nm, until at a separation of approximately $\lambda/2$ the SLR had nearly vanished, due to destructive interference of the resonantly scattered light from neighbouring particles.

In Chapter 6, square arrays with an asymmetric two-particle basis were studied. Arrays with an asymmetric two-particle basis were fabricated by EBL and characterized by normal-incidence-extinction measurements. The measured extinction cross-section was compared to a modified simple coupled-dipole model, which had been adapted to accept two different particle polarizabilities. It was found when the incident electric field was polarized perpendicular to the particle-pair axis that two sharp SLRs were observed. Investigation of the electric field distributions of these modes, using finite-element modelling, showed the two modes were symmetric (the dipole moments of particle 1 and 2 are parallel) and anti-symmetric (the dipole moments of particle 1 and 2 are anti-parallel). The anti-symmetric mode of an asymmetric particle pair has a non-zero net dipole moment, in contrast to a symmetric pair, thus allowing coupling of light to this mode. Further measurements on particle arrays, where the asymmetry of the pair was varied, confirmed the nature of the two SLRs: the asymmetric mode disappeared for a symmetric particle pair. For normal-incidence light, the anti-symmetric mode of a symmetric pair has zero net dipole moment and can not be coupled to by radiation.

In summary, the investigations reported here have advanced the understanding of the in-plane dipolar coupling of plasmonic particles in arrays with a pitch comparable to the wavelength. In particular, SLRs were studied in different array geometries with the diffraction edge in the same spectral position, finding that they all display SLRs but at slightly different spectral positions. Studying rectangular arrays and chains found that the particles couple together in the direction that is orthogonal to the

applied electric field with their far-field component of the scattered electric field. For particle pairs, the centre-to-centre separation is important and leads to retardation of the scattered electric field between the particles in the pair. When the centre-to-centre separation approaches $\lambda/2$ the light scattered between the particles in the pair interferes destructively and destroys the coherent interaction between the dipoles. Arrays with an asymmetric two-particle basis may support both symmetric and anti-symmetric SLRs when illuminated with an electric field polarized perpendicular to the particle-pair axis.

7.2 Future work

In this section, possible extensions to the work reported in this thesis are suggested.

7.2.1 Direct extensions

A possible direct extension would be to experimentally measure the dispersion relation of SLRs in arrays with a one-particle basis. For non-normal incidence, two different frequencies of incident light will be diffracted in the plane of the particles, in contrast to one frequency for normal incidence (see Figure 3.10b), and this will change the optical response of the array. Further dispersion measurements will also confirm the physical cause of the small dip observed in transmission, which in previous studies [80] has been suggested as being attributed to divergence of the incident beam.

In Chapter 6 the anti-symmetric mode of a particle pair was excited by introducing asymmetry in the pair, which provided a non-zero net dipole moment for the anti-symmetric mode. The anti-symmetric mode of a symmetric particle pair may be excited by breaking the symmetry of the excitation of the light, i.e. by illuminating the array by non-normal incidence. It would be interesting to compare the relative strengths and widths of the symmetric and antisymmetric SLRs associated with a symmetric pair and asymmetric pair. A good starting point would be to reproduce the data set of Figure 6.4, but with a symmetric pair illuminated by non-normal incidence light.

In Chapter 5 the SLR dependence on the centre-to-centre separation between a symmetric particle pair was studied and the SLR was found to reduce for the perpendicular polarization of the electric field, nearly disappearing completely, for separations of approximately $\lambda/2$ (see Figure 5.13b). The S-factor calculated extinction cross-section of a 450 nm pitch square array with an asymmetric basis showed that for a centre-to-centre

separation of approximately $\lambda/2$ and with the electric field polarized perpendicular to particle-pair axis, the symmetric SLR completely vanished (see Figure 6.8b). It would be interesting to explore this centre-to-centre dependence of the relative strengths of the symmetric and anti-symmetric SLRs of asymmetric pairs by experiment.

7.2.2 Graphene-like plasmonic lattices

An extension of the work presented in this thesis would be to experimentally explore the similarities between graphene, where electrons hop between lattice sites, and graphene-like (i.e. honeycomb) plasmonic lattices. Previous reported work has explored this theoretically in Refs. [129, 130], but it has yet to be followed up by experiment. Fabrication challenges will be to reduce the length scale from approximately 500 nm reported in this work to approximately 100 nm, which is required to achieve the large wavevectors needed for the Dirac-like modes. These smaller pitch arrays would be non-diffracting in the spectral region of the particle plasmon resonance in contrast to the diffracting arrays investigated in this thesis.

7.2.3 Surface lattice resonance mediated lasing

An extension of the work presented here would be to use surface lattice resonances (SLRs) for lasing by tuning the SLR wavelength of the array to the emission wavelength of a dye-doped polymer. The features of the SLR, such as resonant enhanced scattering in the plane of the particles, can be used as an optical resonator for a laser. The dye-doped polymer can then be pumped at its absorption wavelength using a laser pulse, which puts the dye molecules into an excited state from which stimulated emission may occur. Early studies have observed lasing by tuning the spectral position of the diffraction edge [131] or SLR [55] to the dye emission wavelength, but it is underdetermined which conditions yield a lower laser threshold and a higher intensity [132].

7.3 Publications and presentations

7.3.1 Refereed papers

- 'Excitonic surface lattice resonances' (in preparation for Journal of Optics).

- 'Surface lattice resonances in plasmonic arrays of asymmetric disc dimers' (under review for ACS Photonics).
- 'Plasmonic surface lattice resonances in arrays of metallic nanoparticle dimers' (accepted for publication in Journal of Optics).
- Humphrey, A.D. and Barnes, W.L. Plasmonic surface lattice resonances on arrays of different lattice symmetry. *Phys. Rev. B*, **90**, 075404, (2014). Ref. [56].

7.3.2 Oral presentations

- Humphrey A.D., Meinzer, N. and Barnes, W.L. A Study in Asymmetry: Resonances in Arrays of Asymmetric Disc Dimers (invited). *PIERS 2015*, *Prague, Czech Republic* (July 2015).
- Barnes, W.L. and Humphrey, A.D. Plasmonic Crystals (invited). *Applied Nano Photonics*, *Bad Bentheim, Germany* (June 2015).
- Humphrey, A.D. and Barnes, W.L. Plasmonic Surface Lattice Resonances for Different Lattice Symmetries. *Nanolight 2014*, *Benasque, Spain* (March 2014).

7.3.3 Poster presentations

- Humphrey A.D., Meinzer, N. and Barnes, W.L. Narrow Surface Lattice Resonances on Arrays of Plasmonics Particle Pairs. *NANOMETA 2015*, *Seefeld, Austria* (January 2015).
- Meinzer, N., Humphrey A.D. and Barnes, W.L.. Asymmetric dot dimers - optical properties and interactions. *NANOMETA 2015*, *Seefeld, Austria* (January 2015).

References

[1] Hutter, E. and Fendler, J.H. Exploitation of Localized Surface Plasmon Resonance. *Advanced Materials*, **16**, 1685 (2004). 1

[2] Bingham, J.M., Willets, K.A., Shah, N.C., Andrews, D.Q., and Van Duyne, R.P. Localized Surface Plasmon Resonance Imaging: Simultaneous Single Nanoparticle Spectroscopy and Diffusional Dynamics. *Journal of Physical Chemistry C Letters*, **113**, 16839 (2009).

[3] Sung, J., Hicks, E.M., Van Duyne, R.P., and Spears, K.G. Nanoparticle Spectroscopy: Dipole Coupling in Two-Dimensional Arrays of L-Shaped Silver Nanoparticles. *Journal of Physical Chemistry C*, **111**, 10368 (2007). 1

[4] Meinzer, N., Barnes, W.L., and Hooper, I.R. Plasmonic meta-atoms and metasurfaces. *Nature Photonics*, **8**, 889 (2014). 1, 3

[5] Murray, W.A. and Barnes, W.L. Plasmonic Materials. *Advanced Materials*, **19**, 3771 (2007). 2

[6] Kreibig, U. and Vollmer, M. *Optical Properties of Metal Clusters*. Springer-Verlag Berlin Heidelberg, Germany (2010). ISBN 978-3-642-08191-0. 3, 38

[7] Bohren, C.F. and Huffman, D.R. *Absorption & Scattering of Light by Small Particles*. Wiley-VCH Verlag GmbH & Co., Weinheim (2004). 3, 14, 38, 39, 40, 43, 45

[8] Chan, G.H., Zhao, J., Schatz, G.C., and Van Duyne, R.P. Localized Surface Plasmon Resonance Spectroscopy of Triangular Aluminum Nanoparticles. *Journal of Physical Chemistry C*, **112**, 13958 (2008). 4

[9] Langhammer, C., Yuan, Z., Zorić, I., and Kasemo, B. Plasmonic Properties of Supported Pt and Pd Nanostructures. *Nano Letters*, **6**, 833 (2006). 4

[10] Lynch, D.W. and Hunter, W.R. *Handbook of Optical Constants of Solids*. Academic, New York (1985). 10, 11, 41, 44, 47, 69

[11] Johnson, P.B. and Christy, R. Optical Constants of the Noble Metals. *Physical Review B*, **6**, 4370 (1972). 10, 11, 41

[12] Mock, J.J., Smith, D.R., and Schultz, S. Local Refractive Index Dependence of Plasmon Resonance Spectra from Individual Nanoparticles. *Nano Letters*, **3**, 485 (2003). 10

[13] Murray, W.A., Auguié, B., and Barnes, W.L. Sensitivity of Localized Surface Plasmon Resonances to Bulk and Local Changes in the Optical Environment. *Journal of Physical Chemistry C*, **113**, 5120 (2009). 10

[14] Link, S. and El-Sayed, M.A. Spectral Properties and Relaxation Dynamics of Surface Plasmon Electronic Oscillations in Gold and Silver Nanorods. *Journal of Physical Chemistry B*, **103**, 8410 (1999). 11

[15] Barbic, M., Mock, J.J., Smith, D.R., and Schultz, S. Single crystal silver nanowires prepared by the metal amplification method. *Journal of Applied Physics*, **91**, 9341 (2002). 11, 12

[16] Link, S., Mohamed, M.B., and El-Sayed, M.a. Simulation of the Optical Absorption Spectra of Gold Nanorods as a Function of Their Aspect Ratio and the Effect of the Medium Dielectric Constant. *Journal of Physical Chemistry B*, **103**, 3073 (1999). 11, 13

[17] van der Zande, B.M.I., Böhmer, M.R., Fokkink, L.G.J., and Schönenberger, C. Aqueous Gold Sols of Rod-Shaped Particles. *Journal of Physical Chemistry B*, **101**, 852 (1997). 11

[18] Mohamed, M.B., Ismail, K.Z., Link, S., and El-Sayed, M.A. Thermal Reshaping of Gold Nanorods in Micelles. *Journal of Physical Chemistry B*, **102**, 9370 (1998). 11

[19] Funston, A.M., Novo, C., Davis, T.J., and Mulvaney, P. Plasmon Coupling of Gold Nanorods at Short Distances and in Different Geometries. *Nano Letters*, **9**, 1651 (2009). 11, 13, 24

[20] Pérez-Juste, J., Rodríguez-González, B., Mulvaney, P., and Liz-Marzán, L.M. Optical Control and Patterning of Gold-Nanorod-Poly(vinyl alcohol) Nanocomposite Films. *Advanced Functional Materials*, **15**, 1065 (2005). 12

[21] Kabashin, A.V., Evans, P., Pastkovsky, S., Hendren, W., Wurtz, G.A., Atkinson, R., Pollard, R., Podolskiy, V.A., and Zayats, A.V. Plasmonic nanorod metamaterials for biosensing. *Nature Materials*, **8**, 867 (2009).

[22] Wurtz, G.A., Dickson, W., O'Connor, D., Atkinson, R., Hendren, W., Evans, P., Pollard, R., and Zayats, A.V. Guided plasmonic modes in nanorod assemblies: strong electromagnetic coupling regime. *Optics Express*, **16**, 7460 (2008). 12

[23] Mock, J.J., Barbic, M., Smith, D.R., Schultz, D.A., and Schultz, S. Shape effects in plasmon resonance of individual colloidal silver nanoparticles. *Journal of Chemical Physics*, **116**, 6755 (2002). 12, 14, 16, 50

[24] Anker, J.N., Hall, W.P., Lyandres, O., Shah, N.C., Zhao, J., and Van Duyne, R.P. Biosensing with plasmonic nanosensors. *Nature Materials*, **7**, 442 (2008). 12

[25] Jin, R., Cao, Y., Mirkin, C.A., Kelly, K.L., Schatz, G.C., and Zheng, J.G. Photoinduced Conversion of Silver Nanospheres to Nanoprisms. *Science*, **294**, 1901 (2001). 13, 15

[26] Jayabalan, J., Singh, A., and Chari, R. Effect of edge smoothening on the extinction spectra of metal nanoparticles. *Applied Physics Letters*, **97**, 041904 (2010). 13

[27] Henson, J., DiMaria, J., and Paiella, R. Influence of nanoparticle height on plasmonic resonance wavelength and electromagnetic field enhancement in two-dimensional arrays. *Journal of Applied Physics*, **106**, 093111 (2009). 13, 15, 30

[28] Pain, H.J. *The Physics of Vibration and Waves*. John Wiley & Sons Ltd., Chichester, 6th edition (2006). 14

[29] Sönnichsen, C., Franzl, T., Wilk, T., von Plessen, G., Feldmann, J., Wilson, O., and Mulvaney, P. Drastic Reduction of Plasmon Damping in Gold Nanorods. *Physical Review Letters*, **88**, 077402 (2002). 16, 17

[30] Sherry, L.J., Jin, R., Mirkin, C.A., Schatz, G.C., and Van Duyne, R.P. Localized Surface Plasmon Resonance Spectroscopy of Single Silver Triangular Tanoprisms. *Nano Letters*, **6**, 2060 (2006). 15

[31] Hecht, E. *Optics*. Addison Wesley, forth edition (2002). 17, 50

[32] Griffiths, D.J. *Introduction to Electrodynamics*. Pearson Bejamin Cummings, third edition (2008). 18

[33] Gunnarsson, L., Rindzevicius, T., Prikulis, J., Kasemo, B., Käll, M., Zou, S., and Schatz, G.C. Confined Plasmons in Nanofabricated Single Silver Particle Pairs: Experimental Observations of Strong Interparticle Interactions. *Journal of Physical Chemistry B*, **109**, 1079 (2005). 20, 21, 23, 24, 26, 56, 117, 138

[34] Aćimović, S.S., Kreuzer, M.P., González, M.U., and Quidant, R. Plasmon Near-Field Coupling in Metal Dimers as a Step toward Single-Molecule Sensing. *ACS Nano*, **3**, 1231 (2009). 23

[35] Rechberger, W., Hohenau, a., Leitner, a., Krenn, J.R., Lamprecht, B., and Aussenegg, F.R. Optical properties of two interacting gold nanoparticles. *Optics Communications*, **220**, 137 (2003). 23, 108, 117

[36] Fromm, D.P., Sundaramurthy, A., Schuck, P.J., Kino, G., and Moerner, W.E. Gap-Dependent Optical Coupling of Single "Bowtie" Nanoantennas Resonant in the Visible. *Nano Letters*, **4**, 957 (2004). 23

[37] Tabor, C., Murali, R., Mahmoud, M., and El-Sayed, M.A. On The Use of Plasmonic Nanoparticle Pairs As a Plasmon Ruler: The Dependence of the Near-Field Dipole Plasmon Coupling on Nanoparticle Size and Shape. *Journal of Physical Chemistry A*, **113**, 1946 (2009). 24

[38] Jain, P.K., Huang, W., and El-Sayed, M.A. On the Universal Scaling Behavior of the Distance Decay of Plasmon Coupling in Metal Nanoparticle Pairs: A Plasmon Ruler Equation. *Nano Letters*, **7**, 2080 (2007). 24, 117

[39] Su, K.H., Wei, Q.H., Zhang, X., Mock, J.J., Smith, D.R., and Schultz, S. Interparticle Coupling Effects on Plasmon Resonances of Nanogold Particles. *Nano Letters*, **3**, 1087 (2003). 24

[40] Dahmen, C., Schmidt, B., and von Plessen, G. Radiation Damping in Metal Nanoparticle Pairs. *Nano Letters*, **7**, 318 (2007). 24, 25, 26

[41] Olk, P., Renger, J., Wenzel, M.T., and Eng, L.M. Distance Dependent Spectral Tuning of Two Coupled Metal Nanoparticles. *Nano Letters*, **8**, 1174 (2008). 24, 26

[42] Haynes, C.L., McFarland, A.D., Zhao, L., Van Duyne, R.P., Schatz, G.C., Gunnarsson, L., Prikulis, J., Kasemo, B., and Käll, M. Nanoparticle Optics: The Importance of Radiative Dipole Coupling in Two-Dimensional Nanoparticle Arrays. *Journal of Physical Chemistry B*, **107**, 7337 (2003). 26, 27, 29, 63, 79

[43] Lamprecht, B., Schider, G., Lechner, R.T., Ditlbacher, H., Krenn, J.R., Leitner, A., and Aussenegg, F.R. Metal Nanoparticle Gratings: Influence of Dipolar Particle Interaction on the Plasmon Resonance. *Physical Review Letters*, **84**, 4721 (2000). 27, 28, 29, 59, 82

[44] Auguié, B. and Barnes, W.L. Collective Resonances in Gold Nanoparticle Arrays. *Physical Review Letters*, **101**, 143902 (2008). 28, 29, 60, 63, 79, 91

[45] Chu, Y., Schonbrun, E., Yang, T., and Crozier, K.B. Experimental observation of narrow surface plasmon resonances in gold nanoparticle arrays. *Applied Physics Letters*, **93**, 181108 (2008). 29, 30, 60, 79

[46] Zhou, W. and Odom, T.W. Tunable subradiant lattice plasmons by out-of-plane dipolar interactions. *Nature Nanotechnology*, **6**, 423 (2011). 30, 31, 32, 60

[47] Kravets, V.G., Schedin, F., and Grigorenko, A.N. Extremely Narrow Plasmon Resonances Based on Diffraction Coupling of Localized Plasmons in Arrays of Metallic Nanoparticles. *Physical Review Letters*, **101**, 087403 (2008). 31, 60, 79, 108

[48] Kravets, V.G., Schedin, F., Pisano, G., Thackray, B., Thomas, P.A., and Grigorenko, A.N. Nanoparticle arrays : From magnetic response to coupled plasmon resonances. *Physical Review B*, **90**, 125445 (2014). 31, 107, 108

[49] Thackray, B.D., Kravets, V.G., Schedin, F., Auton, G., Thomas, P.A., and Grigorenko, A.N. Narrow Collective Plasmon Resonances in Nanostructure Arrays Observed at Normal Light Incidence for Simplified Sensing in Asymmetric Air and Water Environments. *ACS Photonics*, **1**, 1116 (2014). 31, 60, 63, 68, 111

[50] de Waele, R., Koenderink, A.F., and Polman, A. Tunable Nanoscale Localization of Energy on Plasmon Particle Arrays. *Nano Letters*, **7**, 2004 (2007). 33

[51] Zou, S. and Schatz, G.C. Silver nanoparticle array structures that produce giant enhancements in electromagnetic fields. *Chemical Physics Letters*, **403**, 62 (2005). 33

[52] Väkeväinen, A.I., Moerland, R.J., Rekola, H.T., Eskelinen, A., Martikainen, J.P., Kim, D.H., and Törmä, P. Plasmonic Surface Lattice Resonances at the Strong Coupling regime. *Nano Letters*, **14**, 1721 (2014). 33, 91

[53] Rodriguez, S.R.K. and Gómez Rivas, J. Surface lattice resonances strongly coupled to Rhodamine 6G excitons: tuning the plasmon-exciton-polariton mass and composition. *Optics Express*, **21**, 27411 (2013). 33, 91

[54] Stehr, J., Crewett, J., Schindler, F., Sperling, R., Von Plessen, G., Lemmer, U., Lupton, J.M., Klar, T.A., Feldmann, J., Holleitner, A.W., Forster, M., and Scherf, U. A Low Threshold Polymer Laser Based on Metallic Nanoparticle Gratings. *Advanced Materials*, **15**, 1726 (2003). 33

[55] Zhou, W., Dridi, M., Suh, J.Y., Kim, C.H., Co, D.T., Wasielewski, M.R., Schatz, G.C., and Odom, T.W. Lasing action in strongly coupled plasmonic nanocavity arrays. *Nature Nanotechnology*, **8**, 506 (2013). 33, 163

[56] Humphrey, A.D. and Barnes, W.L. Plasmonic surface lattice resonances on arrays of different lattice symmetry. *Physical Review B*, **90**, 075404 (2014). 34, 35, 164

[57] Wokaun, A., Gordon, J.P., and Liao, P.F. Radiation Damping in Surface-Enhanced Raman Scattering. *Physical Review Letters*, **48**, 957 (1982). 42

[58] Meier, M. and Wokaun, A. Enhanced fields on large metal particles: dynamic depolarization. *Optics Letters*, **8**, 581 (1983). 42

[59] Moroz, A. Depolarization field of spheroidal particles. *Journal of the Optical Society of America B*, **26**, 517 (2009). 42

[60] Jensen, T., Kelly, L., Lazarides, A., and Schatz, G.C. Electrodynamics of Noble Metal Nanoparticles and Nanoparticle Clusters. *Journal of Cluster Science*, **10**, 295 (1999). 42, 47

[61] Maradudin, A.A., Sambles, R.J., and Barnes, W.L. *Modern Plasmonics*. Elsevier Science (2014). 42

[62] Kuwata, H., Tamaru, H., Esumi, K., and Miyano, K. Resonant light scattering from metal nanoparticles: Practical analysis beyond Rayleigh approximation. *Applied Physics Letters*, **83**, 4625 (2003). 42, 43

[63] Mie, G. Beiträge zur Optik trüber Medien, speziell kolloidaler Metallösungen. *Annalen der Physik*, **25**, 377 (1908). 43

[64] SPlaC: SERS and Plasmonics Codes. www.victoria.ac.nz/raman/book/codes.aspx (Accessed: 27th September 2015). 45

[65] Vieu, C., Carcenac, F., Pépin, A., Chen, Y., Mejias, M., Lebib, A., Manin-Ferlazzo, L., Couraud, L., and Launois, H. Electron beam lithography: resolution limits and applications. *Applied Surface Science*, **164**, 111 (2000). 47

[66] Broers, A.N., Hoole, A.C.F., and Ryan, J.M. Electron beam lithography - Resolution limits. *Microelectronic Engineering*, **32**, 131 (1996). 48

[67] Stepanova, M. and Dew, S. *Nanofabrication - Techniques and Principles*. Springer-Verlag Wien, first edition (2012). ISBN 978-3-7091-0423-1. 48

[68] Hu, M., Novo, C., Funston, A., Wang, H., Staleva, H., Zou, S., Mulvaney, P., Xia, Y., and Hartland, G.V. Dark-field microscopy studies of single metal nanoparticles: understanding the factors that influence the linewidth of the localized surface plasmon resonance. *Journal of Materials Chemistry*, **18**, 1949 (2008). 50

[69] Sherry, L.J., Chang, S.H., Schatz, G.C., Van Duyne, R.P., Wiley, B.J., and Xia, Y. Localized Surface Plasmon Resonance Spectroscopy of Single Silver Nanocubes. *Nano Letters*, **5**, 2034 (2005).

[70] Knight, M.W., Fan, J., Capasso, F., and Halas, N.J. Influence of excitation and collection geometry on the dark field spectra of individual plasmonic nanostructures. *Optics Express*, **18**, 2579 (2010).

[71] Fan, J.A., Bao, K., Lassiter, J.B., Bao, J., Halas, N.J., Nordlander, P., and Capasso, F. Near-Normal Incidence Dark-Field Microscopy: Applications to Nanoplasmonic Spectroscopy. *Nano Letters*, **12**, 2817 (2012).

[72] Sönnichsen, C., Franzl, T., Wilk, T., von Plessen, G., and Feldmann, J. Plasmon resonances in large noble-metal clusters. *New Journal of Physics*, **4**, 93.1 (2002). 50

[73] Olson, J., Dominguez-Medina, S., Hoggard, A., Wang, L.Y., Chang, W.S., and Link, S. Optical characterization of single plasmonic nanoparticles. *Chemical Society Review*, **44**, 40 (2015). 50

[74] Sönnichsen, C. and Alivisatos, A.P. Gold Nanorods as Novel Nonbleaching Plasmon-Based Orientation Sensors for Polarized Single-Particle Microscopy. *Nano Letters*, **5**, 301 (2005). 50

[75] Murphy, D.B. *Fundamentals of Light Microscopy and Electronic Imaging*. Wiley-Liss (2001). 50, 75

[76] Sönnichsen, C., Geier, S., Hecker, N.E., von Plessen, G., Feldmann, J., Ditlbacher, H., Lamprecht, B., Krenn, J.R., Aussenegg, F.R., Chan, V.Z.H., Spatz, J.P., and Möller, M. Spectroscopy of single metallic nanoparticles using total internal reflection microscopy. *Applied Physics Letters*, **77**, 2949 (2000). 50

[77] Lindfors, K., Kalkbrenner, T., Stoller, P., and Sandoghdar, V. Detection and Spectroscopy of Gold Nanoparticles Using Supercontinuum White Light Confocal Microscopy. *Physical Review Letters*, **93**, 037401 (2004). 50

[78] Hicks, E.M., Zou, S., Schatz, G.C., Spears, K.G., Van Duyne, R.P., Gunnarsson, L., Rindzevicius, T., Kasemo, B., and Käll, M. Controlling Plasmon Line Shapes through Diffractive Coupling in Linear Arrays of Cylindrical Nanoparticles Fabricated by Electron Beam Lithography. *Nano Letters*, **5**, 1065 (2005). 59

[79] Sung, J., Hicks, E.M., Van Duyne, R.P., and Spears, K.G. Nanoparticle Spectroscopy: Plasmon Coupling in Finite-Sized Two-Dimensional Arrays of Cylindrical Silver Nanoparticles. *Journal of Physical Chemistry C*, **112**, 4091 (2008). 59

[80] Rodriguez, S.R.K., Schaafsma, M.C., Berrier, A., and Gómez Rivas, J. Collective resonances in plasmonic crystals: Size matters. *Physica B*, **407**, 4081 (2012). 60, 63, 82, 162

[81] Auguié, B. and Barnes, W.L. Diffractive coupling in gold nanoparticle arrays and the effect of disorder. *Optics Letters*, **34**, 401 (2009). 60, 79, 115, 119

[82] Purcell, E.M. and Pennypacker, C.R. Scattering and Absorption of Light by Nonspherical Dielectric Grains. *The Astrophysical Journal*, **186**, 705 (1973). 60

[83] Draine, B.T. and Flatau, P.J. Discrete-dipole approximation for scattering calculations. *Journal of the Optical Society of America A*, **11**, 1491 (1994). 60

[84] Burrows, C. *Plasmonic resonances of metallic nanoparticles in arrays and in isolation.* Ph.D. thesis, University of Exeter (2010). 60, 62

[85] Stratton, J.A. *Electromagnetic Theory.* McGraw-Hill, New York (1941). 61

[86] Draine, B.T. The Discrete-Dipole Approximation and Its Application to Interstellar Graphite Grains. *The Astrophysical Journal*, **333**, 848 (1988). 61

[87] Zou, S., Janel, N., and Schatz, G.C. Silver nanoparticle array structures that produce remarkably narrow plasmon lineshapes. *Journal of Chemical Physics*, **120**, 10871 (2004). 63, 68, 79

[88] Zhao, L., Kelly, K.L., and Schatz, G.C. The Extinction Spectra of Silver Nanoparticle Arrays: Influence of Array Structure on Plasmon Resonance Wavelength and Width. *Journal of Physical Chemistry B*, **107**, 7343 (2003). 63, 64

[89] Parsons, J. *Nanoparticles and nanocomposites for display applications.* Ph.D. thesis, University of Exeter (2009). 64

[90] Auguié, B. *Optical properties of gold nanostructures.* Ph.D. thesis, University of Exeter (2009). 66, 80

[91] Markel, V.A. Divergence of dipole sums and the nature of non-Lorentzian exponentially narrow resonances in one-dimensional periodic arrays of nanospheres. *Journal of Physics B*, **38**, L115 (2005). 68

[92] Dhatt, G. and Touzot, G. *The Finite Element Method Displayed.* John Wiley & Sons, Chichester, first edition (1984). 68

[93] Peterson, A.F., Ray, S.L., and Mittra, R. *Computational Methods for Electromagnetics.* Wiley-IEEE Press, first edition (1997). ISBN 0780311221. 69

[94] Hibbins, A.P., Evans, B.R., and Sambles, J.R. Experimental Verification of Designer Surface Plasmons. *Science*, **308**, 670 (2005). 69

[95] Murray, W.A., Suckling, J.R., and Barnes, W.L. Overlayers on Silver Nanotriangles: Field Confinement and Spectral Position of Localized Surface Plasmon Resonances. *Nano Letters*, **6**, 1772 (2006). 69

[96] Lockyear, M.J., Hibbins, A.P., and Sambles, J.R. Microwave Surface-Plasmon-Like Modes on Thin Metamaterials. *Physical Review Letters*, **102**, 073901 (2009). 69

[97] Rance, H.J., Hooper, I.R., Hibbins, A.P., and Roy Sambles, J. Structurally dictated anisotropic "designer surface plasmons". *Applied Physics Letters*, **99**, 181107 (2011). 69

[98] Ansys HFSS. www.ansys.com (Accessed: 4th March 2014). 69

[99] Starkey, T.A. *Towards Bio-inspired Photonic Vapour Sensors*. Ph.D. thesis, University of Exeter (2014). 69

[100] Kittel, C. *Introduction to Solid State Physics*. Wiley, New York, third edition (1967). 69

[101] Kopp, M. *An Introduction to HFSS: Fundamental Principles, Concepts, and Use*. Ansoft, Pittsburgh, PA, first edition (2009). 70

[102] Malinsky, M.D., Kelly, K.L., Schatz, G.C., and Van Duyne, R.P. Nanosphere Lithography: Effect of Substrate on the Localized Surface Plasmon Resonance Spectrum of Silver Nanoparticles. *Journal of Physical Chemistry B*, **105**, 2343 (2001). 73

[103] Hulteen, J.C., Treichel, D.A., Smith, M.T., Duval, M.L., Jensen, T.R., and Van Duyne, R.P. Nanosphere Lithography: Size-Tunable Silver Nanoparticle and Surface Cluster Arrays. *Journal of Physical Chemistry B*, **103**, 3854 (1999).

[104] Jensen, T.R., Schatz, G.C., and Van Duyne, R.P. Nanosphere Lithography: Surface Plasmon Resonance Spectrum of a Periodic Array of Silver Nanoparticles by Ultraviolet - Visible Extinction Spectroscopy and Electrodynamic Modeling. *Journal of Physical Chemistry B*, **103**, 2394 (1999). 73

[105] Evlyukhin, A.B., Reinhardt, C., Zywietz, U., and Chichkov, B.N. Collective resonances in metal nanoparticle arrays with dipole-quadrupole interactions. *Physical Review B*, **85**, 245411 (2012). 79, 111

[106] Kuznetsov, A.I., Evlyukhin, A.B., Gonçalves, M.R., Reinhardt, C., Koroleva, A., Arnedillo, M.L., Kiyan, R., Marti, O., and Chichkov, B.N. Laser Fabrication of Large-Scale Nanoparticle Arrays for Sensing Applications. *ACS Nano*, **5**, 4843 (2011). 79

[107] Rayleigh, L. On the Dynamical Theory of Gratings. *Proceedings of the Royal Society of London. Series A*, **79**, 399 (1907). 80

[108] Vitrey, A., Aigouy, L., Prieto, P., García-Martín, J.M., and González, M.U. Parallel Collective Resonances in Arrays of Gold Nanorods. *Nano Letters*, **14**, 2079 (2014). 80

[109] Nikitin, A.G., Kabashin, A.V., and Dallaporta, H. Plasmonic resonances in diffractive arrays of gold nanoantennas: near and far field effects. *Optics Express*, **20**, 27941 (2012). 80

[110] Hibbins, A.P. *Grating Coupling of Surface Plasmon Polaritons at Visible and Microwave Frequencies*. Ph.D. thesis, University of Exeter (1999).

[111] Ng, B., Hanham, S.M., Giannini, V., Chen, Z.C., Tang, M., Liew, Y.F., Klein, N., Hong, M.H., and Maier, S.A. Lattice resonances in antenna arrays for liquid sensing in the terahertz regime. *Optics Express*, **19**, 14653 (2011). 80

[112] Vecchi, G., Giannini, V., and Gómez Rivas, J. Surface modes in plasmonic crystals induced by diffractive coupling of nanoantennas. *Physical Review B*, **80**, 201401 (2009). 80

[113] Hohenau, A., Krenn, J.R., Beermann, J., Bozhevolnyi, S.I., Rodrigo, S.G., Martin-Moreno, L., and Garcia-Vidal, F. Spectroscopy and nonlinear microscopy of Au nanoparticle arrays: Experiment and theory. *Physical Review B*, **73**, 155404 (2006). 82

[114] Kataja, M., Hakala, T.K., Julku, a., Huttunen, M.J., van Dijken, S., and Törmä, P. Surface lattice resonances and magneto-optical response in magnetic nanoparticle arrays. *Nature Communications*, **6**, 7072 (2015). 91, 101

[115] Abass, A., Rodriguez, S.R.K., Gómez Rivas, J., and Maes, B. Tailoring Dispersion and Eigenfield Profiles of Plasmonic Surface Lattice Resonances. *ACS Photonics*, **1**, 61 (2014).

[116] Rodriguez, S.R.K., Abass, A., Maes, B., Janssen, O.T.A., Vecchi, G., and Gómez Rivas, J. Coupling Bright and Dark Plasmonic Lattice Resonances. *Physical Review X*, **1**, 021019 (2011).

[117] Shi, L., Hakala, T.K., Rekola, H.T., Martikainen, J.P., Moerland, R.J., and Törmä, P. Spatial Coherence Properties of Organic Molecules Cou-

pled to Plasmonic Surface Lattice Resonances in the Weak and Strong Coupling Regimes. *Physical Review Letters*, **112**, 153002 (2014).

[118] Murai, S., Verschuuren, M.A., Lozano, G., Pirruccio, G., Rodriguez, S.R.K., and Gómez Rivas, J. Hybrid plasmonic-photonic modes in diffractive arrays of nanoparticles coupled to light-emitting optical waveguides. *Optics Express*, **21**, 4250 (2013).

[119] Offermans, P., Schaafsma, M.C., Rodriguez, S.R.K., Zhang, Y., Crego-Calama, M., Brongersma, S.H., and Gómez Rivas, J. Universal scaling of the figure of merit of plasmonic sensors. *ACS Nano*, **5**, 5151 (2011). 91

[120] DeJarnette, D., Jang, G.G., Blake, P., and Roper, D.K. Polarization angle affects energy of plasmonic features in Fano resonant regular lattices. *Journal of Optics*, **16**, 105006 (2014). 93

[121] Nishijima, Y., Khurgin, J.B., Rosa, L., Fujiwara, H., and Juodkazis, S. Tunable Raman Selectivity via Randomization of a Rectangular Pattern of Nanodisks. *ACS Photonics*, **1**, 1006 (2014). 101

[122] Li, J., Hu, X., Gu, Y., and Gong, Q. Tunable wavelength-division multiplexing based on metallic nanoparticle arrays. *Optics Letters*, **35**, 4051 (2010). 101

[123] Kravets, V.G., Schedin, F., Taylor, S., Viita, D., and Grigorenko, A.N. Plasmonic resonances in optomagnetic metamaterials based on double dot arrays. *Optics Express*, **18**, 9780 (2010). 107, 108

[124] Teperik, T.V. and Degiron, A. Design strategies to tailor the narrow plasmon-photonic resonances in arrays of metallic nanoparticles. *Physical Review B*, **86**, 245425 (2012). 111

[125] Špačková, B. and Homola, J. Sensing properties of lattice resonances of 2D metal nanoparticle arrays: An analytical model. *Optics Express*, **21**, 27490 (2013). 111

[126] Chung, H.Y., Leung, P.T., and Tsai, D.P. Modified Long Wavelength Approximation for the Optical Response of a Graded-Index Plasmonic Nanoparticle. *Plasmonics*, **7**, 13 (2012). 111

[127] Pinchuk, A.O. and Schatz, G.C. Nanoparticle optical properties: Far- and near-field electrodynamic coupling in a chain of silver spherical nanoparticles. *Materials Science and Engineering B*, **149**, 251 (2008). 117

[128] Pinchuk, A. and Schatz, G. Anisotropic polarizability tensor of a dimer of nanospheres in the vicinity of a plane substrate. *Nanotechnology*, **16**, 2209 (2005). 123

[129] Han, D., Lai, Y., Zi, J., Zhang, Z.Q., and Chan, C.T. Dirac Spectra and Edge States in Honeycomb Plasmonic Lattices. *Physical Review Letters*, **102**, 123904 (2009). 163

[130] Weick, G., Woollacott, C., Barnes, W.L., Hess, O., and Mariani, E. Dirac-like Plasmons in Honeycomb Lattices of Metallic Nanoparticles. *Physical Review Letters*, **110**, 106801 (2013). 163

[131] Schokker, A.H. and Koenderink, A.F. Lasing at the band edges of plasmonic lattices. *Physical Review B*, **90**, 1554452 (2014). 163

[132] Dridi, M. and Schatz, G.C. Lasing action in periodic arrays of nanoparticles. *Journal of the Optical Society of America B*, **32**, 818 (2015). 163